Università degli Studi di Parma

Dottorato di Ricerca in Scienze Chimiche

XXII Ciclo (2007-2009)

The role of the shape in multicomponent crystals

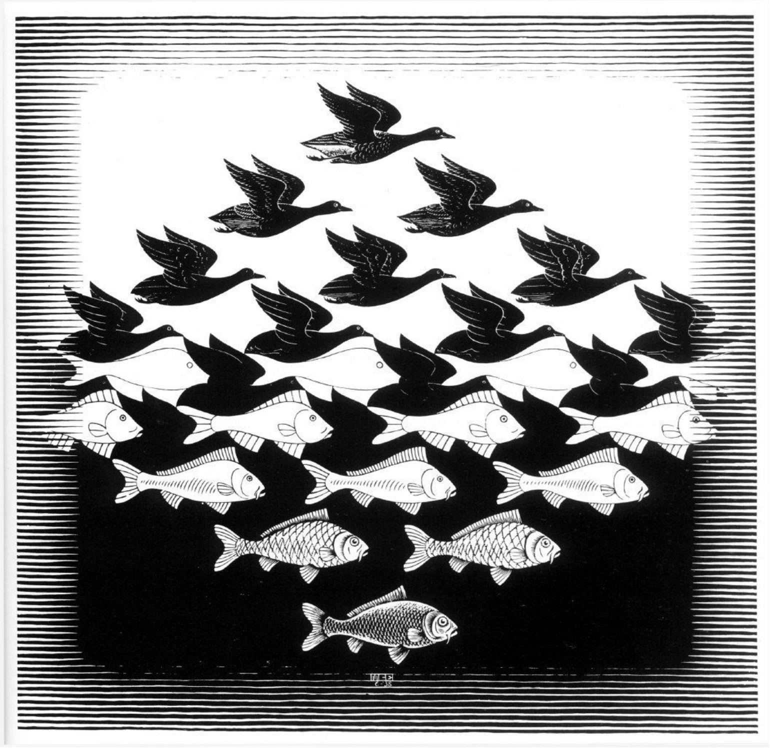

by

Tiziana Chiodo

Supervisors:
Prof. Alessia Bacchi
Prof. Mauro Carcelli

2010

to mum and dad

with love…

Natura abhorret a vacuo

Contents

Introduction

Part I

Part II

Part III

Introduction

… in a standard English dictionary the definition of "shape" reads "outer form", and the definition of "form" reads "shape".

A. Gavezzotti "*Molecular Aggregation: Structure Analysis and Molecular Simulation of Crystals and Liquids"*
(Oxford University Press, Oxford, UK, 2007)

1. Concept of shape and close packing

It is a truth universally acknowledged that the idea of "shape" is a mental picture of the human mind. Nevertheless, univocally defining and quantifying the concept of "shape" could be very difficult because *it is a non-digital but purely analogic entity*.[1] Especially in the field of the biological recognition, several theoretical and empirical methods have been proposed with the aim to rationalize the shape influences on binding modes.[2]

The question of how and why the shape has a key role in orienting and modulating crystal packing efficiency is an area of great scientific interest.[3-6] In order to investigate the features of the aggregation in condensed matter, it is important to determine the ability of the objects of occupying the available space in an efficient manner. This point is the heart of the principle of close packing formulated by Kitaigorodski.[7] From Kitaigorodski's point of view a maximum space occupation confers stability to crystals. As the most efficient packing is the most dense, in a supramolecular structure the molecules are oriented by maximizing the contacts (or, in a complementary perspective, by minimizing the voids). Kitaigorodski recognizes that, since organic crystal structures are close packed, organic molecules crystallize prevalently in space groups containing inversion, screw or glide operations, because they are the operations that maximize the close packing. In this perspective, the analysis of the modes in which the objects can pack in specific arrangements is one of the point addressed by Crystal Structures Prediction (CSP).[8-10]

Unfortunately, it is often very difficult to quantify the tendency of objects having specific shapes to realize close packed arrangements and some model systems and numerical indicators can be proposed with the aim to quantify the shape contribution to crystal packing.

In the early 17th century, Kepler suggested that for a model based on identical spherical objects, the densest packing is obtained by the fcc lattice (commonly known as *cannonball stack* arrangement, Figure 1) and occupies 74% of the available volume.[11]

The numerical indicator of the close packing realized in crystal structures is the *packing coefficient* C_{pack}, defined as:

$$C_{pack} = Z \frac{V_{mol}}{V_{cell}} \quad \textbf{(1)},$$

where Z is the number of the molecules in the unit cell, V_{mol} is the molecular volume and V_{cell} is the cell volume. Among organic molecular crystals, the average value of the packing coefficients is about 0.7-0.8, roughly the same as for close-packed assembly of rigid identical spheres, and this is achieved through the ability of the “bumps” of one molecule to fit into the “hollows” of adjacent molecules.[3] More recent studies based on data from the Cambridge Crystallographic Database (CSD)[12] confirmed Kitaigorodski’s estimate: for a group of 164 hydrocarbons with 12–20 carbon atoms the average value of the packing coefficients was 0.721, with a standard deviation of 0.022.[3] Disordered arrays of spheres can pack with efficiencies between 64% and 70%,[13] and liquids reach packing efficiency of 60% close to their freezing points.[1]

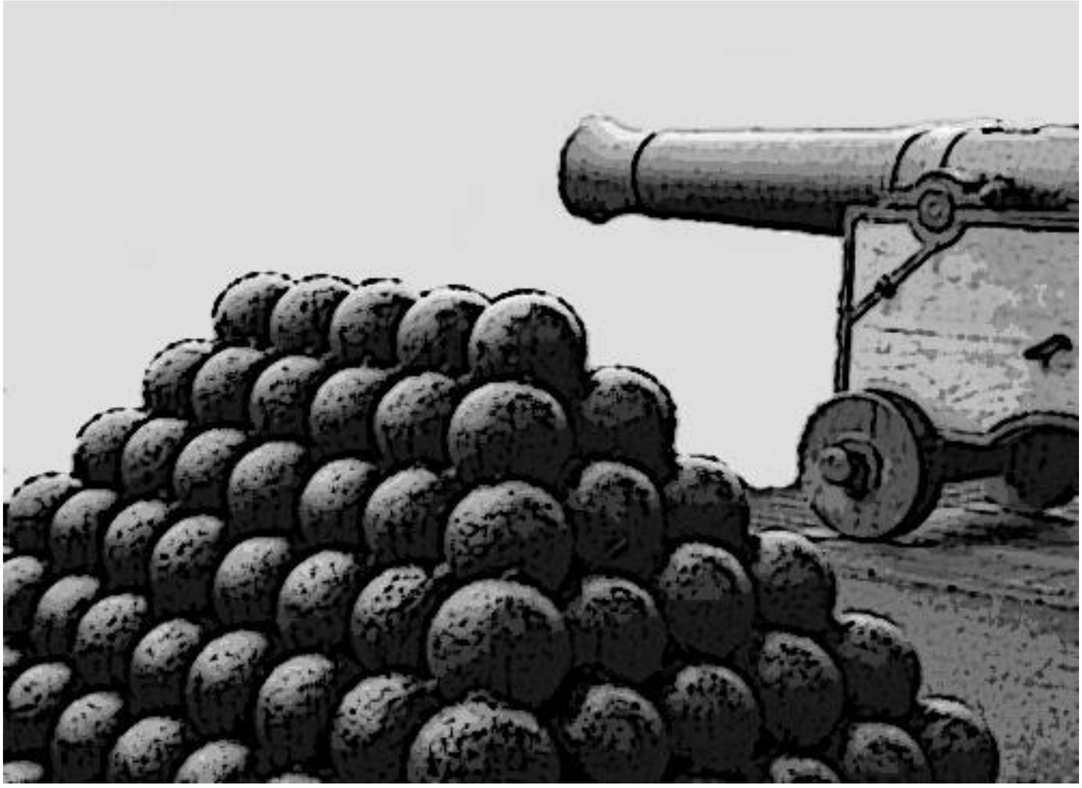

Figure 1. Identical spheres in the cannonball stack arrangement

In order to explore the real cases the problem is defining the most efficient arrangement for objects of arbitrary shapes. A numerical approach is based on the method of the surrounding boxes.[1] If V_{mol} is the volume of the molecule, V_{box} is the total volume of the box surrounding a molecule, N_{in} is the number of sample points internal to the molecule and N_{tot} the total number of box points, the *self-occupation coefficient* $C_{self,\mathrm{occ}}$ is:

$$C_{self,occ} = V_{mol} / V_{box} = N_{in} / N_{tot} \quad \mathbf{(2)},$$

where N_{in}/N_{tot} is the fraction of occupied space in the rectangular box. $C_{self,\mathrm{occ}}$ represents an index of similarity of arbitrary shape objects to parallelepipeds and it can be used as index of the intrinsic ability to occupy space efficiently.

If the complete occupation of the space is possible only for parallelepiped-based arrangements, the point is that molecules do not resemble to parallelepipeds. Nevertheless the use of simple models based on rigid object approach can be a useful tool, in order to explore the real more complexes cases. A conceptually simple model uses the *packing patterns* to describe crystal aggregation in terms of stacking of a discrete number of boxes[5]. The identical boxes, with three unequal sides, $l > m > s$, are stacked with faces touching and edges aligned and hence are described as close packed. There are six ways to close pack four boxes, resulting from three permutations into the two categories of packing patterns. These categories are named 221 and 114, depending on the number of boxes repeated in each directions (Figure 2).[5] In the packing patterns model the unit cells act as containers in which a number of boxes Z can be accommodated. The cell edges L_{cell} are expressed in terms of the molecular dimension L_{mol}. Particularly, all the permutations of the cell axes (L_{cell}) with the molecular axes (L_{mol}) can be used to give the *pattern coefficient* $c_{l,m,s}$:

$$c_{l,m,s} = L_{cell} / L_{mol} \quad \mathbf{(3)}.$$

This model agrees with the experimental data from the CSD:[12] *the packing patterns are applicable to the crystal structures and the unit cell dimensions are related with the molecular dimensions. The most populated packing patterns are those identified by the box model as having the minimum surface area for a giving volume*.[5]

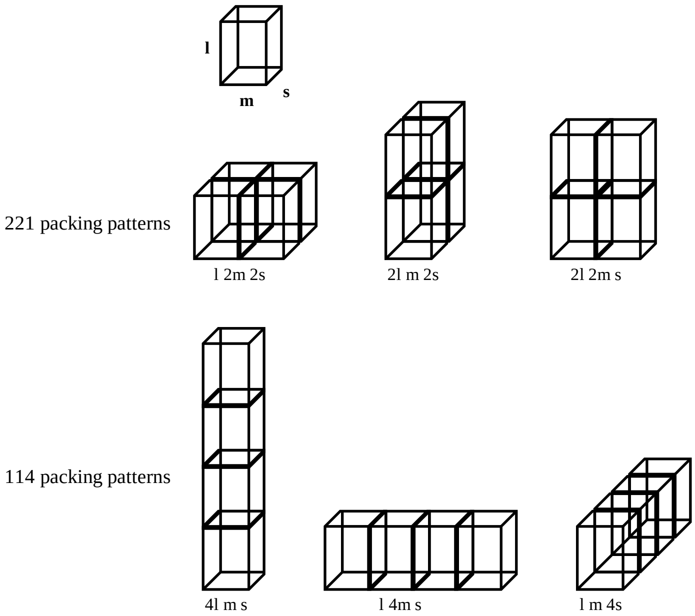

Figure 2. Packing patterns 221 and 114, from top to bottom, respectively. The container dimensions are reported below each patterns, indicating the number of boxes repeated in each dimension

2. Awkward shapes and multicomponent systems

Gavezzotti has shown the existence of a relationship between molecular self-density D_{mol}

$$D_{mol} = M_{mol} / V_{mol} \quad \mathbf{(4)}$$

(where M_{mol} and V_{mol} are the molecular mass and the molecular volume, respectively) and crystal density D_c

$$D_c = M_{cell} / V_{cell} = ZM_{mol} / V_{cell} \quad \mathbf{(5)}$$

(where M_{cell} and V_{cell} are the mass and the volume of the unit cell, respectively). The combination of the equations **4** and **5** and the use of the definition of packing coefficient C_{pack} from the equation **1**, leads to a linear plot D_c vs D_{mol} (Figure 3).[3]

The fact that crystal density correlates very strictly with molecular self-density depends primarily on the heavy atoms contained in the molecule. The slope of about 0.72 represents the average value of the packing coefficient in organic molecular crystals. These numerical considerations partially quantify the close packing principle.

In order to introduce the effect of the shape in this discussion, it is peculiar to observe that the trend of the packing coefficient values follows the trend of the self-occupation coefficients ($C_{self,,occ}$, equation **2**), strictly connected with shape complexity. The features of the linear plot D_c vs D_{mol} at the ends reflect the pure shape effects. The shift from the linearity that appears on the right-upper side of the plot (highlighted green) means an high ability in space filling allowed for compact molecules. Instead the shift towards lower crystal density values appearing on the left-lower side of the plot (highlighted red) represents the cases in which the presence of substituents perturbs the shape regularity of the packing molecules. “Awkward” shape molecules find many difficulties to assembly themselves into highly close packed structures. The consequence of this difficulty often result in formation of solvate and hydrate species. Whenever the shape is too complex to allow an efficient self-recognition, the molecules might generate a multicomponent system, in order to respect the close packing principle.[14]

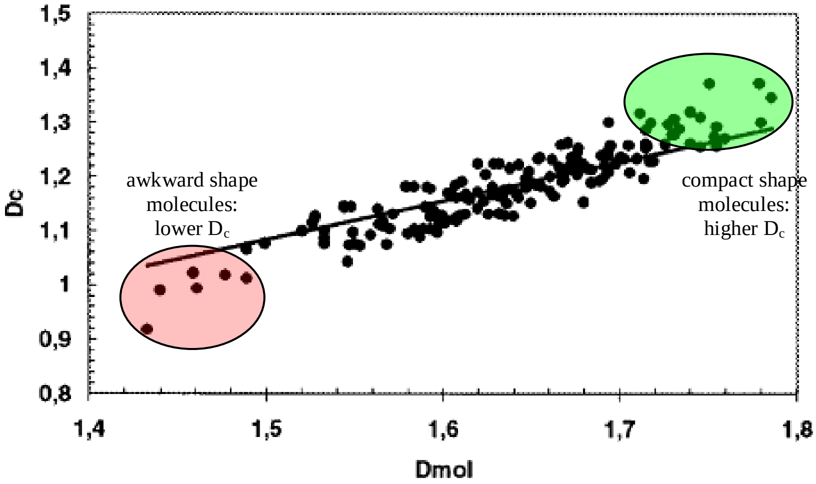

Figure 3. Relationship between crystal density D_c and molecular self-density $D_{mol.}$ The highlight green and red regions represent the case of the highly close packed arrangements formed by the more compact molecules and the systems with low packing efficiency formed by the assembly of awkward shape molecules, respectively

3. Multicomponent system assembly

The multicomponent systems might be thought as combinations of different objects, able to lead together to an efficient space tiling. A multicomponent system can be formed by the association objects that have complementary or identical/similar shape, as appearing in Escher’s works (Figure 4). Particularly, complementary shape, as fishes and birds, are able to fill the space only in particular stoichiometric ratios while for identical/similar shape, as red and grey fishes, a complete space filling is possible in any ratio.

Figure 4. Plane tiling by objects of complementary shape, like fishes and birds (left) or identical shape, like red and grey fishes (right)

The rationalization of the assembly of the multicomponent systems covers a very broad area. On one hand, it is a truth acknowledged that molecules have an innate structural selfishness.[15] On the other hand there are empirical evidences of the formation of systems including more than one molecular species. Basically, there are two approaches to the design of multicomponent assemblies. First, it should be considered that the close packing is easier achieved if the components are “identical”.[5] So, close packed structures derive from the assembly of a single molecular species, if the shapes of the building blocks are enough compact. In the same way, the close packing principle enables the formation of multicomponent systems whenever the space cannot be filled by too complex shape molecules. Second, the crystal packing analysis should include the overall field of the intermolecular interactions.[16] The role of the intermolecular interactions in crystal packing has been largely studied. Particularly, Etter’s principles for hydrogen bonded crystals[17] and Desiraju’s approach of the supramolecular synthons[18] are basic benchmarks in crystal design.

Kitaigorodski’s considerations about the formation of the most densely packed structures are not applicable to the crystals held together by hydrogen bonds or other specific strong and directional supramolecular interactions. These crystals could be considered as exceptions to the close packing principle because the strongly directional nature of such bonds can lead to more open arrangements. The design strategies establishing a synthon hierarchy[18] for relatively strong, specific interactions, such as hydrogen bonds and halogen bonds, is a very useful tool in order to predict molecular recognition in crystal assembly.[19-22] However this approach could fail due to the presence of a multitude of weaker, non-specific interactions that seriously limit the ability to design crystals. The shape acts as an additional empiric parameter accompanying all the energetic considerations, sometimes explained by a trial-and-error screening procedure.[23-24]

The state-of-the-art of Crystal Engineering[25-26] is strongly based on the ability of assembly the multicomponent systems into predictable arrays, by controlling molecular recognition and aggregation *via* supramolecular interactions and coordination bonds.[27-30] The definition of multicomponent system is often open to interpretation, as evidenced by the debate regarding the differences between solvates, pseudopolymorphs and cocrystals.[31-39] A distinction between the two areas of solvates and cocrystals has finally been suggested,[40-42] also if the confine line is very thin. Strictly, the difference is the presence of small molecules that have melting points close to ambient temperature (usually solvent molecules), included in a larger host, in the solvates and of molecules that have similar size and that are solid at ambient temperature in the cocrystals. At this point of the discussion, a brief overview on the two classes of multicomponent systems is reported.

4. Inclusion compounds …

In the field of the inclusion compounds a subjectivity in the assignment of the definitions of "host" and "guest" is not immune to liberties of interpretations. Generally the host is identified as a molecule, or a supramolecular motif, with binding sites capable to capture guest molecules. Cram defined a host macrocycle as a molecule that possess convergent binding sites, whereas a guest binds divergently.[43] In order to put constraints on interpretative freedom, a list of the levels of solid-state inclusions has been proposed as well.[44] Weber gave a good background on the key principles of design of inclusion compounds,[45] according with the fact that molecular recognition is the heart of the inclusion chemistry and that host-guest affinity depends on both the presence of specific intermolecular interactions and size and shape factors.

Looking on Weber's studies, inclusion compound chemistry has grown dramatically. Host species have been classified into two main types: (i) molecules able to fitting convex guests into the concave cavity of the host (cyclodextrins, cyclophanes, calixarenes and carcerands)[46] and (ii) molecules forming inclusion lattices by packing in porous structures.[47] The chemistry of the porous networks has been extensively studied in view of potential utilization of these materials for gas storage devices,[48-49] heterogeneous catalysts[50] and sensors.[51]

Many classifications have been proposed, to put in order into this large area. On one side, a classification is based on the topology of the pores. This classification leads to identify four types of pores: (i) the 0D cavities, that are the only ones completely surrounded by the wall molecules; (ii) the channels (1D); (iii) the layers (2D); (iv) the intersecting channels (3D).[52] On the other side, porous coordination compounds have been classified in three categories: 1st, 2nd and 3rd generation.[53] The 1st generation compounds have porous frameworks, which are sustained only by guest molecules and show irreversible framework collapse on removal of guest molecules. The 2nd generation compounds have stable and robust porous frameworks, which show permanent porosity also without any guest molecules into the pores. The 3rd generation compounds have flexible dynamic frameworks, which respond to external stimuli and change their channels or pores reversibly. A further classification of the porosity discusses as it is possible to identify a conventional porosity and a virtual one, a sort of porosity without pores.[54]

Alternatively to the covalently bound preformed host receptors and metal organic framework (MOF), the class of the porous non-covalent systems, based on the assembly *via* supramolecular interactions, growth esponentially.[55] Some of these have been discovered serendipitously while others have been targeted at specific purpose. In 1968, Toda evidenced that the high inclusion ability of diol and bisphenol compounds is connected with the presence of a steric crowding around the hydroxyl groups.[56] This is the starting point for the introduction of the dumbbell shaped molecules into the field of the inclusion compounds.[57] The dumbbell shaped objects have the intrinsic shape complexity that makes them enable to arrange into close packed networks. Dumbbell shaped molecules are good candidates to build inclusion lattices. Particularly, wheel-and-axle diols, having two bulky and relatively rigid end groups (wheels) bonded to a linear rigid link (axle), have been extensively studied.[58-62] These compounds offer the opportunity of acting on the axle, by modulating and designing new supramolecular[63] or hybrid organic-inorganic spacers.[64-66]

5. … and cocrystals

The cocrystals represent the second class of multicomponent systems. Cocrystal formation implies that the molecules of a given compound “recognizes” the molecules of another specific compound. The role of the shape in the recognition process is currently an unclear subject of discussion.

The exact origin of the term “cocrystal” is unclear, but it is generally recognized that it was introduced into the lexicon of organic solid-state chemistry by Etter and co-workers.[67] Zaworotko and co-workers have given a definition of a pharmaceutical cocrystal,[68] wherein a pharmaceutical cocrystal represents a new solid form of an active pharmaceutical ingredient (API) consisting of the API and a counter-molecule, the pharmaceutical cocrystal former. A similar design has been developed in the area of molecular semiconducting materials by MacGillivray and co-workers, involving a molecular semiconductor building block (SBB) and a semiconductor cocrystal former (SCF).[69]

The modularity of cocrystal design[70] is an area of great interest that brings together supramolecular chemists, materials scientists, and (co)crystal engineers, as cocrystallization has proven to be a versatile approach for the construction of functional solids. Currently, established and proposed applications of the cocrystals range from the area of advanced pharmaceutical materials,[71-75] molecular semiconductors[69] and optical materials,[76] to media for stereocontrolled synthesis.[77] Cocrystals are obtained by the careful selection of molecules that are chosen to interact specifically with one another, following a design strategy based on the approach of the supramolecular synthons.[18] This approach is an useful guideline for cocrystal design, but in order to accurately rationalise (and predict) cocrystal formation, the shape should be considered as well, as recently resulted from a statistical analysis on the cocrystals of the CSD.[78] The main point is that intermolecular recognition, leading to the formation of a multicomponent system, implies an approach between two species with a significant decrease of the potential energy of the system. The factors that act on this process are, from one side, the formation of specific interactions between the molecules, due to the presence of complementary functional groups. On the other side, the recognition depends on the shape, according to Kitaigorodski's close packing principle.[7] The problem of how the molecules are held together by supramolecular interactions and how it is possible to predict in the best way the formation of specific motifs is a currently field of discussion in computational chemistry.[79] The second aspect, the shape, due to a real limitation in the ability of quantify an analogic entity, is a less clear subject of discussion.

6. Aim of the work

In both solvates and cocrystals, the role of the shape is often introduced into discussions to rationalize *a posteriori* unexpected results, but not as *a priori* starting point of design.

This work aims to validate and rationalize the role of the shape in multicomponent systems, with the purpose to introduce new guidelines in supramolecular design.

This study involves both areas of the multicomponent systems: solvates and cocrystals. Particularly, for the solvates two test-cases are proposed. On one hand, the analysis of the role of the wheel-and-axle shape, to promote the formation of host frameworks, is explored. On the other hand, the design and the characterization of porous systems, based on 1D-nanochannels, is proposed. In the first case, the awkward molecular shape is recognised to be the key element that promotes the formation of host frameworks. In the second one, the inclusion properties are related with the shape features of tunable supramolecular motifs. In both cases, the stability of the inclusion networks are studied, by analysing the mechanism of the processes of solvation and desolvation.

In order to evaluate the role of molecular shape in cocrystallization, a study on the solid-state self-assembly through a mechanochemical screening is proposed. This approach is based on the use of rigid target-molecules and aims to obtain a predictive model for cocrystal formation. The results of this study provide useful qualitative and semi-quantitative benchmarks for cocrystal design.

References

1. A. Gavezzotti, *Molecular Aggregation: Structure Analysis and Molecular Simulation of Crystals and Liquids* (Oxford University Press, USA, 2007)
2. G. A. Arteca, *Molecular Shape Descriptors, Reviews in Computational Chemistry,* 1996, 9, 191-253 (Edited by K. B. Lipkowitz and D. B. Boyd, VCH, Weinheim)
3. J. D. Dunitz, G. Filippini, A. Gavezzotti, A Statistical Study of Density and Packing Variations among Crystalline Isomers, *Tetrahedron*, 2000, 56, 6595-6601
4. D. M. P. Mingos and A. L. Rohl, Size and Shape Characteristics of Inorganic Molecules and Ions and Their Relevance to Molecular Packing Problems, *J. Chem. Soc. Dalton Trans.*, 1991, 3419-3425
5. E. Pidcock and W. D. S. Motherwell, A Novel Description of the Crystal Packing of Molecules, *Crystal Growth & Design*, 2004, 4, 611-620
6. S. Reichling and G. Huttner, How to Find Correlations between Molecular Shape and Packing in a Molecular Crystal: Application of a Novel Strategy to Recognize n-Point Polyhedra in Three-Dimensional Space, *Eur. J. Inorg. Chem.*, 2000, 857-877
7. A. I. Kitaigorodski, *Organic Chemical Crystallography* (Consultants Bureau, New York, 1961)
8. J. D. Dunitz, G. Filippini, A. Gavezzotti, Molecular Shape and Crystal Packing: a study of C12H12 Isomers, Real and Imaginary, *Helv. Chim. Acta*, 2000, 83 (9), 2317-2335
9. J. D. Dunitz and A. Gavezzotti, Attractions and Repulsions in Organic Crystals: What Can Be Learned From the Crystal Structures of Condensed-Ring Aromatic Hydrocarbons?, *Acc. Chem. Res.*, 1999, 32, 677-684
10. J. D. Dunitz, Are Crystal structures predictable?, *Chem. Commun.*, 2003, 5, 545-548
11. G. Keplero, *De nive sexangula*, 1611
12. F. H. Allen, The Cambridge Structural Database: a Quarter of a Million Crystal Structures and Rising, *Acta Crystallogr.*, Sect. B., 2002, 58, 380-388
13. S. Torquato, T. M. Truskett, P. G. Debenedetti, Is random Close Packing of Spheres Well Defined?, *Phys. Rev. Letters*, 2000, 84, 2064-2067
14. C. H. Gorbitz and H. P. Hersleth, On the inclusion of Solvent Molecules in the Crystal Structures of Organic Compounds, *Acta Cryst.*, 2000, B56, 526-534
15. J. D. Dunitz in *Perspective in Supramolecular Chemistry: The Crystal as a Supramolecular entity*, Ed. G. R. Desiraju, Wiley, Amsterdam, 1995
16. J. J. Novoa and E. D'Oria in *Engineering of Cristalline Materials Properties: State of the Art in Modeling, Design and Applications,* J. Novoa, D. Braga, L. Addadi (Editors)
17. M. C. Etter, Encoding and Decoding Hydrogen-bond Patterns of Organic Compounds, *Acc. Chem. Res.*, 1990, 23 (4), 120-126
18. G. R. Desiraju, Supramolecular Synthons in Crystal Engineering-A New Organic Synthesis, *Angew. Chem. Int. Ed.*, 1995, 34, 2311-2327
19. B. K. Saha, A. Nangia, M. Jaskólki, Crystal Engineering With Hydrogen Bonds and Halogen Bonds, *CrystEngComm*, 2005, 7, 355-358
20. C. B. Aakeröy, J. Desper, B. A. Helfrich, P. Metrangolo, T. Pilati, G. Resnati, A. Stevenazzi, Combining Halogen Bonds and Hydrogen Bonds in the Modular Assembly of Heteromeric Infinite 1-D chains, *Chem. Commun.*, 2007, 4236-4238

21. K. Bouchmella, B. Boury, S. G. Dutremez, A. van der Lee, Molecular Assemblies from Imidazolyl-Containing Haloalkenes and Haloalkynes: Competition between Halogen and Hydrogen Bonding, *Chem. Eur. J.*, 2007, 13, 6130-6138

22. C. B. Aakeröy, I. Hussain, S. Forbesa, J. Desper, Exploring the Hydrogen-Bond preference of N–H Moieties in Co-crystals Assembled *via* O–H(acid)···N(py) Intermolecular Interactions, *CrystEngComm.*, 2007, 9, 46-54

23. S. L. Morisette, O. Amarsson, M. L. Peterson, J. F. Remenar, M. J. Read, A. V. Lemmo, S. Ellis, M. J. Cima, C. R. Gardner, High-Throughput Crystallization: Polymorphs, Salts, Co-crystals and Solvates of Pharmaceutical Solids, *Adv. Drug Delivery Rev.*, 2004, 56, 275-300

24. G. P. Stahly, Diversity in Single- and Multiple-Component Crystals. The Search for and Prevalence of Polymorphs and Cocrystals, *Cryst. Growth Des.*, 2007, 1007-1026

25. D. Braga and F. Grepioni (Editors), *Making Crystal by Design* (Whiley-VCH, 2006)

26. J. Novoa, D. Braga, L. Addadi (Editors), *Engineering of Crystalline Materials Properties: State of the Art in Modeling, Design and Applications* (Proceedings of the NATO Advanced Study Institute, held 7-17 June 2007, Erice, Italy)

27. D. Braga, F. Grepioni and G. R. Desiraju, Crystal Engineering and Organometallic Architecture, *Chem. Rev.*, 1998, 98, 1375-405

28. D. Braga, F. Grepioni and A. G. Orpen, *Crystal Engineering: From Molecules and Crystals to Materials*, Kluwer Academic Publishers, Dordrecht, 1999

29. M. D. Hollingsworth, Crystal Engineering: from Structure to Function, *Science*, 2002, 295, 2410-2413

30. L. Carlucci, G. Ciani, D. M. Proserpio, Polycatenation, Polythreading and Polyknotting in Coordination Network Chemistry, *Coord. Chem. Rew.*, 2003, 246, 247-289

31. J . Bernstein, Cultivating Crystal Forms, *Chem. Commun.*, 2005, 5007-5012

32. A.Nangia, Pseudopolymorph: Retain This Widely Accepted Term, *Cryst. Growth Des.*, 2006, 6 (1), 2-4

33. O. Almarsson, M. J. Zaworotko, Crystal Engineering of the Composition of Pharmaceutical Phases. Do Pharmaceutical C-crystals Represent a New Path to Improved Medicines?, *Chem. Commun.*, 2004, 1889-1896

34. G. R. Desiraju, Crystal and Co-crystal, *Cryst. Eng. Comm.*, 2003, 5, 466-467

35. J . D. Dunitz, Crystal and Co-crystal: a Second Opinion, *Cryst. Eng. Comm.*, 2003, 5, 506-506

36. K. R. Seddon, *Pseudo*polymorph: A Polemic**,** *Cryst. Growth Des.*, 2004, 4 (6), 1087-1087

37. G. R. Desiraju, *Cryst. Growth Des.*, Counterpoint: What's in a name?, 2004, 4, 1089-1090

38. J . Bernstein, ...And Another Comment on *Pseudo*polymorphism, *Cryst. Growth Des.*, 2005, 5 (5), 1661

39. D. Braga, F. Grepioni, Making Crystals from Crystals: a Green Route to Crystal Engineering and Polymorphism, *Chem. Commun.*, 2005, 3635-3645

40. K. C. Pich, R. Bishop, D. C. Craig, I. G. Dance, A. D. Rae, M. L. Scudder, Preparation and Crystal Structure of exo-2,-exo-6-dihydroxy-2,6-dimethyl-9-oxabicyclo[3.3.1]nonane, *Struct. Chem.*, 1993, 3, 41-51

41. S . Aitipamula, G. R. Desiraju, M. JaskMlski, A. Nangia, R. Thaimattam, Multiple Molecules in The Crystallographic Asymmetric Unit. Self Host–Guest and Doubly Interpenetrated Hydrogen Bond Networks in a Pair of Keto-Bisphenols, *Cryst. Eng. Comm.*, 2003, 5, 447-450

42. F. H. Herbstein, *Crystalline Molecular Complexes* (Oxford University Press, Oxford, Vol. 1, 2005)

43. D. J. Cram, Preorganization: From Solvents to Spherands, *Angew. Chem .Int. Ed. Engl.*, 1986, 25, 1039-1057

44. G. O. Lloyd, J. Alen, M. W. Bredenkamp, E. J. C. de Vries, C. Esterhuysen, L. J. Barbour, Solid-State Self-Inclusion: The Missing Link, *Angew. Chem. Int. Ed.*, 2006, 45, 5354-5358

45. E. Weber, *Inclusion Compounds*, J. L. Atwood, J. E. D. Davies and D. D. Mac Nicol (Oxford University Press, Oxford, 1991, 4, 188)
46. D. J. Cram, J. M. Cram, *Container Molecules and their guests* (Royal Society of Chemistry, Cambridge 1994)
47. F. Vögtle, *Supramolecular Chemistry*, Wiley (Chichester, UK, 1991)
48. O. M. Yaghi, M. O'Keeffe, N. W. Ockwig, H. K. Chae, M. Eddaoudi, J. Kim, Reticular Synthesis and the Design of New Materials, *Nature*, 2003, 423, 705-714
49. A. J. Blake, N. R. Champness, P. Hubberstey, W. S. Li, M. A. Withersby, M. Schroder, Inorganic Crystal Engineering Using Self-Assembly of Tailored Building-Blocks, *Coord. Chem. Rev.*,1999, 183, 117-138,
50. M. Fujita, Y. J. Kwon, S.Washizu, K. Ogura, Preparation, Clathration Ability, and Catalysis of a Two-Dimensional Square Network Material Composed of Cadmium(II) and 4,4'-Bipyridine, *J. Am. Chem. Soc.*, 1994, 116, 1151-1152
51. J. Reinbold, K. Buhlmann, K. Cammann, A. Wierig, C. Wimmer, E. Weber, Inclusion of Organic Vapours by Crystalline Hosts. Chemical Sensitive Coatings for Sensor Applications, *Sens. Actuators, B* 1994, 18, 77
52. S. Kitagawa, R. Kitaura, S. Noro, Functional Porous Coordination Polymers, *Angew. Chem. Int. Ed*,. 2004, 43, 2334-2375
53. S. Kitagawa, M. Kondo, Functional Micropore Chemistry of Crystalline Metal Complex-Assembled Compounds, *Bull. Chem. Soc. Jpn*,. 1998, 71, 1739-1753
54. L. J. Barbour, Crystal porosity and the Burden of Proof, *Chemm. Commun.*, 2006, 1163-1168
55. J. L. Atwood, J. E. D. Davies and D. D. MacNicol (Editors), *Inclusion Compounds*, Oxford University Press, London, 1991, vol. 4-5
56. F. Toda, K. Akagi, Wheel-And-Axle Design as a Source of Host-Guest Compounds. The Crystal Structure of the 2:1 acetone: tetraphenyl-2,4-hexadiyne-1,6-diol Complex, *Tetrahedron Lett.*, 1968, 3695
57. F. Toda, *Comprehensive Supramolecular Chemistry*, 1996, Vol. 6, Ch. 15, 465-516
58. E. Weber, K. Skobridis, A. Wierig, L. R. Nassimbeni, L. Johnson, Complexation with Diol Host Compounds. Part 10. Synthesis and Solid State Inclusion Properties of bis(diarylhydroxymethyl)-substituted benzenes and biphenyls; X-ray Crystal Structures of Two Host Polymorphs and of a Non-functional Host analogue, *J. Chem. Soc., Perkin Trans.*, 2, 1992, 2123-2130
59. L. Johnson, L. R. Nassimbeni, E. Weber, K. Skobridis, Complexation with Diol Host Compounds. Part 11. Structures and Thermal Analyses of the Inclusion Compounds of 4,4'-bis(diphenylhydroxymethyl)biphenyl, $C_{38}H_{30}O_2$, with acetone, acetophenone, 1,4-dioxane and *p*-xylene, *J. Chem. Soc., Perkin Trans.*, 2, 1992, 2131-2136
60. M. R Caira, A. Jacobs, L. R. Nassimbeni, F.Toda, Inclusion Compounds of 1,1,6,6-tetraphenylhexa-2,4-diyne-1,6-diol with DMF and DMSO: Structures, Selectivity and Kinetics of Desolvation *Cryst. Eng. Commun*., 2003, *5*, 150-153
61. M. R. Caira, L. R. Nassimbeni, F. Toda, D. Vujovic, Inclusion by a Diol Host Compound: Structure and Dynamics of Volatile Guest Exchange, *J. Chem. Soc., Perkin Trans.*, 2, 2001, 2119-2124
62. I. Csoregh, T. Brehmer, S. I. Nitsche, W. Seichter, E. Weber, Anthracene Based Bulky Diol Hosts. Crystal Structures of a Free Host and of Inclusion Compounds with Dipolar Guests, *J. Inclusion Phenom. Macrocyclic Chem*., 2003, 47, 113-121

63. R. K. R. Jetti, F. Xue, T. C. W. Mak, A. Nangia, 4-Tritylbenzoic Acid. A Molecular Scaffold for Wheel-And-Axle Host–Guest Inclusion Compounds With a Supramolecular Axis, *J. Chem. Soc., Perkin Trans.*, 2, 2000, 1223-1232

64. A. Bacchi, E. Bosetti, M. Carcelli, P. Pelagatti, D. Rogolino, G. Pelizzi, “Venetian Blinds” Mechanism of Solvation/Desolvation in Palladium(II) Wheel-and-Axle Organic−Inorganic Diols, *Inorg. Chem.*, 2005, 44, 431-442

65. A. Bacchi, M. Carcelli, E. Bosetti, Engineering Organic/Inorganic Diols that Reversibly Ccapture and Release Volatile Guests, *CrystEngComm*, 2005, 7, 527-537

66. A. Bacchi in *Models, Mysteries and Magic of Molecules*, Ed. C.A.Boyens and J.F.Ogilvie, Springer, 2008, 87-108

67. M. C. Etter, Z. Urbanczyk-Lipkowska, M. Zia-Ebrahimi, T. W. Panunto, Hydrogen Bond-Directed Cocrystallization and Molecular Recognition Properties of diarylureas, *J. Am. Chem. Soc.* 1990, 112 (23), 8415–8426

68. P Vishweshwar, J. A McMahon, J. Zaworotko, Pharmaceutical Co-crystals, *J. Pharm. Sci.* 2005, *95*, 499-516

69. A. N Sokolov, T Friščić, L. R MacGillivray, Enforced Face-to-face Stacking of Organic Semiconductor Building Blocks within Hydrogen-bonded Molecular Co-crystals, *J. Am. Chem. Soc.*2006, 128, 2806-2807

70. G. S Papaefstathiou, A. J Kipp, L. R MacGillivray, Exploiting Modularity in Template-Controlled Synthesis: a New Linear Template to Direct Reactivity within Discrete Hydrogen-Bonded Molecular Assemblies in the Solid-State, *Chem.Commun.*, 2001, 2462-2463

71. W. Jones, W. D. S. Motherwell, A. V. Trask, Pharmaceutical Cocrystals: An Emerging Approach to Physical Property Enhancement, *MRS Bull.* 2006, 31, 875-879

72. A. V. Trask, W. D. S. Motherwell, W. Jones, Pharmaceutical Cocrystallization: Engineering a Remedy for Caffeine Hydration, *Cryst. Growth Des.* 2005, 5, 1013-1021

73. A. V. Trask, W. D. S. Motherwell, W. Jones, Physical stability enhancement of theophylline via cocrystallization, *Int. J. Pharm.* 2006, 320, 114-123

74. A. J. Cruz Cabeza, G. M. Day, W. D. S. Motherwell, W. Jones, Prediction and Observation of Isostructurality Induced by Solvent Incorporation in Multicomponent Crystals, *J. Am. Chem. Soc.*, 2006, 128 (45), 14466-14467

75. S. Karki, T. Friščić, W. Jones, W. D. S. Motherwell, Screening for Pharmaceutical Cocrystal Hydrates via Neat and Liquid-Assisted Grinding, *Molecular Pharmaceutics*, 2007, 4 (3), 347-354

76. M. C. Etter, G. M Frankenbach, D. A Adsmond, Using Hydrogen Bonds to Design Acentric Organic Materials for Nonlinear Optical Users, *Mol. Cryst. Liq. Cryst.* 1990, 187, 25-39

77. L. R. MacGillivray, G. S. Papaefstathiou, T. Friščić, T. D. Hamilton, D.-K Bučar, Q Chu, D. B Varshney, I. G. Georgiev, Supramolecular Control of Reactivity in the Solid State: From Templates to Ladderanes to Metal-Organic Frameworks, *Acc. Chem. Res.* 2008, 41, 280-291

78. L. Fábián, Cambridge Structural Database analysis of molecular complementarity in cocrystals, *Cryst. Growth Des.* 2009, 9, 1436-1443

79. J. D. Dunitz and A. Gavezzotti, Molecular Recognition in Organic Crystals: Directed Intermolecular Bonds or Nonlocalized Bonding?, *Angew. Chem. Int. Ed.* 2005, 44, 1766-1787

PART I

Wheel-and-axle shape and inclusion compounds

1. Introduction

The phenomenon of inclusion implies the capture of guest molecules by host compounds and depends on molecular recognition. The formation of host-guest adducts is driven by the intermolecular interactions (that include week non-covalent interactions,[1] aromatic interactions[2-3] and hydrogen bonds[4-5]) together with the shape complementarity effect[6] (depending on the close packing principle[7]).

At the present time, many types of organic host compounds are known, some serendipitously discovered and others specifically targeted at specific guests. The analysis of the inclusion compounds of the Cambridge Structural Database (CSD)[8] shows that 20 common solvents appear at least 50 times in the organic crystal structures.[9-10] Actually, solvent inclusion in organic crystal is commensurate with its usage. The discovery of many crystal structures able to include solvent molecules is related to the increase of the complexity of the synthesized molecules. In fact, the probability to observe solvate formation is positively correlated with the increase of the shape complexity, which implies low self-packing efficiency.[11]

In the previous section it has been described as, due to their intrinsic irregularity, awkward shape molecules cannot pack efficiently.[12] The “wheel-and-axle” compounds[13] are dumbbell-like molecules that are good candidates for hosting small guests in the crystal lattice. They are constituted by two bulky and relatively rigid end groups (wheels) bonded to a linear rigid link (axle) (Scheme 1). Typical end groups may be triptycyls, diaryls, or triaryls and common links are azo, allenyl, or alkynyl functionalities,[14-16] as well as inorganic links.[17-18] The wheels can be decorated by hydrogen bonding groups, that may define anchoring points for the guests.

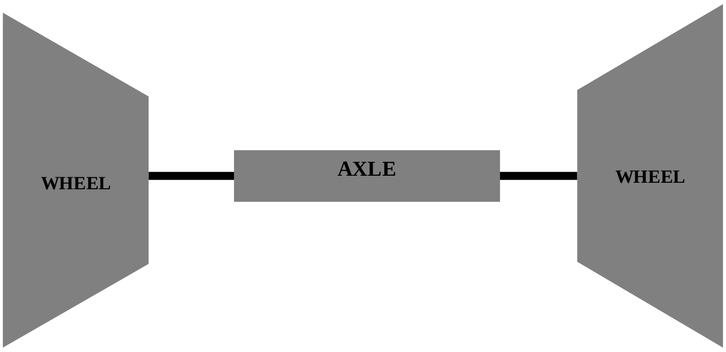

Scheme 1. Wheel-and-axle object

Hybrid organic-inorganic “wheel-and-axle diols” (*waads*) offer wide opportunity of design, because it is possible to tune the inorganic link by using the coordination geometry of the metallic centre. In order to have a dumbbell-shaped molecule, it is important to choose a metal able to give a planar coordination with large ligands arranged at opposite sides. Particularly, *trans*-palladium complexes with triarylcarbinol ligands (Scheme 2) show suitable structural requisites to get host-guest systems with reversible inclusion properties.[17-18]

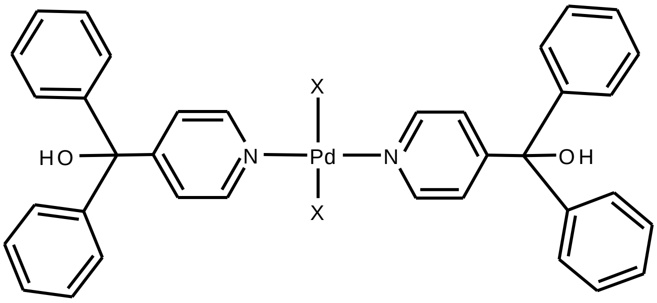

Scheme 2. Organic-inorganic *waad* (X = Cl, I, CH_3)

These dynamic frameworks can create pores “on demand” to accommodate small guest molecules. The reversible dynamic reorganization between the non-solvate and the solvate phases requires two conditions: (i) a bistable network, that can switch between the two states represented by the initial close (self-mediated) and the final open (guest-mediated) host networks, through a low cost structural rearrangement; (ii) an easily accessible migration path for the outcoming and incoming guest molecules. The reversibility of guest uptake/release can be interpreted according to a model where the host molecules may pack in arrays held together by hydrogen bonds between the terminal –OH groups and the coordinated X anions on the axle (Scheme 3, top), or use the –OH function to catch guest molecules (Scheme 3, bottom).[19] The conversion between the two states is realized by the simple oscillation of the molecules around their centres of mass (Scheme 3, inset).

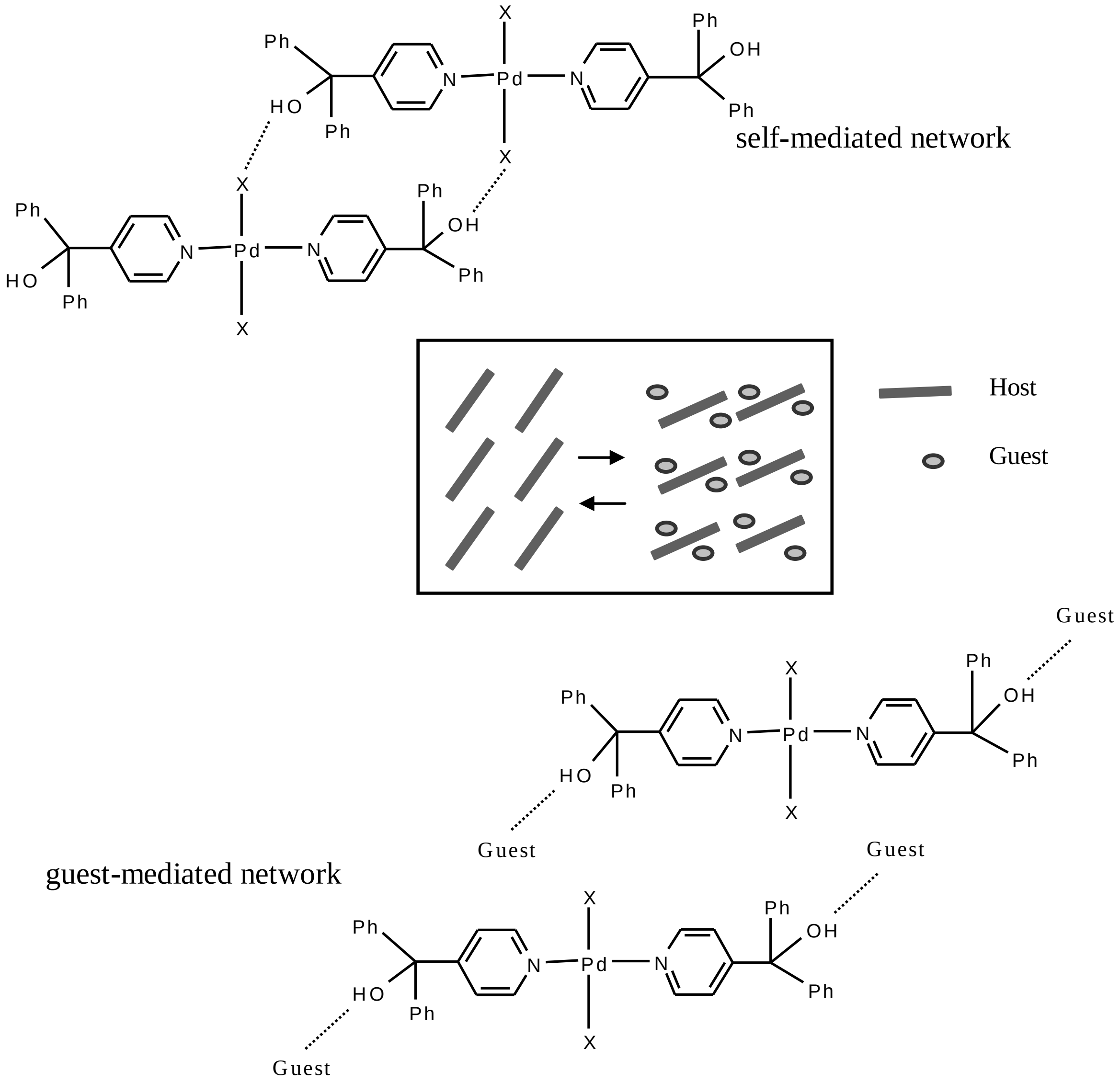

Scheme 3. Reversible mechanism of solvation/desolvation in organic-inorganic *waads*

2. Experiment design

This part of the work aims to validate and to rationalize the role of wheel-and-axle shape in order to promote the formation of inclusion networks.

First, the influence on inclusion properties of shape modifications, induced by changing the metal stereochemistry and the wheel hindrance, are analysed (Scheme 4). The obtained results show that the wheel-and-axle shape is a valid means to induce the formation of inclusion lattices. Particularly, it is shown that both axle linearity and wheel bulkiness are peculiar to establish inclusion properties.

Then, the synthesis and the characterization of new elongated metal-organic *waads* based on an iminic ligand are reported (Scheme 5). Both the structures and the properties of these systems are investigated. With respect to the previously described palladium complexes with triarylcarbinol ligands,[17-18] they have a similar scaffold, but the molecular length and the hindrance of the terminal groups are increased. The iminic function on the molecular axle provides a further functional site, while the larger molecular dimensions and anisotropy should enhance the intrinsic complexity of the molecule and its propensity to include small guests.

Finally, the solid-state properties of new bent-axle metal-organic system based on the same iminic ligand are described, obtaining a further validation of the importance of the wheel-and-axle shape in inclusion compound chemistry.

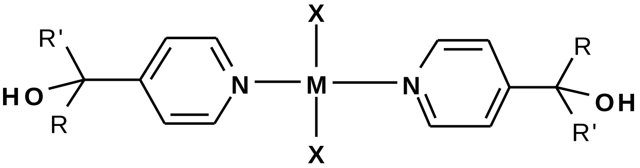

M = Zn
R and R' = Ph

M = Pd
$R = CH_3$ and R' = H

Scheme 4. Organic-inorganic system with less hindered wheels or bent axle

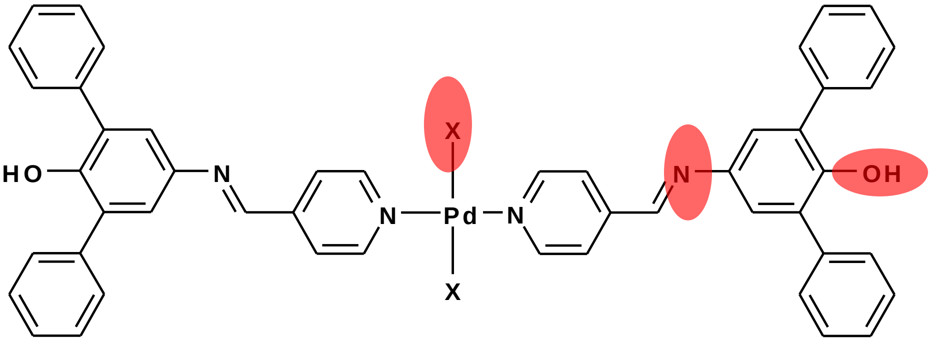

Scheme 5. Elongated organic-inorganic *waad*. The lighted red points are the main sites involved in the control of the crystal structure

3. Validation of wheel-and-axle shape[20]

The shape of the metal-organic *waads* may be easily tuned by choosing the suitable metal ion. In fact, the axle geometry basically derives from the coordination geometry of the metallic centre. A family of bent molecules [Zn(**LOH**)$_2$X$_2$], obtained by coordinating α-(4-pyridyl)benzhydrol (**LOH**) to zinc halogenides, has been recently described (Scheme 4).[21] These tetrahedrally coordinated compounds are accommodated in quadrangular networks based on –OH···X hydrogen bonds (X=Cl, Br) (Figure 2, left). Quadrangular networks cannot be obtained with a square planar stereochemistry on the metal, due to reciprocal hindrance of the aromatic rings in the middle of the supramolecular squares. The roughness of the network offers the opportunity to relax the steric tension and enables the molecules to arrange into a square-based lattice.

In order to clarify all the factors that tune the wheel-and-axle shape, the analysis on the role of the axle is followed by the validation of the role of the wheels. Particularly, the steric demand of the wheel substituents is analyzed by synthesizing the family of less bulky complexes $\mathrm{Pd}\mathbf{L^1}_2\mathrm{X}_2$ ($\mathbf{L^1}$= (1S)-1-(4-pyridinyl)ethanol; X= Cl, Br, I), where the steric hindrance reduction is achieved by the substitution of the two aromatic rings at the wheels by one methyl and one hydrogen (Scheme 4). $\mathbf{L^1}$ reacts with $Pd(PhCN)_2Cl_2$, K_2PdBr_4 and K_2PdI_4 in a 2:1 stoichiometry giving the complexes $\mathrm{Pd}\mathbf{L^1}_2\mathrm{Cl}_2$ (**1a**), $\mathrm{Pd}\mathbf{L^1}_2\mathrm{Br}_2$ (**1b**) and $\mathrm{Pd}\mathbf{L^1}_2\mathrm{I}_2$ (**1c**), respectively. The complexes are characterized through IR and ^{1}H NMR spectroscopy, elemental analysis and single crystal X-ray diffraction. As usual, palladium has a square planar coordination, with two anions and two $\mathbf{L^1}$ molecules in *trans* each other, coordinated by the 4-pyridyl nitrogen. In the IR spectra, the most significant band is ν(O-H). In the complexes, its values are higher than in $\mathbf{L^1}$ (3171 cm^{-1}) and follow the trend (**1a**) (3453 cm^{-1}) < (**1b**) (3473 cm^{-1}) < (**1c**) (3488 cm^{-1}); this sequence agrees with the hydrogen bonds strength, that depends on the halide anions interacting with the hydroxyl group (Table 2). In ^{1}H NMR spectra the *orto* and *meta* pyridyl protons of the coordinated pyridyl rings are deshielded with respect to the free ligand.

1a, **1b** and **1c** do not form solvates, in fact they are recollected as non-solvates from several recrystallizations in different solvents (acetone, CH_2Cl_2, CH_2Cl_2/EtOH). This behaviour is rationalized by crystal structure analysis. It shows that **1a-c** are isomorphous homochiral complexes and crystallize in the acentric $P2_1$ space group. As commonly observed for this class of compounds, pyridines are tilted by angles ranging between 76 and 88° from the coordination plane, as a consequence of the steric hindrance of the halide ligand on the metal, and they are tilted by 17-20° between themselves (Figure 1). The –OH groups are in *anti* position each other (O-C···C-O=149-152°), roughly mimicking the general tendency of metal-organic *waad* to achieve centrosymmetry.

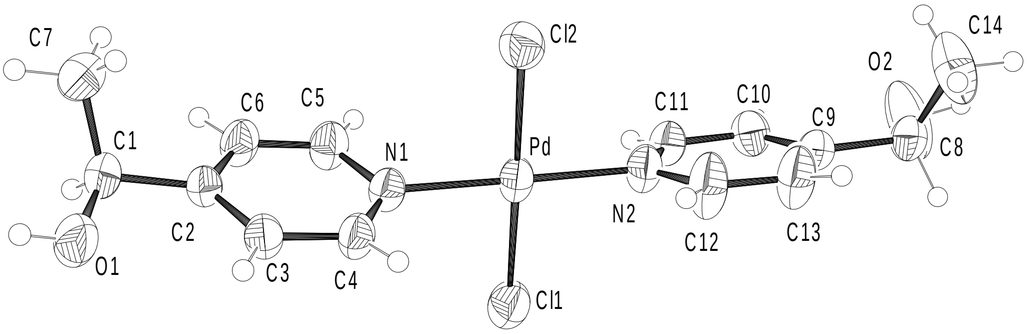

Figure 1. Molecular structure and labelling of **1a**, isostructural with **1b** and **1c**, with thermal ellipsoids at the 50% probability level

The solid state organization of **1a-c** follows a quadrangular pattern based on –OH···X hydrogen bonds, in analogy to the one observed for the above described zinc complexes [Zn(**LOH**)$_2$X$_2$] (Figure 2, right). In **1a-c** the planar arrangement of the supramolecular squares is permitted by the modest steric demands of the terminal substituents, that can be easily accommodated without the need of puckering the hydrogen bonded layer. In every case, the layers are staggered, so that the quadrangular cavities seen in Figure 2 are filled by the halides belonging to the adjacent layer properly shifted, and the structures are not porous. The shift between the square grids is such that halogen-halogen contacts occur across every second layer. These interhalide interactions are stronger for the larger atoms, and, in the case of **1c,** it is shorter than the sum of van der Waals radii (r_I=1.98Å). With respect to a distance Cl···Cl=4.281(1), Br···Br=3.943(2) and I···I=3.909(1) Å it shows the contribution of I···I stabilization to the packing of **1c.**[22]

It is possible to conclude that the bistable network sketched in Scheme 3, that enables guest capture, needs a remarkable steric hindrance around the carbinol groups and a linear stereochemistry of the axle. The release of the steric tensions obtained by bending the axle (Zn complexes) or by reducing the wheels complexity (**1a-c**) allows the formation of square grids, without any clathrating properties of the material.

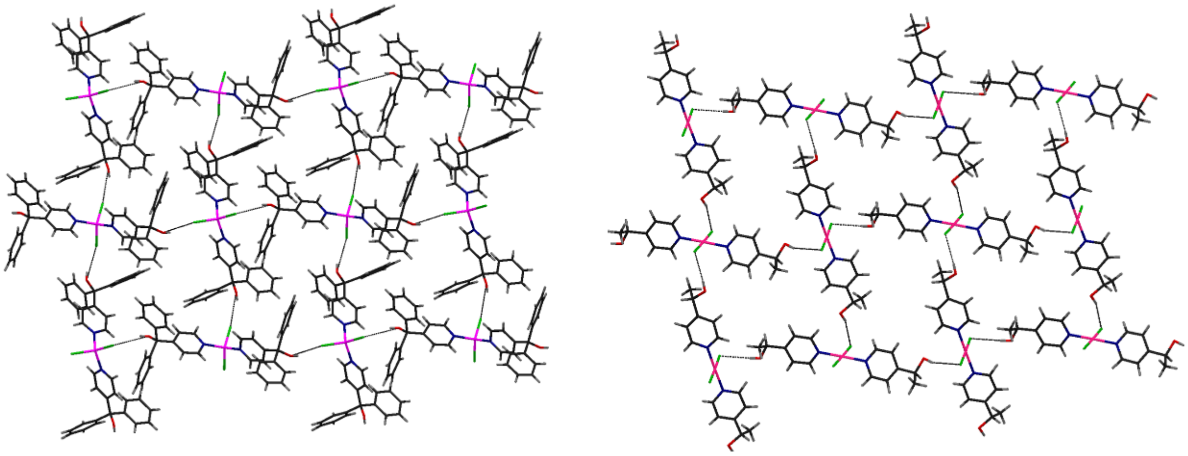

Figure 2. Supramolecular square patterns in the crystal organization of [Zn(**LOH**)$_2$Cl$_2$] (left)[21] and **1a** (right)

4. Design and synthesis of new *waad* systems[20]

The new ligand 2,6-diphenylphenol 4-pyridyl aldimine (**L**^{2}) has been designed in order to prepare new *waads* by complexation to palladium halides (Scheme 5). The structure of the ligand will be discuss in Part II. The new complexes **2-11** (Table 1) possess an additional acceptor site for hydrogen bonds (the iminic group), and the anisotropy of their shape is enhanced by the elongation of the axle and the increase of the widening of the wheels with respect to the complexes of **L**^{1} and **LOH**.

X = Br	n = 1	THF	**2**
		$CHCl_3$	**3**
	n = 2	TBME	**4**
		EtOH	**5**
	n = 0		**6**
X = Cl	n = 1	THF	**7**
		$CHCl_3$	**8**
		TBME	**9**
		toluene	**10**
	n = 0		**11**

Table 1. The species **2-11** isolated for *waad* system Pd**L**$^2_2$X$_2$·nG

The complexes Pd**L**$^2_2$Br$_2$·THF (**2**) and Pd**L**$^2_2$Cl$_2$ (**11**) are obtained by reacting **L**^{2} with K_2PdBr_4 in THF and $Pd(PhCN)_2Cl_2$ in CH_2Cl_2, respectively. Their spectroscopic characterization does not show any remarkable feature. Also in this case, in fact, as for the complexes of **L**^{1}, in the IR spectra the most significant band is ν(O-H), which in the complexes assumes an higher value than in **L**^{2}; in ^{1}H NMR spectra, upon coordination, the *ortho* and *meta* protons of the pyridyl rings are deshielded in comparison to the free ligand. The X-ray single crystal diffraction analysis of **2** confirms the predicted structure and suggests the stoichiometry ratio host/guest 1:1. It is important to notice that **2** easily loses solvents, also if it is kept at 4°C.

The clathrating ability of the two *waad*s **2** and **11** is tested by recrystallization in various solvents (Table 1). Particularly, **2** is recrystallized from chloroform and tert-butyl methyl ether (TBME), obtaining the solvates $\mathrm{Pd}\mathbf{L^2}_2\mathrm{Br_2{\cdot}CHCl_3}$ (**3**) and $\mathrm{Pd}\mathbf{L^2}_2\mathrm{Br_2{\cdot}2TBME}$ (**4**), whose X-ray structures are also determined. On the contrary, the slow evaporation at room temperature of a solution of **2** in absolute ethanol gives an intractable sticky solid. Only when pentane was added to a saturated solution of **2** in $CHCl_3$/EtOH (1:1), after slow evaporation at 4°C, an heterogeneous, but microcrystalline precipitate was obtained. Visual inspection shows the presence of two different products, including yellow parallelepiped and red, little, block microcrystals. After several attempts, some X-ray quality crystals of the two forms are obtained; the crystallographic analysis shows that the red block microcrystals are the non-solvate $\mathrm{Pd}\mathbf{L^2}_2\mathrm{Br_2}$ (**6**) and that the yellow ones belong to the solvate species $\mathrm{Pd}\mathbf{L^2}_2\mathrm{Br_2{\cdot}2EtOH}$ (**5**), respectively.

The composition of the heterogeneous precipitate is easily checked by X-ray powder diffraction (XRPD). With this aim the experimental powder pattern of the mixture is compared with the simulated ones of **5** and **6**. XRPD experiment suggests that in the mixture, together with **5** and **6**, another species (**6’**) is present (see Supplementary Material, S1). The thermal behaviour of the heterogeneous precipitate is analysed by variable temperature XRPD between room temperature and 240°C. In particular, the evolution of the system is followed by examining the X-ray powder diffraction spectrum in the 2θ range between 4.9-6.9°, that includes the three characteristic peaks 5.82 (**5**), 6.47 (**6**) and 6.01° (**6’**). They correspond to the reflections [100] of **5**, [200] of **6** and, probably, [200] of **6’** (for this index attribution see crystallographic discussion of **6**). Figure 3 shows the XRPD pattern of the mixture of **5**, **6** and **6’** at different temperature values (top) and peak intensity variation with the temperature (bottom). It seems that **6’** is another non solvate species, in fact the intensity of its characteristic peak increases while temperature increases. In particular, it is reasonably to think that **6’** is a polymorph with higher symmetry than **6** (see crystallographic discussion of **6**). Anyway, as already noticed for **2**, guest release begins near room temperature where the two concomitant non-solvate polymorphs **6** and **6’** are present together. Upon heating, **5** converts quantitatively into the apohost, without the appearance of any transient amorphous phase during the transition. The complete desolvation occurs between 90 and 100 °C. Between 100 and 200 °C **6** and **6’** coexist; above 230°C, only **6’** remains and it is hypothesized to be the more symmetric form favoured at higher temperatures. Hot-stage microscopy confirmed the transition from the solvate to the apohost without any crystallinity loss and the subsequent melting of **6’** at about 330°C.

6’ is quantitatively obtained and completely characterized by IR and elemental analyses by heating the product of the recrystallization in CH_2Cl_2/EtOH at 240°C. The ability of this apohost species to uptake again the guest by solvent vapour exposition and to re-convert into **5** is checked as well. With this purpose a crystalline sample of **6’** is exposed to vapours of ethanol for 2 weeks, but spectroscopic and analytical data (IR and X-ray powder diffraction) show that **6’** remains unchanged.

$Pd\mathbf{L}^{2}{}_{2}Cl_2$ (**11**) is able to includes THF (**7**), $CHCl_3$ (**8**), TBME (**9**) and toluene (**10**); the single crystal X-ray structures of these solvates are determined. Unfortunately, they easily tend to release the guest as well as the bromide derivates. The behaviour of a freshly prepared sample of **8** is analysed by variable temperature X-ray powder diffraction. The release of the solvent goes with the formation of an amorphous phase: from 55 °C until the melting, that starts at 160 °C, only the amorphous is present (see Supplementary Material, S2). During the heating no decomposition of the amorphous occurs: after 6 h at 60°C, the elemental analysis are still in agreement with the $Pd\mathbf{L}^{2}{}_{2}Cl_2$ formula and the IR spectrum is practically indistinguishable from the IR spectrum of **11**. The thermal behaviour, particularly the formation of the amorphous phase until the melt, is also confirmed by hot-stage microscopy experiment.

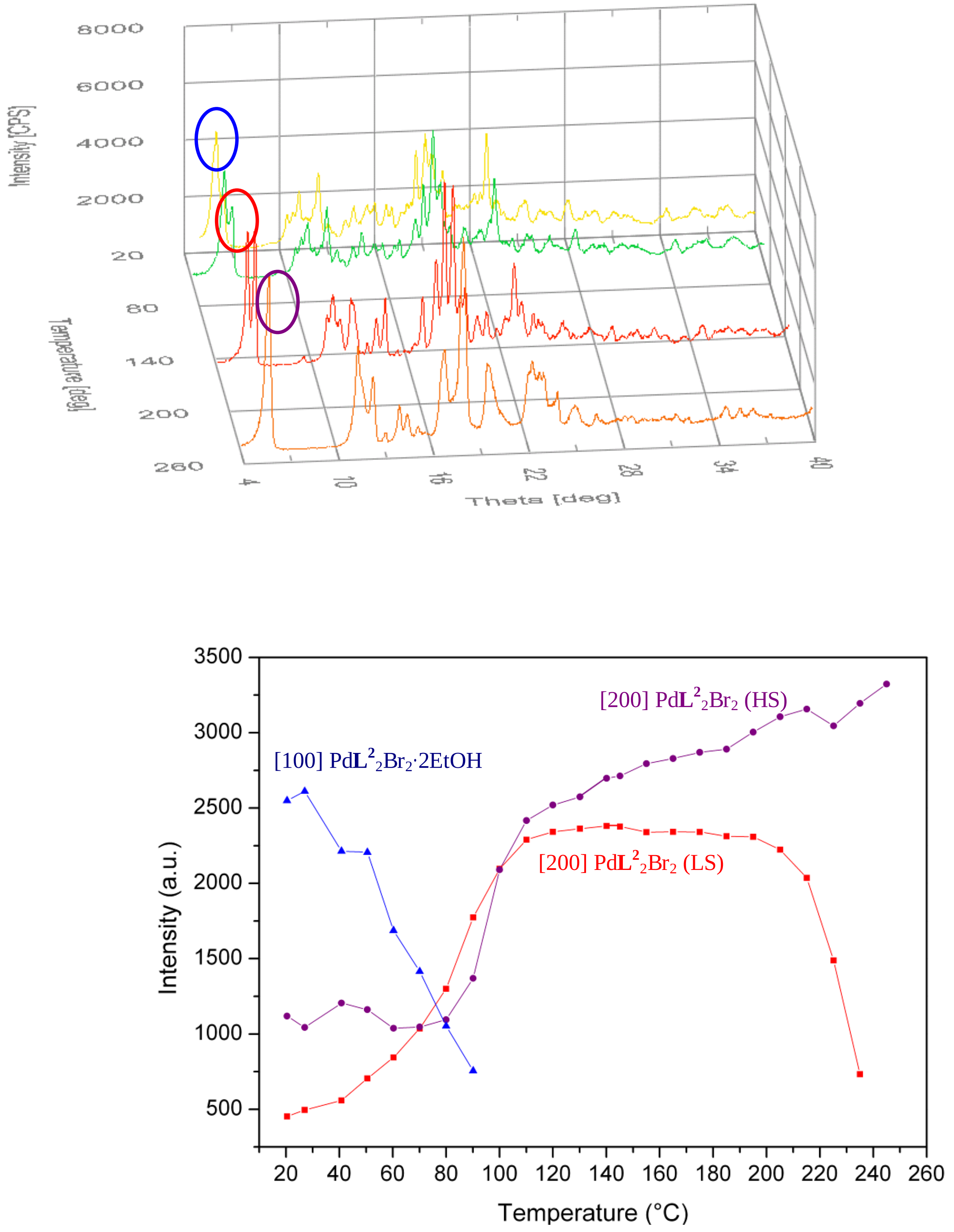

Figure 3. Variable temperature XRPD pattern of a mixture of **5**, **6** and **6’** (top) and intensities of the reflections [100] of **5** (blue), [200] of **6** (red) and [200] of **6’** (scarlet) in function of the temperature (bottom). LS and HS indicate the polymorph with lower symmetry **6** and the polymorph with higher symmetry **6’**, respectively

5. Structures of the *trans*-Pd$\mathbf{L}^2{}_2$Br$_2$ compounds (2-6)

From a mixture CH_2Cl_2/EtOH, the non solvate **6** Pd$\mathbf{L}^2{}_2$Br$_2$ is obtained, concomitantly with the solvate **5** Pd$\mathbf{L}^2{}_2$Br$_2\cdot$2EtOH,

The supramolecular structure of **6** includes two crystallographically independent molecules. Both lie on an inversion centre and differ only in the orientation the external aromatic substituents (Figure 4). The O···O distance, representing the length of the wheel-and-axle complex, is 25.1 Å, the Br···Br axle, that is the axle diameter in its largest point, is 4.9 Å and the wheels width is 11.5 Å, indicating the extreme H···H separation. Pyridine rings are tilted by 51 and 61° relatively to the square planar coordination plane for the two molecules, while they are perfectly coplanar between themselves and the overall organic backbone of the axle is planar.

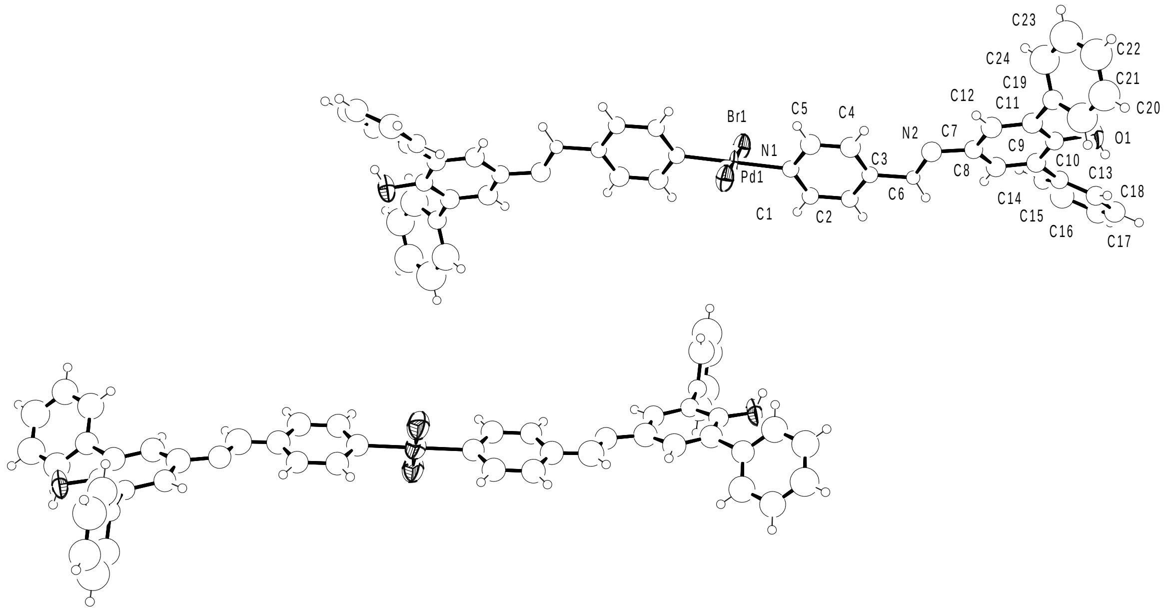

Figure 4. Molecular structure of **6**, with thermal ellipsoids at the 50% probability level. Both independent molecules are shown, labelling is reported only for one of them. In both cases the metal is on a centre of symmetry

The self-recognition pattern of the apohost molecule Pd$\mathbf{L}^2{}_2$Br$_2$ reflects the flexibility of the molecular shape. For each independent molecules, bromine atoms are nested in the recess of the slightly acidic C(sp^2)-H atoms of neighbouring complexes of the same kind (Br···H=3.101-3.653 Å) generated by a glide plane ***c*** (Figure 5). The close supramolecular association between akin molecules involves also C-H···π contacts. The extension of this pattern leads to the formation of structural moduli consisting of sheets of parallel molecules of the same kind, alternately tilted across a glide symmetry operation (Figure 6).

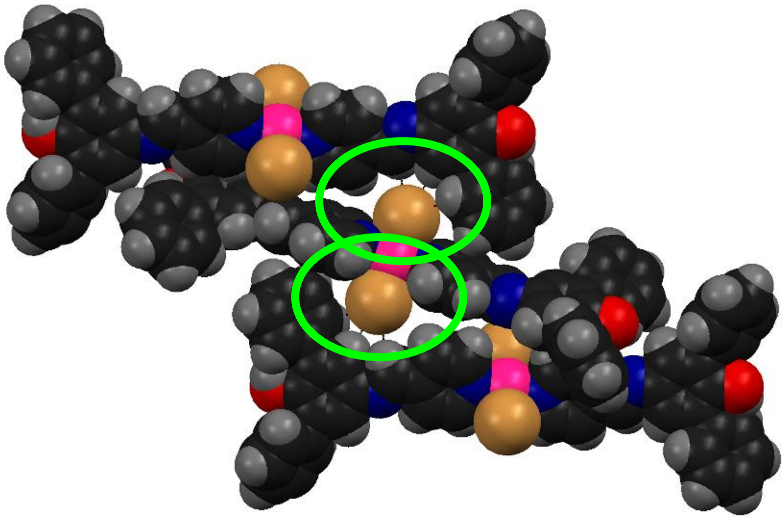

Figure 5. Molecular association by Br…H contacts between molecules of the same kind of **6**. The green circles highlight the nests containing the bromide atoms

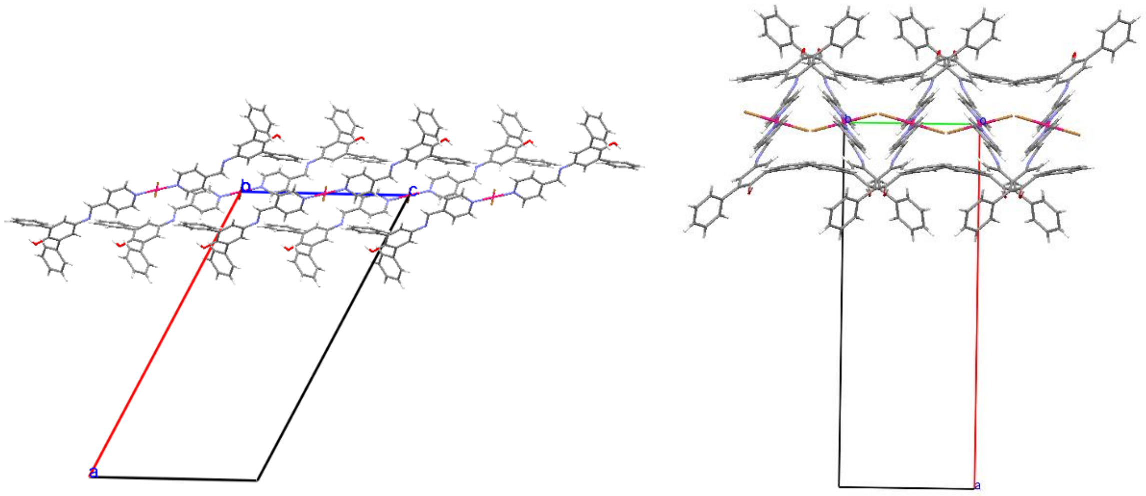

Figure 6. Sheets of molecules associated as shown in Figure 5 in the crystal packing of **6**, viewed down ***b*** (left) and down ***c*** (right)

The sheets expose the –OH groups at the external ridges, and they are associate together by OH···O weak contacts (O2-H··O1 (x, y, z-2)=3.05(3) Å, O-H···O=166(2)°). This interactions involve pairs of molecules with mismatched conformation, because the two independent molecules are segregated in separate alternate sheets, with the OH groups interposed between them (Figure 7).

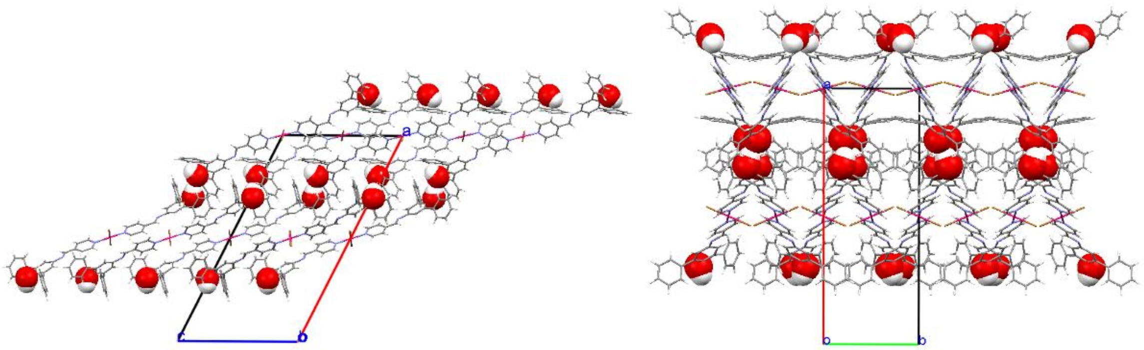

Figure 7. Associations of molecular sheets in **6**, viewed down ***b*** (left) and down ***c*** (right), occurring by OH···OH hydrogen bonds. OH groups are evidenced

In order to interpret the relationships with the observed polymorphism of **6** at high temperature, evidenced by X-ray powder diffraction experiments, and to describe the inclusion properties of the system, the analysis of the metrics of the packing of **6** is a basic point of discussion. The two independent molecules in **6** are related by a pseudo two-fold axis located at (0.25, 0, 0), so that the crystal packing mimics a C2/c pseudo-symmetry after an origin shift. The actual achievement of this higher symmetry by equalizing the two molecules is unfavourable with the current cell dimensions, since it would result in short repulsive contacts between aromatics occurring especially along ***a***. The higher symmetry could be realized with an elongation of ***a***, which could be revealed by a shift towards lower 2θ values for the [200] reflection: this is what effectively happens in **6'** ($\theta = 6.01^\circ$; $\theta = 6.47^\circ$ for [200] in **6**; see X-ray powder diffraction experiments) and the reason because this polymorph could be described as an higher symmetry form of **6**.

The modular structure of **6** also enables to interpret of formation of host-guest adducts. The host $\mathrm{Pd}\mathbf{L}^{2}{}_{2}\mathrm{Br}_{2}$ includes guests with 1:2 and 1:1 stoichiometry, as reported in Table 1. All these solvate compounds have very similar crystal structure. The degree of solvation modulates the crystallographic symmetry on a common metric pattern which refers to the crystal packing of **6**. Figure 8 shows the molecular structure of $\mathrm{Pd}\mathbf{L}^{2}{}_{2}\mathrm{Br}_{2}$ in **5**, which well represent all the members of the family. It is practically undistinguishable from the non solvate form **6**, from which it differs only for the orientation of the terminal aromatic rings. In fact, while the molecular conformation is conserved in all the solvates, the terminal aromatic rings show the largest variability among the four species **2-5** (Figure 9).

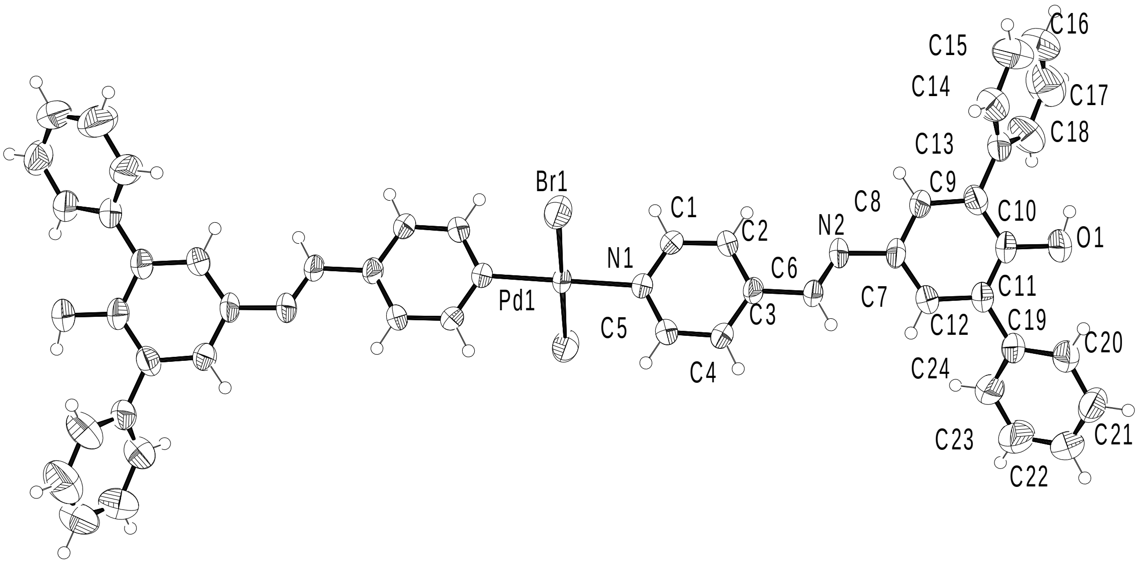

Figure 8. Molecular structure of Pd$\mathbf{L}^2{}_2$Br$_2$ in **5**, with thermal ellipsoids at the 50% probability level. The molecule is centrosymmetric

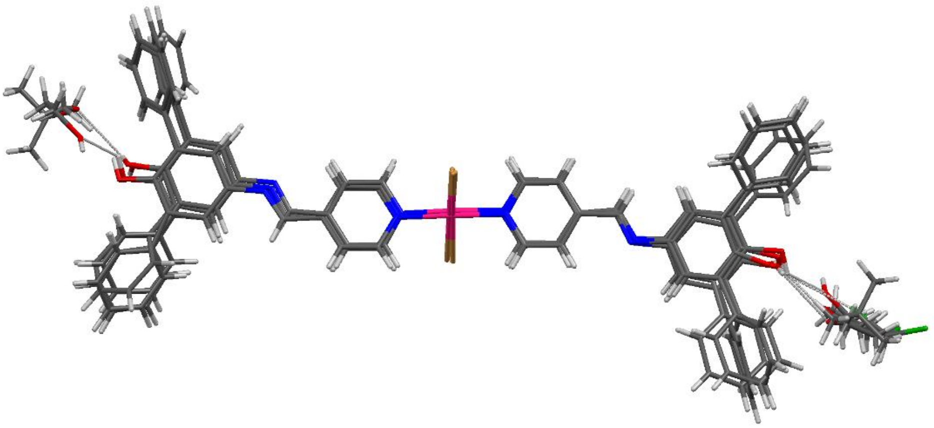

Figure 9. Similarity of the molecular structure of **2-5**, showing that the guests occupy the same sites. 1:2 solvates (**4** and **5**) interact with two guest molecules on both sides, while 1:1 solvates (**2** and **3**) interact only to one guest at the site here on the right

As observed in the non solvate host **6**, in the solvate species the molecular association is realized by the same pattern of contacts involving Br and CH groups, so that the sheets of host molecules are perfectly preserved (Figure 10). The key feature for guest uptake is represented by the OH groups pending along the ridge of these sheets. The guest is always hydrogen bonded to one (1:1 solvates **2** and **3**) or both (1:2 solvates **4** and **5**) the OH groups at the molecular ends (Table 2), and consequently the molecule is either centrosymmetric (in **4** and **5**) or pseudo-centrosymmetric (in **2** and **3**), depending on the degree of solvation.

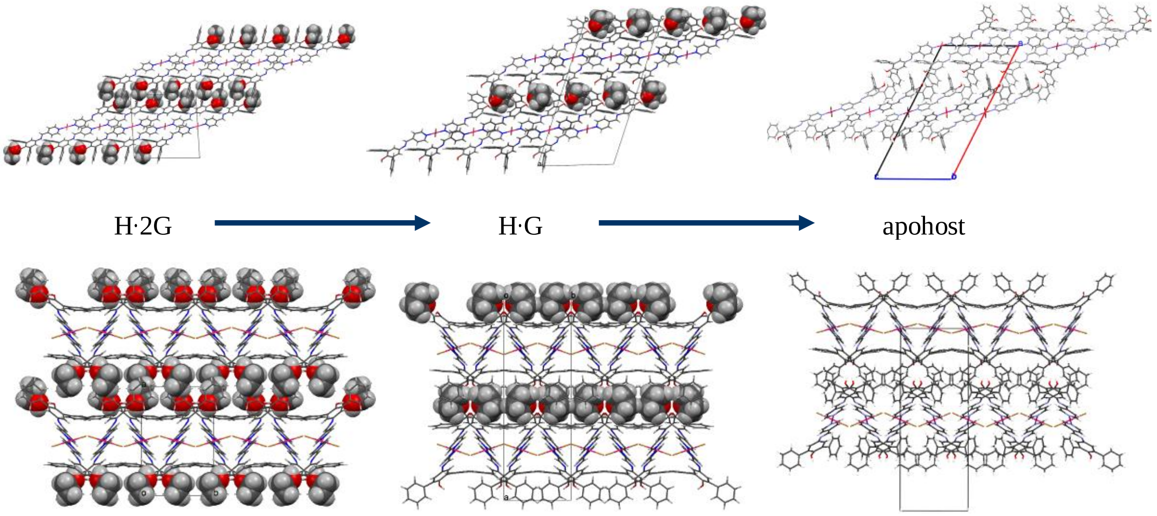

Figure 10. Comparison between the supramolecular motifs between the 1:2 solvates (**5**, left) and the 1:1 solvates (**2**, middle) and the apohost (**6**, right). Projections down ***b*** on the top and down ***c*** on the bottom represent the continous path for the guest release

This structural model describes that the solvation process of $Pd\mathbf{L}^{2}_{2}Br_{2}$ with 1:1 and 1:2 host/guest ratios occurs by gradual occupation of the space between the molecular sheets and concomitant replacing of the OH···O hydrogen bonds of **6** by OH···Guest contacts. Initially only one array of OH groups is employed to attach the first equivalent of guest molecules in the 1:1 compounds **2** and **3**, so that the one half of the solvation sites are occupied alternatively along the intersheets space (Figure 10, middle). Then the second equivalent of guest molecules is included by filling completely the space between the sheets. The introduction of the first array of guest molecules destroys the molecular centrosymmetry of $Pd\mathbf{L}^{2}_{2}Br_{2}$ by removing the equivalence between the OH groups. The overall cell symmetry is then modified from the higher C2/c symmetry potentially exhibited by **6’** to the Cc setting observed in **2** and **3**. The introduction of the guest has also the effect of modifying the β angle of the cell, whose dimensions are otherwise conserved (Figure 10, Table 4). The second array of guests (G) restores the molecular centre of symmetry for **4** and **5**, the cell constant **a** is halved and the overall symmetry becomes $P2_1/c$, while β is further reduced. This structural description allows to outline the continuous path of conversion H·2G → H·G → H, that leads from the 1:2 inclusion compound H·2G to the pure host (H) (Figure 10). This conversion takes advantage of the flexibility of the host framework, which may adapt to different compositions by slight modifications of the cell geometry. This ability derives from the opportunity to switch from the self-mediated network, sustained by OH···OH interactions, to the guest-mediated network, based on OH···G hydrogen bonds by a small structural rearrangement.

The generally high values of the thermal parameters of the guests in **2-5** indicates that a partial desolvatation before and during data collection takes place.

	Host-Host			*Host-Guest*		
	D…A (Å)	D-H...A (°)	symmetry	D…A (Å)	D-H…A (°)	symmetry
1a	O1…Cl2 3.362(3) O2…Cl1 3.313(4)	163.8 163.8	-x+2,y-1/2,-z+2 -x,y+1/2,-z+1			
1b	O1…Br2 3.53(1) O2…Br1 3.49(1)	172.1 140.4	-x+2,y-1/2,-z+2 -x,y+1/2,-z+1			
1c	O1…I1 3.77(1) O2…I2 3.71(1)	148.8 137.3	-x+2,y-1/2,-z+2 -x,y+1/2,-z+1			
2				O1…O_{THF} 2.71(5)	114	
3				O1…Cl_{CHCl3} 3.28(5)	117	
4				O1…O_{TBME} 2.88(3)	99	
5				O_{EtOH}…O1 2.68(1) O_{EtOH}…N2 3.10(1)	139 143	 x, 1/2-y, ½+z
6	O2…O1 3.05(3)	166	x, y, z-2			
7	O2…Cl1 3.304(3)	136.6	-x-1, -y+3, -z+2	O1…O_{THF} 2.773(7)	160.3	
8	O2…Cl1 3.219(6)	139	-x-1, -y+3, -z+2	C_{CHCl3}…O2 3.65(3)	157	-x+2,-y+2,-z+3
9	O1…Cl1 3.319(9)	123.6	-x-1, -y+3, -z+2	O2…O_{TBME} 2.92(2)	128.3(8)	
10	O1…Cl2 2.208(8)	141.8	-x-1, -y+3, -z+2			

Table 2. Host-host and host-guest contacts in the crystal organization of the complexes **1-10**

6. Structures of the *trans*-$PdL^2_2Cl_2$ compounds (7-10)

The simple substitution of chloride for bromide in Pd$\mathbf{L}^2_2$Cl$_2$ produces a remarkable effect on the solid state organization, because the chlorine is a significantly better hydrogen bond acceptor than the bromine. By crystallization in different solvents (THF, chloroform, toluene and tert-butylmethylether) only isomorphous solvate species [Pd$\mathbf{L}^2_2$Cl$_2$]$_2$·**2**G may be isolated (Table 1). The main feature of the supramolecular organization of these compounds is shown for **8** in Figure 11. The overlap between all the species **7-10,** that appears in Figure 12, highlights that the same motifs is found in all the crystals. In all cases a pair of Pd$\mathbf{L}^2_2$Cl$_2$ molecules associate in a centrosymmetric dimer assembled by OH···Cl hydrogen bonds (Table 2). The dimer [Pd$\mathbf{L}^2_2$Cl$_2$]$_2$ possesses two external pending OH groups that are used to anchor two hydrogen bond accepting guests by OH···G interactions (G = THF, tert-butylmethylether, Table 2). Toluene and chloroform are included by plain clathration, but occupy the same site as the hydrogen bonded guests. This suggests an inclusion mechanism involving the overall molecular shape, besides specific host-guest hydrogen bonds. This description agrees with the host/guest 1:1 stoichiometry, by considering a single *waad* as host and appears as the host/guest 1:2 stoichiometry, if the host is described as the supramolecular dimer involving a pairs of molecules.

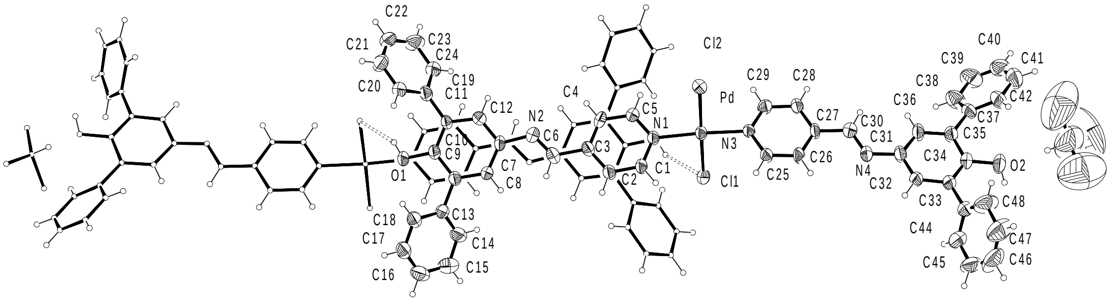

Figure 11. Dimeric association in centrosymmetric $[\mathrm{Pd}\mathbf{L}^{2}{}_{2}\mathrm{Cl}_{2}]_{2}\cdot 2\mathrm{CHCl}_{3}$ units for **8**, by OH···Cl hydrogen bonds, with thermal ellipsoids at the 50% probability level

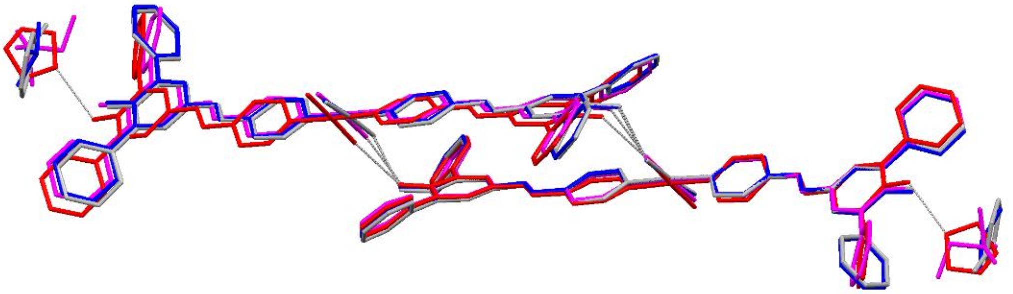

Figure 12. Dimeric association in the compounds **7-10**

With respect to the molecular conformation in **7-10**, it does not change significantly. The main difference is the orientation of one aromatic ring, that is tilted in the pair **7**-**9** respect the **8**-**10** ones (Figure 12). Into the dimers, the units $\mathrm{Pd}\mathbf{L}^{2}{}_{2}\mathrm{Cl}_{2}$ share some general features: the complex $\mathrm{Pd}\mathbf{L}^{2}{}_{2}\mathrm{Cl}_{2}$ is not centrosymmetric, but the iminic bonds of the two $\mathbf{L}^{2}$ ligands are both oriented in *anti*; the pyridine rings are tilted by angles varying between 46.8 and 79.5° relatively to the square coordination plane; the pyridines are also tilted by 10-28° between themselves, contrarily to the situation observed in the bromide complexes, where they are coplanar. The two molecular halves are differentiated in the dimer formation because the ligand $\mathbf{L}^{2}$ is hydrogen bonded to the guest on one side and it is involved in the OH···Cl hydrogen bond on the other side, where it is constrained to closely stack to its counterpart belonging to the second partner in the dimer, at a distance of 3.6Å. The dimer is a supramolecular object with a length of 40Å (O···O distance) and its shape can be described as a wheel-and-axle with a central bulge. $[Pd\mathbf{L}^2{}_2Cl_2]_2$ units assemble in sheets of stacked molecules, where the chlorine atoms not involved in dimer formation are nested between the CH groups of the pyridine, iminic and phenolic aromatic rings (Figure 13), in analogy to the pattern previously described of the complexes **2-6**. These sheets are decorated by guest molecules at the extremities of the dimers that fill the space between consecutive sheets (Figure 14). This motif is analogous to the one observed for the bis-solvate complexes **4** and **5**, if the supramolecular dimers $[Pd\mathbf{L}^2{}_2Cl_2]_2$ are thought as host species, at the same way as the $Pd\mathbf{L}^2{}_2Br_2$ monomers.

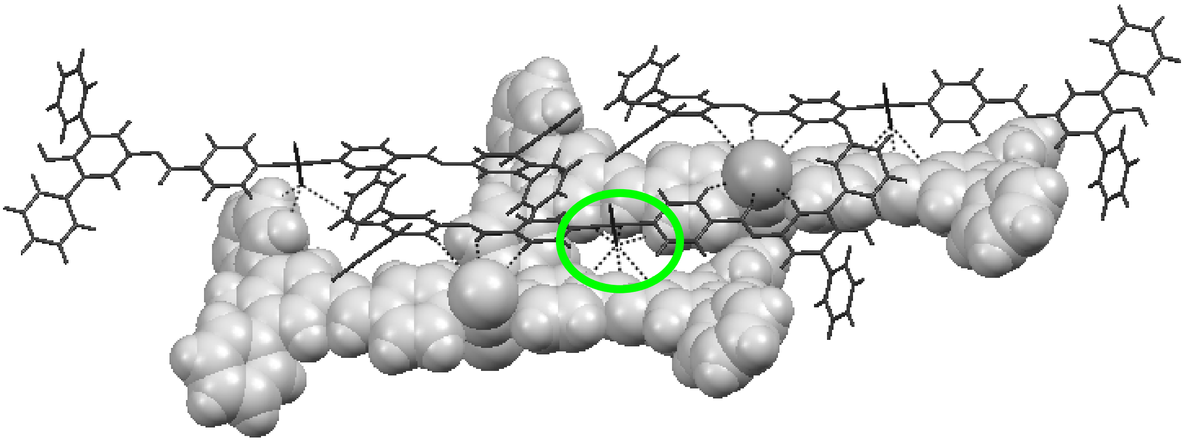

Figure 13. Interaction of a dimeric unit (dark sticks) by Cl···H contacts with neighbouring molecules (light, spacefilling). Only one dimeric unit is represented. The green circles highlight the nest containing the chlorine atom

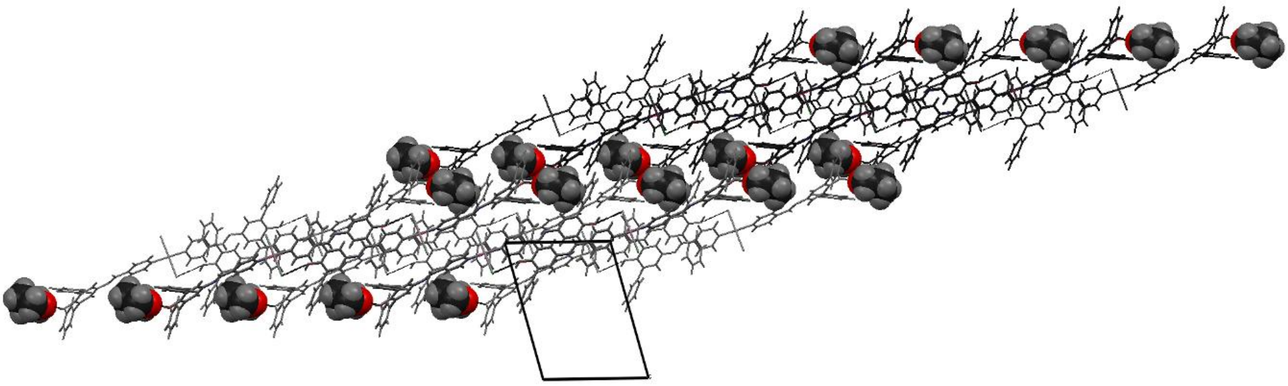

Figure 14. Crystal packing of sheets of dimeric units in **7**, with guests (spacefilling) anchored between the sheets

7. Structures of the bent-axle compounds Zn**L**$^2_2$X$_2$ (12-14)

The definition of “wheel-and-axle” implies that an object should be based on a linear relatively rigid axle with large substituents at the ends. Both the components (the axle and the wheels) are peculiar in order the preserve the overall shape and the consequent packing features.

Organo-metallic *waads* enable to easily perturb the dumbbell shape, acting on the axle by inserting suitable metal ions with different coordination geometries. In the previous sections it has been remembered that the remarkable differences in the supramolecular motifs observed for the complexes Zn(**LOH**)$_2$X$_2$[21] demonstrate the importance of the axle linearity on the control of the solid-state assembly. This control involves the axle geometry together with the features of the wheels and it is strictly connected with the properties of the supramolecular network. Indeed the assemblies of bistable chain-based systems are induced by steric factors, that may be relaxed by reducing the wheels or by bending the axle. The opportunity to obtain alternative motifs implies the loss of the inclusion properties of the material, or at least the impossibility of obtaining the same packing pattern.

It has been shown that the ligand **L**^{2} offers wide opportunities in the design of organo-metallic host species (the wheel-and-axle compounds **2-11**). Nevertheless the ligand alone is not enough to promote the formation of the inclusion network. With the aim to further validate the importance of both wheel hindrance and axle linearity, **L**^{2} is used to coordinate the zinc in a family of bent-axle compounds. In these complexes, the different stereochemistry of the metal tunes the wheel-and-axle shape, leading to a tetrahedral geometry.

The complexes Zn**L**$^2_2$X$_2$ (X = Cl, Br, I) **12-14** (Scheme 6) are obtained by reacting **L**^{2} with ZnCl$_2$, ZnBr$_2$ and ZnI$_2$, respectively.

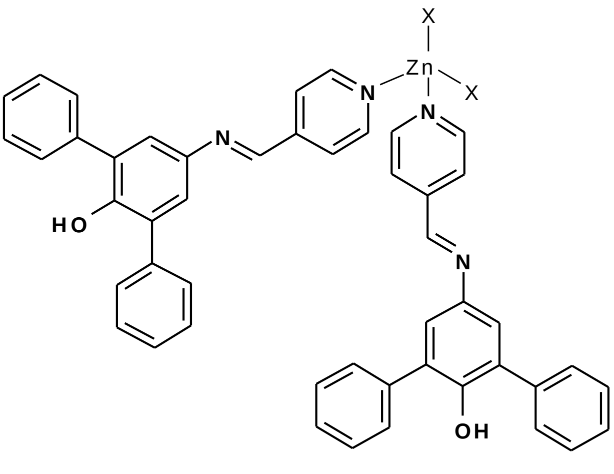

Scheme 6. Bent-axle Zn**L**$^2_2$X$_2$ complexes (X = Cl, Br, I)

In all cases the reaction is carried out in a mixture ethanol/CH_2Cl_2. Both spectroscopic and elemental analysis suggest that **12**, **13** and **14** do not form solvates, in fact small non-solvate crystals are collected from recrystallization in different solvents (THF, CH_2Cl_2 and TBME for **12**, **13** and **14**, respectively). Unfortunaltely, the complexes **12** and **13** give crystals of very poor quality (see crystallographic data in Table 6), but the crystal structure analysis is enough to get a packing overview that rationalizes the inability in guest capture. It definitely shows that all the compounds **12-14** are able to close-pack, without any clathrating properties. The sheet motif peculiar of the crystal structures of the $Pd\mathbf{L}^2_2X_2$ complexes does not form, because the release of the steric tensions, obtained by bending the axle, enables the formation of different supramolecular motifs.

The structural analysis of the compounds **12-14** shows that in all cases the zinc has a tetrahedral coordination (Figure 15). All the complexes crystallize in tetragonal space groups, adopting the crystallographic symmetry, $P4_2$ (**12** and **13**) or $P\ \bar{}4\ 2_1\ c$ (**14**).

The complexes $Zn\mathbf{L}^2_2Cl_2$ (**12**) and $Zn\mathbf{L}^2_2Br_2$ (**13**) present a crystal structure based on –OH···Cl (3.147 Å) and –OH···Br (3.308 Å) hydrogen bonds, respectively. Each molecule is involved in four hydrogen bonds, with two donors OH groups and two halogenide acceptors. A $Zn\mathbf{L}^2_2X_2$ molecule encodes in itself the opportunity to generate a tetrahedral supramolecular synthon[22] which may expand in a 3D network through the covalent linking provided by the metal.

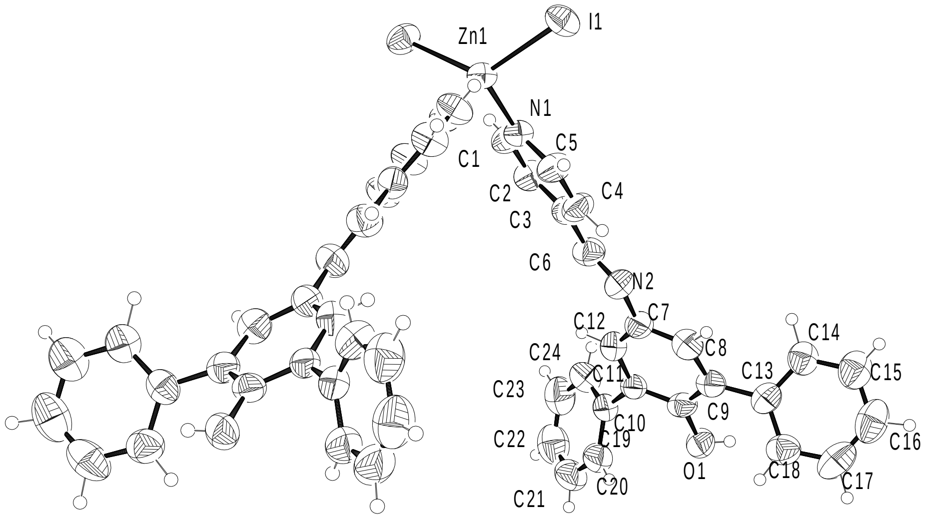

Figure 15. Molecular structure and labelling of **14** with thermal ellipsoids at the 50% probability level

The resulting structural motif is an example of 3D hydrogen bonded array of coordination complexes. The tetrahedral nodes are centered on the metal ions[23-24] and the long organic moieties act as spacers in a diamondoid network with wide pores (Figure 16). The overall structural compactness is achieved by a quadruple interpenetration of four equivalent diamondoid frameworks, which interact by C-H···π contacts (Figure 17). It is worth of note that a diamondoid network has been described also for the tetrahedral complex Zn(**LOH**)$_2$I$_2$.[21] Nevertheless this compound shows remarkably different supramolecular features, due to the switch from the –OH···X to the –OH···OH hydrogen bond, with the formation of tetrahedral nodes (OH)$_4$.

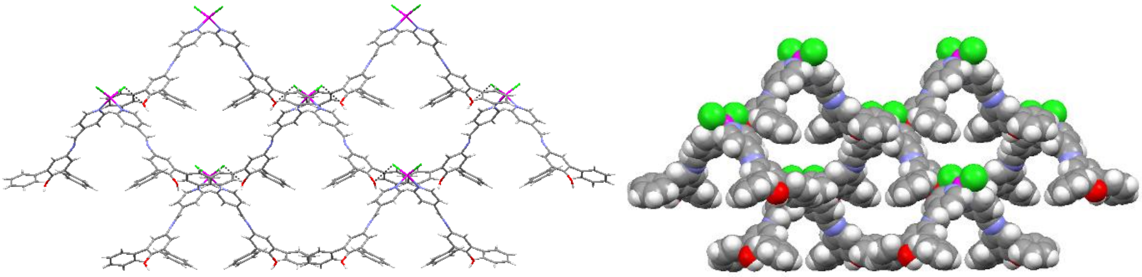

Figure 16. Diamondoid network in crystal structure of **12** (left); the tetrahedral nodes are centered on the metal ion and large pores are evidenced by spacefill model (right)

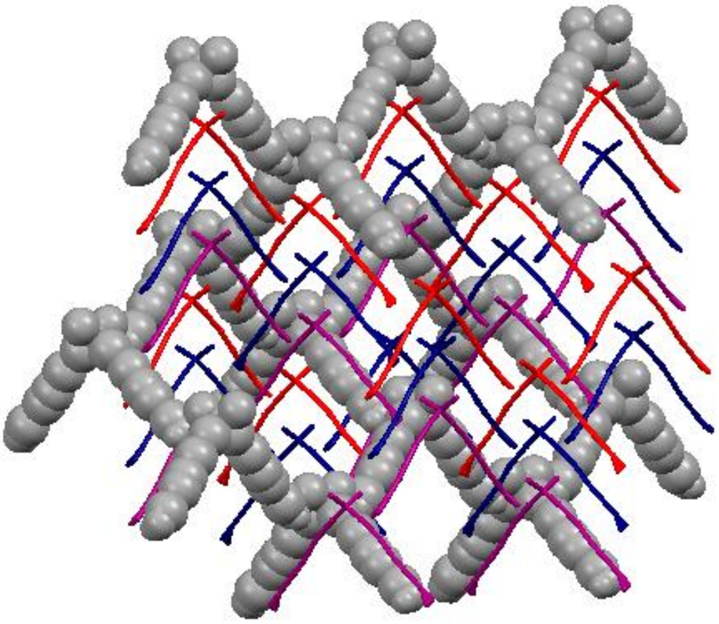

Figure 17. Schematic representation of the quadruple interpenetration of four equivalent diamondoid networks of **12.** Each tetrahedral arrangement that forms a porous framework is highlighted by a different colour

Unlike **12** and **13**, the complex Zn**L**$^2{}_2$I$_2$ (**14**) follows the quadrangular pattern based on –OH···I hydrogen bonds (3.706 Å) (Figure 18, left), in analogy to the ones observed for the previously described zinc complexes Zn(**LOH**)$_2$X$_2$ (X = Cl, Br).[21] The square grid cannot be formed in the analogous palladium complexes Pd**L**^{2}$_2$X$_2$ (X = Cl, Br), because of it is disfavoured by steric hindrance of the aryl rings of the ligand. The tetrahedral zinc complex **14** crystallizes by puckering the square grid and the corrugation imposed by the metal geometry allows to locate the aryl moieties. Similar to the square arrangement previously described for the complexes Zn(**LOH**)$_2$X$_2$ (X = Cl, Br) and **1a-c** Pd(**L**^{1})$_2$X$_2$ (X = Cl, Br, I), the puckered layers are staggered, so that the quadrangular cavities are filled by the molecules of the adjacent layer properly shifted, and the resulting structure is not porous (Figure 18, right).

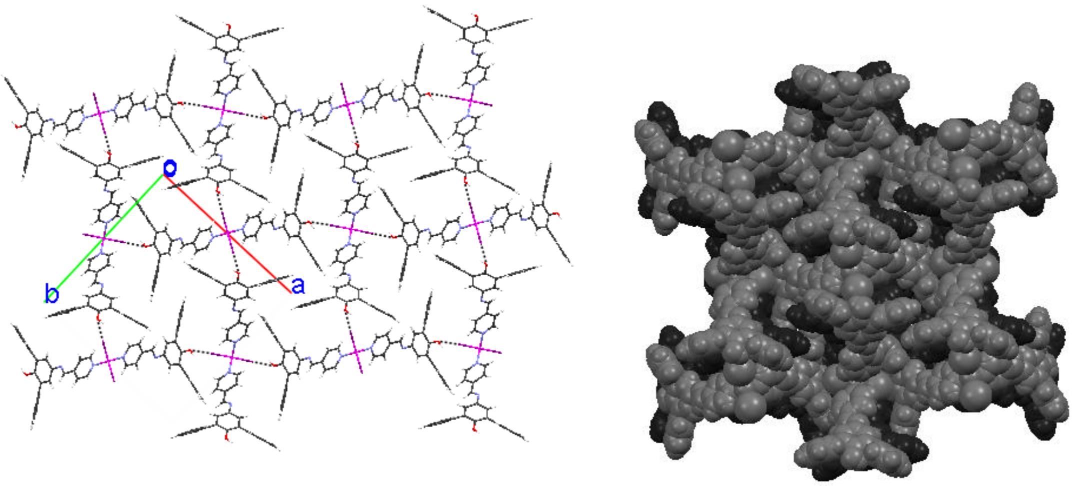

Figure 18. Supramolecular square patterns in the crystal organization of **14**, viewed down ***c*** (left) and staggered arrangement of the puckered layers into a non-porous structure (right)

8. Experimental

(1S)-1-(4-pyridinyl)ethanol (**L**^{1}) is commercially available; it is recrystallized from boiling CH_2Cl_2. The synthesis of the 2,6-diphenylphenol 4-pyridil aldimine (**L**^{2}) is reported in the Part II. [Pd(PhCN)$_2$Cl$_2$] is synthesized following literature methods. Reagent grade solvents are used without further purification. Proton NMR spectra are recorded at 25°C on a Bruker 300 FT spectrophotometer by using $SiMe_4$ as internal standard, while IR spectra are obtained with a Nicolet 5PCFT-IR spectrophotometer in the 4000-400 cm^{-1} range, using KBr disks. Elemental analyses are performed by using a Carlo Erba Model EA 1108 apparatus. Powder XRD patterns are collected using CuK$_\alpha$ radiation with a Thermo ARL X'TRA powder diffractometer equipped with a Thermo Electron solid state detector. Temperature dependent experiments are performed in air by using an Anton Paar TTK450 chamber controlled by the diffractometer software. Experiments are carried out with temperature steps of 10°C, increasing temperature by 5 °C/min, from room temperature to 240 °C (**5**) or to 160 °C (**8**) in the 2θ range 4.9-6.9° (**5**) and 4-40° (**8**). In addition, for **5** complete scans between 4° and 40°

are carried out at room temperature, 55, 155 and 240°C. Peaks intensity is extracted by fitting experimental data with the Pearson VII function. A Nikon Optihot2-Pol, polarizing light microscope, equipped with a Linkam HFS91 hot stage and a Linkam TP93 heating system is used.

Synthesis

$PdL^1{}_2Cl_2$ (1a). A CH_2Cl_2 solution (10 ml) of $Pd(PhCN)_2Cl_2$ (156 mg, 0.41 mmol) is slowly added to a CH_2Cl_2 solution (40 ml) of **L^1** (100 mg, 0.81 mmol). The mixture is stirred magnetically at room temperature for 4 hours. Then it is concentrated until yellow powder precipitates. The solid is filtered off, washed with small amounts of diethyl ether and dried *in vacuo*. Single crystals for X-ray diffraction are obtained by slow evaporation at room temperature of an acetone solution. Yield 81 %; mp: 190°C (dec.). Elemental anal. for $C_{14}H_{18}Cl_2N_2O_2Pd$ (mw: 423.64): calcd (%) C 39.69, H 4.28, N 6.61; found (%) C 40.19, H 4.23, N 6.60. IR (KBr, cm^{-1}): ν(O-H) 3453 (s, br). ^1H NMR (300 MHz, $CDCl_3$): $\delta = 9.19$ (d, J=6.7 Hz, 4H, C4(5-11-12)-H), $\delta = 7.78$ (d, J=6.7 Hz, 4H, C3(6-10-13)-H), $\delta = 5.37$ (m, 2H, C1(8)-H), $\delta = 2.07$ (s, br, 2H, O1(2)-H), $\delta = 1.91$ (d, J=6.6 Hz, 6H, C7(14)-H).

$PdL^1{}_2Br_2$ (1b). A solution of K_2PdBr_4 (205 mg, 0.41 mmol) in H_2O (10 ml) is slowly added to a THF solution (40 ml) of **L^1** (100 mg, 0.81 mmol) The mixture is stirred magnetically at room temperature for 4 hours. Then, **1b** is obtained following the same procedure as **1a**. Yield 84 %; mp: 200°C (dec.). Elemental anal. for $C_{14}H_{18}Br_2N_2O_2Pd$ (mw: 512.53): calcd (%) C 32.81, H 3.54, N 5.47; found C 33.22, H 3.45, N 5.23. IR (KBr, cm^{-1}): ν(O-H) 3473 (s, br). ^1H NMR (300 MHz, DMSO): $\delta = 8.70$ (d, J=6.1 Hz, 4H, C4(5-11-12)-H), $\delta = 7.46$ (d, J=6.1 Hz, 4H, C3(6-10-13)-H), $\delta = 5.59$ (d, J=6.5, 2H, O1(2)-H,), $\delta = 4.77$ (m, 2H, C1(8)-H), $\delta = 1.31$ (d, J=6.5 Hz, 6H, C7(14)-H).

$PdL^1{}_2I_2$ (1c). K_2PdI_4 is prepared by dissolving PdI_2 (135 mg, 0,41 mmol) with an excess of KI in H_2O. Then, the red solution is slowly added to a solution of **L^1** (100 mg, 0.81 mmol) in THF (40 ml). **1c** is separate as already described for **1a**. Single crystals for X-ray diffraction are obtained by slow evaporation from EtOH at room temperature. Yield 54%; mp: 200°C (dec.). Elemental anal. for $C_{14}H_{18}I_2N_2O_2Pd$ (mw: 606.53): calcd (%) C 27.72, H 2.99, N 4.62; found (%) C 27.33, H 2.66, N 4.25. IR (KBr, cm^{-1}): ν(O-H) 3488 (s, br). ^1H NMR (300 MHz, DMSO): $\delta = 8.77$ (d, J=6.2 Hz, 4H, C4(5-11-12)-H), $\delta = 7.46$ (d, J=6.2 Hz, 4H, C3(6-10-13)-H), $\delta = 5.60$ (d, J=4.4, 2H, O1(2)-H,), $\delta = 4.77$ (m, 2H, C1(8)-H), $\delta = 1.32$ (d, J=6.5 Hz, 6H, C7(14)-H).

Pd$L^2_2Br_2$·THF (2). K_2PdBr_4 (71 mg, 0.14 mmol) in H_2O (10 ml) is added to **L^2** (100 mg, 0.29 mmol) in THF (40 ml). The mixture is stirred magnetically at room temperature for 4 hours. A yellow powder is separated, filtered off, washed with small amounts of diethyl ether and dried *in vacuo*. Single crystals for X-ray diffraction are obtained by slow evaporation at room temperature of a THF solution. Yield 78 %. Elemental anal. for $C_{48}H_{36}Br_2N_4O_2Pd$·THF (mw: 1039.18): calcd (%) C 60.10, H 4.27, N 5.39; found (%) C 59.61, H 3.75, N 5.79. IR (KBr, cm^{-1}): ν(O-H) 3528 and 3470, ν(C=N) 1616. ^{1}H NMR (300 MHz, $CDCl_3$): δ = 8.97 (d, J=8.3 Hz, 4H, C1(5-25-29)-H), δ = 8.91 (s, 2H, C6(30)-H), δ = 8.62 (s, 2H, O1(2)-H), δ = 7.95 (d, J=8.3 Hz, 4H, C2(4-26-28)-H), δ = 7.62 (d, J=8.3 Hz, 8H, C14(18-20-24-38-42-44-48)-H), δ = 7.48 (d, J=8.3 Hz, 8H, C15(17-21-23-39-41-45-47)-H), δ = 7.41-7.33 (m, 8H, C8(12-16-22-32-36-40-46)-H), δ = 3.63 (t, J=12 Hz, 4H, THF), δ = 1.80 (t, J=12 Hz, 4H, THF) .

X-ray quality crystals of Pd$\mathbf{L}^2_2Br_2$·$CHCl_3$ (**3**) and Pd$\mathbf{L}^2_2Br_2$·2TBME (**4**) (TBME = tert-butyl methyl ether) are obtained by slow evaporation at room temperature of solutions of **2** in the appropriate solvents.

A saturated solution of **2** in $CHCl_3$/EtOH is stratified with pentane and kept at 4°C; after some weeks a precipitate is obtained, together with some X-ray quality single crystals of Pd$\mathbf{L}^2_2Br_2$·2EtOH (**5**) (yellow) and Pd$\mathbf{L}^2_2Br_2$ (**6**) (red). Another polymorph of formula Pd$\mathbf{L}^2_2Br_2$ (**6’**) is obtained by heating the heterogeneous precipitate at 240°C. m.p.: 330°C. Elemental anal. for $C_{48}H_{36}Br_2N_4O_2Pd$ (mw: 967.07): calcd (%) C 59.61, H 3.75, N 5.79; found (%) C 58.72, H 3.63, N 5.65. IR (KBr, cm^{-1}): ν(O-H) 3528, ν(C=N) 1615.

Pd$L^2_2Cl_2$ (11). A CH_2Cl_2 solution (10 ml) of $Pd(PhCN)_2Cl_2$ (55 mg, 0.14 mmol) is slowly added to a CH_2Cl_2 solution (40 ml) of **L^2** (100 mg, 0.29 mmol). The mixture is stirred magnetically at room temperature for 24 hours, concentrated and pentane is added to induce the precipitation of a yellow powder. The solid is filtered off, washed with small amounts of diethyl ether and dried *in vacuo*. Yield 84%. Elemental anal. for $C_{48}H_{36}Cl_2N_4O_2Pd$ (mw: 878.17): calcd (%) C 65.65, H 4.13, N 6.38; found (%) C 65.49, H 4.16, N 6.37. IR (KBr, cm^{-1}): ν(O-H) 3515 and 3412 (s, br), ν(C=N) 1617. ^{1}H NMR (300 MHz, $CDCl_3$): δ = 8.93 (s, 2H, C6(30)-H), δ = 8.89 (d, J=8.2 Hz, 4H, C1(5-25-29)-H), δ = 7.95 (d, J=8.2 Hz, 4H, C2(4-26-28)-H), δ = 7.84 (s, 2H, O1(2)-H), δ = 7.62 (d, J=8.2 Hz, 8H, C14(18-20-24-38-42-44-48)-H), δ = 7.47 (d, J=8.2 Hz, 8H, C15(17-21-23-39-41-45-47)-H), δ = 7.41-7.30 (m, 8H, C8(12-16-22-32-36-40-46)-H).

X-ray quality crystals of Pd$\mathbf{L}^2_2Cl_2$·THF (**7**), Pd$\mathbf{L}^2_2Cl_2$·$CHCl_3$ (**8**), Pd$\mathbf{L}^2_2Cl_2$·TBME (**9**) and Pd$\mathbf{L}^2_2Cl_2$·toluene (**10**) are obtained by slow evaporation at room temperature of solutions of **11** in the appropriate solvents.

$ZnL^2{}_2Cl_2$ (12). An ethanolic solution (10 ml) of $ZnCl_2$ (19 mg, 0.14 mmol) is slowly added to a CH_2Cl_2 solution (40 ml) of **L^2** (100 mg, 0.29 mmol). The mixture is stirred magnetically at room temperature for 4 hours. Then it is concentrated until yellow powder precipitates. The solid is filtered off, washed with small amounts of diethyl ether and dried *in vacuo*. Single crystals for X-ray diffraction (poor quality) are obtained by slow evaporation of a solution in THF kept at 4°. Yield 87 %; Elemental anal. for $C_{48}H_{36}Cl_2N_4O_2Zn$ (mw: 837.12): calcd (%) C 68.87, H 4.33, N 3.35; found (%) C 67.94, H 4.34, N 3.50. IR (KBr, cm^{-1}): ν(O-H) 3373 (s, br), ν(C=N) 1620. ^1H NMR (300 MHz, $CDCl_3$): δ = 8.92 (d, J=6.1 Hz, 2H, C1(5-)-H), δ = 8.62 (s, 1H, C6-H), δ = 8.00 (d, J=6.1 Hz, 2H, C2(4)-H), δ = 7.59-7.48 (m, 12H, C8(12-13-14-15-16-17-18-19-120-21-22-23-24)-H), δ = 5.56 (s, 1H, O1-H).

$ZnL^2{}_2Br$ (13). An ethanolic solution (10 ml) of $ZnBr_2$ (32 mg, 0.14 mmol) is slowly added to a CH_2Cl_2 solution (40 ml) of **L^2** (100 mg, 0.29 mmol). Then, **12** is obtained following the same procedure as **11**. Single crystals for X-ray diffraction (poor quality) are obtained by slow evaporation of a solution in CH_2Cl_2 kept at 4°. Yield 90 %; Elemental anal. for $C_{48}H_{36}Br_2N_4O_2Zn$ (mw: 926.08): calcd (%) C 62.25, H 3.91, N 3.02; found (%) C 61.65, H 3.69, N 3.43. IR (KBr, cm^{-1}): ν(O-H) 3517 (s, br), ν(C=N) 1618. ^1H NMR (300 MHz, $CDCl_3$): δ = 8.98 (d, J=6.01 Hz, 2H, C1(5-)-H), δ = 8.62 (s, 1H, C6-H), δ = 8.00 (d, J=6.0 Hz, 2H, C2(4)-H), δ = 7.59-7.44 (m, 12H, C8(12-13-14-15-16-17-18-19-120-21-22-23-24)-H), δ = 5.57 (s, 1H, O1-H).

$ZnL^2{}_2I_2$ (14). An An ethanolic solution (10 ml) of ZnI_2 (46 mg, 0.14 mmol) is slowly added to a CH_2Cl_2 solution (40 ml) of **L^2** (100 mg, 0.29 mmol). Then, **13** is obtained following the same procedure as **11**. Single crystals for X-ray diffraction are obtained by slow evaporation of a solution in TBME kept at 4°. Yield 88 %; Elemental anal. for $C_{48}H_{36}Il_2N_4O_2Zn$ (mw: 1020.08): calcd (%) C 56.52, H 3.56, N 2.75; found (%) C 55.71, H 3.62, N 2.80. IR (KBr, cm^{-1}): ν(O-H) 3515 (s, br), ν(C=N) 1617. ^1H NMR (300 MHz, $CDCl_3$): δ = 9.04 (d, J=6.0 Hz, 2H, C1(5-)-H), δ = 8.64 (s, 1H, C6-H), δ = 8.00 (d, J=6.0 Hz, 2H, C2(4)-H), δ = 7.62-7.42 (m, 12H, C8(12-13-14-15-16-17-18-19-120-21-22-23-24)-H), δ = 5.59 (s, 1H, O1-H).

X-ray Crystallography

MoKα radiation (λ=0.71073 Å) on a SMART AXS 1000 CCD diffractometer is used for all compounds. All data are collected at room temperature (293 K). Lorentz, polarization, and absorption corrections are applied.[25] Structures are solved by direct methods using SIR97[26] and refined by full-matrix least-squares on all F^2 using SHELXL97[27] implemented in the WingX package.[28] Hydrogen atoms are introduced in idealized positions riding on their carrier atoms. Anisotropic displacement parameters are refined for all non-hydrogen atoms, apart from **2**, **3** and **6**, where only heavy atoms were refined anisotropically. In general these compounds tend to show relevant mosaicity and tend to partially loose crystallinity upon storage; consequently, in many cases the diffraction quality did not allow a straightforward refinement of the molecular models. Aromatic rings were constrained to a regular geometry in **2**, **3**, **4**, **6** and **10**; restraints on thermal displacement parameters of the host molecules were used in **2**, **3** and **9**; geometry of the host molecules was partially restrained in **2** and **3**; geometry and thermal displacement parameters of the guest were restrained in **2**, **3**, **5** and **8**; isotropic restraints on C, N and O were applied in **4**; antibumping restraints among H atoms were applied in **2** and **3**. Nevertheless, some undesiderable short H…H contacts persisted in **2** and **3** due to the poor quality of diffraction data. The setting of the unit cell for **6** was chosen in order to better compare the packing metrics with **2-5**. Compounds **2** and **3** are described in the space group Cc, even if they reveal a remarkable pseudosymmetry towards C2/c. The higher symmetry would however imply disorder for the aromatic rings, and has been discarded. The refinement of the structural models presented here for **2** and **3** has proven to be quite problematic because of the poor quality of the data. In both cases we have chosen to keep simple isotropic, geometrically restrained models that best represented the minimum information needed for the discussion and comparison of the general structural features among **2-6**, in order to avoid the risk of overfitting data with parameters describing details not accessible to the present quality of the experiment.

Tables 3-6 summarize crystal data and structure determination results. Hydrogen bonds have been analyzed with SHELXL97[27] and PARST97[29] and are reported in Table 2; extensive use was made of the Cambridge Crystallographic Data Centre packages[30] for the analysis of crystal packing.

Table 3. Crystal data for compounds **1a-c**

Compound	**1a**	**1b**	**1c**
Formula	$C_{14}H_{18}Cl_2N_2O_2Pd$	$C_{14}H_{18}Br_2N_2O_2Pd$	$C_{14}H_{18}I_2N_2O_2Pd$
Molecular weight	423.60	512.52	606.50
Crystal system	monoclinic	monoclinic	monoclinic
Space group	$P\ 2_1$	$P\ 2_1$	$P\ 2_1$
Z	2	2	2
a/Å	6.4238(5)	6.6809(7)	6.875(1)
b/Å	14.710(1)	14.844(2)	15.151(3)
c/Å	8.7750(6)	8.6727(9)	8.967(2)
β/°	100.176(1)	101.713(2)	102.513(3)
$V/Å^3$	816.1 (1)	842.2(2)	911.8(3)
ρ /Mg m^{-3}	1.724	2.021	2.209
θ range for data collection/°	2.36 - 27.12	2.40 - 28.33	2.33 - 26.76
Unique reflections	8679	10113	9730
Observed reflections [I>2σ(I)]	3507	4013	3866
Data/ restraints/ parameters	3507/ 1/ 195	4013/ 1/ 197	3866/ 3/ 196
Goodness-of-fit on F^2	1.056	1.019	1.065
R_1 [on I>2σ(I)]	0.0235	0.0833	0.0486
wR_2 [on I>2σ(I)]	0.0621	0.2110	0.1253
R_1 (all data)	0.0244	0.0923	0.0566
wR_2 (all data)	0.0630	0.2242	0.1372

Table 4. Crystal data for compounds **2-6**

Compound	**2**	**3**	**4**	**5**	**6**
Formula	$C_{52}H_{44}Br_2N_4O_3Pd$	$C_{49}H_{37}Br_2Cl_3N_4O_2Pd$	$C_{58}H_{60}Br_2N_4O_4Pd$	$C_{52}H_{48}Br_2N_4O_4Pd$	$C_{48}H_{36}Br_2N_4O_2Pd$
Molecular weight	1039.13	1086.40	1143.32	1059.16	967.03
Crystal system	monoclinic	monoclinic	monoclinic	monoclinic	monoclinic
Space group	C c	C c	$P\ 2_1/c$	$P\ 2_1/c$	$P\ 2_1/c$
Z	4	4	2	2	4
a/Å	30.31(1)	32.04(6)	17.54(2)	15.075(2)	30.12(3)
b/Å	9.506(4)	9.80(2)	9.98(1)	10.003(1)	10.043(5)
c/Å	15.217(6)	15.72(3)	15.75(2)	15.795(2)	15.740(8)
β/°	109.603(7)	110.89(2)	91.61(1)	93.286(2)	116.83(4)
$V/Å^3$	4130(3)	4611(2)	2756(5)	2377.9(4)	4248(6)
ρ /Mg m^{-3}	1.671	1.565	1.378	1.479	1.512
θ range for data collection/°	1.43 - 23.51	1.36 - 18.94	1.16 - 19.04	1.35 - 23.26	0.76 - 18.92
Unique reflections	15417	11645	13927	19685	20638
Observed reflections [I>2σ(I)]	5924	3640	2206	3412	3357
Data/ restraints/ parameters	5924/ 222/ 161	3640/ 120/ 166	2206/ 200/ 270	3412/ 17/ 289	3357/ 0/ 163
Goodness-of-fit on F^2	1.129	0.926	0.797	0.988	1.004
R_1 [I>2σ(I)]	0.1465	0.0946	0.0722	0.0539	0.0940
wR_2 [I>2σ(I)]	0.3458	0.2236	0.1406	0.1362	0.2066
R_1 (all data)	0.1843	0.1703	0.2123	0.0720	0.2106
wR_2 (all data)	0.3743	0.2593	0.1785	0.1459	0.2407

Table 5. Crystal data for compounds **7-10**

Compound	**7**	**8**	**9**	**10**
Formula	$C_{52}H_{44}Cl_2N_4O_3Pd$	$C_{49}H_{37}Cl_5N_4O_2Pd$	$C_{53}H_{48}Cl_2N_4O_3Pd$	$C_{55}H_{44}Cl_2N_4O_2Pd$
Molecular weight	950.21	997.48	966.25	970.24
Crystal system	triclinic	triclinic	triclinic	triclinic
Space group	P -1	P -1	P -1	P -1
Z	2	2	2	2
a/Å	14.2831(6)	14.793(2)	14.383(1)	14.887(3)
b/Å	11.7255(5)	10.924(1)	11.418(1)	10.877(2)
c/Å	15.2836(6)	16.200(2)	15.924(1)	16.305(3)
α/°	99.462(1)	100.689(2)	98.07(2)	100.371(4)
β/°	102.573(1)	107.777(2)	102.73(2)	107.165(3)
γ/°	109.408(1)	106.575(2)	108.08(2)	106.752(3)
V/$Å^3$	2277.1(2)	2280.2(5)	2362.6(3)	2311.9(8)
ρ /Mg m^{-3}	1.386	1.453	1.358	1.394
θ range for data collection/°	1.41 - 27.51	1.38 - 20.91	1.35 - 18.80	1.37 - 23.31
Unique reflections	28013	15493	12734	20297
Observed reflections [I>2σ(I)]	10406	4796	3665	6657
Data/ restraints/ parameters	10406/ 0/ 561	4796/ 6/ 552	3665/ 552/ 574	6657/ 2/ 472
Goodness-of-fit on F^2	0.775	0.882	0.723	0.695
R_1 [on I>2σ(I)]	0.0412	0.0516	0.0493	0.0567
wR_2 [on I>2σ(I)]	0.0754	0.1123	0.0597	0.0784
R_1 (all data)	0.1120	0.0985	0.1461	0.2263
wR_2 (all data)	0.0882	0.1262	0.0755	0.1069

Table 6. Crystal data for compounds **12-14**

Compound	**12**	**13**	**14**
Formula	$C_{48}H_{36}Cl_2N_4O_2Zn$	$C_{48}H_{36}Br_2N_4O_2Zn$	$C_{48}H_{36}I_2N_4O_2Zn$
Molecular weight	837.12	926.08	1020.08
Crystal system	tetragonal	tetragonal	tetragonal
Space group	P 4_2	P 4_2	P -4 21 c
Z	2	2	4
a/Å	19.595(2)	19.589(7)	18.9037(1)
b/Å	19.595(2)	19.589(7)	18.9037(1)
c/Å	5.2472(4)	5.149(2)	11.8392(6)
V/$Å^3$	2014.8(3)	1975.8(1)	4232.7(2)
ρ /Mg m^{-3}	1.380	1.556	1.601
θ range for data collection/°	1.04 - 23.25	1.04 - 18.98	1.52 - 24.28
Unique reflections	2896	1582	3429
Observed reflections [I>2σ(I)]	2005	906	2866
Data/ restraints/ parameters	2896 / 6 / 211	1582 / 6 / 81	3429 / 0 / 330
Goodness-of-fit on F^2	1.182	1.123	1.042
R_1 [on I>2σ(I)]	0.1098	0.1128	0.0321
wR_2 [on I>2σ(I)]	0.2912	0.2888	0.0605
R_1 (all data)	0.1391	0.1448	0.0526
wR_2 (all data)	0.3138	0.3096	0.0672

9. Conclusions

In this section the role of molecular shape in the formation of inclusion networks is explored. The results successfully describe how the rational design of awkward shape molecules, having low self-packing efficiency, enables the formation of host-guest adducts.

Wheel-and-axle diols (*waads*) are good candidates as host species. They have a molecular skeleton in which a rigid linear axle is present together with large ending wheel groups. They are able to arrange into bistable chain-based systems, by switching from self-mediated to guest-mediated networks. Both the linearity of the axle and the wheels hindrance are basic points of discussion in order to keep the overall molecular shape.

This part of the work starts with the validation of the wheel-and-axle shape, showing how the tuning of the dumbbell shape, achieved by bending the axle and by reducing the wheel of the molecule, implies the loss of the chlatrating ability.

First, the supramolecular structures of a family of bent-axle molecules previously studied are compared with the features found in new organo-metallic systems with less hindered wheels. The structural role of the wheels is clearly crucial: if large wheels are substituted by less bulky groups, with the axle substantially unaffected, the packing is reached by superposition of sheets of supramolecular squares, without leaving voids for any guests. The square motif is analogous to the pattern observed for previously studied complexes with bent axle and unaffected wheels.

Second, the design, the synthesis and the characterization of new elongate *waad* systems are proposed. These larger diols show good propensity to include guest species, in 1:1 or 1:2 stoichiometry. The anchoring sites play a marginal role and the overall shape is the key of control of the multicomponent assembly. The role of the anion is also highlighted, because the crystal packing is sensitive to the change of the anion as well. The solid-state properties of these systems are carefully analyzed. Unfortunately all the inclusion compounds easily desolvate and they are not able to reabsorb guest by vapour exposition. Probably the inability in uptaking guest molecules is correlated with the strength of the sum of the interactions linking the long molecules of the complexes, together with the formation of amorphous phases during the desolvatation and with problems in the topological rearrangement of highly anisotropic systems. Other analyses on the local factors that enable the guest-uptake from vapour as well as the reversibility of the guest-uptake and release mechanism need additional studies and more careful considerations.

Finally, the effect of the axle bending is again explored, by the description of the crystal aggregation motifs found in a class of new bent-axle complexes.

References

1. C. Guilera and J. W. Steed, Topological Control in Coordination Polymers by Non-Covalent Forces, *Chem. Commun.*, 1999, 1563-1564
2. C. A. Hunter, The Role of Aromatic Interactions in Molecular Recognition, *Chem. Soc. Rev.*, 1994, 101-109
3. L. R. MacGillivray, R. H. Groeneman, J. L. Atwood, Design and Self-Assembly of Cavity-Containing Rectangular Grids, *J. Am. Chem. Soc.*, 1998, 120, 2676-2677
4. C. B. Aakeröy, A. M. Betty, D. S. Leinen, A Versatile Route to Porous Solids: Organic-Inorganic Hybrid Materials Assembled through Hydrogen Bonds, *Angew. Chem. Int. Ed.*., 1999, 38, 1815-1819
5. C. B. Aakeröy, A. M. Betty, D. S. Leinen, K. L. Lorimer, Deliberate Combination of Coordination Polymers and Hydrogen Bonds in a Supramolecular Design Strategy for Inorganic/Organic Hybrid Networks, *Chem. Commun* ., 2000, 935-936
6. S. A. Bourne in *Engineering of Crystalline Materials Properties: State of the Art in Modeling, Design and Applications*, J. Novoa, D. Braga, L. Addadi (Editors), (Proceedings of the NATO Advanced Study Institute, held 7-17 June 2007, Erice, Italy)
7. A. I. Kitaigorodski, *Organic Chemical Crystallography* (Consultants Bureau, New York, 1961)
8. F. H. Allen, The Cambridge Structural Database: a Quarter of a Million Crystal Structures and Rising, *Acta Crystallogr.*, Sect. B, 2002, *58*, 380–388
9. A. Nangia and G. R. Desiraju, Pseudopolymorphism: Occurrences of Hydrogen Bonding Organic Solvents in Molecular Crystals, *Chem. Commun* ., 1999, 605-606
10. A. Bacchi in *Engineering of Crystalline Materials Properties: State of the Art in Modeling, Design and Applications*, J. Novoa, D. Braga, L. Addadi (Editors), (Proceedings of the NATO Advanced Study Institute, held 7-17 June 2007, Erice, Italy)
11. C. H. Gorbitz, H. P. Hersleth, On the Inclusion of Solvent Molecules in the Crystal Structures of Organic Compounds, *Acta Cryst.*, 2000, B56, 526-534
12. J. D. Dunitz, G. Filippini, A. Gavezzotti, Molecular Shape and Crystal Packing: a Study of $C_{12}H_{12}$ Isomers, Real and Imaginary, *Tetrahedron*, 2000, 56, 6595-6601
13. F. Toda, *Comprehensive Supramolecular Chemistry*, 1996, Vol. 6, Ch. 15, 465-516
14. T.L. Roex, L.R. Nassimbeni, E. Weber, Selectivity and Structure of Mixed Guest Clathrates, *New J. Chem.*, 2008, 32, 856-863
15. M.R.Caira, A.Jacobs, L.R. Nassimbeni, F. Toda, Inclusion Compounds of 1,1,6,6-tetraphenylhexa-2,4-diyne-1,6-diol with DMF and DMSO: Structures, Selectivity and Kinetics of Desolvation, *CrystEngComm,* 2003, 5, 150-153
16. M.R.Caira, L.R Nassimbeni, F.Toda, D. Vujovic, Inclusion by a Diol Host Compound: Structure and Dynamics of Volatile Guest Exchange, *J. Chem. Soc., Perkin Trans. 2*, 2001, 2119-2124
17. A. Bacchi, E. Bosetti, M. Carcelli, P. Pelagatti, D. Rogolino, G. Pelizzi, "Venetian Blinds" Mechanism of Solvation/Desolvation in Palladium(II) Wheel-and-Axle Organic-Inorganic Diols, *Inorg. Chem.*, 2005, 44, 431-442
18. A. Bacchi, M. Carcelli, E. Bosetti, Engineering Organic/Inorganic Diols that Reversibly Capture and Release Volatile Guests, *CrystEngComm*, 2005, 7, 527-537
19. A. Bacchi in *Models, Mysteries and Magic of Molecules*, Ed. C.A.Boyens and J.F.Ogilvie, Springer, 2008, 87-108

20. A. Bacchi, M. Carcelli, T. Chiodo, F. Mezzadri, Effects of “Changing the Wheels” on the Inclusion Properties in Metal–Organic Diols, *CrystEngComm*, 2008, 10, 1916-1927

21. A. Bacchi, E. Bosetti, M. Carcelli, Unusual Hydrogen Bonded $(OH)_4$ Tetrahedral Nests Organize Zinc(II) Coordination Complexes in a Non-Covalent Diamondoid Network, *CrystEngComm*, 2007, 9, 313-318

22. G.R. Desiraju, Supramolecular Synthons in Crystal Engineering - A New Organic Synthesis, *Angew. Chem. Int. Ed. Engl.*, 1995, 34, 2311

23. Bauo-Qing Ma, Hao-Ling Sun, Song Gao, Assembly of Hydrogen Bonded Diamondoid Networks Based on Synthetic Metal-Organic Tetrahedral Nodes, *Inorg. Chem.*, 2005, 44, 837-839

24. M. Munakata, L. Ping Wu, M. Yamamoto, T. Kuroda-Sowa, M. Maekawa,, Construction of Three-Dimensional Supramolecular Coordination Copper(I) Compounds with Channel Structures Hosting a Variety of Anions by Changing the Hydrogen-Bonding Mode and Distances *J. Am. Chem. Soc.*, 1996, 118, 3117-3124

25. (a) SAINT: SAX, Area Detector Integration, Siemens Analytical instruments INC., Madison, Wisconsin, USA. (b) G.Sheldrick, SADABS: Siemens Area Detector Absorption correction Software, 1996, University of Goettingen, Germany

26. A.Altomare, M.C.Burla, M.Cavalli, G.Cascarano, C.Giacovazzo, A.Gagliardi, A.G.Moliterni, G.Polidori, R.Spagna, *Sir97: A New Program For Solving and Refining Crystal Structures*, 1997, Istituto di Ricerca per lo Sviluppo di Metodologie Cristallografiche CNR, Bari

27. G.Sheldrick, *Shelxl97. Program for structure refinement*. University of Goettingen, Germany, 1997

28. L.J.Farrugia, *J. Appl. Cryst.* 1999, 32, 837-838

29. M.Nardelli, *J. Appl. Cryst.* 1995, 28, 659

30. (a) F. H.Allen, O.Kennard, R.Taylor, *Acc. Chem. Res.*, 1983, 16, 146-153. (b) I. J.Bruno, J. C.Cole, P. R.Edgington, M.Kessler, C. F.Macrae, P. McCabe, J. Pearson, R.Taylor, *Acta Crystallogr.*, 2002, B58, 389-397

PART II

Design and properties of tunable hydrogen-bonded molecular solids

1. Introduction

The ability to predict the assembly of molecules into extended ordered networks is a central aspect in supramolecular chemistry.[1-2] Much effort is directed to increase the choice of reliable building blocks to realize extended architectures held together by selective and directional hydrogen bonds[3] and weak non-covalent forces[4] and to better understand how the molecular building blocks could be assembled into architectures with a precise and predictable connectivity. The hydrogen bond[3] enables a good control on the solid-state assembly, due to its selectivity, strength and directionality. There are many reports on design strategies based on the complementary geometry between functional groups and on the numeric balance between hydrogen bond donors and acceptors.[5-7] The use of specific functional group enables to obtain specific hydrogen bonded motifs. They might be discrete (0D),[8] unidimensional (1D),[9] bidimensional (2D)[10] or tridimensional (3D)[11] supramolecular archictectures.

This part of the work takes aim at the rational design of 1D supramolecular motifs held together by hydrogen bonds. Chain motifs are achieved by head-to-tail hydrogen bond interactions between bifunctional molecules. The point of discussion is how it is possible to tune the geometric properties of these chains through small changes on the organic skeleton of the molecular building blocks. In this sense, the adjective “tunable” refers to the opportunity in changing the overall shape of the hydrogen bonded motifs. From a crystal enigineering point of view, the interest is on the solid-state properties of the resulting molecular solids. Particularly, both the opportunity to design host-guest systems and the properties of the obtained multicomponent assemblies are correlated with the geometric features of the hydrogen bonded chains. In this perspective the shape of the supramolecular motif is the key regulating the overall crystal structure and the properties of the lattice.

2. Experiment design

Pyridineoximes are building blocks well suited for the synthesis of hybrid organic-inorganic materials, due to the consistency in their primary hydrogen bond interactions.[12] The presence of the pyridine ring makes these compounds versatile building blocks in coordination chemistry, while the OH group is connected with a potential solid-state clathrating ability based on hydrogen interactions involving the host-guest pairs.

In the previous section, the importance of the organic pyridineiminic moiety on the clathrating ability of the wheel-and-axle hybrid organic-inorganic diols has been described.[13]

With the aim to realize new elongated ligands for the synthesis of the hybrid metallo-organic diols described in the first section (Scheme 1), an aryl-imino spacer is introduced between the pyridine moiety and the hydroxil function of the previously used pyridineoximes.[12] In a crystal engineering perspective, the molecular features are introduced as point of discussion in order to describe the solid-state supramolecular organization. The main points of analysis are: (i) the geometry of the O-H group, (ii) the rigidity of the molecular skeleton, (iii) the presence/absence of spacer groups, (iv) the presence/absence of bulky aryl groups around the OH, (v) the position of the pyridinic nitrogen atom (*ortho*, *meta* or *para* iminic substituited compounds).

A discussion about the *para*-pyridyl imino compounds is first reported. Then, the *meta* and *ortho* derivates are described, since they exhibit a different behaviour.

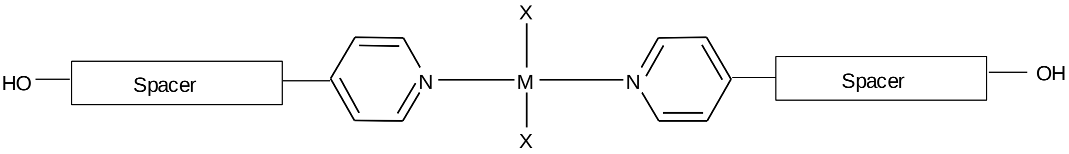

Scheme 1 Diolic hybrid organic-inorganic complex (M = metal, X = anion)

3. A discussion on the supramolecular structures of a class of 4-pyridyl imino compounds[14]

In this section, the synthesis and solid state organization of the 4-pyridyl imino compounds **1-4** (Scheme 2) is reported. All the iminic compounds **1-4** are synthesized by a condensation reaction between a carbonylic compound and an aromatic amine. The reactivity between the molecular precursor is analyzed, particularly referring to the co-crystallization between 4-aminobenzylalcohol and 4-acetylpyridine (compound **5,** Figure 6). The formation of the co-crystal **5** is analyzed by screening the reactivity trends of **6**, **7** and **8** and the results are then discussed in terms of the amine crystal packing features.[15-17]

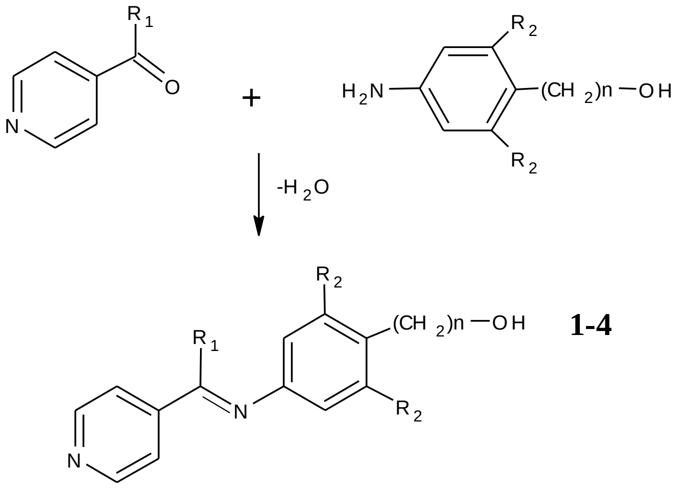

6-8

1-4

	R_1	R_2	n
1	CH_3	H	0
2	H	H	0
3	H	Ph	0
4	H	H	1
6		H	0
7		Ph	0
8		H	1

Scheme 2 Synthesis of **1**, **2**, **3** and **4**, from their molecular precursor **6**, **7** and **8**

3.1. Results and discussion

Compounds **1**, **2**, **3** (**L**^{2} in Part I) and **4** are synthesized as shown in Scheme 2, starting from 4-acetylpyridine or 4-pyridinecarboxaldehyde and an aromatic amine: 4-aminophenol (**6**), 3,5-diphenyl-4-hydroxyaniline (**7**) or 4-aminobenzylalcohol (**8**). The condensation reactions give **1-4** with good yields; the synthesis of **4** is conducted under nitrogen to prevent the decomposition of the amine.

Single crystals suitable for X-ray diffraction experiments are obtained by slow evaporation at room temperature of saturated solutions of **1** and **2** in THF and methanol, respectively, by cooling at -12 °C a saturated toluene solution of **3** and by stratifying pentane over a saturated solution of **4** at 4°C. The molecular structures of **1-4** are shown in Figure 1. In these compounds, the pyridine and the phenyl rings are in *trans*; molecular conformations are described by means of the dihedral angle δ described by the mean planes A and B between the two aromatic rings (Figure 2; Table 1).

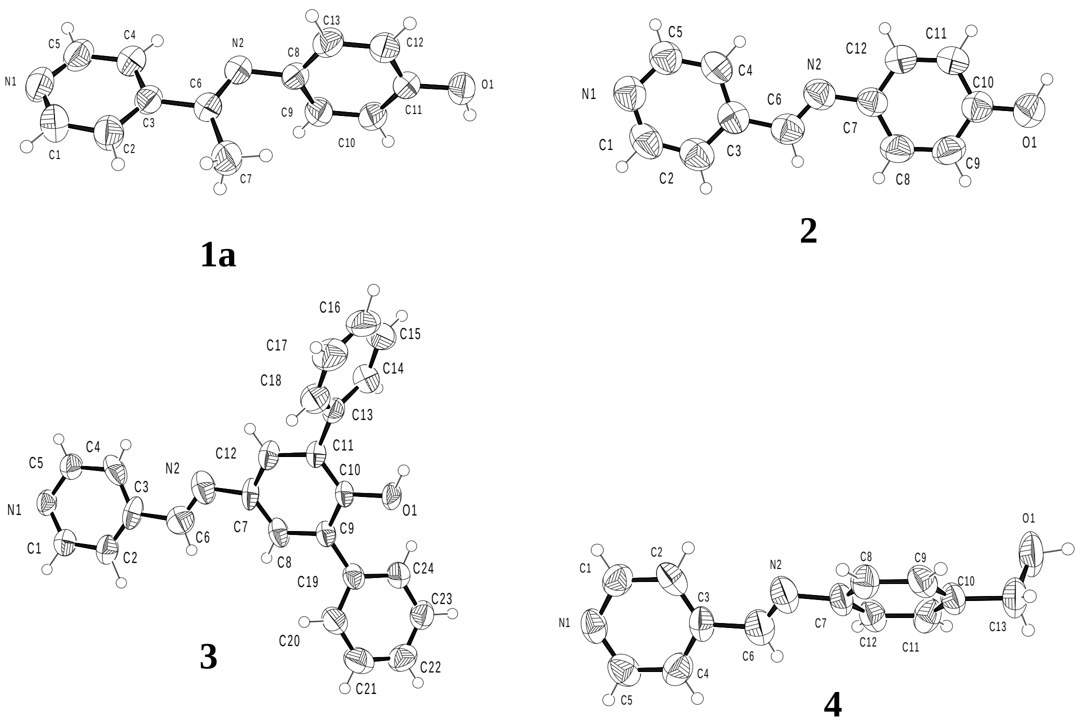

1a

2

3

4

Figure 1. Molecular structures and labelling of **1a**, **2**, **3** and **4**, thermal ellipsoids at the 50% probability level. Molecular **1b** is omitted

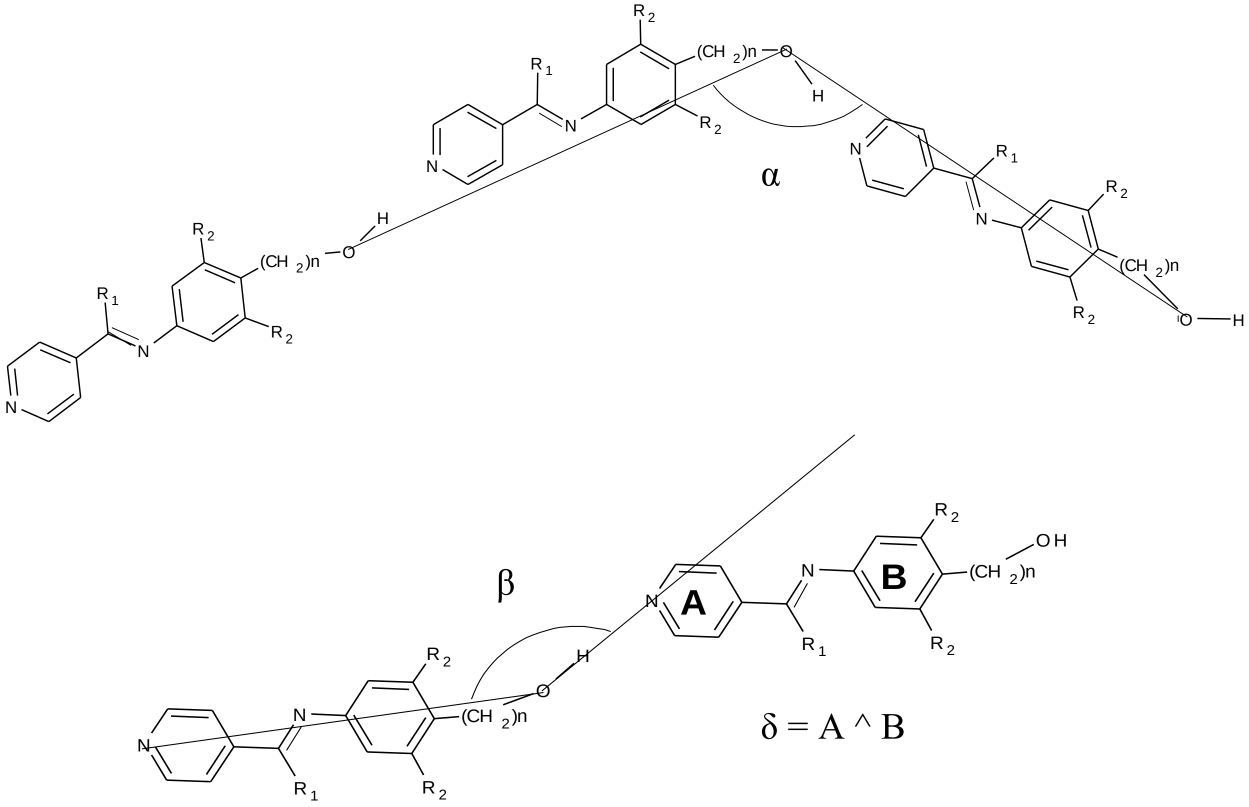

Figure 2. Representation of the geometrical descriptors α, β and δ

	δ (°)	α (°)	β (°)	d(O··· N) (Å)	O-H··N (°)	Symmetry
1a	84	107	110	2.794(2) O1…N3	172	x+1, y, z-1
1b	90	107	113	2.758(2) O2…N1	169	
2	9	121	111	2.769(3) O1…N1	175	x, y-1/2, -z-1
3	23	162	143	2.695(3) O1…N1	138	x-2, -y-3/2, z-1/2
4	55	180	172	2.805(4) O1…N1	165	x+1, y, z+1

Table 1. Values of molecular and supramolecular descriptors of **1**, **2**, **3** and **4**

Compound **1** crystallizes with two independent molecules **1a** and **1b** in the asymmetric unit. These molecules are substantially identical, also in their supramolecular features (see below the 2D-fingerprint plots discussion) and they differ only slightly in the value of δ. In both cases, the presence of the methyl group induces the mutual orthogonal orientation of the pyridine and of the pheyl ring (δ=84 and 90° for **1a** and **1b**); the substitution of the methyl group with an hydrogen atom significantly reduces the angle δ (9, 23 and 55° in **2**, **3** and **4**, respectively). The compounds that crystallize in crystal structures with Z′ > 1 are a current field of interest and debate.[18] It has been hypothesized that they are kinetic products,[19] blocked in “frozen” conditions. These low symmetry systems could evolve to higher symmetry thermodynamic forms in which the equivalence of the molecules is observed. The slurry technique has been used to check this possibility. With this aim a suspension of **1** in pentane has been stirred for one week, but no phase modification has been observed by analysing the slurry product with X-ray powder diffraction.

The general feature of the crystal structures of **1**–**4** is the tendency to give polar supramolecular chains sustained by hydrogen bonds involving the OH groups and the pyridine nitrogen atoms N_{py}, as in the pyridineoxime (Figure 3).[12] These chains are assembled in an antiparallel arrangement and interact by means of CH···O and CH···π contacts (Figure 4). Two parameters can be used to describe the supramolecular chain arrangements (Figure 2):

- the angle α between the two vectors connecting the oxygen atoms of three consecutive molecules, representing the chain folding;

- the angle β formed by the vector defined by the hydrogen bond O…N_{py} and the vector which describes the molecular long axis; β expresses the bending of the hydrogen bond respect to the chain direction. The values of these descriptors are reported in Table 1. In **1** the chains are based on a regular alternation of **1a** and **1b**, connected by two slightly different OH···N_{py} hydrogen bonds. Due to the hydrogen bond directionality, a zigzag arrangement of the chains is observed (**1a**: α=107°, β=110°; **1b**: α=107°, β=113°). These values of α and β reflect the bending of the C-O-H bond angle, centered on the oxygen, that acts as a node between the long molecular axis containing C-O and the almost linear hydrogen bond direction (**1a**: 172°; **1b**: 169°), containing O-H. The chains are associated by C-H···O interactions (Figure 4). In **2** the substitution of the methyl group with the hydrogen atom allows the coplanar arrangement of the two aromatic rings (δ=9°). The chains are associated by weak C-H···O contacts, and edge-to-face C-H···π interactions (Figure 4). In **3** the supramolecular chains are quite linear (α=162°, β=143°), due to the presence in *ortho* to the hydroxyl group of the two phenyl rings, whose hindrance forces the hydrogen bond direction. This steric influence compensates the bending on the oxygen atom, resulting in an hydrogen bond less linear in **3** respect to **2** (O-H…N = 138 and 175° for **3** and **2**, respectively). Between the chains there are C-H···N_{im} and edge-to-face C-H···π interactions (Figure 4). In compound **4** the hydrogen bonds are collinear with the chain direction (α=180°, β=172°) due to the conformational freedom that derives from the presence of the methylenic group. As in the preceding examples, chains interact by means of and edge-to-face C-H···π interactions (Figure 4).

The supramolecular arrangements in **1-4** are analysed also by means of the Hirshfeld Surfaces[20] and of the corresponding 2D-fingerprint plots[21-22] (Figure 5). The 2D-fingerprint plots suggest that these compounds share some similar structural features: the hydrogen bond OH···N_{py} (labelled A), some degree of CH···π interaction (labelled B), and H···H contacts of about 2.2-2.4 Å, in the limit of the van der Waals radii[23] (labelled C). 2D-fingerprint plots also confirm that, from a supramolecular perspective, molecules **1a** and **1b** are identical, since their diagrams are identical and mirror-like. The A trace in the fingerprint plot of **3** reflects the marginally longer hydrogen bond.[24] The B traces are less pronounced in **2** and **3** than in **1** and **4**, where two “wings” appear in the plots, showing that in these latter structures the CH…π interactions are more significant. The intermolecular H···H contacts in the limit of the van der Waals radii show up as a characteristic hump in the central region of the plot of **1**, **3** and **4**. The sparse region of blue points (labelled D) in **1** and **4** fingerprint plots arises from the H···H contacts involving respectively the methyl and methylenic groups and the aromatic moieties;

this feature is absent in the 2D-fingerprint plot of **2**, whose supramolecular structure is largely dominated by the π···π stacking motif. The diffuse blue region (labelled E) results from a small part of the surface with large distances to the nearest atoms and it suggests a less than ideal packing arrangement for the molecule in the crystal.

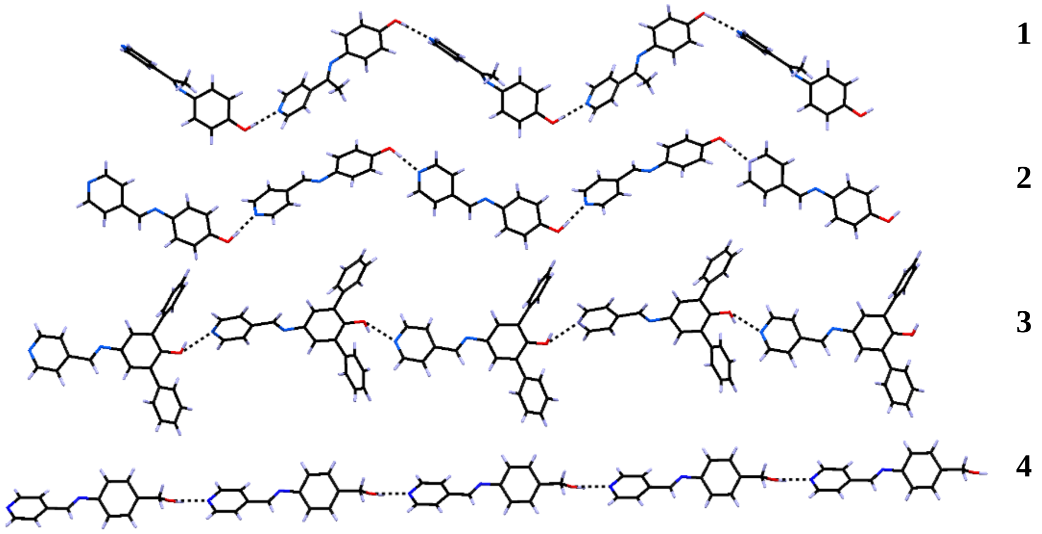

Figure 3. Chains arrangement in the supramolecular structure of **1**, **2** , **3** and **4**. For a better comparison the aryl group of the central molecule in each chain is placed on the plane of the figure

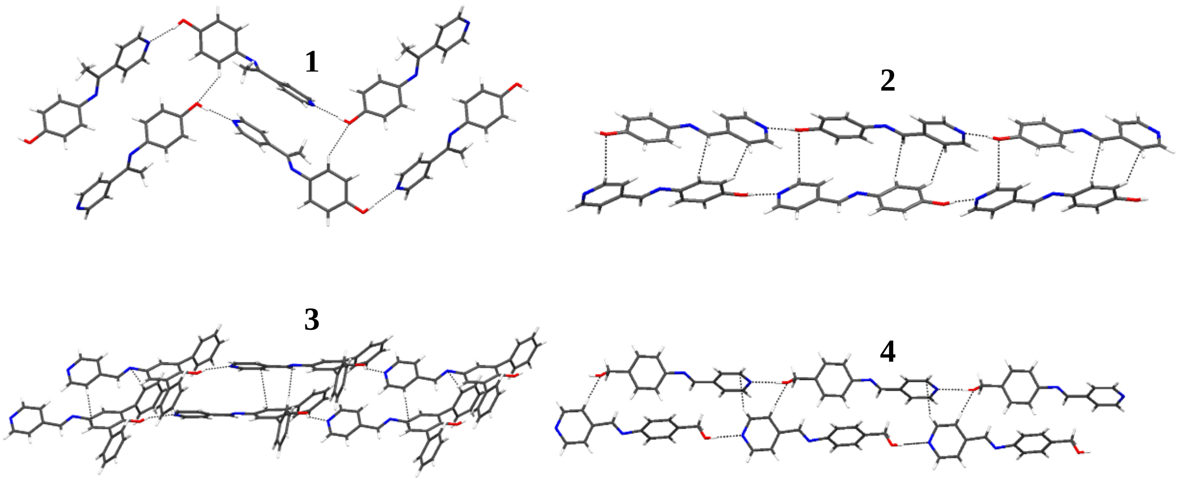

Figure 4. Interaction between chains in supramolecular structure of **1**, **2**, **3** and **4**

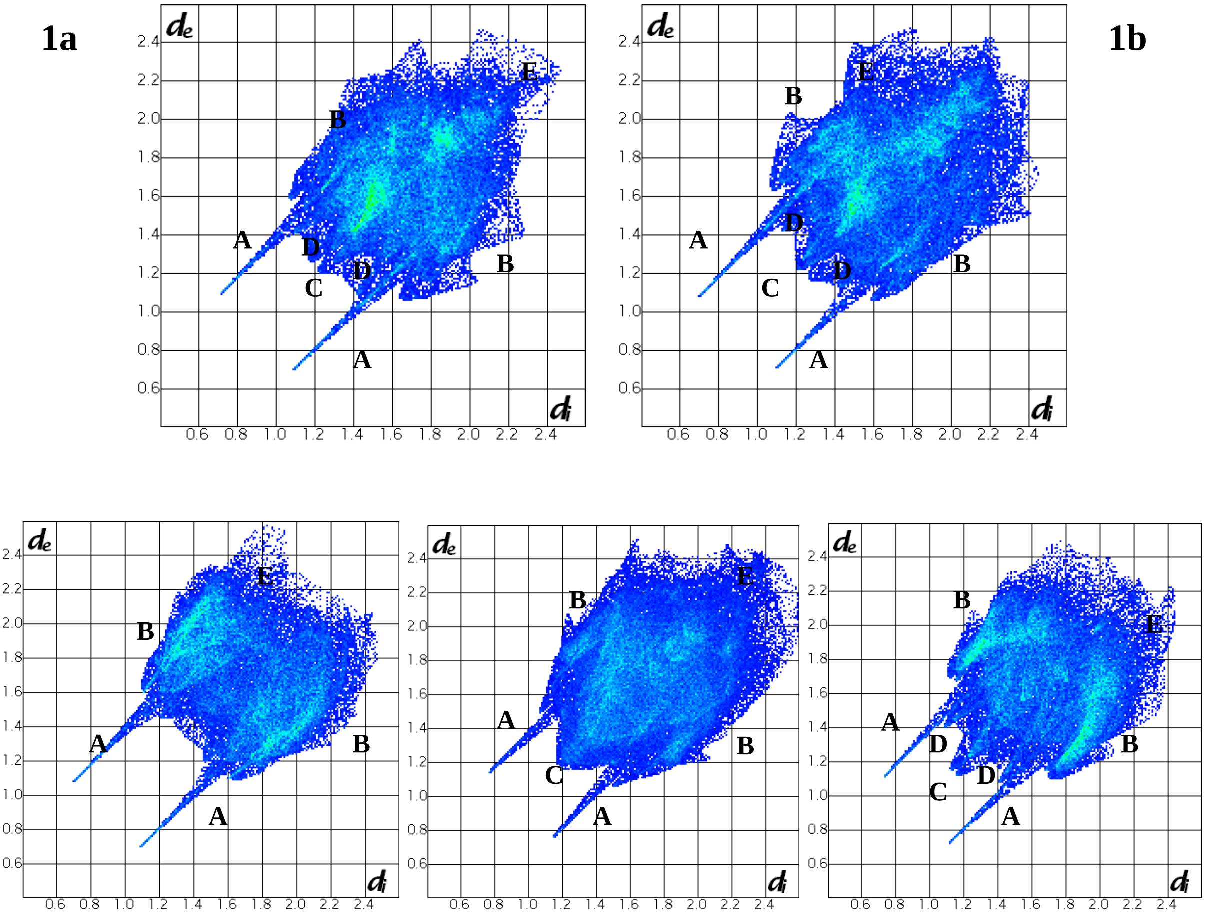

1a **1b**

2 **3** **4**

Figure 5. 2D-fingerprint plots of **1a**, **1b**, **2**, **3** and **4**

In conclusion, in these compounds there is a control on the supramolecular features due to the presence of local, structural factors: the tetrahedral geometry of the O-H group, the rigidity of the molecular skeleton, the presence/absence of the CH_2 group, the presence/absence of bulky aryl groups. The simplest systems **1** and **2** form zig-zag chains, because the directions of the hydrogen bond and of the molecular axis have a junction in the tetrahedral oxygen node. If the other CH_2 junction is introduced (**4**), the chain results linear; the chain is also linear if the bulky aryls (**3**) force the hydrogen bond to bend along the direction of the molecular long axis. Whenever the organic backbone is slightly changed, the entity of the various local contributes to the packing could vary, giving the opportunity to tune the shape of the resulting supramolecular motifs.

3.2. Co-crystal formation, reactivity and supramolecular structures of the amines

During the attempt of reaction between 4-acetylpyridine and 4-aminophenol in THF, the co-crystal **5** (Figure 6) is serendipitously isolated.[25] The packing of **5** is based on the hydrogen bonded network with three donors (NH_2, OH) and three acceptors (N_{py}, C=O, OH) (Table 2). The supramolecular chains contain the regular alternation of the two molecular components linked together by N-H…O=C and O-H…N_{py} hydrogen bonds [O2…N1 2.835(2) Å, 178°; N2…O1(x+1, y, z+1) 3.123(2) Å, 168°]. Chains associate themselves in layers in an antiparallel mode (Figure 7), by N-H…OH hydrogen bonds [N2…O2(-x+2, y+1/2, -z+1/2) 3.032(2) Å, 171°].

To understand the reasons for co-crystal formation, the single crystal X-ray structures of the amines **6**-**8** and their reactivity towards 4-pyridinecarboxaldehyde and 4-acetylpyridine are investigated (Table 3).

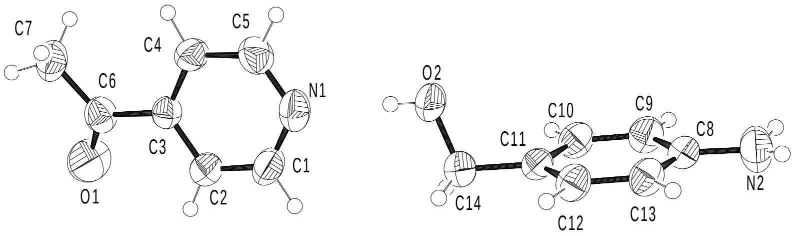

Figure 6. Molecular structure and labelling of the co-crystal **5**, thermal ellipsoids at the 50% probability level

	d(X···Y) (Å)	X-H···Y (°)	Symmetry
O2···N1	2.835(2)	178	
N2···O2	3.032(2)	171	-x+2, y+1/2, -z+1/2
N2···O1	3.123(2)	168	x+1, y, z+1

Table 2. Hydrogen bonds in the supramolecular structure of **5**

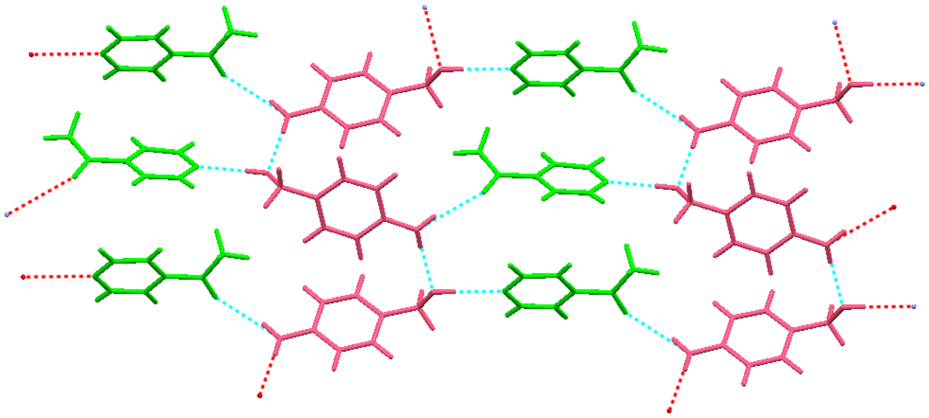

Figure 7. Supramolecular organization of **5**, with the two molecular components highlighted by different colours

	4-pyridinecarboxaldehyde	4-acetylpyridine
6	Formation of **2**	Formation of **1**
7	Formation of **3**	No reaction
8	Formation of **4**	Formation of cocrystal **5**

Table 3. The reactivity of the amines **6**, **7** and **8**

In accordance to the higher reactivity of aldehydes respect to ketones, the amines **6-8** condense with 4-pyridinecarboxaldehyde, giving the compounds **2**, **3** and **4**. Different is the case of 4-acetylpyridine: it reacts with **6** to form **1**, but, after four days refluxing in toluene, with some drops of acetic acid as catalyst, 4-acetylpyridine and **7** are recovered still unreacted. Finally, 4-acetylpyridine does not condense with **8** but it gives the co-crystal **5**.

Single crystals of **7** and **8** suitable for X-ray diffraction are obtained from $CHCl_3$ and THF (Figure 8), while **6** was already X-ray characterized.[26] It is well known the OH and NH_2 groups are, from the structural point of view, complementary.[27] **7** effectively shows a chain-based supramolecular organization sustained by O-H···N hydrogen bonds [O1…N1(x, y, z-1) 2.862(2) Å, 160°]; this is the commonest synthon among aminols.[27] Molecules of the same chain interact also by N-H···π interactions, while neighbouring antiparallel chains interact by C-H···O contacts (Figure 9). The crystal packing of **8** is based on hydrogen-bonded chains, sustained by N-H···O hydrogen bonds [N1…O1(x-1/2, -y+1/2, z) 3.198(4) Å, 165°]; also in this case, the chains are antiparallel and neighbouring chains interact by O-H···N [O1…N1(-x+1, -y, z+1/2) 2.801(5) Å, 178°] and N-H···π contacts (Figure 9).

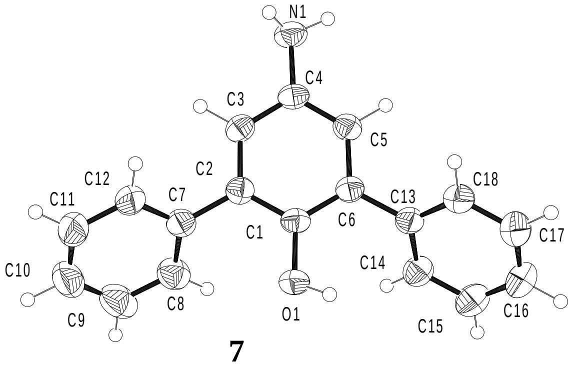

7

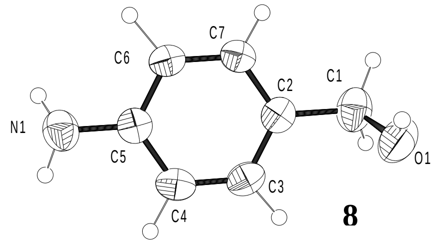

8

Figure 8. Molecular structures and labelling of **7** and **8**, thermal ellipsoids at the 50% probability level

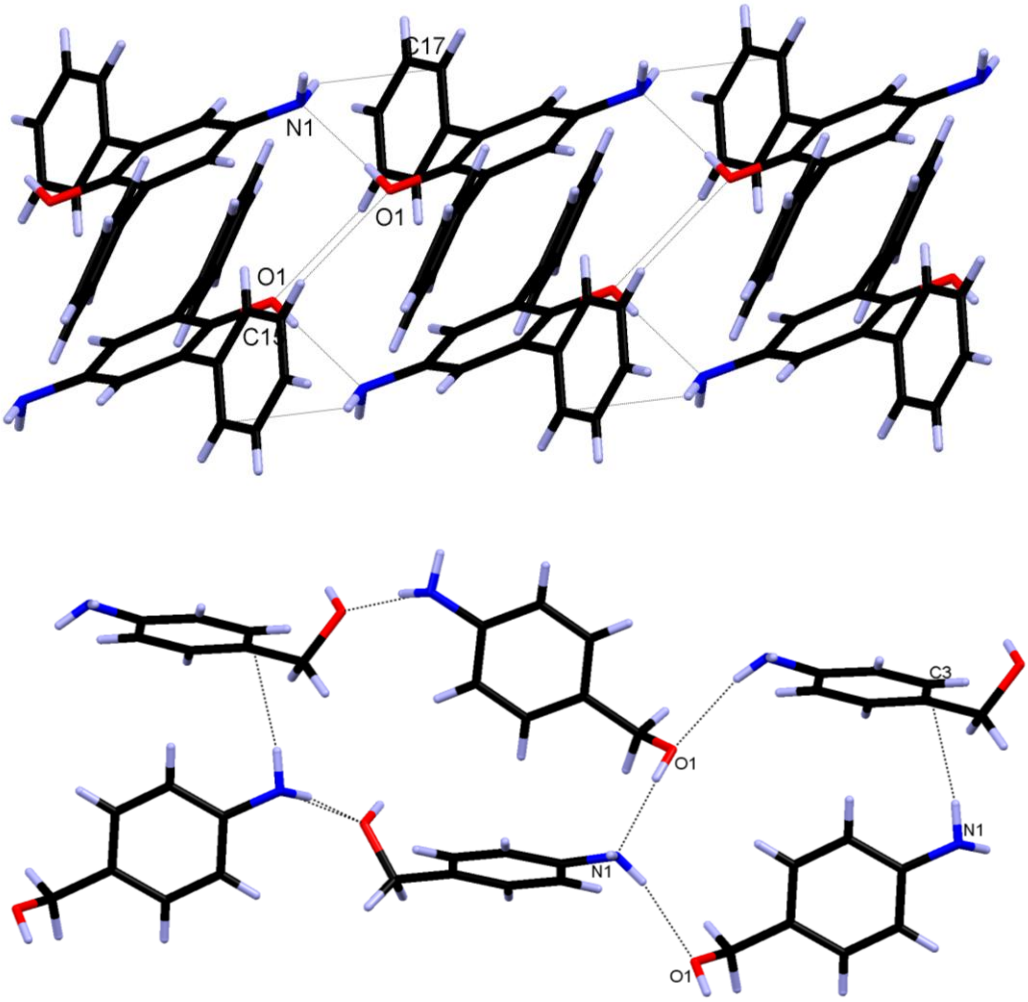

Figure 9. Supramolecular structures of **7** (top) and **8** (bottom)

The key factor in the co-crystal formation is probably the possibility to involve the molecular components in the co-crystal in a greater number of interactions respect to the free components alone.[28] In this perspective, the different behaviour of the three amines is related to their supramolecular interactions (Table 4). Amine **6** has three hydrogen bond acceptors and three hydrogen bond donors (O-H···N, N-H···O, N-H···O). All these atoms are involved in intermolecular hydrogen bonds and there is not any energetic gain in the co-crystallization. Amine **8** potentially has three hydrogen bond acceptors and three hydrogen bond donors, but only two acceptors and two donors are effectively involved in supramolecular interactions in its crystal structure (O-H...N, N-H…O). In fact, the aminic group is involved as a donor in an hydrogen bond, but also in an interaction with the aromatic C3. Amine **8** in the co-crystal **5** is able to increase its intermolecular contacts by additional amine-ketone interaction, involving the stronger hydrogen bond acceptor nitrogen pyridinic atom. Amine **7** does not use all its potential three acceptors and three donors in its supramolecular arrangement, but in this case co-crystal formation is not realized probably due to the aromatic rings steric hindrance around the oxydrilyc moiety.

		D…A	D-H…A	Symmetry
6	O1-H…N1	2.785(3)	165	x-1/2, -y+1/2, z+1/2
	N1-H1…O1	3.145(3)	156	+x+1/2, -y, -z
	N1-H2…O1	3.367(3)	162	x+1/2, -y+1/2, z+1/2
7	O1-H…N1	2.862 (2)	160	x, y, z-1
8	O1-H…N1	2.801(5)	178	-x+1, -y, z+1/2
	N1-H1…O1	3.198(4)	165	x-1/2, -y+1/2, z

Table 4. Hydrogen bonds in the supramolecular structures of **6**, **7** and **8**

2D-fingerprint plots for amine **8** alone and for **8** in the co-crystal **5** are compared (Figure 10). The main features of both structures are due to the hydrogen bond network based on the shorter OH···N (labelled A) and longer NH···O hydrogen bonds (B). Some degree of CH···π interactions (C), NH···π interactions (D) and H···H contacts (E), in the limit of the van der

Waals radii are also observed. The H···H region is quite a spike in **8**, due to the close $CH_2\cdots\pi$ contact. The broadness of the H···H contacts area in **5** may be related to differing contact geometries, because of the presence of both $CH_3\cdot\cdot\ \pi$ and $OH\cdot\cdot\ \pi$ close interactions.

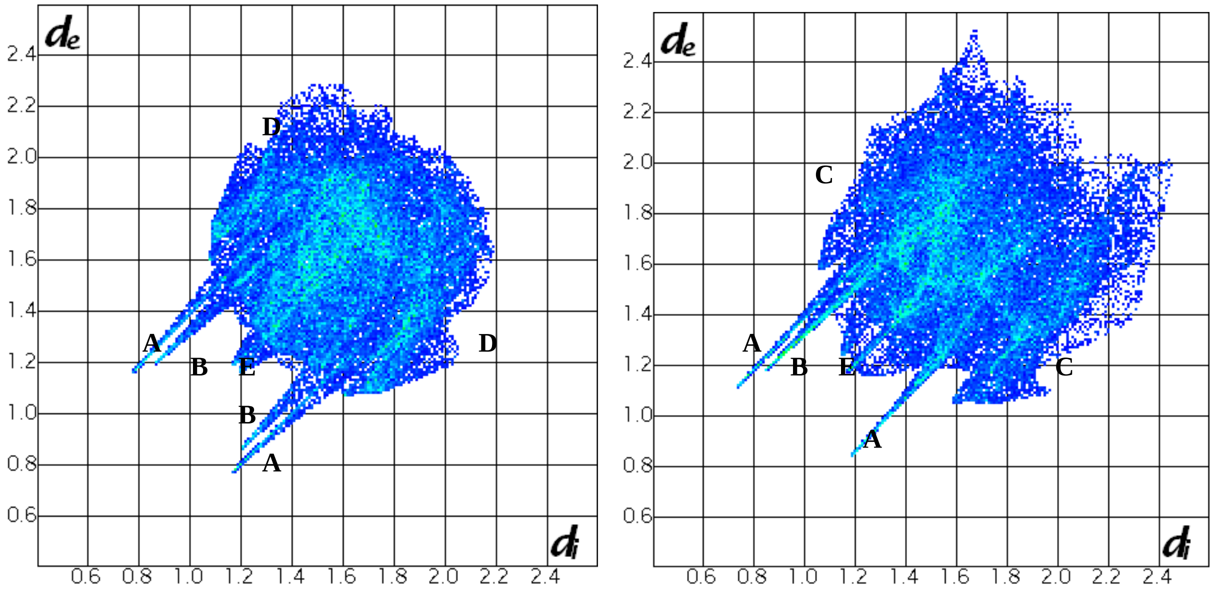

8 **5**

Figure 10. 2D-fingerprint plots of amine **8** (left) and of the same amine in the co-crystal 5 (right)

3.3. Experimental

4-acetylpyridin, 4-pyridinecarboxaldehyde, 4-aminophenol, 3,5-diphenyl-4-hydroxyanilin and 4-aminobenzylalcohol are commercially available. Reagent grade solvents are mostly used without further purification. THF dry is used for the synthesis of **5**. Proton NMR spectra are recorded at 25°C on a Bruker 300 FT spectrophotometer by using $SiMe_4$ as internal standard, while IR spectra are obtained with a Nicolet 5PCFT-IR spectrophotometer in the 4000-400 cm^{-1} range, using KBr disks. Elemental analyses are performed by using a Carlo Erba Model EA 1108 apparatus.

Synthesis of 1. 0.28 ml (2.36 mmol) of 4-acetilpyridine are added to a solution containing 250 mg (2.36 mmol) of 4-aminophenol in 20 ml of toluene. The solution is refluxed for 24 hours, concentrated and by cooling a brown solid precipitated. It is filtered, washed with small amounts of ethyl ether and dried *in vacuo*. Yields 77%; mp: 235 °C. Elemental analysis for $C_{13}H_{12}N_2O$ (mw: 212.25): calcd (%) C 73.57, H 5.70, N 13.20; found (%) C 73.20, H 5.27, N 12.90. IR (KBr, cm^{-1}): $\nu(O\text{-}H)_{br}$ 3419. ^1H NMR (d6-DMSO, 25 °C, ppm): δ 9.28 (s, 1H, O1-

H, D_2O exchangeable), δ 8.70 (d, J = 1.3 Hz, 2H, C1(5)-H), δ 7.87 (d, J = 1.3 Hz, 2H, C2(4)-H), δ 6.80-6.71 (m, 4H, C9(10-12-13)-H), δ 2.26 (s, 3H, C7-H).

Synthesis of 2. 0.23 ml (2.36 mmol) of 4-pyridinecarboxaldehyde are added to a solution containing 250 mg (2.36 mmol) of 4-aminophenol in 20 ml of toluene. The solution is refluxed for 12 hours, then it is concentrated and by cooling a yellow solid is collected, washed with small amounts of ethyl ether and dried *in vacuo*. Yields 84%; mp: 212 °C. Elemental analysis for $C_{12}H_{10}N_2O$ (mw: 200.22): calcd (%) C 71.99, H 5.03, N 13.99; found (%) C 72.12, H 5.04, N 13.96. IR (KBr, cm^{-1}): ν(O-H)$_{br}$ 3420. ^{1}H NMR ($CDCl_3$, 25 °C, ppm): δ 8.77 (d, J = 1.2 Hz, 2H, C1(5)-H), δ 8.50 (s 1H C6-H), δ 7.77 (d, J = 1.2 Hz, 2H, C2(4)-H), δ 7.26 (d, J = 5.4, 2H C9(11)-H), δ 6.92 (d, J = 5.4, 2H C8(12)-H), δ 5.37 (s, 1H, O1-H, D_2O exchangeable).

Synthesis of 3. 0.09 ml (0.96 mmol) of 4-pyridinecarboxaldehyde are added to a solution containing 250 mg (0.96 mmol) of 3,5-diphenyl-4-hydroxyaniline in 20 ml of toluene. After 12 hours refluxing, the solution is concentrated to obtain a yellow solid, that is filtered, washed with small amounts of ethyl ether and dried *in vacuo*. Yields 88%; mp: 239 °C. Elemental analysis for $C_{24}H_{18}N_2O$ (mw: 350.44): calcd (%) C 82.26, H 5.18, N 7.99; found (%) C 82.06, H 5.27, N 7.93. IR (KBr, cm^{-1}): ν(O-H)$_{br}$ 3422. ^{1}H NMR ($CDCl_3$, 25 °C, ppm): δ 8.73 (d, J = 7.2 Hz, 2H, C1(5)-H), δ 8.60 (s, 1H, C6-H), δ 7.84 (d, J = 7.2 Hz, 2H, C2(4)-H), δ 7.62 (d, J = 7.2 Hz, 4H C14(18-19-20)-H), δ 7.51 (t, J = 7.2 Hz, 4H C15(17-21-23)-H), δ 7.45 (d, J = 7.2 Hz, 2H C16(22)-H), δ 7.34 (s, 2H, C8(12)-H), δ 5.32 (s, 1H, O1-H, D_2O exchangeable).

Synthesis of 4. 0.20 ml (2.03 mmol) of 4-pyridinecarboxaldehyde and 250 mg (2.03 mmol) of 4-aminobenzylalcohol in 20 ml of dry THF are refluxed for 12 hours under N_2. Then the solution is concentrated and by cooling a yellow solid precipitated. It is filtered, washed with small amounts of ethyl ether and dried *in vacuo*. Yields 72%; mp: 241 °C. Elemental analysis for $C_{13}H_{12}N_2O$ (mw: 212.25): calcd (%) C 73.57, H 5.70, N 13.20; found (%) C 73.54, H 5.76, N 13.15. IR (KBr, cm^{-1}): ν(O-H)$_{br}$ 3191. ^{1}H NMR ($CDCl_3$, 25 °C, ppm): δ 8.78 (d, J = 5.2 Hz, 2H, C1(5)-H), δ 8.49 (s 1H C6-H), δ 7.79 (d, J = 5.2 Hz, 2H, C2(4)-H), δ 7.45 (d, J = 8.3 Hz, 2H C8(12)-H), δ 7.28 (d+s, J = 8.3 Hz, 3H C9(11)-H) + O1-H, D_2O exchangeable), δ 4.76 (s, 2H C13-H).

Synthesis of 5. 0.90 ml (8.12 mmol) of 4-acetilpyridine are added to a solution containing 1 g (8.12 mmol) of 4-aminobenzylalcohol in 40 ml of dry THF. The mixture is refluxed for 6 hours under N_2. The solvent is removed and ethyl ether was added until a yellow solid precipitates. Alternatively, the co-crystal **5** is obtained throught a solvent-free reaction by grinding the solid amine and the liquid aldehyde. It is also obtained by seeding the undercooled 1:1 solution of the amine into the liquid ketone. Yields 48%; mp: 73 °C. Elemental analysis for $C_{14}H_{16}N_2O_2$ (mw: 244.12): calcd (%) C 68.83, H 6.60, N 11.46; found (%) C 69.01, H 6.53, N 11.42. IR (KBr, cm^{-1}): ν(N-H) 3440 and 3349, ν(O-H) 3220, ν (C=O) 1687. ^{1}H NMR (D_6-DMSO, 25 °C, ppm): δ 8.82 (d, J = 6.3 Hz, 2H, C1(5)-H), δ 7.82 (d, J = 6.3 Hz, 2H, C2(4)-H), δ 6.97 (d, J = 10.1 Hz, 2H, C9(13)-H), δ 6.52 (d, J = 10.1 Hz, 2H, C10(12)-H), δ 4.94 (s, 2H, N2-H), δ 4.81 (t, J = 7. 1 Hz, 1H, O1-H), δ 4.30 (d, J = 7.1 Hz, 2H, C14-H), δ 4.30 (s, 3H, C7).

X-ray Crystallography

MoKα radiation (λ =0.71073 Å) on a SMART AXS 1000 CCD diffractometer is used for **3** and **7** and on a SMART APEXII CCD diffractometer is used for **4;** CuKα radiation (λ=1.54178 Å) on a Siemens diffractometer is used for **1**, **2**, **5** and **8**. All data are collected at room temperature (293 K). Compound **4** gives crystals with a poor diffracting power, as shown by the low resolution limit achieved in the data collection (1.1Å, Table 5). Lorentz, polarization, and absorption corrections are applied.[29] Structures are solved by direct methods using SIR97[30] and refined by full-matrix least-squares on all F^2 using SHELXL97[31] implemented in the WingX package.[32] Hydrogen atoms are partly located on Fourier difference maps and refined isotropically and partly introduced in calculated positions. Anisotropic displacement parameters are refined for all non-hydrogen atoms. Hydrogen bonds are analyzed with SHELXL97[31] and PARST97,[33] and extensive use is made of the Cambridge Crystallographic Data Centre packages[34] for the analysis of crystal packing. Table 5 summarizes crystal data and structure determination results. Intermolecular contacts are analyzed by 2D-Fingerprint plots of Hirshfield surfaces[20] by using Crystal Explorer.[21-22]

Table 5. Crystal data for compounds **1-8** (crystal data of **6** are in CSD, refcode AMPHOL[26])

Compound	**1**	**2**	**3**	**4**	**5**	**7**	**8**
Formula	$C_{13}H_{12}N_2O$	$C_{12}H_{10}N_2O$	$C_{24}H_{18}N_2O$	$C_{13}H_{12}N_2O$	$C_{14}H_{16}N_2O_2$	$C_{18}H_{15}NO$	C_7H_9NO
Molecular weight	212.25	198.22	350.40	212.25	244.29	261.31	123.15
Crystal system	monoclinic	rhombic	monoclinic	monoclinic	monoclinic	monoclinic	rhombic
Space group	$P2_1/c$	$P2_1ab$	$P\ 2_1/c$	$P\ 2_1/c$	$P\ 2_1/c$	$P\ 2_1/c$	$Pna2_1$
Z	8	4	4	4	4	4	4
a/Å	10.8998(5)	7.7618(6)	6.452(5)	11.738(2)	10.913(4)	11.307(1)	15.0879(7)
b/Å	11.4338(4)	22.981(3)	18.07(1)	7.473(2)	8.774(3)	17.413(2)	7.4306(3)
c/Å	17.9406(5)	5.6539(3)	16.55(1)	13.759(3)	14.000(5)	7.2568(9)	5.7751(1)
β/°	92.393(5)		109.52(3)	113.814(4)	99.55(2)	101.005(2)	
V/Å^3	2233.9(1)	1008.5(1)	1819(2)	1104.1 (4)	1321.9(8)	1402.5(3)	647.46(4)
ρ /Mg m^{-3}	1.262	1.305	1.280	1.277	1.227	1.238	1.263
θ range for data collection/°	4.06 - 70.03	3.85 - 69.99	1.72 - 23.29	1.90 – 18.91	3.20 - 30.05	1.83 - 24.77	5.87 - 70.02
Unique reflections	4234	1037	2623	879	3863	2409	677
Observed reflections [I>2σ(I)]	3638	726	2116	713	2365	1811	617
Data/ restraints/ parameters	4234 / 0 / 294	1037 / 1 / 137	2623 / 70/ 245	879 / 38 / 146	3863 / 0 / 173	2409 / 0 190	677 / 1 / 92
Goodness-of-fit on F^2	1.074	0.958	1.091	1.076	0.868	0.844	1.075
R_1 [I>2σ(I)]	0.0422	0.0430	0.0581	0.0558	0.0495	0.0377	0.0433
wR_2 [I>2σ(I)]	0.1242	0.0991	0.1551	0.1370	0.1426	0.1089	0.1261
R_1 (all data)	0.0478	0.0617	0.0698	0.0684	0.0836	0.0525	0.0458
wR_2 (all data)	0.1291	0.1097	0.1648	0.1477	0.1697	0.1221	0.1287

4. Inclusion properties, polymorphism and desolvation kinetics in a new 1D-nanochannel pyridyl iminophenol compound[35]

The ability to include guest species into a supramolecular host porous framework strongly depends from molecular size and shape factors. On one side, this ability derives from the molecular solid-state organization of the host and on the other side it could be connected to the templating ability of the guest.[36-38]

The previously described families of 4-pyridyl iminophenol compounds have shown that the O-H···N(pyridine) hydrogen bond is a reliable interaction to synthesize non covalent chains whose supramolecular arrangement can be tuned by local structural factors (**1**-**4**, Figure 1 and Figure 3). In particular, for 4-pyridyl 3,5-diphenyl-4-iminophenol (**3**) the relevant steric hindrance around the OH group forces the supramolecular chains to be quite linear and therefore they may pack efficiently. However it is known that phenyl rings should in principle work against an efficient packing and favour the formation of solvate species.[39] It is also reasonably to think that the position of the nitrogen on the pyridine ring may alter the linearity of the chains and results in a less efficient packing. Therefore, the influence of 3- and 2-pyridyl moieties on the supramolecular arrangement of the pyridyl-3,5-diphenyl-4-iminophenols is analyzed. Whilst the 3-pyridyl 3,5-diphenyl-4-iminophenol (**9**) presents the same supramolecular features as the 4-substituted derivative, the 2-pyridyl compound shows significant propensity to include guests. In this compounds the linear folding of the chain is strongly modified by the *ortho*-substitution. This modification enables to obtain the inclusion network. In fact in addition to a non-solvate form (**13**), some solvates have been separated and X-ray characterized by recrystallization in toluene (polymorphs **10a** and **10b**), acetone (**11**) and chloroform (**12**). The polymorphism of the toluene solvates is interpreted with the aid of high pressure X-ray diffraction studies. The kinetic and mechanism of solid/gas solvation/desolvation and the guest exchange processes with the aid of variable temperature X-ray powder diffraction (XRPD) techniques and isothermal thermogravimetry (TGA) experiments are studied as well.

4.1. Results and discussion

Compounds **9** and **10** (Scheme 3) are synthesized in toluene starting from 3- or 2-acetylpyridine and 3,5-diphenyl-4-hydroxyaniline, respectively. From elemental analysis and spectroscopic characterization **9** results non solvate and **10** hemisolvate. Single crystals of **9** suitable for X-ray diffraction analysis are grown by slow evaporation at room temperature of a saturated THF solution. From recrystallization of **10** in toluene, three crystalline forms are obtained (**10a**, **10b** and **10c**). By means of single crystal X-ray diffraction analysis it was possible to determine that **10a** and **10b** are two concomitant polymorphs.[40] Both polymorphs are toluene hemisolvates differing essentially in the arrangement of the host around the guest in the crystal packing. **10c** was detected by XRPD in the product of the recrystallization from toluene, but deeper single crystal structural characterization is not possible. Other solvate forms are isolated by recrystallization of **13** in acetone (**11**) and chloroform (**12**), while, by using the more encumbered solvent t-butyl methyl ether, the non solvate **13** is obtained. Also **11**, **12** and **13** are characterised by single crystals X-ray diffraction analysis. **11** and **12** are, respectively, acetone and chloroform hemisolvates isostructural to **10a**, with the host molecule in a general position and the disordered guest located on an inversion centre.

All the crystallographic data are reported in Table 9.

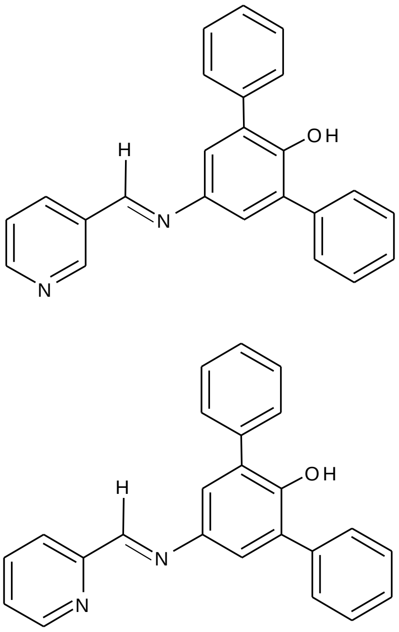

9

13

10a, 10b	**13**·½ toluene
11	**13**·½ acetone
12	**13**·½ chloroform

Scheme 3. Compounds **9-13**

Molecular structures of the non solvate species **9** and **13** are shown in Figure 11. The molecular conformations of compounds **9-13** are described by using δ, the angle between the pyridyl and "central" phenyl ring mean planes, and ε, the angle between the 3- and 5- aryl rings (Figure 12, Table 6). While δ does not present sensible changes in the different compounds, ε is significantly smaller in the solvate forms, since one of the two aryl rings is forced to reorient to make place for the solvation site of the guest (Figure 13).

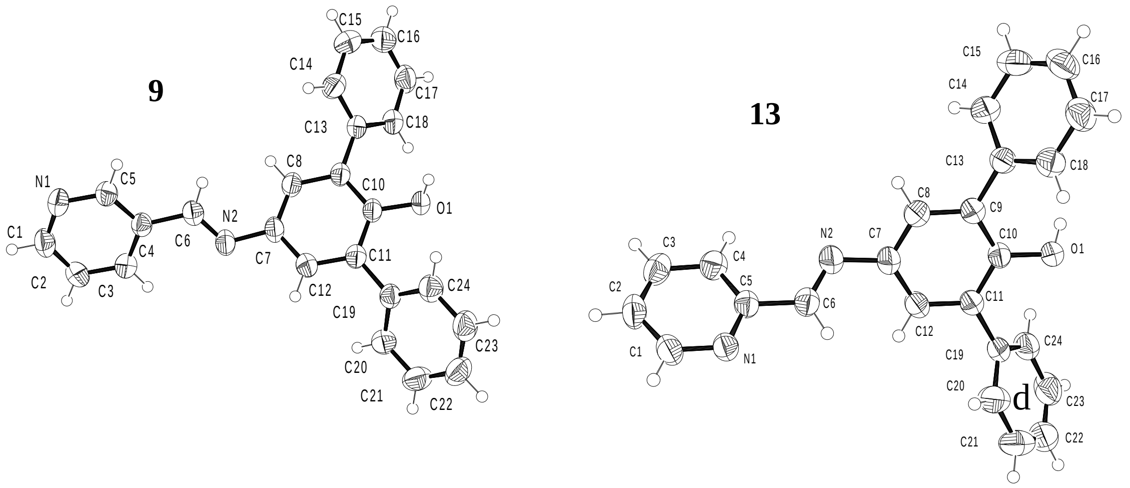

Figure 11. Molecular structure and labelling of **9** and **13**, thermal ellipsoids at the 50% probability level

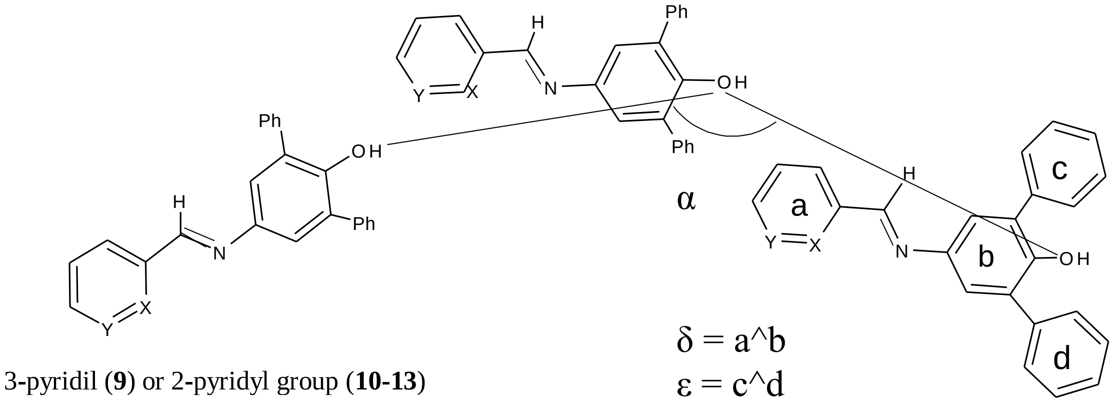

Figure 12. Definition of the of the conformational descriptors δ and ε and of the supramolecular parameter α

	δ (°)	ε (°)	α (°)	O1··· N1(Å)
9	46	76	137	2.68(2) -x, y-1/2, -z+1/2
10a	55	41	118	2.796(5) -x, y+1/2, -z+1/2
10b	53	42	118	2.795(4) -x, y+1/2, -z+1/2
11	51	41	118	2.789(1) -x, y+1/2, -z+1/2
12	50	41	117	2.785(3) -x, y-1/2, -z+1/2
13	55	89	66	2.811(1) x, -y+1/2, z-1/2

Table 6. Values of the geometrical conformational descriptors δ and ε and of the supramolecular parameter α

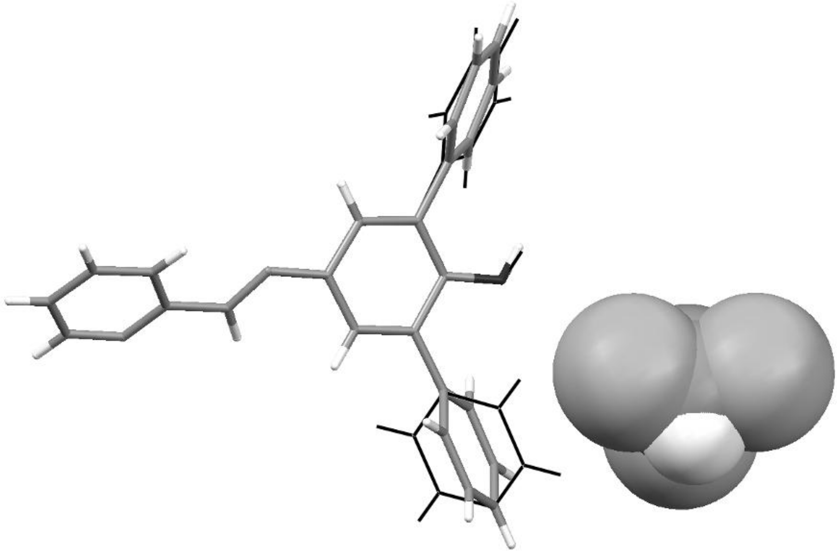

Figure 13. Superimposition of **12** (light capped sticks) and **13** (dark wire), showing the effect of the guest (space filling) on the aryl rings orientation

All the structures of **9-13** are based on the general tendency to the formation of polar supramolecular chains, sustained by hydrogen bonds (Table 6) involving the OH groups and the pyridine nitrogen atoms, as in the previously described 4-pyridyl iminophenol derivatives. The chains have an antiparallel arrangement and they are aligned along *b* in **9-12** and along *c* in **13**.

The angle α between the oxygen atoms of three consecutive molecules (Figure 12, Table 6) is the parameter used to summarize the effects of guest inclusion on the foldings of the hydrogen bonded supramolecular chains (Figure 12, Table 6). In these compounds the general tendency to form linear hydrogen bonded chains is tuned by the steric hindrance and by the local geometry around the –OH, as previously shown for compound **1-4** (Figure 3 and Figure 14). In particular, the 4-pyridyl compound **3** (Figure 1) shows a satisfactory linearity (α = 162°), but on moving to the 3-pyridyl alcohol **9**, the displacement of the hydrogen bond acceptor on the pyridyl ring causes a contraction of the chain (α=137°). This effect is maximized with the 2-pyridyl ring in **13**, where the dramatic shrinkage of the supramolecular chains results in a strong contraction of α=66°. In the same way, a significant increase of the linearity is observed in all the solvate forms (α=118° for **10a**, **10b**, **11** and α=117° **12**), in which the guest species are accommodated (Figure 15). All these forms exhibit identical hydrogen bonded chains extended along *b*; **10b** differs from the others in the mutual displacement of the chains, that are, anyway, along *b* (Figure 16).

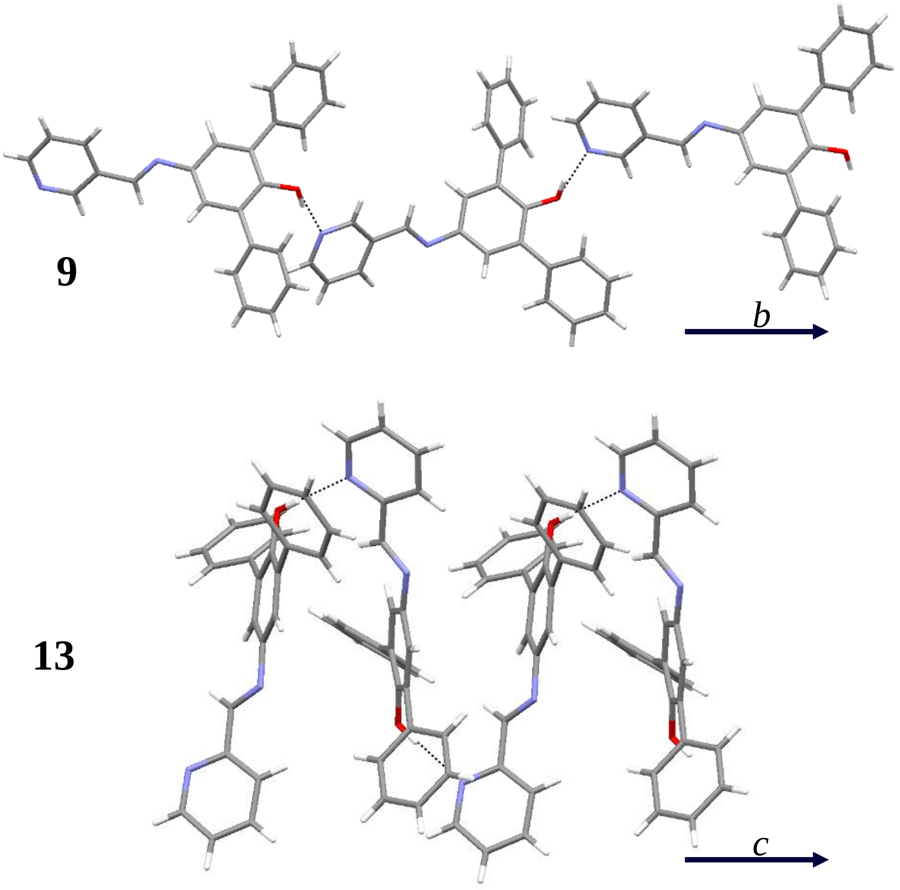

Figure 14. Different extension of the supramolecular chains in the non solvate 3-pyridyl iminophenol **9** and 2-pyridyl iminophenol **13**, from top to bottom, respectively

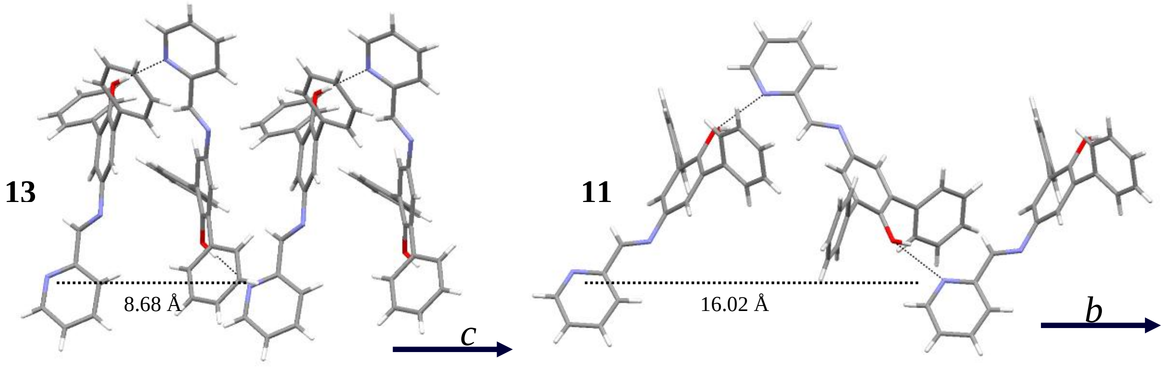

Figure 15. Different extension of the supramolecular chains in the non-solvate **13** (left) and in the acetone hemisolvate **11**, with the acetone molecules omitted (right)

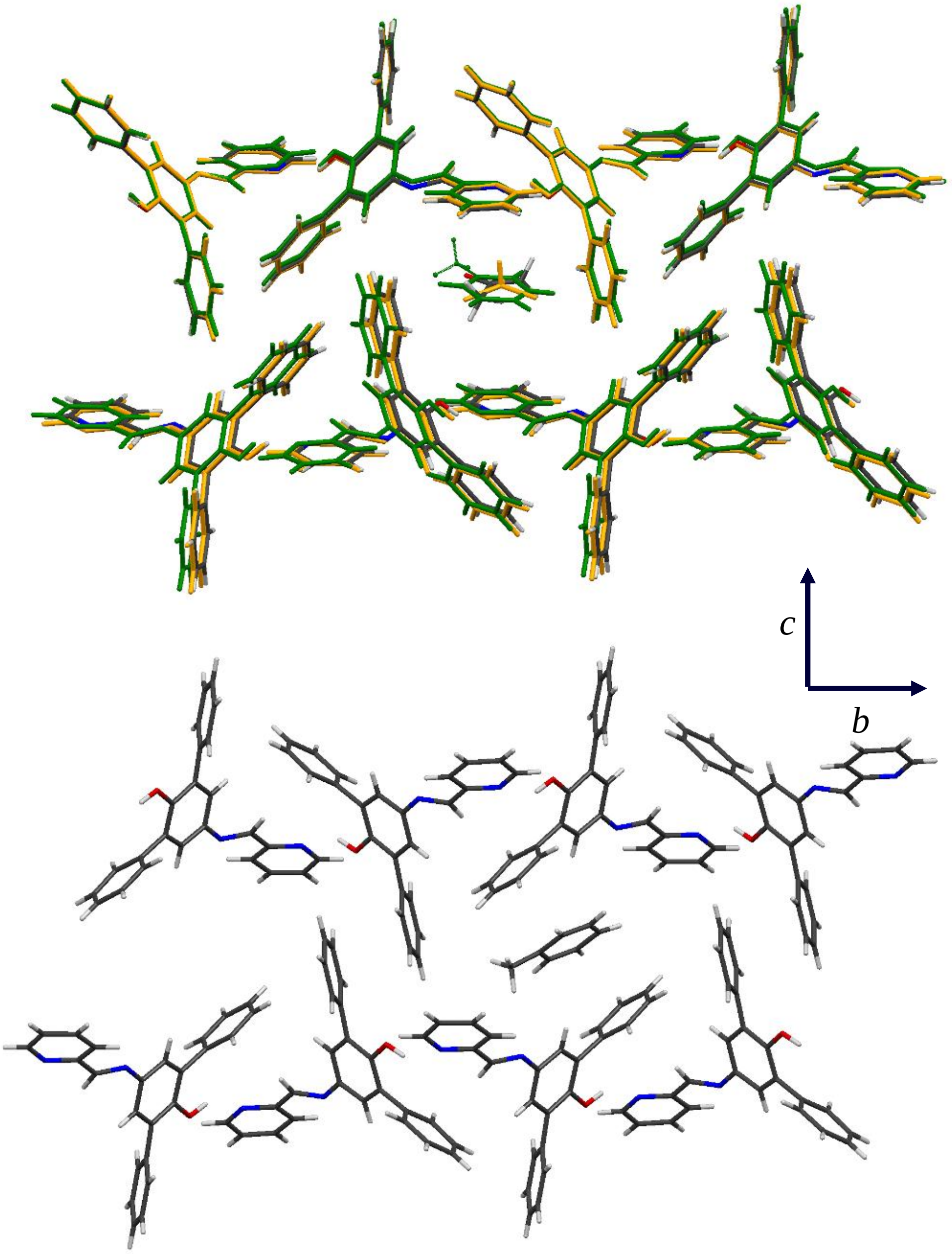

Figure 16. Channels in the host isostructural networks **10a**, **11** and **12** (superimposed, top) and in the host **10b** (bottom)

In all cases the guest molecules are lined along channels orthogonal to the *bc* plane; in **10a**, **11** and **12** these channels are defined by walls constituted by a pair of phenyls and a pair of pyridine groups (Figure 16, top). By contrast, in polymorph **10b** the guest molecules are allocated in channels contoured by four phenyl rings (Figure 16, bottom). So, **10a** and **10b** substantially differ in the reciprocal arrangement of the neighbouring hydrogen bonded chains, that, taken alone, are identical in the two polymorphs. An analysis of the voids filled by the guest species (Figure 17) shows that the microporous network is more open in **10b** than in **10a**. In fact, in **10a**, as in the isostructural **11** and **12,** the microchannels show a bottleneck next to the space filled by the guest molecules, while this shrinkage does not exist in **10b**.

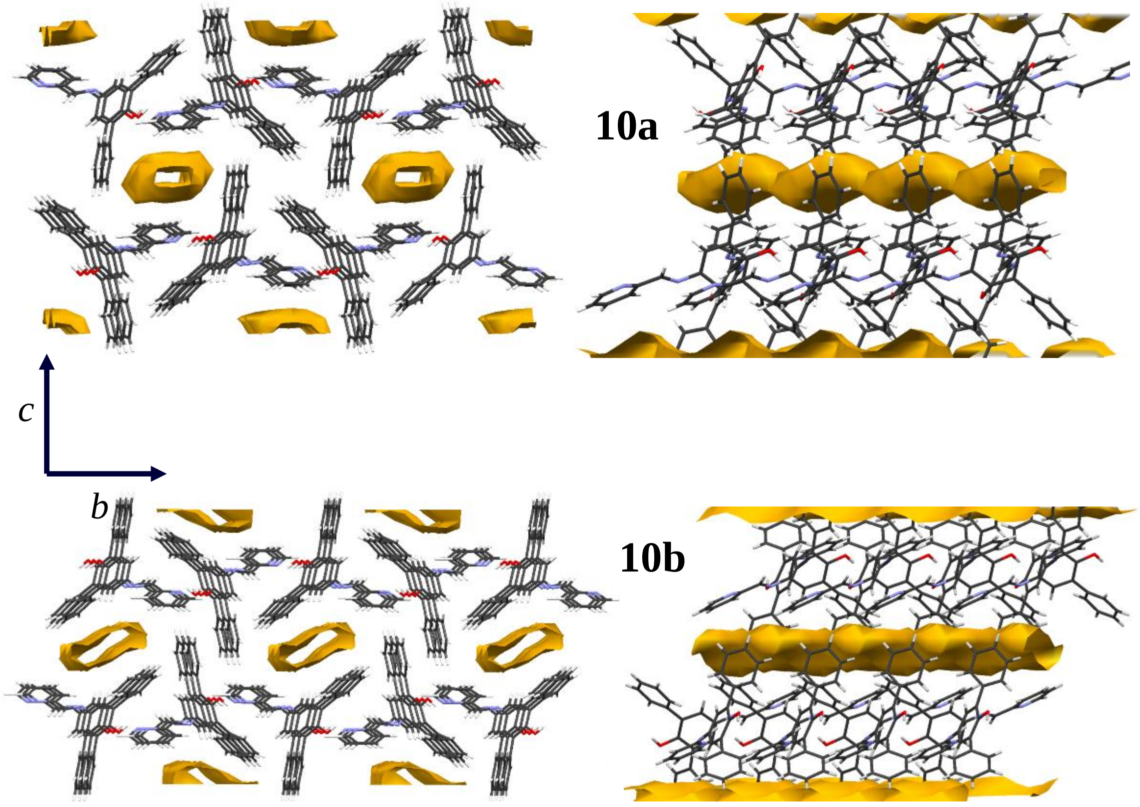

Figure 17. Front (left) and side (right) views of solvent accessible surface (probe radius 1.2Å) of the channels accomodating the toluene guests (not shown) in **10a** (top) and **10b** (bottom)

4.2. Desolvation, guest exchange and ageing processes in the hemisolvate compounds

All the hemisolvate forms **10-12** present the same hydrogen bonded motif. These structural analogy between extended supramolecular chains and the shrinkage observed in the non-solvate **13** ones, together with the presence of channels in the solvate networks, point to a possible direct conversion route between the two states. From the structural discussion, the transition from the solvate state to the non solvate one is supposed to be based on the variation of α during the guest escape through the channels.

Variable temperature XRPD is the means used to follow the desolvation processes of **11** and **10** in the temperature ranges 25-55 and 25-80 °C, respectively.

Upon heating, **11** converts quantitatively into the apohost **13**, without the appearance of any transient amorphous phase during desolvation (Figure 18). Guest loss begins between 30 and 35°C, when the peaks characteristic for **13** appear; **11** and **13** coexist up to 45°C, while the complete desolvation occurs between 45 and 50°C. The reversibility of the process was checked by exposing **13** to vapours of acetone for one week in a closed vessel at room temperature. The XRPD pattern of **13** remains unchanged, implying that the solvation/desolvation process in this system is not reversible.

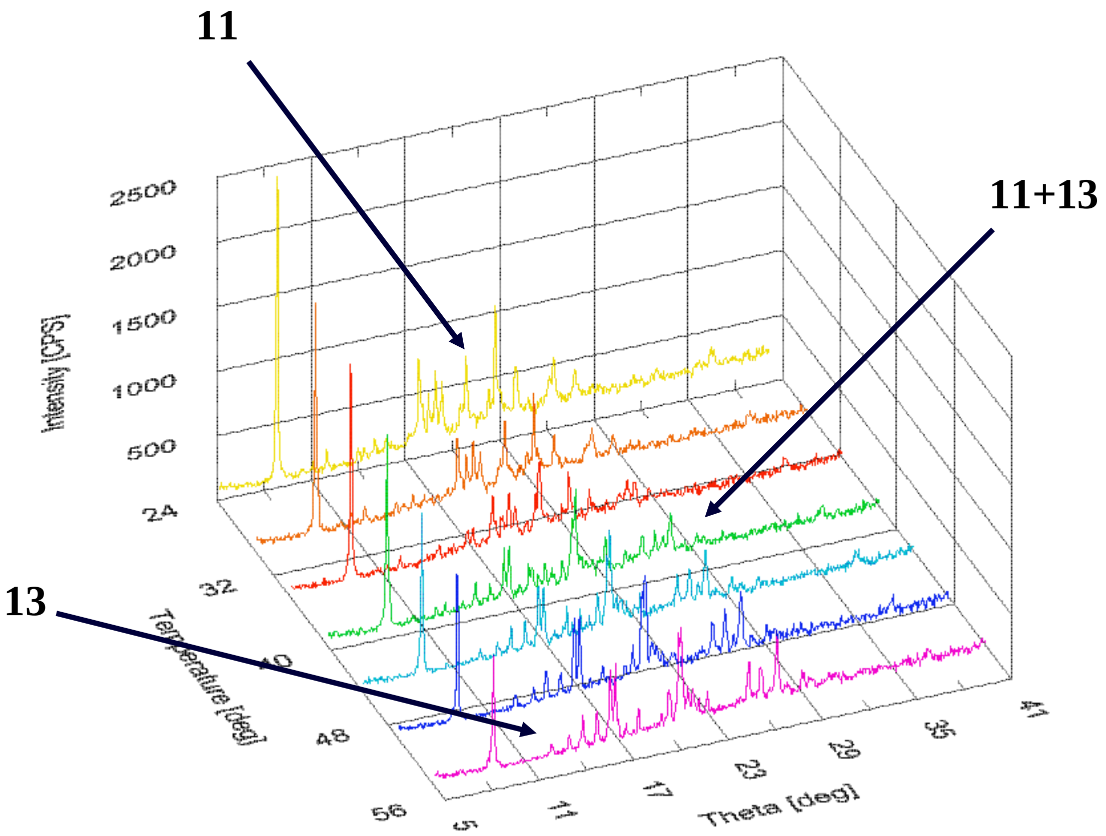

Figure 18. Variable temperature X-ray powder diffraction patterns monitoring the desolvation of **11** to **13**, where the patterns at 25°C and 55°C represent compounds **11** and **13**, respectively

Variable temperature XRPD is also used to follow the desolvation process of **10** (Figure 19, top), that is invariably synthesized as a mixture of three polymorphs (**10a, 10b**, and **10c**). The evolution of the system from room temperature to 80°C is followed by examining, in particular, the XRPD spectra in the 2θ range 7.5-10.0°, that includes the more significant peaks, corresponding to the reflection [002] of **10a** (8.52°) and of **10b** (8.44°), the reflection [100] of **13** (8.72°) and one peak of **10c** (9.90°) (Figure 19, bottom). At room temperature, **10a**, **10b** and **10c** coexist; upon heating, between 50 and 60°C, they convert quantitatively into the apohost **13**, without the appearance of any transient amorphous phase during desolvation. The “more open” form **10b** is the first to disappear and only the non-solvate **13** is observed approximately from 65°C.

Exchange experiments are also performed starting from a solvate, in order to test the accessibility of the channels where the guests are accommodated. These exchange experiments are followed by XRPD (see Supplementary Material, S3 and S4). Guest exchange experiments, performed on small amounts of **10** have shown that acetone is able to completely displace toluene from the channels within a few days. In fact **10** may be quantitatively converted in **11** by exposure to acetone vapours for one week in a closed vessel.

By contrast and rather surprisingly, diethyl ether vapours efficiently extract completely toluene from **10** and produce the pure non-solvate **13** in a few days.[41] This ‘drying’ process is compared with the natural ageing of the powder of **10** exposed to air at room temperature. After ten days of exposition to ether vapours, **10** is converted quantitatively into the non-solvate **13**, while the same quantity of **10,** kept in air in the same conditions, shows only a partial loss of guest. For the air-exposed sample, XRPD revealed the presence in the final powder of a mixture of the toluene solvate forms **10a**, **10b** and **10c** and of the apohost **13** (88%, as estimated by TGA measurements on the aged powder).

All the described processes that enable to obtain the hemisolvate **10** and **11** and the non solvate **13** are summarized in Scheme 4.

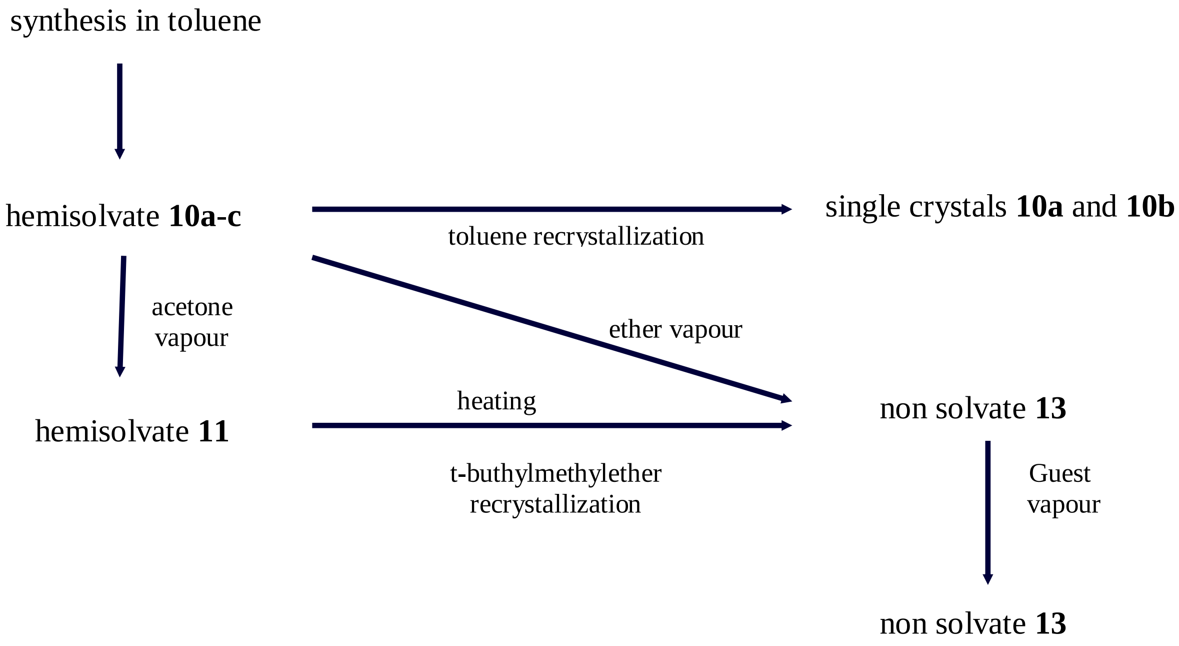

Scheme 4. Summary of the processes that enable to isolate the hemisolvates **10a-c**, **11** and the non solvate **13**

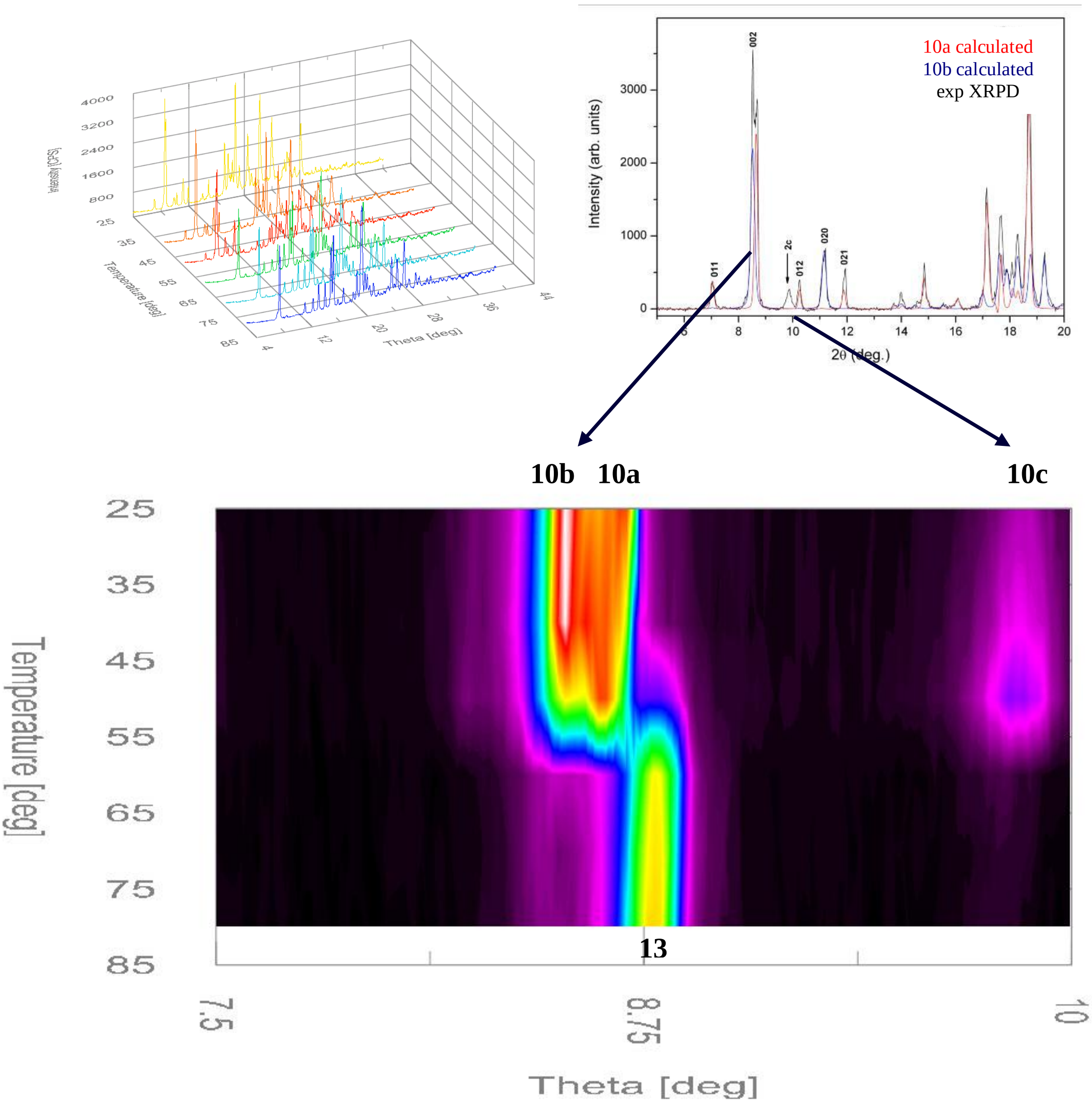

Figure 19. (Top right) Close up of the experimental powder diffraction profile of **10** (black) between 2θ=5-20°, with the most significant peaks indexed, showing the concomitant presence of **10a** (calculated, red), **10b** (calculated, blue) and **10c**. (Top leftt) Variable temperature X-ray powder diffraction spectra monitoring the desolvation of **10**, where the patterns at 25°C and 85°C represent compounds **10** and **5**, respectively. (Bottom) 2θ range (7.5-10.0°) with the peaks corresponding to the reflections [002] of **10a** (8.52°) and **10b** (8.44°)**,** [100] of **13** (8.72°) and with the peak of the uncharacterized form **10c** (9.90°)

4.3. High-pressure X-ray diffraction

The behaviour under pressure of a crystal of **10b** is checked in order to analyse the possible changes of this polymorph. **10b** is the hemisolvate form having wider channels an the evolution of the system under pressure *stimuli* is hypotized to give the more close structure **10a**, the non-solvate **13** or new polymorphs, deviating from the isostructural series. The unit-cell parameters at different pressures are reported in Table 7. In Figure 20 the evolution of the unit-cell parameters and of the unit-cell volume as a function of pressure (0.29, 0.98, 1.34, 2.08 and 2.75 GPa) are shown: a, b and c strongly decrease with pressure, whereas β undergoes a significant increase (about 2.5°). The amount of variation throughout the entire pressure range is close to 5.5%, 4.5% and 4.7% for a, b and c, respectively, indicating a relatively high isotropy under high-pressure deformation. However, in Figure 20 it is possible to note a different compressional behaviour for b and c with respect to a and β: in fact, between 0.29 and 0.98 GPa a significant drop is evident, with a sudden reduction by 3.8% and 3.5% for b and c, respectively. Practically, a large part of the deformation for these two parameters occurs within a very limited pressure range of just 0.69 GPa. This aspect could be related with the presence of the channels, that are orthogonal to the *bc* plane, and their closing around the solvent under pressure effect, until an unknown critical value between 0.29 and 0.98 GPa. As a result of the unit-cell parameters deformation, the unit-cell volume decreases with increasing pressure by about 15%. Between 0.29 and 0.98 GPa a significant jump is shown again, with a decrease at the jump close to 11%. In general, it is observed that the crystal structure can be considered relatively stiff, if we exclude the strong collapse shown between 0.29 and 0.98: evidently, nearly all the deformation is focussed within this limited pressure range.

The analysis of the intensity data collected at all the pressures do not indicate any change in symmetry typical of a phase transformation; moreover, no data are present in the literature to indicate a possible isosymmetric transition (as, for example, recently shown for a silicate mineral family).[42]

Another important aspect revealed by of the high-pressure experiments is about the ageing process of the hemisolvate **10b**, particularly after X-ray exposure. In order to select the most suitable single-crystal, few crystals are checked by X-ray diffraction. In particular, a first experiment fails, due to an unexpected crystal degradation after 5 hours of the sample in the diamond anvil cell (DAC). Such measurement, however, was performed at low pressure (0.1 GPa). Therefore, a second crystal is selected and loaded directly to 0.98 GPa. The degradation in this case does not occur and it is possible to perform, under compression, also the experiments at 2.08 and 2.75 GPa; then, under decompression, measurements at 1.34 GPa and at 0.29 GPa are performed. Each single measurement takes about 8 hours. After the measurement at 0.29 GPa the sample is checked under a polarizing microscope and, again, the crystal is degraded for about 60% of its volume. The hypothesis is that the strong discontinuity found in the unit-cell volume and in *b* and *c* axes between 0.29 and 0.98 GPa could be related to the desolvation processes that are involved with the crystal degradation. Between 0.29 and 0.98 GPa the suddenly compression of *a* and *b* could be related with the closing of the channel around the guest, with a consequent higher stability of the host-guest adduct. At lower pressure, the relaxation of the channels causes the loss of the stability of the solvate form and the degradation of the crystal. The drastic structural changes, that go with the transformation of the solvate into the non-solvate structure, could produce microfractures. Consequently it is no possible to perform further measurements.

P (GPa)	**0**	**0.29**	**0.98**	**1.34**	**2.08**	**2.75**
a (Å)	6.506	6.460	6.221	6.256	6.158	6.148
b (Å)	16.015	16.060	15.454	15.464	15.290	15.296
c (Å)	22.319	22.298	21.519	21.488	21.398	21.269
β (°)	109.99	110.41	111.79	111.67	112.34	112.50
V (Å^3)	2189	2167	1929	1925	1863	1857

Table 7 Unit-cell parameters and cell volume at different pressures for **10b**

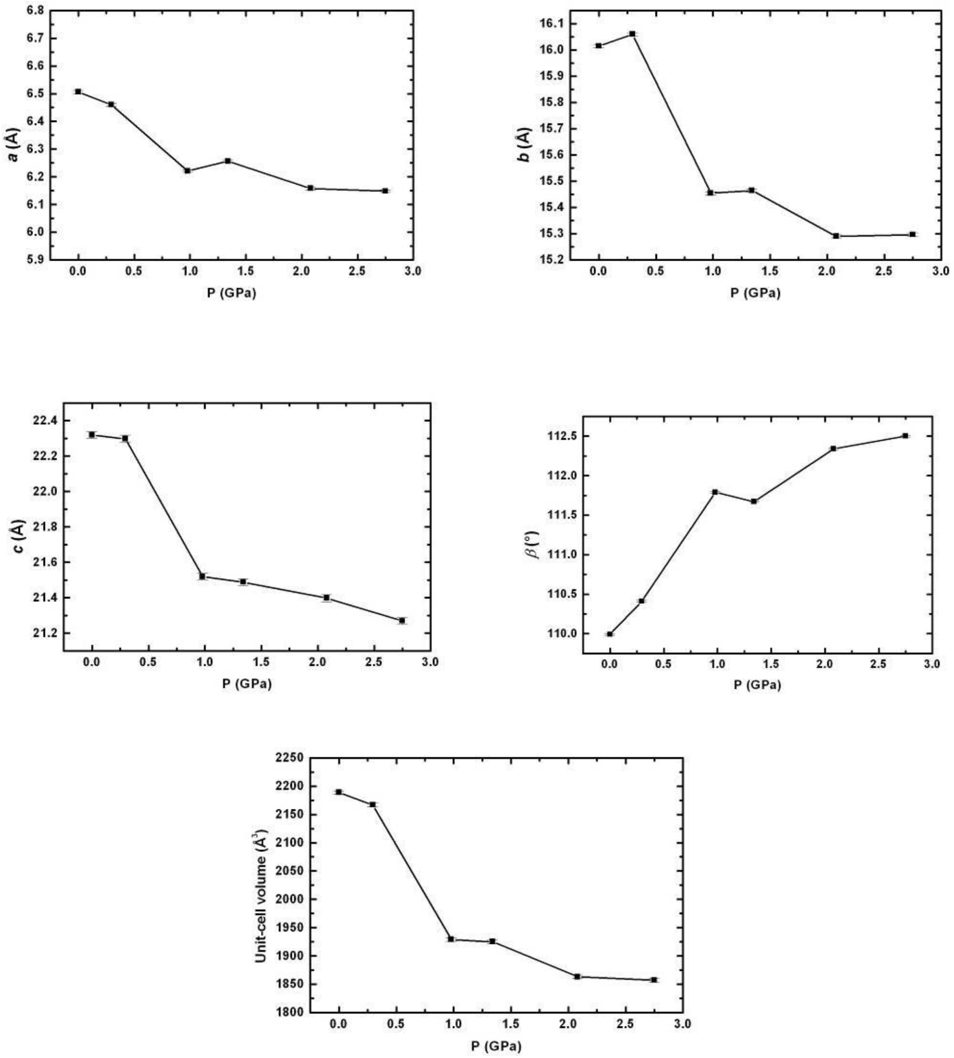

Figure 20. Evolution of the unit-cell parameters (*a*, *b*, *c*, β) and of the unit-cell volume in **10b** as a function of pressure

4.4. Thermal analysis

When a solid sample is heated, one of the many possible changes which it may undergo is the decomposition. Information on the kinetics and on the mechanism of the solid decomposition has both practical and theoretical importance.[43-44] For a heterogeneous reaction of type

$$A(s) \rightarrow B(s) + C(g)$$

the concept of reactant (or product) concentration does not play the significant role that it does in homogeneous reactions and the progress of reaction has to be measured in some other way. Usually the fractional reaction α is defined in terms of the change in mass of the sample. Particularly, α is defined as:

$$\alpha = \frac{m_0 - m}{m_0 - m_f},$$

where m is the mass at the considered step, m_0 is the initial mass and m_f is the mass of the sample when the reaction is complete. A careful definition of α could be very difficult in a heterogeneous process, due to the several factor that have to be taken into account. These include the presence of impurities and defects in the crystal structure as well.[45] It is recognized that the decomposition of solid reactants starts at defective sites of the crystal bulk. Whenever nuclei of solid product form, a strain in the neighbouring unreacted regions appears, resulting in growth of further nuclei. The shape of these nuclei depends on the crystal structure, because of the reaction occur more readily in some directions. The geometry of the processes of nucleation and growth[46-47] leads to specific predictions about the rate of the decomposition.

A kinetic isothermal study thus involves measurement of α as a function of time t at constant temperature T. Kinetic analysis of isothermal results involves attempting to relate the experimentally observed α and t values with values predicted for a limited set of models[48] based on processes of nucleation and growth, diffusion or some geometrical form of progress of the reactant/product interface. The expressions derived from these models can all be written both in integral forms

$$g(\alpha) = k(t-t_0)$$

and in the differential ones

$$d\alpha/dt = kf(\alpha),$$

where $g(\alpha)$ and $f(\alpha)$ are known as *conversion functions*.

The isothermal *α–time* curves $g(\alpha) = k(t)$ derived from these models are known as *conversion functions*.[48] These models include sigmoid curves (A2 –A4), deceleratory geometrical models (R2, R3), deceleratory diffusion models (D2-D4) and deceleratory ‘order of reaction’ models

(F1-F3) and enable to summarize a wide variety of possible kinetic behaviours for isothermal desolvation processes. This theory is used to describe the decomposition processes of the ionic solids, but it can be used with good approximation for the desolvation processes observed in the molecular solids.[48]

This part of the work aims to describe the kinetic isothermal analysis carried out on **10**, **11** and **12** in order to determine the activation energy involved in guest release. This kinetic study enables also to have further elucidations on the possible mechanisms of guest release during heating through a correlation between kinetic behaviour and structural features.

Once the appropriate kinetic model is identified by comparison between experimental and theoretical curves, the value of k at each temperature may be derived. Data from isothermal TGA experiments are analyzed on the initial assumption that a single conversion function and a single set of Arrhenius parameters A and E are applicable over the full range of α at each temperature. The aim is the knowledge of the rate coefficient k as a function of temperature. This coefficient derives from experimental data and appears in the Arrhenius equation:[49]

$$k = A\exp(-E/RT),$$

where T is the temperature in Kelvin, A the reaction frequency factor and E the activation energy. Thus the Arrhenius parameters E and A can be determined by carrying out a series of experiments over a range of different but constant temperatures and by plotting $\ln k$ *versus* $1/T$.

The method

(i) A dynamic TGA experiment is performed. The temperature value is increased by 0.50°C/min. The obtained data give information about solvate stoichiometry and about the temperature range in which the solvent loss takes place;

(ii) the temperature range in which the desolvation process takes place is divided into suitable intervals. The chosen temperatures are the ones used to perform the isothermal experiments;

(iii) the isothermal experiments are carried out at the suitable temperature values;

(iv) the isothermal data are analyzed on the initial assumption that a single conversion function and a single set of Arrhenius parameters A and E are apply over the full range of α:

- experimental time values t are scaled by the reduced time factor $t_{red} = (t - t_0)/(t_{0.5} - t_0)$, where $t_{0.5}$ is the time at which $\alpha = 0.50$ and $k(t_{0.5} - t_0) = 1.0$, thus plots of measured values of α *versus* t_{red} for all experiments including those at different isothermal temperatures should fall on a single curve;
- the resulting calculate curves expressed in the form $\alpha = k(t_{red})$ are compared with the calculated curve for each conversion function and the analysis of the magnitudes and of the

variations of α with t are used to identify the rate equation giving the most acceptable kinetic fit to the data and its range of applicability;

- k value is calculated by the suitable kinetics equations as the slope of the linear plot $g(\alpha) = kt$;
- the calculate k values are used in a conventional Arrhenius $lnk/(RT)^{-1}$ plot to extract the E values.

The results

Both **11** and **12** show a deceleratory, first order desolvation kinetic model F1 (Figure 21). This is a typical model for describing solid phase decomposition reactions in which the interface advances in a single crystallographic direction and it is consistent with the hypothesis of a process where the guest leaves the crystal through channels. In **10** a broader distribution of the experimental curves, falling in between the plots for F1 and R3, is in connection with the presence of different polymorphs (**10a**, **10b** and **10c**). It is then possible a mixed desolvation mechanism, including both F1 and the contracting volume model R3 (Figure 21). These are based on a mechanism in which the interface advances along three directions and could be a contribution of **10b** polymorph, whose more open structure of the channels makes easier for the guest to leave the crystal, and a contribution of **10c** as well. The linear plots that enable to calculate the slope k for each isotherm derive from the functions:

$$g(\alpha) = -\ln(1-\alpha) = k(t-t_0) \quad \text{and} \quad g(\alpha) = 1-(1-\alpha)^{1/3} = k(t-t_0)\,,$$

for F1 and R3, respectively.

The activation energies E for the desolvation processes of **10**, **11** and **12** are calculated from the corresponding Arrhenius plot (Figure 22), where it is also possible to observe that E does not vary significantly by changing the kinetic model for **10**.[48] The values of E increase as the boiling points of the guest species and in accordance with the DSC data (Table 8). The desolvation temperature of **12** (67°C) and **13** (78°C), obtained by DSC measurements, are higher than the boiling points of the corresponding guest (acetone b.p.=56°C; $CHCl_3$ b.p.=61°C), while it is the contrary for **10** (*onset* DSC value 76°C; toluene b.p.=112°C). This is probably due to the higher mobility of the guests in the open channels of **10b**. Anyway, all these features exclude the presence of some preferential intermolecular host-guest contacts and are consistent with the interpretation of the inclusion mechanism based, in these systems, on size and shape control.

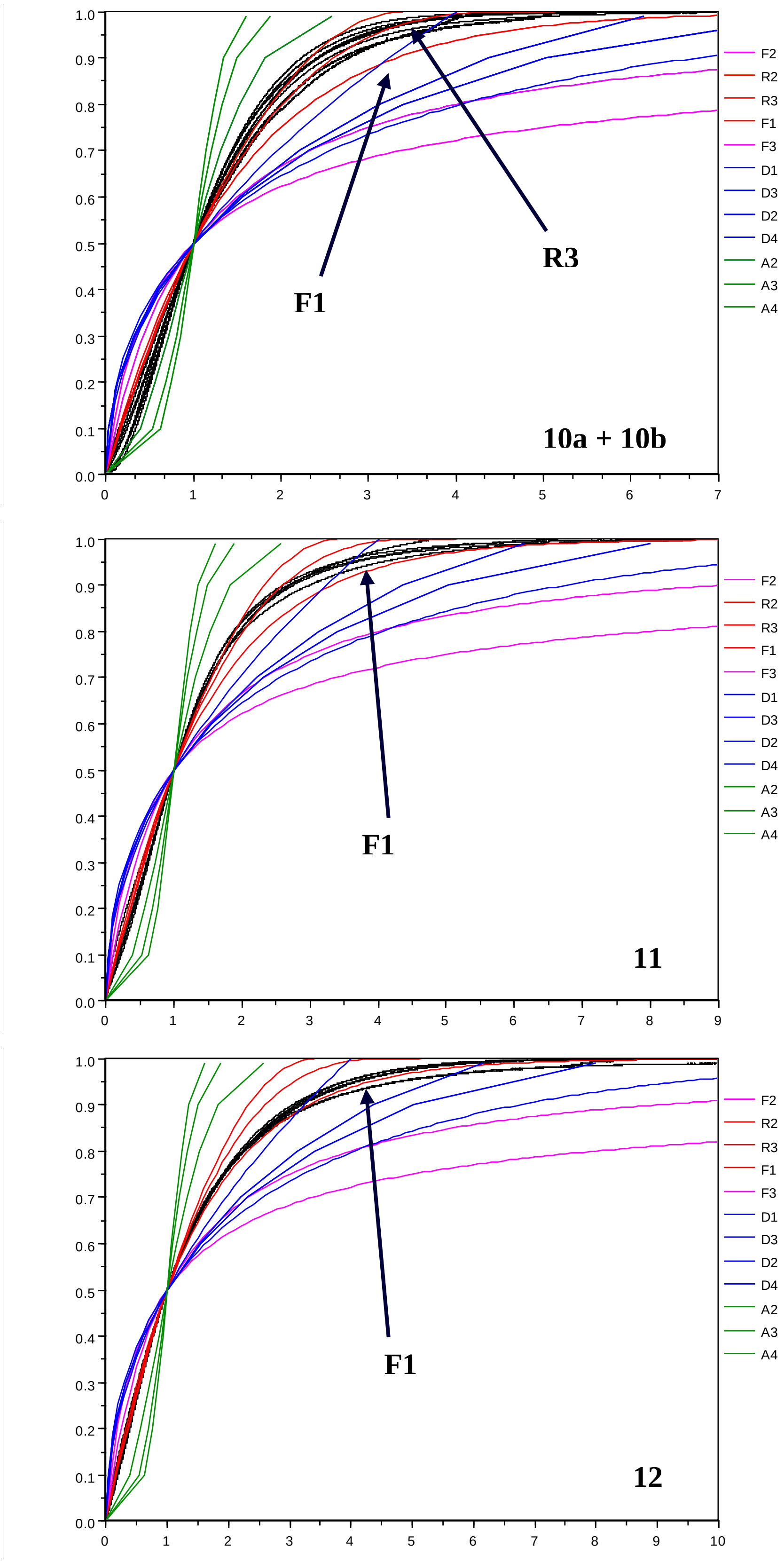

Figure 21. Experimental (black) and theoretical (color) curves (α, t_{red}) for desolvation kinetics of **10** (top, mixture of **10a** and **10b**), **11** (middle) and **12** (bottom). The models corresponding to the theoretical curves are labelled following the literature[49] according to the hypothetical mechanism of guest loss and grouped by color (D1-D4=blue; A2-A4= green; F2-F3=magenta; F1, R2, R3 =red). Best fitting theoretical curves are evidenced in red; F1 is identified in all the graphs and R3 in the top graph

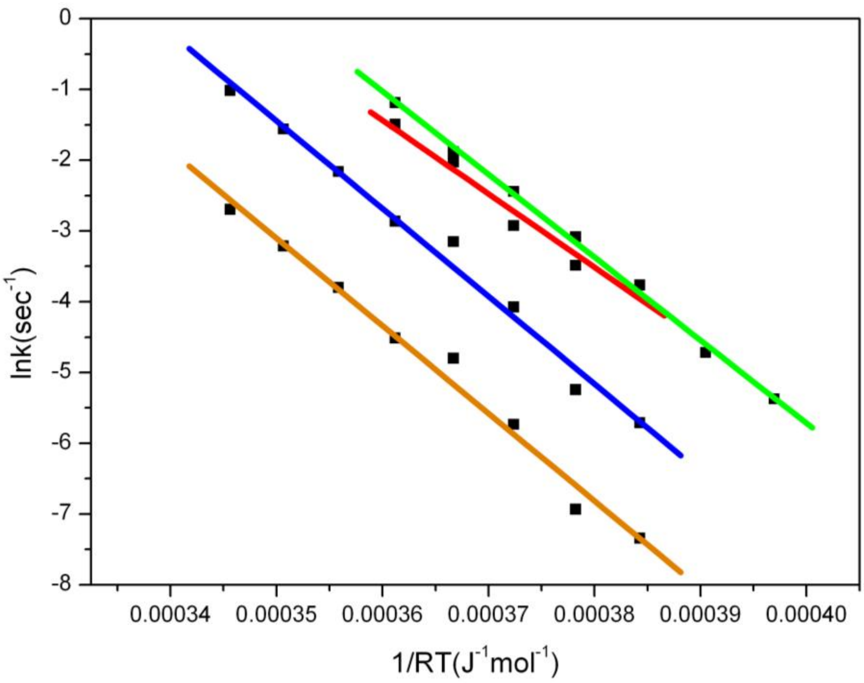

Figure 22. Arrhenius plots for the desolvation process in **10** (blue and yellow lines for the two hypothesized desolvation mechanisms F1 and R3, respectively), **11** (red line) and **12** (green line)

	E (KJ/mol)	T (°C)	Guest b.p. (°C)
10	124	76	112
11	104	67	56
12	117	78	61

Table 8. Activation energy *E* (calculated from isothermal TGA experiments), onset value for the desolvation (measured from DSC data) and guest boiling points for the solvate species **10**, **11** and **12**

4.5. Experimental

2- and 3- pyridinecarboxaldehyde and 3,5-diphenyl-4-hydroxyaniline are commercially available. Reagent grade solvents are used without further purification. Proton NMR spectra are recorded at 25°C on a Bruker 300 FT spectrophotometer by using $SiMe_4$ as internal standard, while IR spectra are obtained with a Nicolet 5PCFT-IR spectrophotometer in the 4000-400 cm^{-1} range, using KBr disks. Elemental analyses are performed by using a Carlo Erba Model EA 1108 apparatus.

Synthesis of 9. 0.09 ml (0.96 mmol) of 3-pyridinecarboxaldehyde are added to a solution containing 250 mg (0.96 mmol) of 3,5-diphenyl-4-hydroxyaniline in 20 ml of toluene. The solution is refluxed for 12 hours, then it is concentrated and by cooling a yellow solid precipitated. It is filtered, washed with small amounts of ethyl ether and dried under vacuum.

Yields 85%. Melting point 85°C. Elemental analysis for $C_{24}H_{18}N_2O$ (m.w.= 350.44): calculated C 82.26%, H 5.18%, N 7.99%; found C 82.66%, H 5.17%, N 7.73%. IR (KBr, cm^{-1}): ν(O-H) 3309. ^1H NMR ($CDCl_3$, 25°C, δ ppm): 9.00 (s, 1H, C5-H), 8.68 (d, J = 1.5 Hz, 1H, C1-H), 8.32 (s, 1H, C6-H), 8.29 (d, J = 1.5 Hz, 1H, C3-H), 7.58-7.18 (m, 13H C2-H, aryl), 5.60 (s, 1H, O-H, D_2O exchangeable). Single crystals suitable for X-ray diffraction analysis are obtained by slow evaporation at room temperature of a saturated THF solution.

Synthesis of 10. 0.09 ml (0.96 mmol) of 2-pyridinecarboxaldehyde are added to a solution containing 250 mg (0.96 mmol) of 3,5-diphenyl-4-hydroxyaniline in 20 ml of toluene. After 12 hours refluxing, the solution is concentrated and by cooling a brown solid was isolated. Yields 76%. Melting point 162.5°C. Elemental analysis for $C_{24}H_{18}N_2O \cdot 1/2$ toluene (m.w.= 396.51): calculated C 83.30 %, H 5.59 %, N 7.07%; found C 82.96%, H 5.27%, N 7.23%. IR (KBr, cm^{-1}): ν(O-H) 3280. ^1H NMR ($CDCl_3$, 25 °C, δ ppm): 8.83 (s 1H C6-H), 8.70 (d, J = 7.7 Hz, 1H, C1-H), 8.28 (d, J = 7.7 Hz, 1H, C4-H), 7.90 (t, J = 7.7 Hz, 2H C2(3)-H), 7.60-7.20 (m, 17H, aryl), 5.62 (s, 1H, O-H, D_2O exchangeable), 2.35 (s, 3H, CH_3-toluene). Thermogravimetric data: experimental mass loss 11.1 %, calculated for 1/2 toluene molecule 11.6%. By slow evaporation at room temperature of a satured solution of **10** in toluene, well shaped crystals of two different polymorphs (**10a** and **10b)** are isolated.

Synthesis of 11. 100 mg of **10** are dissolved in acetone. After evaporation at room temperature, a yellow solid is obtained. Yields 95%. Melting point 159.9 °C. Elemental analysis for $C_{24}H_{18}N_2O \cdot 1/2$ acetone (m.w. = 373.47): calculated C 82.01 %, H 5.67 %, N 7.60 %; found C 81.53 %, H 5.69 %, N 7.42 %. IR (KBr, cm^{-1}): ν(O-H) 3275, $\nu(C{=}O)_{acetone}$ 1711. ^1H NMR ($CDCl_3$, 25°C, δ ppm): 8.84 (s 1H C6-H), 8.71 (d, J = 7.7 Hz, 1H, C1-H), 8.29 (d, J = 7.7 Hz, 1H, C4-H), 7.92 (t, J = 7.7 Hz, 2H C2(3)-H), 7.60-7.20 (m, 17H, aryl), 5.48 (s, 1H, O-H, D_2O exchangeable), 2.17 (s, 6H, CH_3-acetone). Thermogravimetric data: experimental mass loss 7.7%, calculated for 1/2 acetone molecule 7.6%.

Synthesis of 12. 100 mg of **10** are dissolved in chloroform. After solvent evaporation, a brown solid is obtained. Yields 95%. Melting point 159.4°C. Elemental analysis for $C_{24}H_{18}N_2O \cdot 1/2$ chloroform (m.w. = 410.13): calculated C 71.75 %, H 4.55 %, N 6.83 %; found C 71.38 %, H 4.50 %, N 6.54 %. IR (KBr, cm^{-1}): ν(O-H) 3274. ^1H NMR ($CDCl_3$, 25 °C, δ ppm): 8.84 (s 1H C6-H), 8.73 (d, J = 7.7 Hz, 1H, C1-H), 8.26 (d, J = 7.7 Hz, 1H, C4-H), 7.91 (t, J = 7.7 Hz, 2H C2(3)-H), 7.60-7.20 (m, 17H, aryl), 5.66 (s, 1H, O-H, D_2O exchangeable). Thermogravimetric data: experimental mass loss 13.7 %, calculated for 1/2 chloroform molecule 14.6 %.

Synthesis of 13. 100 mg of **10** are dissolved in t-butyl methyl ether. After solvent evaporation, a yellow solid is obtained. Yields 95%. Melting point 158.3°C. Elemental analysis for $C_{24}H_{18}N_2O$ (m.w. = 350.44): calculated C 82.26%, H 5.18 %, N 7.99 %; found C 82.73 %, H 5.16 %, N 7.55 %. IR (KBr, cm^{-1}): ν(O-H) 3420. ^1H NMR ($CDCl_3$, 25 °C, δ ppm): 8.80 (s 1H C6-H), 8.70 (d, J = 4.6 Hz, 1H, C1-H), 8.25 (d, J = 4.6 Hz, 1H, C4-H), 7.86 (t, J = 4.6 Hz, 2H C2(3)-H), 7.55-7.45 (m, 17H, aryl), 5.55 (s, 1H, O-H, D_2O exchangeable).

Thermal analysis. TGA measures are performed on a Perkin Elmer Thermogravimetrical Analyser TGA7 and DSC on a Mettler Toledo DSC 821e. For TGA analyses the samples are placed in open platinum pans, for DSC in close and vented aluminium pans. The dynamic TGA traces are obtained on heating the samples at 0.5°/min from 25 to 120 °C. The TGA isothermal traces are obtained by keeping suitable temperature values until the plateau is reached. The DSC traces are obtained on heating the samples under nitrogen at 5°C/min from 25 to 180°C.

X-ray powder diffraction. Powder XRD spectra are collected using CuKα radiation with a Thermo ARL X'TRA powder diffractometer equipped with a Thermo Electron solid state detector. Variable temperature experiments are performed in air by using an Anton Paar TTK450 chamber controlled by the diffractometer software, with temperature steps of 10°C, increasing temperature 5 °C/min, from room temperature to 80°C for **10** and with temperature steps of 5°C, increasing temperature 5 °C/min, from room temperature to 55 °C for **11**.

High-pressure X-ray diffraction. A single-crystal of **10b** is selected for high-pressure, X-ray diffraction investigation. The crystal, observed under a polarized microscope, is twin- and inclusion-free, with a crystal size of 175×120×70 μm. It is loaded in an ETH-type (DAC)[50] using as gasket a T301 steel foil, which is pre-indented to 110 μm with a hole 250 μm in diameter. Silicon oil is used as pressure transmitting medium and chips of ruby is loaded with the crystal and used as internal pressure standard.[51] The unit-cell parameters are determined, at room temperature and at six different pressures (0.0, 0.29, 0.98, 1.34, 2.08 and 2.7 GPa), on a STOE STADI4 four-circle diffractometer (monochromatized MoKα radiation) equipped with an Oxford Diffraction CCD detector. The unit-cell edge data were collected up to $2\theta_{max}$ = 60° using an exposure time of 60 s and a ω-scan of 1°. The sample-detector distance was 60 mm. CrysAlis Red[52] was used to determine the unit-cell parameters at different pressures (Table 2).

X-ray Crystallography. MoKα radiation (λ=0.71073 Å) on a SMART AXS 1000 CCD diffractometer is used for **9**, **10a**, **10b** and **13**; Cu Kα radiation (λ=1.54178 Å) on a Siemens diffractometer is used for **11** and **12**. All data are collected at room temperature (293 K).

Lorentz, polarization, and absorption corrections are applied.[29] Structures are solved by direct methods using SIR97[30] and refined by full-matrix least-squares on all F^2 using SHELXL97[31] implemented in the WingX package.[32] Hydrogen atoms are introduced in idealized positions riding on their carrier atoms and refined isotropically. Anisotropic displacement parameters are refined for all non-hydrogen atoms. In compounds **10a**, **10b**, **11** and **12** a positional disorder is found for the guest species. Table 8 summarizes crystal data and structure determination results. Hydrogen bonds are analyzed with SHELXL97[31] and PARST97[33] and are reported in Table 61; extensive use is made of the Cambridge Crystallographic Data Centre packages[34] for the analysis of crystal packing.

Table 9. Crystal data for compounds **9-13**

Compound	**9**	**10a** **toluene hemisolvate**	**10b** **toluene hemisolvate**	**11** **acetone hemisolvate**	**12** **chloroform hemisolvate**	**13** **apohost**
Formula	$C_{24}H_{18}N_2O$	$C_{27.5}H_{22}N_2O$	$C_{27.5}H_{22}N_2O$	$C_{25.5}H_{21}N_2O_{1.5}$	$C_{24.5}H_{18.5}Cl_{1.5}N_2O$	$C_{24}H_{18}N_2O$
Molecular weight	350.40	396.47	396.47	379.44	410.09	350.40
Crystal system	monoclinic	monoclinic	monoclinic	monoclinic	monoclinic	monoclinic
Space group	$P2_1/c$	$P2_1/c$	$P2_1/c$	$P2_1/c$	$P2_1/c$	$P2_1/c$
Z	4	4	4	4	4	4
a/Å	10.3664(5)	6.565(2)	6.4967(6)	6.4271(2)	6.4550(4)	10.5928(9)
b/Å	21.577(1)	16.094(4)	15.986(2)	16.020(1)	15.9725(8)	21.188(2)
c/Å	8.3503(4)	21.032(6)	22.257(2)	20.388(3)	20.6186(9)	8.6774(7)
β/°	100.986(9)	99.746(9)	110.005(3)	95.111(5)	94.630(8)	106.529(2)
$V/Å^3$	1833.6(2)	2190 (1)	2172.0(3)	2090.9(3)	2118.9(2)	1867.1(3)
ρ /Mg m^{-3}	1.269	1.202	1.212	1.205	1.286	1.247
θ range for data collection/°	1.89 - 23.27	1.60 - 25.03	1.60 - 23.30	3.51 - 70.05	3.50 – 70.10	1.92 - 23.27
Unique reflections	2637	3859	3130	3958	4014	2691
Observed reflections $[I>2\sigma(I)]$	2189	1924	1741	3690	3149	2236
Data/ restraints/ parameters	2637 / 0 / 245	3859 / 13 / 264	3130 / 12 / 259	3958 / 0 / 274	4014 / 9 / 282	2691 / 0 / 246
Goodness-of-fit on F^2	1.066	1.102	0.971	1.043	0.979	1.019
R_1 $[I>2\sigma(I)]$	0.0315	0.1054	0.0683	0.0409	0.0562	0.0337
wR_2 $[I>2\sigma(I)]$	0.0800	0.3241	0.2054	0.1141	0.2114	0.0889
R_1 (all data)	0.0393	0.1678	0.1134	0.0430	0.0682	0.0414
wR_2 (all data)	0.0847	0.3536	0.2266	0.1160	0.2344	0.0951

5. Conclusions

This part of the work aims to describe crystal structures and solid-state properties of a wide class of pyridyl imino compounds. The common feature that results from X-ray single crystal structure determination is the assembly of supramolecular structures based on tunable 1D hydrogen-bonded motifs. Whenever the skeleton of the organic building block is changed, the hydrogen-bonded chain assumes particular geometric features. Particularly, it is possible to frustrate the linear folding in order to obtain a supramolecular host. The solid-state inclusion propensity of this species is correlated with the formation of a 1D nanochannel host framework, that can be differently arranged in concomitant polymorphs. High-pressure X-ray diffraction and thermal analyses allow to correlate channels elasticity and desolvation kinetics with the supramolecular structures of solvate and apohost forms.

In this case, the importance of the shape in the design of the multicomponent system depends on the possibility to tune a supramolecular array, in order to obtain the formation of a specific predicted motif.

References

1. G.R. Desiraju, *Crystal Engineering: The Design of Organic Solids*, 1989, Elsevier, Amsterdam
2. J. M. Lehn, *Supramolecular Chemistry*, 1995, VCH, Weinheim
3. L. J.Prins, D. N.Reinhoudt, P. Timmerman, Noncovalent Synthesis Using Hydrogen Bonding, *Angew. Chem., Int. Ed. Engl*, 2001, 40, 2382-2426
4. G.R. Desiraju, Supramolecular Synthons in Crystal Engineering - A New Organic Synthesis, *Angew. Chem, Int. Ed. Engl.*, 1995, 34, 2311-2321
5. C. B. Aakeröy, Crystal Engineering: Strategies and Architectures, *Acta Crystallogr.*, Sect. B, 1997, 53, 569-586
6. B. Moulton, M. J. Zaworotko, From Molecules to Crystal Engineering: Supramolecular Isomerism and Polymorphism in Network Solids, *Chem. Rev.*, 2001, 101, 1629-1658
7. L. Brammer, Developments in Inorganic Crystal Engineering, *Chem. Soc Rev.*, 2004, 33, 476-489
8. K. Folting, W. M. Lipscomb, B. Jerslev, The Structure of *N*-methyl-*p*-chlorobenzaldoxime and Refinement of the Structures of `*syn*'- and `*anti*'-*p*-chlorobenzaldoxime, *Acta Crystallogr.*, 1964, 17, 1263-1275
9. M. Bailey, C. J. Brown, The Crystal Structure of Terephthalic Acid, *Acta Crystallogr.*, 1967, 22, 387
10. L.Leiserowitz, Molecular Packing Modes. Carboxylic Acids, *Acta Crystallogr.*, Sect. B, 1976, 32, 775
11. O. Saied, T. Maris, J. D. Wuest, Deformation of porous molecular networks induced by the exchange of guests in single crystals, *J. Am. Chem. Soc.*, 2003, 125, 14956-14957
12. C. B. Aakeröy, A. M. Beatty, D. S. Leinen, New Building Blocks for Crystal Engineering. Syntheses and Crystal Structures of Substituted Oxime Pyridines, *CrystEngComm*, 2000, 27-41
13. A. Bacchi, M. Carcelli, T. Chiodo, F. Mezzadri, Effects of “Changing the Wheels” on the Inclusion Properties in Metal-Organic Diols, *CrystEngComm*, 2008, 10, 1916-1927

14. A. Bacchi, M. Carcelli, T. Chiodo, G. Cantoni, C. De Filippo, S. Pipolo, A Discussion on the Solid State Organization of 4-Pyridyl Imino Cmpounds and on the Co-Crystallization between their Molecular Precursors, *CrystEngComm*, 2009, 11, 1433-1441
15. V. R. Vangala, B. R. Bhogala, A. Dey, G. R. Desiraju, C. K. Broder, P. S. Smith, R. Mondal, J. A. K. Howard, C. C. Wilson, Correspondence between Molecular Functionality and Crystal Structures. Supramolecular Chemistry of a Family of Homologated Aminophenols, *J. Am. Chem. Soc*, 2003, 125, 14495-14509
16. F. H. Allen, V. J. Hoy, J. A. K. Howard, V. R. Thalladi, G. R. Desiraju, C. C. Wilson, G. J. McIntyre, Crystal Engineering and Correspondence between Molecular and Crystal Structures. Are 2- and 3-Aminophenols Anomalous? *J. Am. Chem. Soc*, 1997, 119 (15), 3477-3480.
17. A. Dey, M. T. Kirchner, V. R. Vangala, G. R. Desiraju, R Mondal, J. A. K. Howard, Crystal Structure Prediction of Aminols: Advantages of a Supramolecular Synthon Approach with Experimental Structures, *J. Am. Chem. Soc*, 2005, 127, 10545-10559
18. A. Gavezzotti, Structure and Energy in Organic Crystals with Two Molecules in the Asymmetric Unit: Causality or Chance?, *CrystEngComm*, 2008, 10, 389-398
19. S. Roy, R. Banerjee, A. Nangia, G. J.Kruger, Conformational, Concomitant Polymorphs of 4,4-Diphenyl-2,5-cyclohexadienone: Conformation and Lattice Energy Compensation in the Kinetic and Thermodynamic Forms, *Chem.Eur.J.*, 2006, 12, 3777 – 3788
20. F. L. Hirshfeld, Bonded-Atom Fragments for Describing Molecular Charge Densities, *Theor. Chim. Acta*, 1977, 44, 129-138
21. D. Grimwood, S. K. Wolff, J. J. McKinnon, M. A. Spackmann, D. Jayatilaka, *Crystal Exploreer*, University of Western Australia, Crowley, ver. 2.1, 2008
22. M.A.Spackman, J.J.McKinnon, D. Jayatilaka, Electrostatic Potentials Mapped on Hirshfeld Surfaces Provide Direct Insight Into Intermolecular Interactions in Crystals, *CrystEngComm*, 2008, 10, 377–388
23. R. Scott Rowland, R. Taylor, Intermolecular Nonbonded Contact Distances in Organic Crystal Structures: Comparison with Distances Expected from van der Waals Radii, *J. Phys. Chem*., 1996, 100, 7384-7391
24. J.J. McKinnon, M.A. Spackmana, A.S. Mitchell, Novel Tools for Visualizing and Exploring Intermolecular Interactions in Molecular Crystals, *Acta Crystallogr.*, Sect. *B*, 60, 2004, 627-668
25. T. Sujiyama, J. Meng, T. Matsuura, Intermolecular Interactions in the Formation of Two-Component Molecular Crystals Composed of Chloronitrobenzoic Acids and 4-Benzoylpyridine, *J.Mol.Struct.*, 2002, 611, 53-64
26. C. J. Brown, The Crystal Structure of *p*-Aminophenol, *Acta Crystallogr.*, 1951, 4, 100-103
27. O. Ermer, A. Eling, Molecular Recognition Among Alcohols and Amines: Super-Tetrahedral Crystal Architectures of Lnear Ddiphenol-Diamine Complexes and Aminophenols, *J. Chem. Soc., Perkin Trans. 2*, 1994, 925-944
28. C. B. Aakeröy, D. J. Salamon, Building Co-Crystals with Molecular Sense and Supramolecular Sensibility, *CrystEngComm*, 2005, 7, 439-448
29. (a) SAINT: SAX, Area Detector Integration, Siemens Analytical instruments INC., Madison, Wisconsin, USA. (b) G.Sheldrick, SADABS: Siemens Area Detector Absorption correction Software, 1996, University of Goettingen, Germany

30. A.Altomare, M.C.Burla, M.Cavalli, G.Cascarano, C.Giacovazzo, A.Gagliardi, A.G.Moliterni, G.Polidori, R.Spagna, *Sir97: A New Program For Solving and Refining Crystal Structures*, 1997, Istituto di Ricerca per lo Sviluppo di Metodologie Cristallografiche CNR, Bari
31. G.Sheldrick, *Shelxl97. Program for structure refinement*. University of Goettingen, Germany, 1997
32. L.J.Farrugia, *J. Appl. Cryst.* 1999, 32, 837-838
33. M.Nardelli, *J. Appl. Cryst.* 1995, 28, 659
34. (a) F. H.Allen, O.Kennard, R.Taylor, *Acc. Chem. Res.*, 1983, 16, 146-153. (b) I. J.Bruno, J. C.Cole, P. R.Edgington, M.Kessler, C. F.Macrae, P. McCabe, J. Pearson, R.Taylor, *Acta Crystallogr.*, 2002, B58, 389-397
35. A. Bacchi, M. Carcelli, T. Chiodo, F. Mezzadri, F Nestola, A. Rossi, Inclusion Properties, Polymorphism and Desolvation Kinetics in a New 2-Pyridyl Iminophenol Compound with 1D Nanochannels, *Crystal Growth & Design*, 2009, 9 (8), 3749-3758
36. R.J. Sarma, J.B. Baruah, Supramolecular and Host-Guest Chemistry of *Bis*-Phenol and Analogues, *Cryst.Growth Design*, 2007, 7, 989-1000
37. L. R. Nassimbeni, Physicochemical Aspects of Host-Guest Compounds. *Acc. Chem. Res.*, 2003, 36, 631-637
38. *Crystal Design: Structure and Function*, R.G Desiraju Ed.; John Wiley & Sons Ltd., Chichester, 2003
39. E. Weber, *Shape and symmetry in the design of new hosts*, vol. 6, ch. 17 in *Comprehensive Supramolecular Chemsitry*, D. D. MacNicol, F. Toda, R. Bishop, Eds., Pergamon, Oxford, 1996
40. J. Bernstein, R. J. Davey, J.Henck, Concomitant Polymorphs, *Angew. Chem. Int. Ed.*, 1999, 38, 3440-3461
41. K. Kuruma, H. Nakagawa, T. Imakubo, K. Kobayashi, Guest-Exchange and Guest-Release via Gas–Solid Contact in Clathrate Crystals Based on 2,5-Bis(9-hydroxyfluoren-9-yl)thieno[3,2-*b*]thiophene as a Host Compound, *Bull.Chem.Soc.Jpn.* 1999, 72, 1395-1401
42. S. Ohi, A. Miyake, N. Shimobayashi, M. Yashima, M. Kitamura, An Isosymmetric Phase Transition of Othopyroxene Found by High-Temperature X-Ray Diffraction , *American Mineralogist*, 2008, 93, 1682-1685
43. A. K. Galwey, M. E. Brown, *Thermal Decomposition of Ionic Solids*, Elsevier, Amsterdam, 1999
44. S.Vyazovkin, Computational Aspects of Kinetic Analysis, *Int. Rev. Phys. Chem.*, 2000, 19, 45
45. V. V. Boldyrev, Topochemistry of Thermal Decompositions of Solids, *Thermochim. Acta*, 1986, 100, 315
46. M. E. Brown, D. Dollimore, A. K. Galwey, *"Reaction in the Solid State", Comprehensive Chemical Kinetics,* Vol. 22, Elsevier, Amsterdam, 1980
47. A. K. Galwey, Solid State Decompositions: the Interpretation of Kinetic and Microscopic Data and the Formulation of a Reaction Mechanism, *Thermochim. Acta*, 1985, 96, 259
48. M. E. Brown, *Introduction to thermal analysis*, Kluwer Academic Publishers, 2001
49. K. J. Laidler, Unconventional Applications of the Arrhenius Law, *J. Chem. Educ.*, 1972, 49, 343
50. R.D. Miletich, R. Allan, W.F. Kuhs, *High-pressure single-crystal technique*. In *High-temperature and high-pressure crystal chemistry*. R.M. Hazen, R.T. Downs, Eds., Reviews in Mineralogy and Geochemistry, Mineralogical Society of America and the Geochemical Society, Washington D.C., 2000, 35-59
51. H.K. Mao, J. Xu, P.M. Bell, *J. Geophys. Res.* 1986, 91, 4673–4676
52. Oxford Diffraction. CrysAlis RED. Oxford Diffraction Ltd, 2007, Abingdon, England

PART III

On the validation and rationalization of the role of molecular shape in cocrystallization

1. Introduction

"Molecular recognition" is a process of extraordinarily selectivity. It implies that two molecules approach one another in a particular way, so that the potential energy of the pair decreases significantly.[1] The specific pathway of approach is a result of the ability of the molecules to interact through some specific interactions. A better understanding of the factors that regulate the process of molecular recognition is fundamental for the complete understanding of the highly efficient and specific intermolecular events involved in biological problems, such us the formation of the enzyme-co-enzyme-substrate complexes or the reconstitution processes that regenerate ribosomal particles from their dissociated components.[2-3]

The analysis of factors that influence the recognition between the molecules is the central point of discussion in supramolecular chemistry. An excellent example of a highly selective interaction is the hydrogen bond, that plays a key role in numerous solid-state assembly processes.[4-10] Actually, structures held together by hydrogen bonds may form exceptions to the Kitaigorodski's principle of close-packing,[11-12] because of the strongly directional nature of such bond. Such directionality can lead to more open arrangements of molecules, as exemplified by the structure of ice. In contrast, molecules of many organic hydrocarbons are able to assemble into stable crystalline arrays without strong and directional hydrogen bonding, exploiting instead the presence of a multitude of weak interactions that stabilize a close-packed network.

The crystallization process has been used since immemorial time as a method of purification. Two outcomes are possible when a solution containing two ore more different solutes is allowed to evaporate (Figure 1). In one case, the appearance of separate molecular solids could take place. This is a demonstration of the innate structural selfishness of the molecules[13] and it forms the foundation of recrystallization as means for purification. Conversely, if the homomeric intermolecular forces are dominated by the heteromeric ones, the formation of a multicomponent crystalline system could be observed.

Cocrystallization is an attempt to bring together different molecular species within a periodic crystalline lattice. Consequently, each cocrystal structure contains important information about the way in which intermolecular strong and weak forces compete and collaborate in the creation of an energetically balanced system.[13] Due to the high selectivity in their assembly, the cocrystals are now recognized as tools for the study and classification of molecular packing patterns, hydrogen-bonding motifs and supramolecular synthons.[14-17] From this perspective *the cocrystals have become a solid-state target for the non-covalent synthesis.*[18]

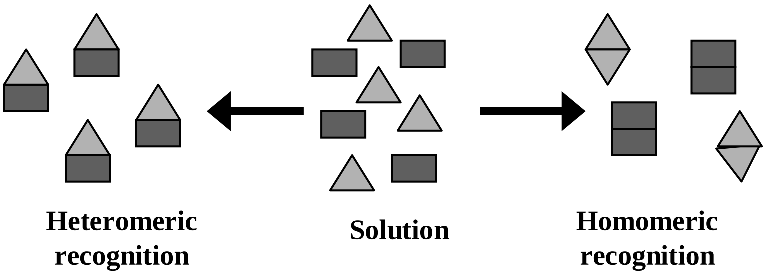

Figure 1. Recrystallization (homomeric recognition, right) and cocrystallization (heteromeric recognition, left)

Cocrystallization between two molecular components (the cocrystal formers) leads to a new supramolecular arrangement and, subsequently, leads to new solid-state properties. In the pharmaceutical field, the crystal structure of an active pharmaceutical ingredient (API) could influence its bioavailability and the choice of its solid dosage form. Pharmaceutical cocrystals provide a potent alternative to pharmaceutical salts, usually obtained as hydrates,[19] as vehicles for changing drug formulations without varying the active principles. Through formation of a cocrystal it could be possible to improve some physical properties of an API, such as dissolution characteristics,[20-21] hydratation stability,[22-24] melting points[25-26] or tableting properties.[27]

The versatility of their applications makes cocrystal chemistry a very active and challenging research area of the modern solid-state chemistry. The number of new perspectives, involving design, preparation and characterization of cocrystal forms, is exponentially growing. Particularly, the development of mechanochemistry,[28] i.e. synthesis induced by mechanical force, offers the opportunity to perform cocrystal synthesis using simple and solvent-free approaches.[29] At this point a brief overview of mechanochemistry, and particularly of mechanochemical cocrystallization, is given.

1.1. Mechanochemistry: a solvent-free route for the preparation of molecular and supramolecular materials

Solid-state solvent-free reactions open new perspectives in the synthesis of crystalline materials from preformed crystalline reactants.[30] Mechanochemical reactions[31-33] represent an alternative, and sometimes even the only, way to prepare new systems based on covalent organic[34] or inorganic[35] networks, coordination bonds[36] or supramolecular adducts.[37]

From the experimental point of view (Scheme 1), mechanosynthesis[38-39] consists of mixing together the reactants by grinding them either manually, using a mortar and pestle, or mechanically, by using a ball or vibratory mill.[40] The products of the grinding or milling experiment usually appear as powdered crystalline materials. Unfortunately, the small size of particles obtained from these processes prevents their structural characterization by single crystal diffraction techniques. However, sometimes it is possible to obtain the mechanochemical product from solution, by optimizing crystallization conditions.[41] Nevertheless it is very likely that the product obtained from solution will be different from the one obtained by grinding. Seeding of a supersaturated solution with the powder obtained by grinding provides a useful means to obtain the desired phase in the form of single crystals.[42] The opportunities in product characterization have recently become enhanced by the integration of advanced methods of solid-state analysis, such as structure solution from X-ray powder diffraction (XRPD) data,[43] aided also by crystal structure prediction (CSP),[44] solid-state NMR spectroscopy (SS NMR),[45] particularly useful to differentiate between cocrystal or salt formation,[46-47] and terahertz time-domain spectroscopy (THz-TDS).[48]

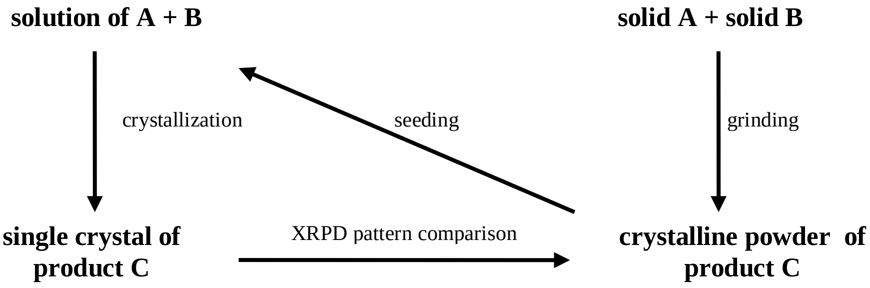

Scheme 1. Experimental approach to the solid-state synthesis and characterization

A solid-state solvent-free reaction is basically diffusion controlled, because the rate of product formation depends on the ability to bring the reactants into contact. Thus, the success of the reaction requires the intimate mixing of reactants over a large contact area (and a small particle size). Other factors that affect the solid-state reaction efficiency are the time of the mixing, as well as the temperature and the pressure of the experiment. Sometimes the heat produced in the course of the reaction could induce local melting of the reactants or at the interface between different particles, making the reaction effectively a liquid-phase process. If a small amount of solvent is added the reaction could become easier. This method is known as kneading[49] and is based on the idea that a small (catalytic) amount of solvent is a means to increase the rate of the cocrystallization, acting as lubricant for the molecular diffusion. The experiment of kneading involves manual grinding, with a mortar and pestle, in the presence of a liquid phase. The amount of liquid used for kneading is significantly less than employed in solution cocrystallization. Kneading technique has several practical industrial applications, developed particularly for the preparation of pharmaceutical powders[50-51].

1.2. Mechanochemical approach to cocrystal preparation

A currently highly interesting area of mechanochemistry is the synthesis of multicomponent crystals (cocrystals) by grinding.[52] The first example of the cocrystal preparation by grinding dates back to 1893.[53] The reported formation of a multicomponent system by the equimolar reaction *p*-benzoquinone and hydroquinone leads to the development of the idea that supramolecular synthesis in the solid-state allows the observation of a different degree of molecular recognition with respect to the synthesis in solution[54-55]

The study of macroscopic mechanisms of the grinding leads to the conclusion that solid-state cocrystallization is based on a combination of different mechanisms. Each of these mechanism involves a different type of intermediate phase. The process could be based on molecular diffusion,[56-57] it could involve eutectic formations[58] or it could be mediated by an amorphous phase.[59] The cocrystallization controlled by molecular diffusion occurs in cases where the reactants have high vapour pressures in the solid-state and the rapid product formation results from the contact between solid reactants. In such cases, highly efficient reactivity can be observed also without excessive mechanochemical agitation. For such system, grinding merely increases the rate of the reaction, by helping the exposure of new reactant surface. In mechanochemical cocrystallization mediated by an eutectic liquid phase the product cocrystal is formed from a liquid phase that gradually disappears as the reaction becomes nearer to completion. Microscopy revealed that most of reactant material is converted into a liquid and that the nucleation of the cocrystal results in the gradual solidification of the eutectic melt.[60] The formation of an amorphous intermediate usually takes place in the cocrystallization processes involving non-volatile solids held together by strong supramolecular interactions. This is the case for many pharmaceutical cocrystallizations.[61] The common feature of these mechanisms is that the intermediate bulk phase exhibits higher mobility and energy of the reactants with respect to their starting crystalline forms.[62]

Recent perspectives in mechanochemical preparation of cocrystals are largely based on the use of a small quantity of solvent. Liquid-assisted grinding[63-64] (LAG) represents an efficient alternative to the neat (or dry) grinding for screening for cocrystals,[65] salts[66] and polymorphs.[67] The liquid added to the grinding reaction is recognized to play a catalytic role[68] ascribed to the physical effect of increasing molecular mobility through the lubricanting action of the solvent. Nevertheless the presence of the liquid seems to have, in some cases, other profound effects on the outcome of the cocrystallization. Indeed the addition of a liquid to the grinding mixture could lead to the formation of multicomponent inclusion systems, in which the host porous framework includes the solvent molecules.[69] In these solvated cocrystals the liquid molecules act as templating agents and their presence and properties are crucial elements in enabling the cocrystallization. The solvent and its properties could also be an essential requisite for achieving a higher cocrystallization yield, a higher crystallinity of the product and controlled polymorph formation.[70] The liquid plays a key role in controlling the outcome of the grinding experiment. The profound effect of the liquid is ascribed on one hand on the observation that sometimes two compounds do not give a cocrystal by neat grinding, but the addition of a small amount of liquid enables the reaction.[71] One the other hand it is possible that the cocrystallization does not take place from solution but cocrystals are easily obtained by LAG.

The three-component phase diagrams give an explanation for difficulties encountered in attempts to obtaining from solution the same cocrystals as prepared by solid-state reactions (Figure 2). These diagrams are derived from the analysis of the behaviour of the system nicotinamide – cinnamic acid in water and in methanol.[72] The highlighted red regions are the most important in the discussion of the behaviour in solution, while the highlighted green regions correspond to the composition of the reaction mixture upon liquid-assisted grinding. In a congruent system (Figure 2, top) the cocrystal formers have similar solubilities in the given solvent. In this cases reducing the amount of solvent results in cocrystal formation, as

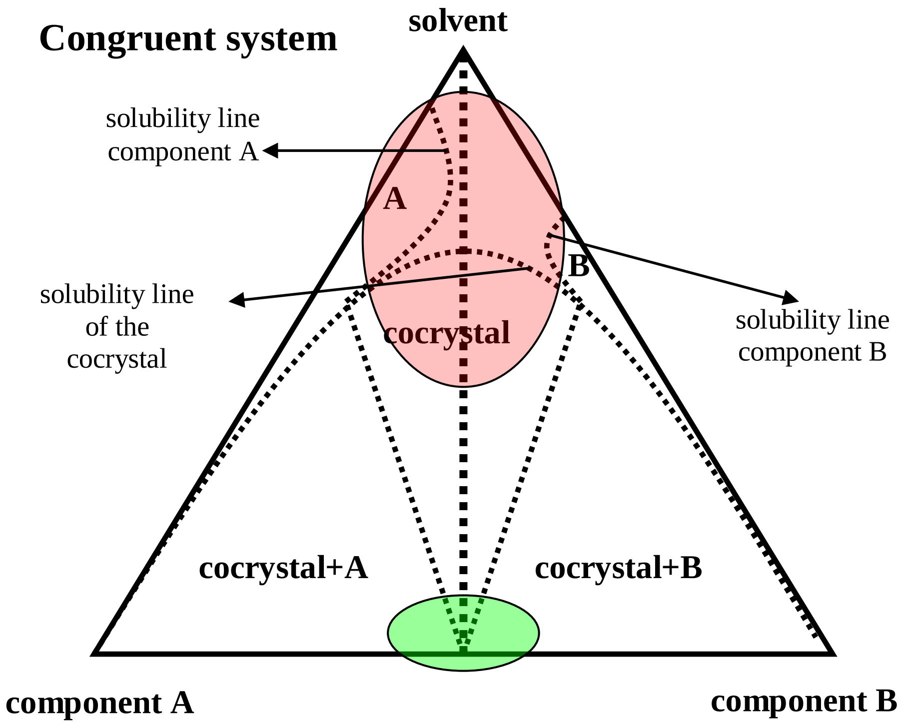

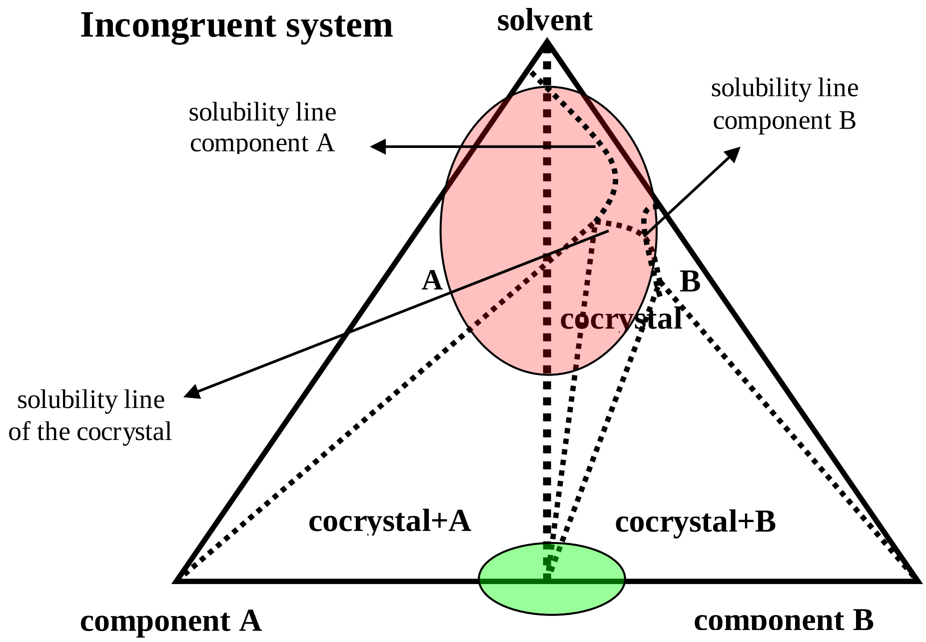

Figure 2. Three component phase diagrams of a congruent and of an incongruent system

the dotted line goes through the region corresponding to the undersaturated solution and immediately crosses the solubility line of the cocrystal. In an incongruent system (Figure 2, bottom) the two components have sensitive differences in solubility and solvent removal leads to the precipitation of the individual components, starting from the less soluble compound. In both cases, the liquid-assisted grinding mixture involve a region in which the cocrystal is the most stable species, consequently obtained during the experiment.

2. Study of the solid-state self-assembly through a mechanochemical screening: investigating the role of molecular shape in cocrystallization

The prediction of the cocrystal formation and the rationalization of the mechanisms and of the factors that steer the formation of heteromolecular assemblies are sometimes very confusing propositions. On one hand most crystalline molecular solid are homomeric because close-packed assemblies of discrete building blocks are more easily achieved if the components are "identical".[73] On the other hand there are recent numerous reports on synthesis of binary, ternary and even quaternary cocrystals.[74-75]

In order to rationalize the formation of heteromolecular crystals, energetic considerations of the advantages of the forming a multicomponent system with respect to two homomeric ones must be a priority. The problem lies in the multitude of weak and non-specific interactions which limits the ability to predict cocrystal formation. These limitations are usually handled by a trial-and-error cocrystal screening procedure.[76] For practical applications, it would be important to identify the principal factors that control the cocrystallization, so as to reduce the number (and the costs) of cocrystal screening experiments.

Cocrystal design is traditionally based on a supramolecular synthon approach.[77] This approach assumes that the synthon hierarchy is the key factor regulating the formation of specific motifs and architectures in the cocrystal. The supramolecular synthon approach is definitely pragmatic in predicting the behaviour of systems in which the driving forces underlying molecular assembly are specific strong and directional interactions, such as hydrogen or halogen bonds.[78] In some cases it is even possible to split the recognition into sequential processes.[79-80]

At this point it is necessary to point out the reliability of strategies based on hierarchy of supramolecular synthons in cocrystal design. Aakeröy and co-workers proposed a comparative study on the extent of cocrystal formation between selected oximes and nitrogen-containing heterocycles.[81] The oximes contained the same functional group responsible for heteromeric recognition, exhibited similar steric and solubilities features, but covered a different range of pK_a values. The differences in pK_a values of the oximes and, consequentely, the different ΔpK_a values for the investigated oximes-N-heterocycle pairs cause the variation in hydrogen bond strength acting as a driving-force for cocrystallisation. This study demonstrated that ΔpK_a is a useful guideline in cocrystal design. Nevertheless there are exceptions[82] and other factors should be considered in order to accurately rationalise (and predict) cocrystallisation.

Molecular shape is often discussed as an important factor in solid-state molecular assembly. Unfortunately, the discussions of molecular shape are typically vague. Due to its analogic nature and the consequent difficulties in its quantification, there is not a direct correspondence between molecular shape and efficiency of supramolecular assembly. Consequently, each correlation is usually introduced as an individual *a posteriori* observation rather than being based on a systematically collected set of evidences. This is also because the shape-related effects are often overshadowed by the weakest supramolecular forces and are difficult to discern from the effects of solubility and solvent competition.

Recently, a statistical analysis of molecular features in cocrystals structures deposited within the Cambridge Structural Database (CSD)[83] has been proposed by Fábián.[84] Classical inclusion compounds, including molecules larger than 30 heavy atoms, with awkward shape and that cocrystallize predominantly with smaller molecules, were intentional excluded from this analysis. Analysis of the remaining data set of 710 cocrystal structures (each formed by molecules containing 6-30 heavy atoms) led to the identification of molecular properties that could be significant for cocrystal formation. A set of quantitative structure-activity relationship (QSAR) descriptors were used to characterize the molecules able to form cocrystals. Notably, descriptors of molecular shape and size were defined according to the proposed box model.[73] In this model the van der Waals volume of the molecule is enclosed in a rectangular box (Figure 3). The long (L), medium (M) and short (S) axes of the box refer to the size of the molecule, while their ratio provide information about molecular shape. For example, planar molecules have a small S/L ration, while rod-shaped molecules are characterized by a small M/L ratio. The density plots, correlating these ratios for each pair of molecules that form cocrystals, showed significant correlation, suggesting that the molecular shape plays a noticeable role in directing cocrystal formation. Particularly, it was observed that the shapes of molecules forming cocrystals tend to be similar.

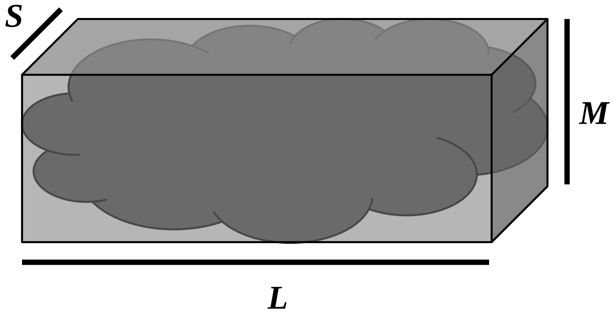

Figure 3. Representation of the molecular shape descriptors L, M and S in the box model

Understanding of how these observed shape relationships can be applied to specific cases and how they can be quantified are important pragmatic aspects. The study described herein approaches to this problem from an empirical aspect. By analysing a particular situation, this study proposes qualitative and semi-quantitative guidelines on how molecular shape can aid cocrystal design.

2.1. Experiment design

In order to understand how the shape factor could influence the cocrystallization, a screening for cocrystal formation between selected test molecules is conducted. Mechanochemical liquid-assisted grinding (LAG)[85] is chosen as means to screen the cocrystal formation. The efficiency of LAG in cocrystal screening lies in the ability to avoid the effects of solubility and solvent competition.[29] Presumably, removing these interferences would enable the validation of molecular shape effects in cocrystallization. To reinforce the significance of the results, particularly in context of independence from the grinding liquid, the screen is carried out using nitromethane ($MeNO_2$) and ethanol (EtOH). These two solvents are selected because they exhibit very different polarity and ability to form hydrogen bonds.[86-87] The liquid is added to the solid reaction mixture in catalytic amount, (30 µl for an amount of 200-300 mg of solid reagents). Each experiment takes 20 minutes of grinding, and it is performed in a mixer mill operating at a frequency of 30 Hz/sec.

The careful choice of the synthon and of the cocrystal building block is a key point in the design of the screen. On one hand, there is the necessity to use functional groups that are mutually complementary in terms of hydrogen bonding. On the other hand, the supramolecular synthon resulting from such complementarity should be sufficiently sensitive to crystal packing, so as to allow the recognition of the influence of building block shape. In addition to the rigidity of the building blocks, required for shape analysis, the complementary functionalities involved within the synthon should be sufficiently small to have only minor impact on the overall molecular shape. For this reason some common synthon formers, such as pyridines or benzimidazoles,[81] could not be used, as they would significantly affect the expected shape of the molecule. Consequently, oxime and carboxylic acid groups are selected as suitable candidates for this study, due to their ability to guide cocrystallisation via the week and discrete $R_2^2(7)$ oxime - carboxylic acid (OXCA) hydrogen-bonded synthon (Scheme 2).

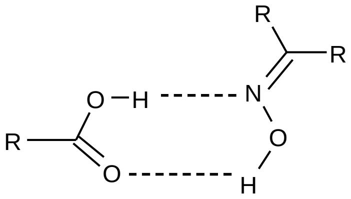

Scheme 2. The oxime - carboxylic acid $R_2^2(7)$ heterosynthon used for the cocrystal design

The usefulness of this assembly is, *inter alia*, demonstrated by the cocrystallization of (E)-benzaldehyde oxime (**3**) and 3,4,5-trifluorobenzoic acid (**l**) (Crystallographic data of cocrystal **3l** are reported in the Table 8). These two compounds form a cocrystal, but the obtained supramolecular dimer is not sustained by the OXCA $R_2^2(7)$ synthon. Instead, cocrystal formation is achieved through the π-π interaction involving the aryl ring of **3** and the fluorinated electron-poor ring of **l** (Figure 4). This confirms that the synthon $R_2^2(7)$ is weak enough to be overshadowed by other effects and other synthons. Consequently, it is assumed that the selected synthon is sufficiently sensitive to detect crystal packing effects.

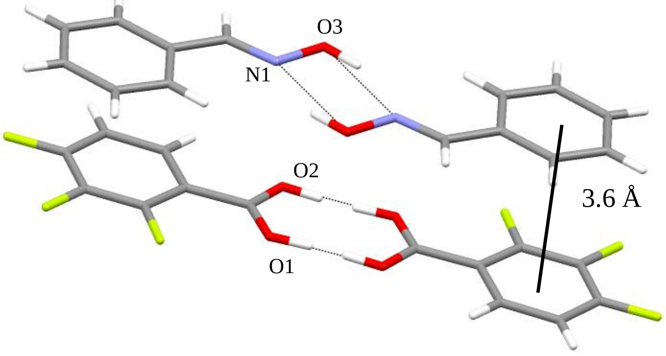

Figure 4. (E)-benzaldehyde oxime - 3,4,5-trifluorobenzoic acid **3l** cocrystal

To ensure the rigidity and the diversity of molecular shapes in the screen, molecules based on rigid bornyl and adamantyl groups are utilised as approximately spherical building block, while flat building block are achieved using phenyl groups (Scheme 3). Molecular shape is quantified through S/L and M/L descriptors (Table 1). The calculations of molecular shape descriptors are performed by. L. Fábián at the Cambridge Crystallographic Data Centre (CCDC). According to a recent application,[88] SPARC[89] is used for $\mathrm{p}K_\mathrm{a}$ calculations of all the test molecules (Table 1). It is necessary to point out that the $\mathrm{p}K_\mathrm{a}$ of the oximes corresponds to the deprotonation of the corresponding conjugated acid. Thus, a higher $\mathrm{p}K_\mathrm{a}$ value corresponds to a stronger base and a weaker conjugated acid. For the selected acids, SPARC $\mathrm{p}K_\mathrm{a}$ calculation enables to arbitrarily identify three situations: weak acids (**a**, **b**, **c**, **f**, **g** and **h**, having $\mathrm{p}K_\mathrm{a}>4$), strong acids (**e**, **i**, **j** and **k**, having $\mathrm{p}K_\mathrm{a}<3{,}4$) and an intermediate acid (**d**, having $3{,}4 \leq \mathrm{p}K_\mathrm{a} \leq 4$).

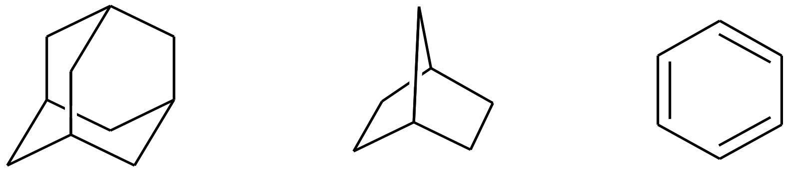

Adamantyl
(spherical)

Bornyl
(spherical)

Phenyl
(flat)

Scheme 3. Molecular shapes and related substituents used for the cocrystal design

The outcomes of LAG cocrystallization experiments are analysed primarily by X-ray powder diffraction (XRPD) (see Supplementary Material, S5-S48) and reflectance infrared spectroscopy (FTIR-ATR). These two solid-state methods allow the identification of the grinding products as the cocrystal, or the simply mixture of reactants. Thermal properties of the cocrystals are elucidated by differential scanning calorimetry (DSC) and, to discern the possibility of solvate formation, by thermogravimetric analysis (TG) (see Supplementary Material, S49-S76).

Following solvent-independent mechanochemical screening, cocrystallization from solution is conducted in order to obtain single crystal of selected cocrystals. For these systems, single crystal X-ray diffraction is utilised for structural analysis, to confirm the occurrence of the predicted supramolecular motif. Unfortunately, suitable single crystals for structure determination cannot be obtained in all cases, illustrating the general difficulties related to cocrystallization from solution.

Abbreviation	Compound	Scheme	pKa	S/L	M/L
1	2-adamantanone oxime	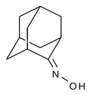	2,85	0,7006	0,7318
2	(1R)-camphor oxime	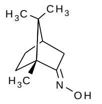	2,83	0,7578	0,7911
3	(E)-benzaldehyde oxime	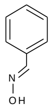	0,93	0,3494	0,6795
4	acetophenone oxime	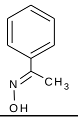	1,74	0,4126	0,6633
a	benzoic acid	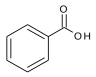	4,19	0,3624	0,7375
b	p-toluic benzoic acid	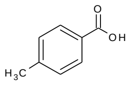	4,37	0,4008	0,6605
c	p-fluoro benzoic acid	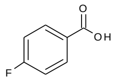	4,14	0,3492	0,7065
d	p-nitro benzoic acid	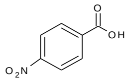	3,43	0,3305	0,6387
e	3,5-difluoro benzoic acid	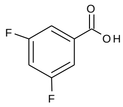	3,32	0,3686	0,8088
f	adamantane carboxylic acid	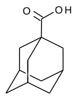	4,79	0,7206	0,7832
g	adamantine acetic acid	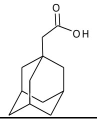	4,75	0,7055	0,7114
h	3-chloro adamantane carboxylic acid	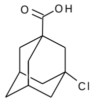	4,35	0,7829	0,8931
i	3,5-dinitro benzoic acid	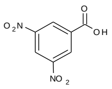	2,38	0,3733	0,9376
j	3,5-dinitro- p-toluic acid	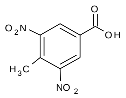	2,59	0,4485	0,9340
k	3,5-trifluoromethyl benzoic acid	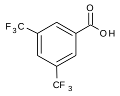	2,97	0,4866	0,8769

Table 1. The model compounds and their molecular descriptors

2.2. Results

Crystallographic data for cocrystals of spherical and flat oximes are given in Tables 7 and 8, respectively. Table 2 reports the data of the hydrogen bonds for the cocrystals.

The analysis of the cocrystal screen using XRPD shows that the spherical oxime **1** cocrystallizes with the spherical weak acids **f** and **h** and with the flat strong acids **e**, **i**, **j** and **k**. Suitable single crystals for X-ray analysis of cocrystals **1e**, **1f**, **1h** and **1i** are grown by recrystallization of the ground material from a 9:1 mixture of $MeNO_2$ and MeOH. In all cases the supramolecular motif sustaining the cocrystal is the OXCA $R_2^2(7)$ heterosynthon. Fragment of single crystal diffraction structures of the cocrystals between the spherical oxime **1** with the spherical acids **f** and **h** are reported in Figure 5.

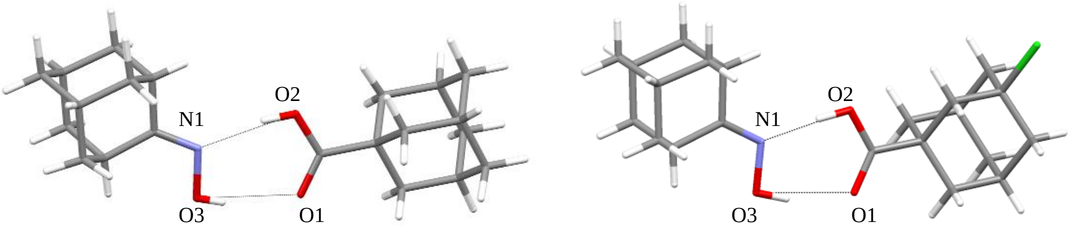

Figure 5. Cocrystal **1f** (left) and **1h** (right)

Flat weak acid do not cocrystallize with **1** but the increase of the acidity enables cocrystallization between mismatched shape molecules. Particularly, the formation of tetrameric units including two oxime-acid adducts is observed for the crystal structure of **1i** (Figure 6). Instead by using the strong flat acid **e**, introducing less distortions in the global shape, the tetramer does not form. In this case the main feature observed in the supramolecular assembly is the stacking involving the aryl ring of the acid molecule of a pair and the synthon of the neighbouring pair (Figure 7).

	d(O2··· N1) (Å)	O2-H2O··N1 (°)	d(O3··· O1) (Å)	O3-H3O···O1(°)	Symmetry
1e	2.632(2)	174	2.757(2)	163	
1f	2.724(2)	167	2.770(3)	165	
1h	2.668(2)	173	2.756(2)	164	
1i	2.578(2)	177	3.004(2)	150	
2f	2.721(3)	172	2.733(3)	155	
2i	2.584(4) 2.577(3)	166 171	2.903(3) 2.908(3)	155 155	
4d	2.697(2)	166	2.715(2)	169	-x, -y+1, -z+2
4e	2.698(2) 2.671(2)	176 175	2.755(2) 2.768(2)	161 163	
4i	2.629(1)	169	2.733(1)	167	

Table 2. Hydrogen bonds lengths and angles for the cocrystals. Two values are reported for the structure **2i**, including two independent units

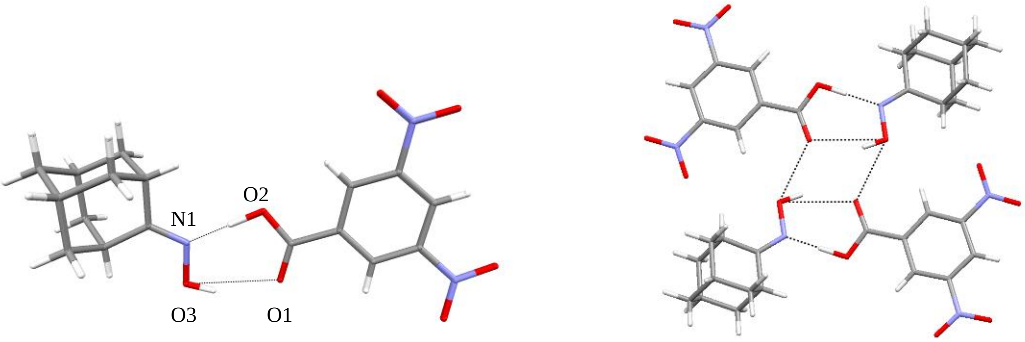

Figure 6. Cocrystal (left) and centrosimmetrical tetramer (right) formed by **1i**

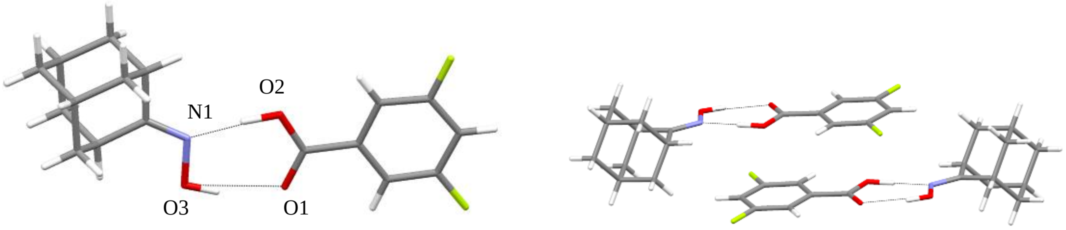

Figure 7. Cocrystal **1e** (left) and arrangement in its supramolecular structure (right)

Similar to **1**, the second explored spherical oxime **2** is able to cocrystallize with the weak spherical acids **f** and **h**, but also with **g**, and with the flat strong acids **e**, **i**, **j**, **k**. In all cases the supramolecular assemblies are sustained by the expected $R_2^2(7)$ OXCA heterosynthon. Single crystals of the products **2f** and **2i** are prepared by recrystallization of the LAG products from a 9:1 mixture of $MeNO_2$ and MeOH. The combination of the spherical shapes forming a discrete assembly in the cocrystal **2f** is shown in Figure 8. Similar to the cocrystal **1i**, the formation of a pseudo-centrosimmetrical tetrameric unit (due to the enantiopurity of the oxime) is observed in the cocrystal **2i** (Figure 9).

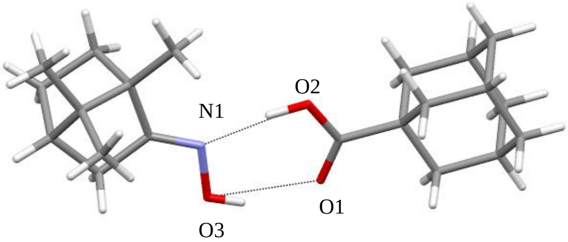

Figure 8. Cocrystal **2f**

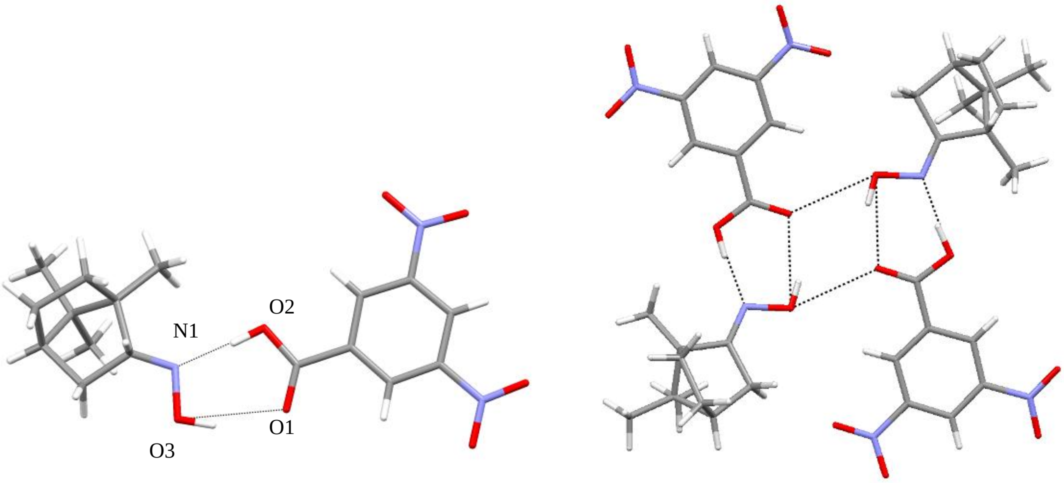

Figure 9. Cocrystal (left) and pseudocentrosimmetrical tetramer (right) formed by **2i**

The flat-shaped oxime **3** and **4** are not able to form cocrystal with the weak spherical acids **f**, **g** and **h**. However, they cocrystallize with all the flat strong acids **e**, **i**, **j** and **k**. Surprisingly, the oximes **3** and **4** also form cocrystals with the flat acid **d**, having an intermediate acidity. In all the cases the supramolecular motif sustaining the cocrystal is the $R_2^2(7)$ OXCA heterosynthon.

Due to the high solubility of the oxime **3**, single crystal growth for the cocrystals **3d**, **3e**, **3i**, **3j** and **3k** results very difficult. Indeed the precipitation of the acid alone is often observed and, consequently, only one cocrystal structure can be determined. Single crystals of **3i** grow from a solution of the grinding product in THF. The structure corresponds to a solvate phase in which the formation of tetrameric units is observed as well. Disordered molecules of solvent (THF) lie into the channels interposed between the tetramers (Figure 10).

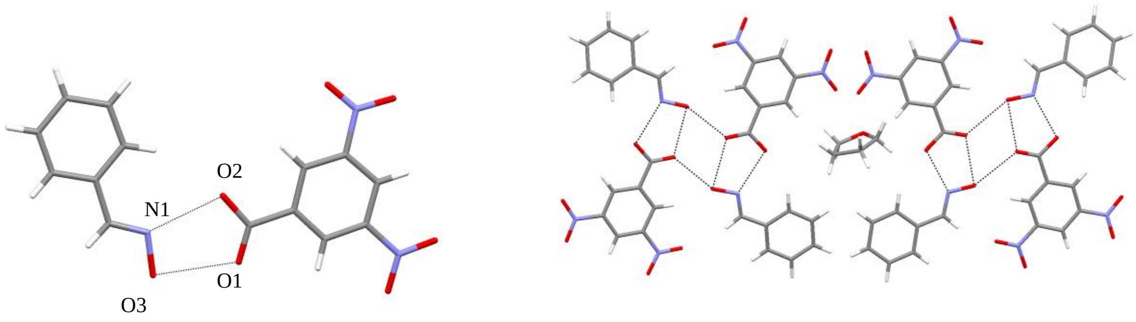

Figure 10. Cocrystal (left) and tetrameric unit (right) formed by **3i.** Disordered molecules of solvent are placed into the channels between the tetramers

In order to validate the results of this mechanochemical screening, the evaluation of the stability of the cocrystal **3i** become a necessity. Actually, the possibility to add the compound **3i** in the class of the cocrystal successfully formed needs the test of the events following the desolvation. With this aim, a small amount of the grinding product **3i**, after XRPD measurement, that reveals the formation of a new compound, is analysed by TG. Thermogravimetric analysis demonstrates a loss of weight upon heating, interpreted as the loss of solvent. The resulting solid is again analysed by XRPD, which suggests the existence of a non-solvate stable cocrystal. The same non-solvated form is obtained by EtOH grinding, while thermal analysis suggests that $MeNO_2$ grinding leads to a $MeNO_2$ solvate cocrystal. The described analysis uses a combination of LAG, XRPD and TG (Scheme 4) in order to assess the effect of solvent in the cocrystallization process.

Single crystals of **4d** and **4i** are grown from acetonitrile. Fragment of their crystal structures are shown in Figure 11 (left and middle, for **4d** and **4i**, respectively), and compared to the previously reported structure of the cocrystal **4a**[90] (right). Single crystals of **4e** are grown from a 9:1 mixture of $MeNO_2$ and MeOH. Also the structure of **4e**, similar to the supramolecular assembly observed in the cocrystal **2e,** shows the occurrence of a stack between the fluorinated aryl ring of the acid and the synthon of the neighbour dimer (Figure 12).

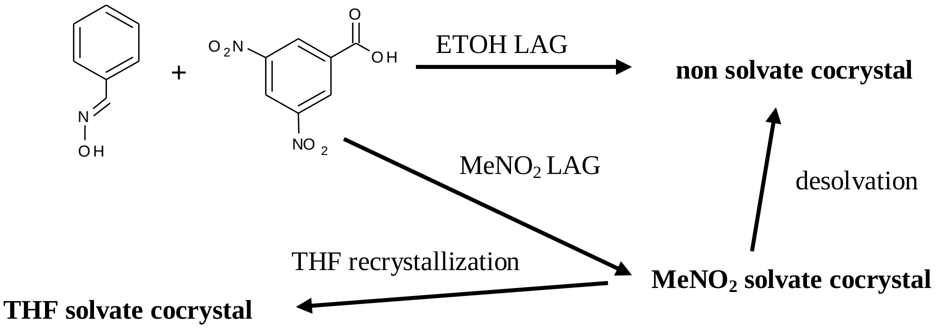

Scheme 4. Behaviour of the system **3i**

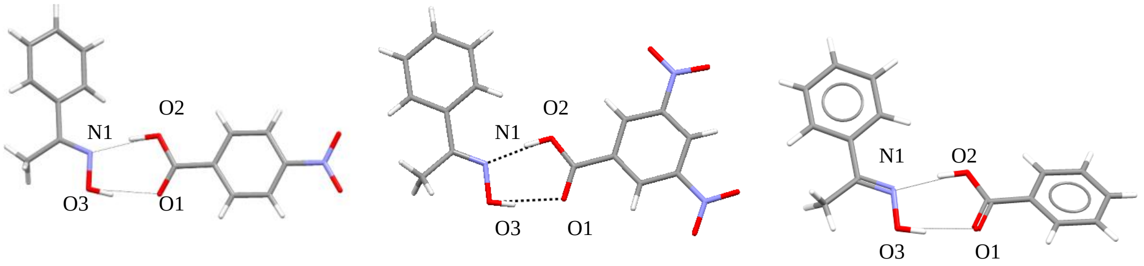

Figure 11. Cocrystal **4d** (left), **4i** (middle) and **4a** (right)

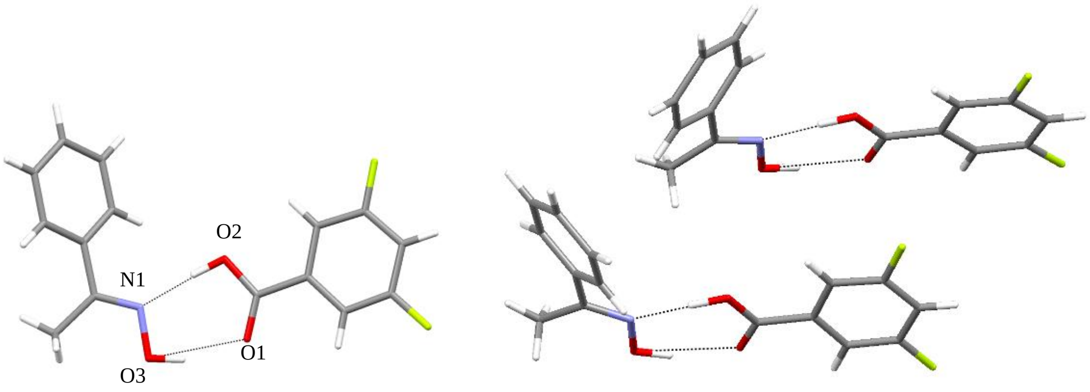

Figure 12. Cocrystal **4e** (left) and its supramolecular structure (right)

The ability of acetophenone oxime **4** to cocrystallize with benzoic acid **a** is probably due to the increase of the basicity with respect to (E)-benzaldehyde oxime **3**. This increase of basicity is achieved by the effect of the methyl group (Table 1).

The behaviour of oxime **4** is somewhat surprising. Compound **4** is known to have two polimorphs, a monoclinic and a triclinic one, both reported in Cambridge Structural Database (CSD).[83] By using XPRD, it is possible to establish that the commercially available compound is the triclinic polymorph, that crystallizes in the space group P-1. In the LAG experiments which do not result in cocrystals, XPRD shows the appearance of new peaks, which can be ascribed to the monoclinic polymorph of **4**, that crystallizes in the space group C2/c. Such interconversion between polymorphs by grinding is observed only if both the grinding liquid and a carboxylic acid are present.

2.3. Discussion

Application of LAG allows the successful screening of the supramolecular reactivity of the test oximes **1**, **2**, **3** and **4** towards the test acids **a**, **b**, **c**, **d**, **e**, **f**, **g**, **h** and **i**. XRPD represents the fastest and easiest means to identify the cocrystals and the mixtures. In the XRPD patterns of the cocrystals the presence of new peaks with respect to the XRPD patterns of the cocrystal formers clearly demonstrates that cocrystallization occurs and that there is a complete conversion of the starting materials. No particular features in solid-state FTIR spectra are associated with the cocrystallization. The characteristic peaks of the IR spectra (the $\nu_{O\text{-}H}$, the $\nu_{C=O}$ and $\nu_{C=N}$) do not show a change from the pure compounds to the mixtures or to the cocrystals.

The proper interpretation of the cocrystal screen requires careful verification that the new materials obtained by LAG are indeed cocrystals and not salts. The demonstration of the occurrence of the cocrystallization and not of salt formation is indicated by the structure of the carboxylic acid group, in the cocrystal structures obtained by X-ray crystal structure analysis. In all cases, the carboxylic acid group exhibits two considerably different C-O bonds. The formation of a cocrystal, rather than a salt, is also coinfirmed by position of the hydrogen atom in the synthon, observed from the Fourier difference map of electron density.

The proton transfer on the oxime takes place only using stronger acids compared with the test acids selected for the screen. Salt formation is observed upon the attempted cocrystallisation of (1R)-camphor oxime **2** with (1S)-(+)-camphor-10-sulfonic acid **m**. Single crystal X-ray structure determination reveals that the product **2m** is an hydrate salt (crystallographic data for **2m** are reported in Table 8). The XRPD pattern calculated from the obtained single crystal structure, shows that the hydrate salt is also formed upon grinding. Salt formation results from proton transfer from the acid to the nitrogen atom of the oxime (Figure 13). The water molecules act as nodes between three acid-base adducts. Each water molecule acts as hydrogen bonds donor towards two oxygen atoms of the sulfonic groups of two acid molecules and acts as hydrogen bonds acceptor, interacting with the protonated nitrogen atom of the oxime. Hydrogen bond distances and angles for the salt **2m** are reported in Table 3.

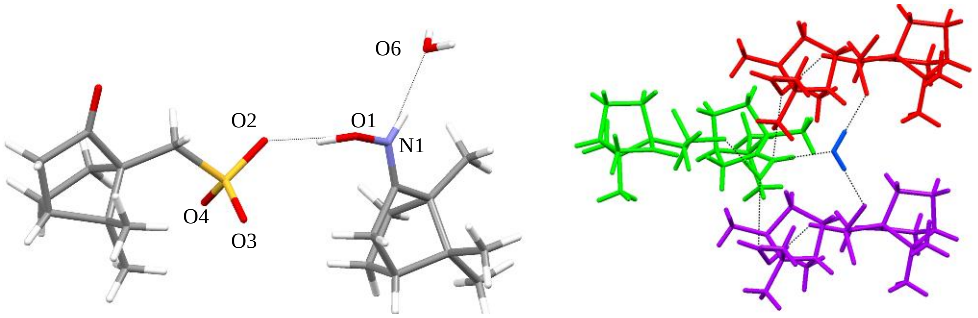

Figure 13. Hydrate salt camphor-10-sulphonic-acid - camphor oxime **2m**

d(O1··· O2) (Å)	O1-H1O··O2 (°)	d(O6··· O3) (Å)	O6-H6O···O3(°)	d(O6··· O4) (Å)	O6-H6O··O4 (°)	d(N1··· O6) (Å)	N1-H1N··O6 (°)
2.557(2)	169	2.773(2) (-x+1, y-1/2, -z+1)	171	2.810(2) (-x+1, y+1/2, -z+1)	172	2.663(2)	160

Table 3. Hydogen bond lengths and angles for the salt **2m**

Table 4 resumes the results of LAG screening. The shaded regions correspond to the cases of mismatched shape combinations and the symbols '+' and '-' indicate cocrystals and mixtures of the separate components, respectively. In the cases of mismatched molecular shapes, the cocrystallization is possible only in presence of a significant ΔpK_a between the potential cocrystal building blocks. This happens by using the strong acids **e**, **i**, **j**, **k**, that give cocrystal with all the oximes. In these cases the ΔpK_a is enough large to overshadow the differences in molecular shape. The cocrystallization is not expected, from consideration of molecular shapes, in two shaded areas. The first is the combination of spherical oximes **1**-**2** with flat acids **a**-**d**, not enough strong. The second corresponds to cocrystallization experiments involving flat oximes **3** and **4** with spherical acids **f**-**h**. These two regions correlate well with the expected mismatch of molecular shapes. The light regions correspond to combinations of similar shape. In these regions the role of the shape appears in the ability of the oxime **1** and **2** to cocrystallize with the acid **f**-**h** and of the oxime **3** and **4** to cocrystallize with the acid **d**. The ability of oxime **4**, but not of oxime **3**, to cocrystallize with acid **1** is correlated with the ΔpK_a of the pair, being **4** more basic with respect to **3**.

	1	**2**	**3**	**4**
a	-[a]	-	-	+[b]
b	-	-	-	-
c	-	-	-	-
d	-	-	+	+
e	+	+	+	+
f	+	+	-	-
g	-	+	-	-
h	+	+	-	-
i	+	+	+	+
j	+	+	+	+
k	+	+	+	+

Table 4. Results of cocrystal screening experiments; shaded regions correspond to the cases of shape mismatch; a) Symbols '+' and '-' indicate cocrystal formation, recognised through PXRD, IR and DSC analysis; b) the cocrystal was prepared and characterised previously[90]

2.4. Correlation between supramolecular descriptors

In order to introduce a semi-quantitavive approach to this study, the 44 oxime-carboxylic acid pairs are characterized by a set of numerical supramolecular descriptors. Three intermolecular features are considered and used to describe each pair:

(i) the similarity in shape between the potential cocrystal formers, quantified by shape molecular descriptors[73] (calculated by L. Fábián, CCDC);

(ii) the difference in pK_a between oxime and carboxylic acid (calculated using SPARK);[89]
(iii) the strength of the heterodimeric interaction, calculated using PIXEL[91-92] (calculated by A. J. Cruz Cabeza, CCDC).

The similarity in shape is quantified by the differences (Δ) between the molecular shape descriptors. Particularly Δ(S/L) is defined as:

$\Delta(S/L) = | S/L_{oxime} - S/L_{acid} |$

and ΔM/L is

$\Delta(M/L) = | M/L_{oxime} - M/L_{acid} |$.

The sum Δ(S/L) + Δ(M/L) is the parameter chosen to describe the total change in molecular shape.

The ΔpK_a of each pair simply corresponds to the difference:

$\Delta pK_a = pK_{a\ oxime} - pK_{a\ acid}$.

The ΔpK_a, calculated in this way, appears with negative values in every case. Positive values correspond only to the pairs **1i**, **ij**, **2i** and **2j**, due to the very low pK_a values of the strong acids. For the less basic oximes **3** and **4**, the ΔpK_a values of their pairs with the strong acids **i** and **j** are also negative. With this definition, the increase in ΔpK_a refers to the shift towards positive values. The increase in ΔpK_a derives from the use of a stronger acid or of a stronger base as well. In the same way, the shift towards more negative values indicates a low value in ΔpK_a, that derive from the decrease of the acidity, of the basicity or of both of them.

Aakeröy and co-workers reported the reliability of the ΔpK_a as qualitative parameters describing the strength of the interactions in the cocrystals.[81] Nevertheless, a quantification of this feature has never been reported. Actually a previous study in this field have been carried out by Hunter.[93] With the aim to rationalise in the best way the molecular recognition events *in solution*, Hunter proposes the idea that the solute-solute or solute-solvent interactions could be described and quantified by using the molecular electrostatic potential surfaces.

This study would introduce a quantification of the supramolecular interaction in a cocrystal. Particularly, it would to understand how much the ΔpK_a of the pairs oxime-carboxylic acid correlates with the effective sinthon strength. With this aim, PIXEL method[91-92] is used to evaluate intermolecular interactions between the pairs oxime-carboxylic acid. All geometric models are first individually optimised in vacuum with the package Gaussian. Valence electron densities of the optimised models are then calculated and the electron density is output in appropriate box sizes with steps of 0.08 Å. Afterwards, PIXEL densities are condensed into super pixels. It is assumed that all possible cocrystals that would form between oximes and carboxylic acids interact through the OXCA $R_2^2(7)$ heterosynthon

(Scheme 2). The heterosynthons of this kind are assumed to be planar. In order to optimise the geometry of the ideal dimers the simplest pair oxime (**3**) and carboxylic acid (**a**) is chosen. The planarity of the synthon is assumed and the intermolecular parameters d and Θ are defined (Figure 14): *d* is the distance between the two molecules and Θ is the angle of interaction. Single point energy calculations of the molecular pair **3a** at different *d* and Θ values are performed using the parameters described by A. Gavezzotti[94] and the program OPIX.[95]

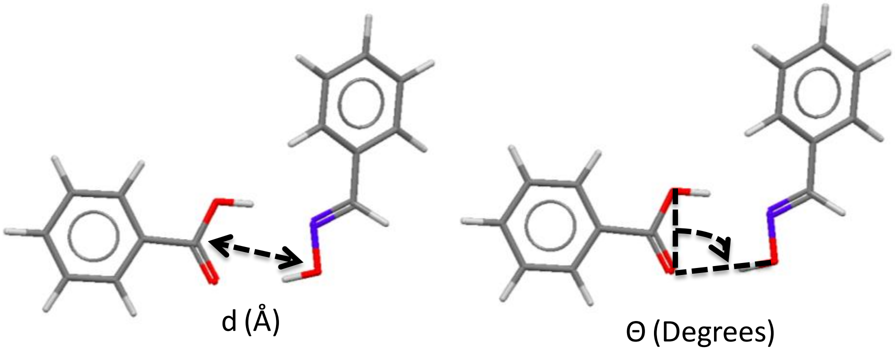

Figure 14. Definition of the intermolecular parameters that are optimised in the **3a** hypothetical dimer

The results on this geometry optimisation of the intermolecular parameters are plotted in Figure 15. From this exploration and analysis of the potential energy surface of the **3a** dimer interaction, the preferred dimer geometry is extracted (Figure 15, b). This is the geometry corresponding at the bottom of the well (Figure 15, a). The geometry of the ideal dimer is assumed to be the same for all the 44 heterodimers and possible cocrystals studied here and a single point PIXEL energy calculations on them is carried out. Total PIXEL energies reflect the strength of the heterosynthon interaction. A more negative energy reflects a more stable interaction.

The total PIXEL interaction energies calculated for the 44 pairs of oxime-carboxylic acids are given in Table 5, together with the Δ(S/L) + Δ(M/L) and the ΔpK_a values. By plotting the ΔpK_a *versus* the calculated PIXEL dimer interaction energies for each oxime family, very good correlations are observed (Figure 16). The R^2 values of 0.9012, 0.9099, 0.8917 and 0.8528 for the families of the oximes **1**, **2**, **3** and **4**, respectively, indicate that these two properties are strongly correlated. This observation is extremely encouraging as it indicates the differences in ΔpK_a values between two molecules is a reliable way of quantifying interaction energies in cocrystals.

For a further analysis of the data and of the correlations, the difference in shape between the heterodimer components *versus* PIXEL dimer interaction energy is plotted (Figure 17). In this plot filled symbols correspond to cocrystals experimentally obtained whereas empty symbols correspond to failed experiments. The plot is arbitrarily divided into four sections marked by the burgundy vertical and blue horizontal dotted lines. Below the blue horizontal dotted line (~ -56 kJ/mol), the dimer interaction is very strong so that cocrystal formation is going to be strongly driven by the heterosynthon energy. In fact, all cocrystals whose heterosynthons have interaction energies below the horizontal blue line are observed experimentally. For heterosynthon interaction energies above the blue dotted line, cocrystal formation derives from a balance between the heterosynthon interaction energies and the packing ability of the cocrystal components. Molecules having similar shape (low value for the descriptor Δ(S/L)+Δ(M/L)) are more likely to crystallise together than molecules having different shapes.[84] The burgundy vertical line divides the plot in a left area (from 0 to 0.3) where molecules have similar shape, and thus cocrystal formation is also driven by packing forces, and a right area where the shape difference between molecules starts being more important.

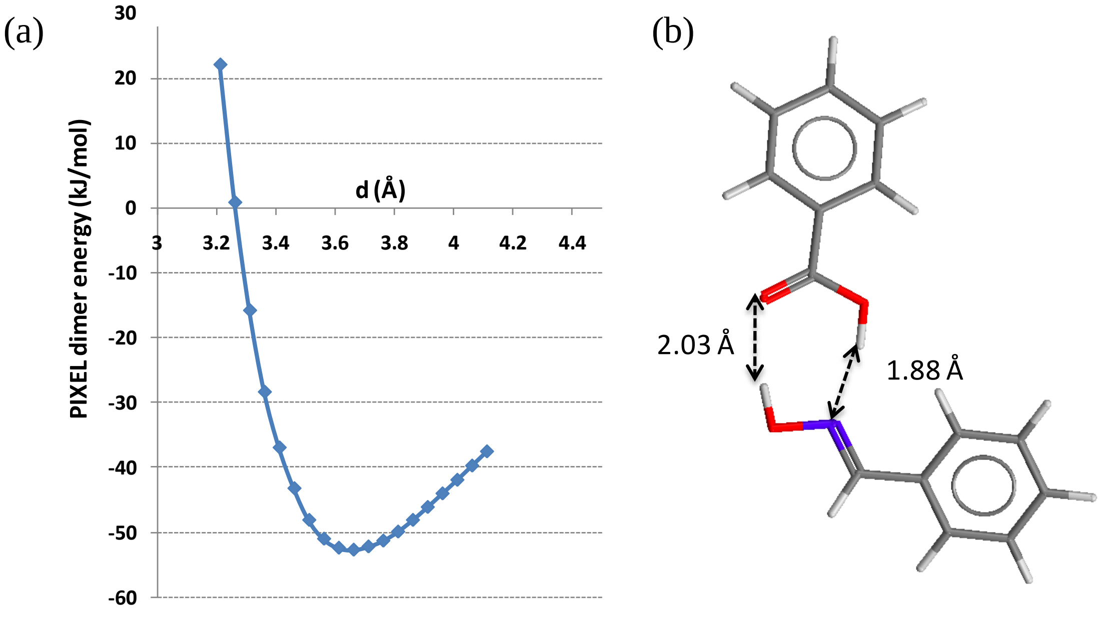

Figure 15. Potential energy curve of the interaction between oxime **3** and carboxylic acid **a** with respect to *d* (a) and geometry of the lowest energy dimer (b). From this exploration and analysis of the potential energy surface of the **3a** dimer interaction, the preferred dimer geometry has been extracted (b). It is the geometry corresponding at the bottom of the well (a).

	1			2			3			4			
	Δ(S/L) + Δ(M/L)	ΔpK_a	PIXEL E	Δ(S/L) + Δ(M/L)	ΔpK_a	PIXEL E	Δ(S/L) + Δ(M/L)	ΔpK_a	PIXEL E	Δ(S/L) + Δ(M/L)	ΔpK_a	PIXEL E	
	0.3439	-1.34	-53.1	0.4490	-1.36	-52.7	0.0710	-3.26	-51.6	0.1244	-2.45	-46.9	**a**
	0.3711	-1.52	-51.9	0.4876	-1.54	-51.5	0.0704	-3.44	-50.6	0.0146	-2.63	-46.2	**b**
	0.3767	-1.29	-52.9	0.4932	-1.31	-52.5	0.0272	-3.21	-51.3	0.1066	-2.40	-46.9	**c**
	0.4632	-0.58	-55.8	0.5797	-0.60	-55.3	0.0597	-2.50	-53.6	0.1067	-1.69	-49.0	**d**
	0.4090	-0.47	-54.0	0.4069	-0.49	-53.7	0.1485	-2.39	-52.2	0.1895	-1.58	-47.4	**e**
f	0.0714	-1.94	-52.6	0.0451	-1.96	-52.2	0.4749	-3.86	-51.6	0.4279	-3.05	-47.2	
g	0.0253	-1.90	-51.7	0.1320	-1.92	-51.3	0.3880	-3.82	-50.5	0.3410	-3.01	-45.9	
h	0.2436	-1.50	-52.4	0.1271	-1.52	-51.9	0.6471	-3.42	-51.0	0.6001	-2.61	-46.8	
	0.5331	0.47	-56.9	0.5310	0.45	-56.5	0.2820	-1.45	-54.5	0.3136	-0.64	-51.0	**i**
	0.4543	0.26	-56.8	0.4522	0.24	-56.2	0.3536	-1.66	-54.5	0.3066	-0.85	-51.4	**j**
	0.3591	-0.12	-55.4	0.3570	-0.14	-55.0	0.3346	-2.04	-53.1	0.2876	-1.23	-50.5	**k**

Table 5. Differences between shape descriptors and pK_a of the target molecules involved in this study. Molecules with the same shadow colour have similar shapes. The grey highlighted regions indicate experimental observation of cocrystal formation

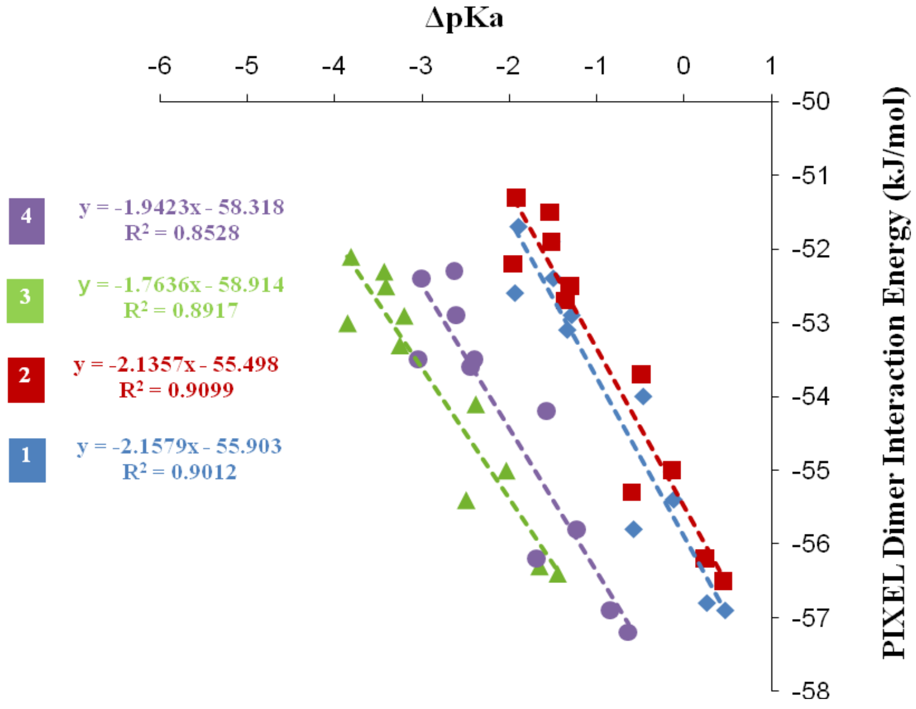

Figure 16. Linear correlations between ΔpK_a and PIXEL Dimer Interaction Energy for the heterodimers formed between the oximes **1** (blue rhombus), **2** (red squares), **3** (green triangles) and **4** (purple circles) and the carboxylic acids (**a-k**)

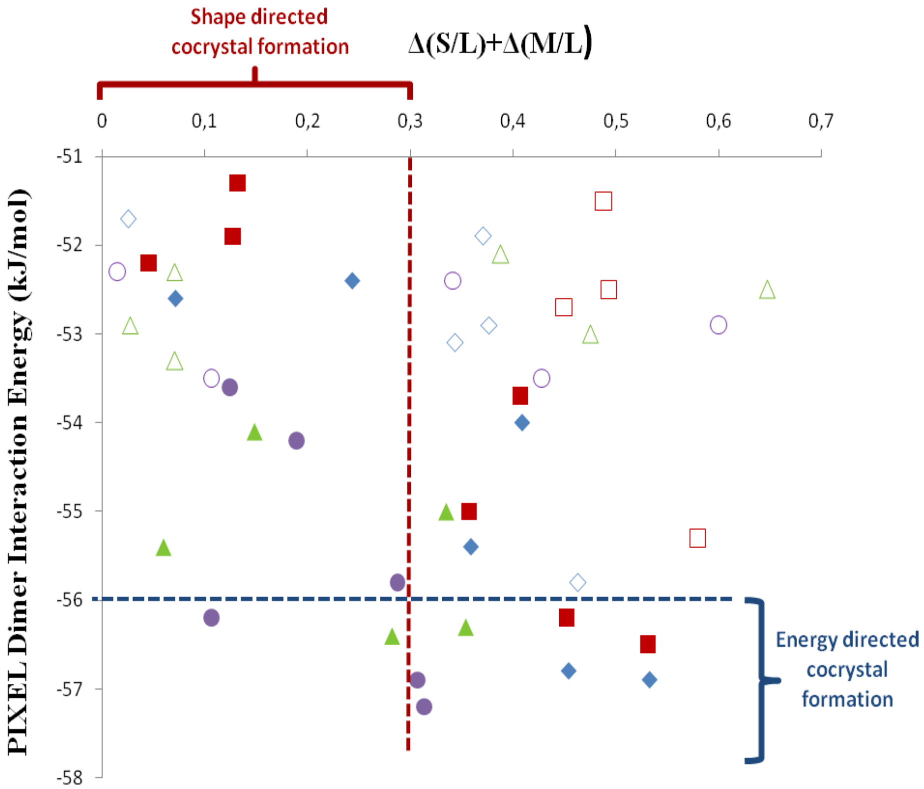

Figure 17. Correlation between PIXEL Dimer Interaction Energy and molecular shape similarity descriptors Δ(S/L)+Δ(M/L) for the pairs formed by the oximes **1** (blue rhombus), **2** (red squares), **3** (green triangles) and **4** (purple circles) and the carboxylic acids (**a-k**). Filled symbols correspond to cocrystals experimentally obtained whereas empty symbols correspond to failed experiments

In summary, the plot of the difference in shape between the heterodimer components against the PIXEL dimer interaction energy shows the following different areas:

i) Left-lower corner: both shape differences and synthon interactions between the two components are favourable for cocrystal formation. Pairs of molecules in this region are most likely to form a cocrystal.

ii) Right-lower corner: Although the shape differences between the molecules are considerable, the strength of the interactions overcomes the packing unfavourable situations and all the potential cocrystals are experimentally observed also in this region. This explains the success of the cocrystal design based on the synthon strength strategy.

iii) Left-upper corner: there might be a balance between shape differences and strength of the interactions for the cocrystals to form. It is possible to observe how less stable heterosynthon interactions still result in the observation of cocrystals because their components have similar shape. 10 out of 16 pairs in this area of the plot correspond to cocrystals observed experimentally.

iv) Right-upper corner: in this area, nor the synthon interactions neither the shape factors would drive cocrystal formation. So pairs in this area are very unlikely to give cocrystals. In fact experimentally we observe that only 5 out of the 19 pairs in this area do actually cocrystallize.

Finally, the interplay between ΔpK_a and molecular shape descriptors becomes apparent when plotting the total change in molecular shape $\Delta(S/L)+\Delta(M/L)$ *versus* ΔpK_a (Figure 18). The plot clearly reveals two important results: (1) The increase of the ΔpK_a value enables cocrystallisation of pairs of molecules with increasingly different shapes and (2) it is possible to define a minimum ΔpK_a value under which cocrystal formation involving oximes and carboxylic acids is no longer likely (-2.50 in the present case). All the pairs corresponding to a combination $\Delta pK_a/\Delta(S/L)+\Delta(M/L)$ falling in the area below the filled symbols, should lead to cocrystals. Salt formation is the limit-case of the energy-directed cocristallization.

In summary, the results reported in Table 4 indicate that cocrystallisation via the OXCA synthon is influenced by similarity in molecular shape. The differences between the shape descriptors S/L and M/L and the pK_a are the parameters most closely related to cocrystallisation success. In particular, cocrystallisation fails in almost all cases where the differences in shape are large, in agreement with the expectations from a statistical overview of the CSD.[84] The exception is made by the pairs of the oximes with the strong acids **e**, **i**, **j** and **k** that readily forms cocrystals with all four oximes, due to the increase of the $\Delta p\mathrm{K}_a$ values and supporting the notion that an higher $\Delta p\mathrm{K}_a$ values are beneficial in overcoming crystal packing effects in cocrystallization. Similarly, the inability of the acid **b** and **c** to form cocrystals with any of the molecules **1-4** and the inability of acid **a** with **3**, can be related to the low ΔpK_a values. It is important to point out that each change in shape inevitably introduces a change in type of intermolecular interactions and it is not yet clear to which extent are the results of this screening related to differences in shape, as opposed to differences in specific weak intermolecular interactions, such as C-H...π bonds, C-H...O bonds or π...π stacking forces. Even if this study on the solid-state effects involved in cocrystallization provided by molecular descriptors is greatly oversimplified, it offers an attractive opportunity to begin quantifying the effects of shape mismatch and provide a benchmark for cocrystal design.

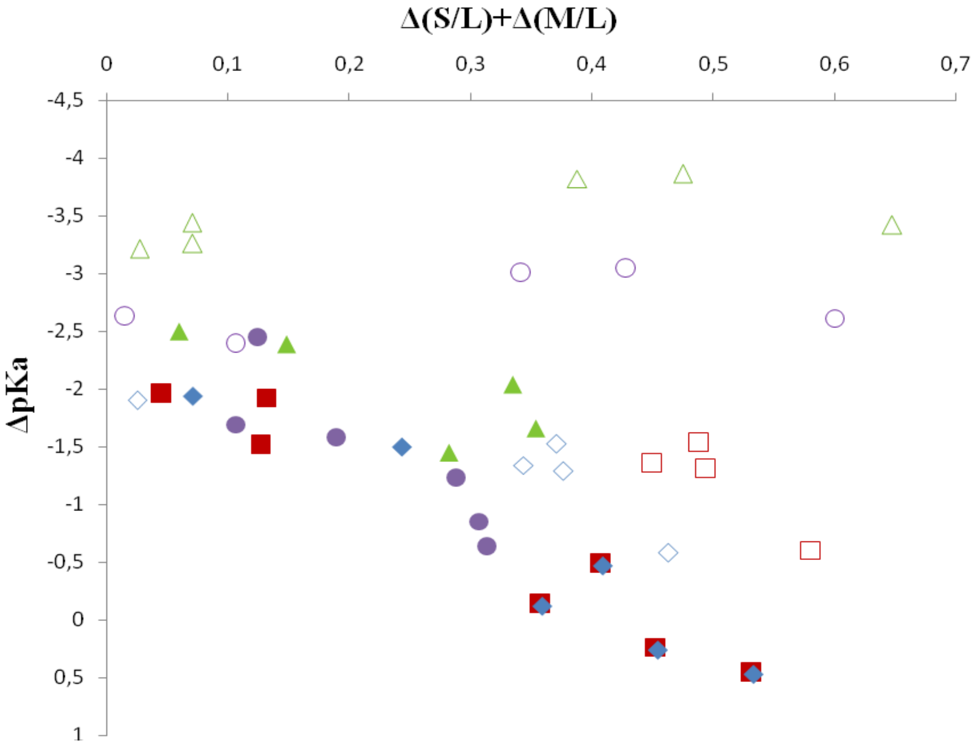

Figure 18. Correlation between ΔpKa and molecular shape similarity descriptors Δ(S/L)+Δ(M/L) for the pairs formed by the oximes **1** (blue rhombus), **2** (red squares), **3** (green triangles) and **4** (purple circles) and the carboxylic acids (**a-k**). Filled and empty symbols represent successful and failed cocrystallisation attempts, respectively

3. Design of a solid-state [2+2] photodimerization using the supramolecular steering group approach

The combination of noncovalent and covalent bonds is of great importance in regulating biologically important processes.[96] The combination of noncovalent and covalent chemistry plays a key role in the fields of catalysis,[97] molecular machines[98] and medicine.[99]

From a crystal engineering perspective, the key point is the application of the principles of the supramolecular chemistry for promoting the formation of specific arrangements suitable for solid-state reactivity.[100] The ability to promote the formation of covalent bonds by solid-state solvent-free reactions[101-102] is a very attractive field, particularly in the area of the environmentally sustainable processes.[103] In addition, the solid-state synthetic procedures provide additional stereochemical and topochemical means of control.[104] This additional abilities of control directly derive from crystal packing effects that enable a peculiar selectivity towards the solid-state reaction outcoming.

This part of the work specifically addresses to the design of reactive multicomponent solids, by using the cocrystal as means to direct the formation of reactive supramolecular structures. This field covers two different areas. On one side, it is possible to approach to the topological control through the use of a templating supramolecular system.[101] On the other side, it is possible to carry out a solid-state synthesis simply using the supramolecular steering group approach, i.e. the solid-state assembly directs the topology of the reactive moieties and enables the solid-state reactivity. One of the most useful application of this method is based on the use of supramolecular systems containing olefinic groups. If these groups are close enough to each other, they are able to react giving the formation of cyclobutane products through [2+2] photodimerization reactions.

The first X-ray diffraction study on the topochemical [2+2] photodimerization dates back from 1970.[105] Schmidt's studies suggest that cinnamic acid photochemically reacts producing a cyclobutane (Scheme 5). The key regulating this reaction is the presence of a supramolecular arrangement of the molecules in the crystal able to give a topological control on the cyclization, because the olefinic double bonds are locked in appropriate distance and adequate orientation by crystal packing. Schmidt postulated the geometric parameters required for the reaction in the solid-states reaction. This reaction is enabled if in the crystal the double bonds are arranged approximately parallel an at a separation less than 4.2 Å. Schmidt also observed that the photodimerization takes place only in the case of the *trans*-isomer of the cinnamic acid.[106] The demonstration of the occurrence of the solid-state photodimerization in olefins was afterwards performed by Thomas and co-workers through single crystal X-ray diffraction studies.[107]

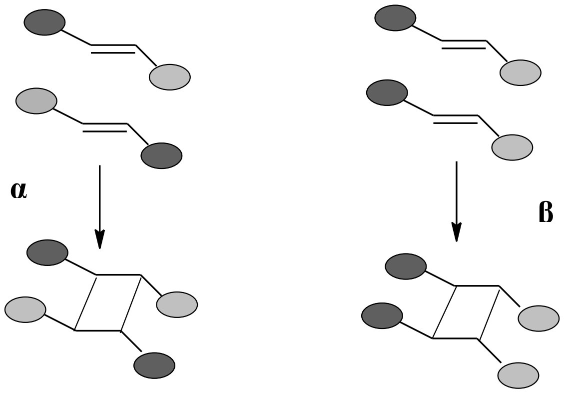

Scheme 5. Representation of the cinnamic acid photodimerization in the solid-state studied by Schmidt. The reaction could lead to the *trans* (α) or to the *cis* isomer (β), depending on the starting mutual orientation of the molecules

This part of the work describes a strategy to achieve topological control over the solid-state photodimerization process of the 2,3,4,5,6-pentafluorocinnamic acid (**pentaF-CA**), by using cocrystals in a supramolecular steering group approach.

3.1. Experiment design

In this study, the design of a solid-state [2+2] photodimerization reaction is based on the structure of the supramolecular assembly observed in the cocrystals of 3,5-difluorobenzoic acid (**e**) with 2-adamantanone oxime (**1**) and acetophenone oxime (**4**) (Figure 7 and 12). The cocrystals **1e** and **4e** are sustained by the OXCA $R_2^2(7)$ hydrogen-bonded ring motif involving the carboxylic acid and the oxime functionality. The resulting supramolecular ring shows a stacking interaction with the fluorinated phenyl ring. The stacking distance is consistent with the threshold distance for the photochemical [2+2] cycloaddition.[106] Nevertheless acid **e** does not have any suitable group for a solid-state reaction.

With the aim of engineering a solid-state reaction, the formation of cocrystals between 2-adamantanone oxime (**1**), (1R)-camphor oxime (**2**), (E)-benzaldehyde oxime (**3**) and acetophenone oxime (**4**) with 2,3,4,5,6-pentafluorocinnamic acid (**pentaF-CA**, Scheme 6) is detected. This acid has three features that make it a good candidate in the purpose of the project: i) the carboxylic acid group, that enables the formation of the $R_2^2(7)$ hydrogen-bonded synthon with the oximes; ii) an electron-deficient aryl ring, due to the presence of the fluorine atoms (this is connected with the possibility to observe the stacking between the fluorinated aryl ring and the supramolecular ring formed by the synthon); iii) the olefinic moiety that could undergo a topochemical [2+2] cycloaddition.

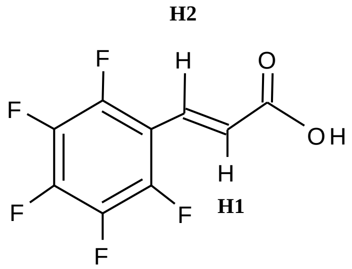

Scheme 6. 2,3,4,5,6-pentafluorocinnamic acid (**pentaF-CA**)

The experiment design (Scheme 7) includes four steeps: i) the cocrystal screening carried out by LAG, in order to establish whether the **pentaF-CA** forms cocrystal with the oximes **1**, **2**, **3** and **4**; ii) single crystal growth and X-ray diffraction structure determination, in order to evaluate if the supramolecular assembly makes the cocrystals good candidates for a solid-state photoreaction; iii) UV-irradiation of the cocrystals in order to achieve the [2+2] cycloaddition; iv) the identification of the outcome of the UV-irradiation, by the use of solution NMR and X-ray diffraction structure determination.

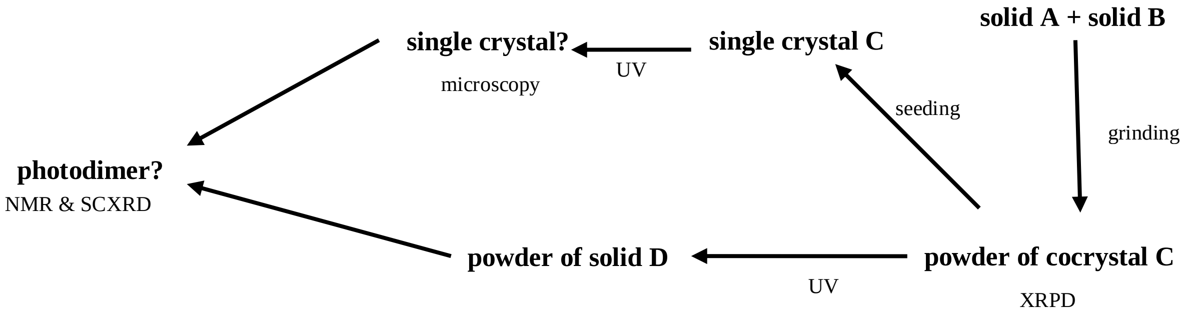

Scheme 7. Design of the [2+2] photodimerization experiment of the (**pentaF-CA**) by the supramolecular steering groups approach

3.2. Results and discussion

The determination of the crystal structure of the pure acid is carried out, using single crystal growth from a 9:1 mixture of $MeNO_2$ and MeOH. In the crystal, two **PentaF-CA** molecules interact through typical $R_2^2(8)$ hydrogen-bonded synthon. The main feature of the supramolecular assembly, in order to design a solid-state reaction experiment, is the parallel arrangement between neighbouring synthons leading the olefinc moiety at a distance of 4.4 Å. This distance is actually the upper limit to observe a solid-state dimerization reaction (Figure 18, crystallographic data and hydrogen bond distances and angles are reported in Table 9 and 6, respectively).

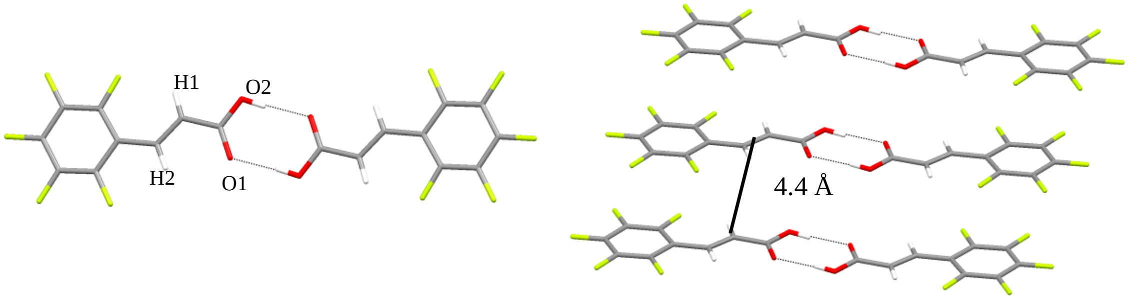

Figure 18. Supramolecular structure of the 2,3,4,5,6-pentafluorocinnamic acid (**pentaF-CA**)

The results of LAG screening experiments show that all the oximes **1**, **2**, **3** and **4** form cocrystals with **pentaF-CA**. All cocrystals are analysed by DSC, which reveals melting points that differ from those of pure components. Unfortunately, single crystal structure could be obtained only for **2pentaF-CA** (Figure 19, crystallographic data and hydrogen bond distances and angles are reported in Tables 9 and 6, respectively), revealing the predicted OXCA $R_2^2(7)$ hydrogen-bonded ring motifs. This supramolecular architecture suggests a potential application for intermolecular topochemical [2+2] photodimerization in the solid-state. Specifically, the stacking between the perfluorinated phenyl ring and the hydrogen-bonded motif of the OXCA steers the olefin moieties into a parallel arrangement at a distance of 3.7Å, which conforms to the criteria for a solid-state photoreaction.

In order to investigate the possibility of a topochemical [2+2] photodimerization in the solid-state, both the pure **pentaF-CA** and the cocrystal **2pentaF-CA** obtained by grinding are exposed under the UV lamp (λ_{UV} = 366 nm). After 10 days of exposure the potential photoproducts are analysed by solution ^{1}H NMR (d6-DMSO). The ^{1}H NMR spectra of the potential photoproduct of pure **pentaF-CA** is simulated by using the software ACD ChemSketch (vers. 2.51, 1997). Particularly, the chemical shift of the protons H1 and H2 in the cyclobutane photodimer is calculated. In fact, the chemical shift of these two protons enables to discriminate between the starting material (in which only the olefin moiety is present) and the product (in which a cyclobutane is present). The simulated spectra of the cyclobutane, for the hydrogen H1 and H2 shows two multiplets at ~5.10 and ~4.40 ppm (the multiplets derive from a coupling with the fluorines). In the experimental ^{1}H NMR spectra of the pure **pentaF-CA** (Figure 20) the two doublets of the starting material at ~7.5 and ~6.6 ppm are present together with the two multiplets at ~4.6 and ~4.1 ppm, that correspond to the product of the photoreaction. The conversion, calcultated from the signal integration, is approximately 18%. Instead, the closer distance between the olefinic moieties found in the cocrystal **2pentaF-CA** is connected with an increase of the reactivity. In the experimental ^{1}H NMR spectra of the cocrystal **2pentaF-CA** (Figure 21) the characteristic signals (pseudo-triplets) of the corresponding cyclobutane at ~4.7 and ~4.1 ppm are present, according with the simulation, together with the doublets at ~7.4 and ~6.6 ppm, belonging to the starting material. In the cocrystal, the decrease of the distance between the olefinic moieties, lead to the increase of the solid-state reactivity and the calcultated conversion is approximately 48%.

	d(O1··· O2) (Å)	O1-H1O··O2 (°)	d(O2··· N1) (Å)	O1-H1O··O2 (°)	d(O3··· O1) (Å)	O1-H1O··O2 (°)
PentaC-FA	2.661(2)	175				
2PentaC-FA			2.654(6)	275	2.747(5)	153

Table 6. Hydogen bond lengths and angles for the acid **PentaF-CA** and for the cocrystal **2PentaF-CA**

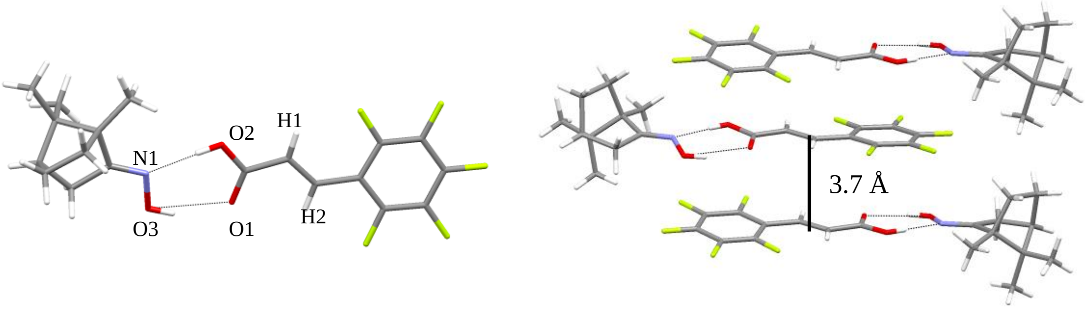

Figure 19. (1R)-camphor oxime – pentaF-CA cocrystal (**2PentaF-CA**). The distance of about 3.7Å is conformed to the criteria for a solid-state photoreaction

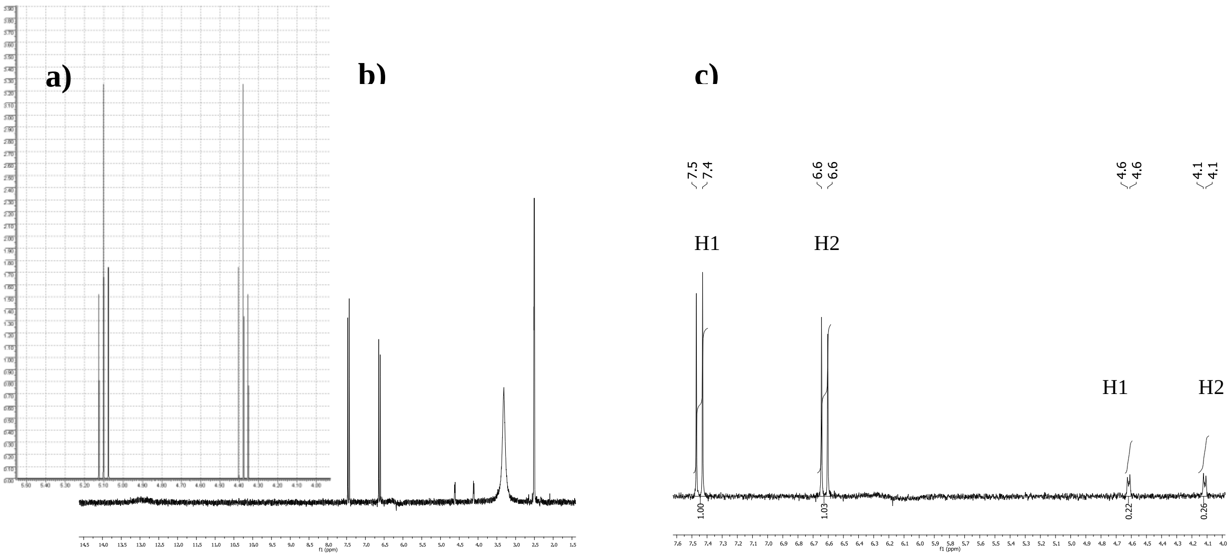

Figure 20. ^{1}H NMR spectra of the pure **PentaF-CA** after 10 days of UV irradiation at 366 nm. The doublets of the starting oleifinic moiety hydrogens are deshielded respect the resulting cyclobutane product ones; the simulated spectra of the cyclobutane a) is shown together with the full spectra b) and the enlargement of the interest region c)

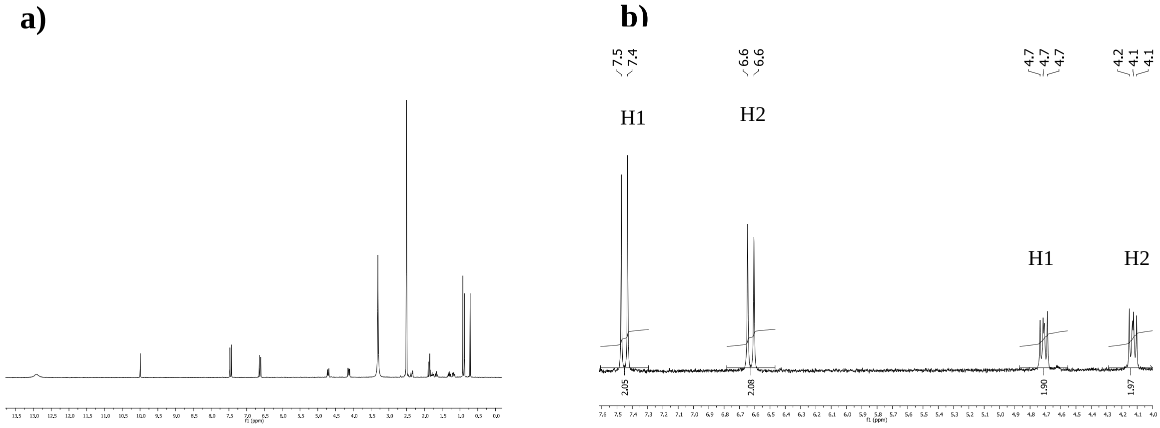

Figure 21. ^{1}H NMR spectra of the purecocrystal **2PentaF-CA** after 10 days of UV irradiation at 366 nm.. The doublets of the starting oleifinic moiety hydrogens are deshielded respect the resulting cyclobutane product ones; the full spectra a) and the enlargement of the interest region b) are shown

4. Experimental

LAG experiments. All materials are commercially available from Sigma-Aldrich Chemical Co. and are used without purification. In a typical grinding experiment, the oxime (100 mg) is placed in a stainless steel grinding jar (10 mL), along with an equimolar amount of the acid. 30 μl of nitromethane or ethanol are added to the grinding mixture before the experiment ($0.12 \leq \eta \leq 0.2$). Two stainless steel balls of 7 mm radius are used for grinding, that is performed for 20 min on a Retsch MM200 grinder mill, operating at a frequency of 30 Hz.

Spectroscopic analysis. Proton ^{1}H NMR spectra are recorded at 25°C on a Bruker 300 FT spectrometer by using $SiMe_4$ as internal standard and d6-DMSO as solvent, while FTIR-ATR spectra are obtained with a Nicolet 5PCFT-IR spectrophotometer in the 4000-400 cm^{-1} range, using the ATR mode.

Thermal analysis. DSC and TG measurements are performed on a Mettler Toledo DSC822 calorimeter and a TGA/SDTA851e thermobalance, respectively. For DSC analysis the sample (10 mg) is placed in pierced-lid aluminium pans, while TG analysis is conducted in open aluminium pans. The DSC and TG traces are obtained on heating the samples under nitrogen at 10°C/min.

X-ray diffraction. Powder XRD (XPRD) spectra are collected using CuKα radiation with a X-Pert MPD powder diffractometer. Single crystal X-ray diffraction data are collected by using the MoKα radiation (λ=0.71073 Å) on a Nonius Kappa CCD diffractometer. All data are collected at room temperature (293 K). Lorentz, polarization, and absorption corrections are applied.[108] Structures are solved by direct methods using SIR97[109] and refined by full-matrix least-squares on all F^2 using SHELXL97[110] implemented in the WingX package.[111] All non-hydrogen atoms are treated in the refinement using the anisotropic model. Hydrogen atoms connected to C atoms are placed in idealised positions, calculated using the relevant stereochemical rules for the parent carbon atom, and refined isotropically. Hydrogen atoms connected to N and O atoms are located from the Fourier electron density map. Hydrogen bonds are analyzed with SHELXL97[110] and PARST97.[112] The Cambridge Crystallographic Data Centre packages[113-114] is used for the analysis of the crystal packing.

Table 7. Crystal data for the cocrystals involving the spherical oximes **1** and **2**

Compound	**1e**	**1f**	**1h**	**1i**	**2f**	**2i**
Formula	$C_{17}H_{19}F_2O_3$	$C_{21}H_{31}NO_3$	$C_{21}H_{30}ClNO_3$	$C_{17}H_{19}N_3O_7$	$C_{21}H_{34}NO_3$	$C_{16}H_{22}N_3O_7$
Molecular weight	323.33	345.47	379.91	377.35	348.51	368.37
Crystal system	monoclinic	monoclinic	monoclinic	triclinic	monoclinic	monoclinic
Space group	$P\ 2_1/n$	$P\ 2_1/c$	$P\ 2_1/c$	P -1	$P\ 2_1$	$P\ 2_1$
Z	4	4	4	2	4	4
a/Ǻ	6.6947(1)	12.8441(4)	14.1976(3)	6.765(1)	12.2182(2)	7.1327(1)
b/Ǻ	25.4533(5)	11.5058(5)	11.7366(3)	10.264(2)	6.8565(1)	21.3536(3)
c/Ǻ	9.2729(2)	13.1813(5)	12.5519(3)	12.704(3)	23.5738(1)	12.3898(2)
α/°				99.13(3)		
β/°	92.148(1)	110.390(3)	111.625(1)	102.49(3)	91.480(1)	104.005(1)
γ/°				90.83(3)		
$V/Ǻ^3$	1579.0(5)	1825.9(1)	1944.33(8)	849.3(3)	1974.21(5)	1830.98(5)
ρ /Mg m^{-3}	1.360	1.257	1.298	1.476	1.223	1.336
θ range for data collection/°	3.69 - 27.54	3.60 - 27.50	3.54 - 30.00	3.60 - 33.18	3.54 – 31.52	3.52 - 32.05
Unique reflections	3609	4155	5595	6320	4764	6478
Observed reflections [I>2σ(I)]	2624	3352	4133	3621	4463	5024
Data/ restraints/ parameters	3609/0/210	4155/0/347	5595/0/241	6320/0/320	4764/1/457	6478/1/505
Goodness-of-fit on F^2	1.013	1.077	1.050	1.021	1.018	1.022
R_1 [I>2σ(I)]	0.0613	0.0761	0.0537	0.0539	0.0488	0.0465
wR_2 [I>2σ(I)]	0.1593	0.2060	0.1084	0.1174	0.1233	0.1207
R_1 (all data)	0.0847	0.0935	0.0810	0.1158	0.0780	0.0690
wR_2 (all data)	0.1776	0.2211	0.1238	0.1430	0.1378	0.1354

Table 8. Crystal data for the cocrystals involving the flat oximes **3** and **4** and the salt **2m**

Compound	**3i**	**4d**	**4e**	**4i**	**3l**	**2m**
Formula	$C_{16}H_{15}N_3O_{75}$	$C_{15}H_{14}N_2O_5$	$C_{15}H_{13}F_2NO_3$	$C_{15}H_{13}N_3O_7$	$C_{14}H_{10}F_3NO_3$	$C_{20}H_{35}NO_6S$
Molecular weight	369.31	302.28	293.26	347.28	297.23	417.55
Crystal system	monoclinic	triclinic	triclinic	monoclinic	Triclinic	monoclinic
Space group	P 2_1/c	P -1	P -1	P 2_1/n	P -1	P 2_1
Z	8	2	4	4	2	2
a/Å	14.4212(1)	7.3570(5)	10.4643(2)	9.9519(2)	7.0153(2)	9.5854(3)
b/Å	28.9374(5)	7.5810(5)	10.7477(2)	15.1087(3)	7.0550(2)	7.1317(2)
c/Å	7.5636(3)	13.2596(10)	13.4623(3)	10.7007(2)	14.3106(5)	16.0570(6)
α/°		74.177(4)	93.687(1)		92.171(1)	
β/°	93.515(1)	84.334(3)	106.125(1)	98.096(1)	96.799(1)	90.332(1)
γ/°		85.036(3)	105.301(1)		110.434(1)	
V/Å^3	3150.4(1)	706.66(9)	1387.39(5)	1592.92(5)	656.65(3)	1097.64(6)
ρ /Mg m^{-3}	1.481	1.421	1.404	1.448	1.503	1.263
θ range for data collection/°	3.43 - 31.51	2.79 - 25.04	3.72 - 33.18	3.85 - 32.05	3.52 - 33.17	3.78 - 30.00
Unique reflections	6150	2423	10370	5508	4882	6068
Observed reflections [I>2σ(I)]	3823	1857	6132	4439	3100	5202
Data/ restraints/ parameters	6150/ 37/ 478	2423 / 0 / 201	10370/0/397	5508/0/233	4882 / 0 / 192	6068/1/258
Goodness-of-fit on F^2	0.823	1.094	1.011	1.033	1.037	1.090
R_1 [I>2σ(I)]	0.1296	0.0498	0.0511	0.0445	0.0604	0.0575
wR_2 [I>2σ(I)]	0.2438	0.1078	0.1180	0.1187	0.1398	0.1213
R_1 (all data)	0.1665	0.0728	0.1026	0.0571	0.1051	0.0738
wR_2 (all data)	0..3128	0.1211	0.1435	0.1296	0.1653	0.1324

Table 9. Crystal data for the acid **PentaF-CA** and for the cocrystal **2PentaF-CA**

Compound	**PentaCA-F**	**2PentaCA-F**
Formula	$C_9H_3F_5O_2$	$C_{19}H_{20}F_5NO_3$
Molecular weight	238.11	405.36
Crystal system	triclinic	orthorhombic
Space group	P-1	P 2_1 2_1 2_1
Z	2	4
a/Å	4.4050(2)	7.1936(3)
b/Å	7.5650(9)	9.0917(4)
c/Å	13.4195(6)	29.9341(15)
α/°	92.855(2)	
β/°	95.314(2)	
γ/°	103.985(2)	
V/Å^3	430.86(6)	1957.7 (2)
ρ /Mg m^{-3}	1.835	1.375
θ range for data collection/°	3.98 - 22.54	3.53 - 22.46
Unique reflections	1112	1483
Observed reflections [I>2σ(I)]	890	1008
Data/ restraints/ parameters	1112 / 0 / 147	1483 / 0 / 256
Goodness-of-fit on F^2	1.103	1.070
R_1 [I>2σ(I)]	0.0381	0.0500
wR_2 [I>2σ(I)]	0.0928	0.0965
R_1 (all data)	0.0517	0.0893
wR_2 (all data)	0.1036	0.1120

5. Conclusions

This part of the work analyses and correlates the main factors involved in the cocrystallization control. According with previous works, the reported results support the fact that ΔpK_a is a useful benchmark in order to predict cocrystal formation.[81] The role of the ΔpK_a in intermolecular recognition is validated and demonstrated by showing that it is strongly correlated with the heterodimer synthon energy obtained by PIXEL calculations.[91-92] Nevertheless it is point out that shape similarity is also involved in the heteromolecular recognition process, due to crystal packing efficiency. This study reveals that, in absence of very large ΔpK_a differences, molecules that likely cocrystallize have similar shape, according with the statistical overview on the cocrystals of the CSD.[84] Shape similarity is correlated with synthon strength and with ΔpK_a, evaluating the entity of the control of the shape in the cocrystallization process. These results provide further means and additional points of discussion in order to understand the factors regulating cocrystallization and introduce a qualitative a partially quantitative approach for cocrystal design.

Finally, it is demonstrated how the cocrystals aid the design of topological photodimerization reactions. These results encourage the utility of applying concepts of supramolecular chemistry and self-assembly to address to covalent synthesis.

References

1. J. D. Dunitz and A. Gavezzotti, Molecular Recognition in Organic Crystals: Directed Intermolecular Bonds or Nonlocalized Bonding?, *Angew. Chem. Int. Ed.* 2005, 44, 1766-1787
2. M. Nomura and V. A. Erdmann, Reconstitution of 50S Ribosomal Subunits from Dissociated Molecular Components, *Nature*, 1970, 228, 744-748
3. M. Nomura, Reflections on the Days of Ribosome Reconstitution Research, *Trends Biochem. Sci.*, 1997, 22, 275-279
4. C. B. Aakeröy, J. Desper, J. F. Urbina, Supramolecular Reagents: Versatile Tools for Non-Covalent Synthesis, *Chem. Commun.*, 2005, 2820-2822
5. C. B. Aakeröy and D. J. Salmon, Building Co-Crystals with Molecular Sense and Supramolecular Sensibility, *CrystEngComm*, 2005, 7, 439-448
6. T. R. Shattock, P. Vishweshwar, Z.Wang, M. J. Zaworotko, 18-Fold Interpenetration and Concomitant Polymorphism in the 2:3 Co-Crystal of Trimesic Acid and 1,2-Bis(4-pyridyl)ethane, *Cryst. Growth. Des.*, 2005, 5, 2046-2049
7. D. Braga and F. Grepioni, Making Crystals from Crystals: a Green Route to Crystal Engineering and Polymorphism, *Chem. Commun.*, 2005, 3635-3645

8. A. V. Trask, J. van de Streek, S. W. D. Motherwell and W. Jones, Achieving Polymorphic and Stoichiometric Diversity in Cocrystal Formation: Importance of Solid-State Grinding, Powder X-ray Structure Determination, and Seeding, *Cryst. Growth. Des*., 2005, 5, 2233-2241
9. A. V. Trask, S. W. D. Motherwell and W. Jones, Solvent-Drop Grinding: Green Polymorph Control of Cocrystallisation, *Chem. Commun*., 2004, 890-891
10. G. R.Desiraju, *Acc. Chem. Res.*, Hydrogen bridges in crystal engineering. Interactions without borders2002, 35, 565-573
11. A. I. Kitaigorodskii, *Organic Chemical Crystallography*, Consultants Bureau, New York, 1961
12. A. I. Kitaigorodskii, *Molecular Crystals and Molecules*, Academic Press, New York, 1973
13. J. D. Dunitz in *Perspective in Supramolecular Chemistry: The Crystal as a Supramolecular entity*, Ed. G. R. Desiraju, Wiley, Amsterdam, 1995
14. M. C. Etter and D. A. Adsmond, The Use of Cocrystallization as a Method of Studying Hydrogen Bond Preferences of 2-Aminopyrimidine, *J. Chem. Soc., Chem. Commun.*, 1990, 589-591
15. M. C. Etter and P W. Baures, Triphenylphosphine Ooxide as a Crystallization Aid, *J. Chem. Soc.*, 1988, 110, 639-640
16. M. C. Etter, Encoding and Decoding Hydrogen-Bond Patterns of Organic Compounds, *Acc. Chem. Res.*, 1990, 23, 120-126
17. M. C. Etter, Hydrogen Bonds as Design Elements in Organic Chemistry, *J. Phys. Chem,* 1991, 95, 4601-4610
18. C. B. Aakeröy in *Making Crystal by Design*, Ed. D. Braga and F. Grepioni, Wiley-VCH, 2006, 209-240
19. P. H. Stahl and C. G. Wermuth, Eds. *Handbook of Pharmaceutical Salts: Properties, Selection and Use*, Wiley-VCH/VHCA: Weinheim/Zurich, 2002.
20. J. F Remenar, S. L. Morissette, M. L.Peterson, B. Moulton, J. M. MacPhee, H. R. Guzman, Ö. Almarsson, Crystal Engineering of Novel Cocrystals of a Triazole Drug with 1,4-Dicarboxylic Acids, *J. Am. Chem. Soc*, 2003, 125, 8456-8457
21. S. L. Childs, L. J. Chyall, J. T. Dunlap, V. N. Smolenskaya, B. C. Stahly, G. P. Stahly, Crystal Engineering Approach to Forming Cocrystals of Amine Hydrochloride with Organic Acids. Molecular Complexes of Fluoxetine Hydrochloride with Benzoic, Succinic, and Fumaric Acids, *J. Am. Chem. Soc.*, 2004, 126, 13335-13342
22. A. V. Trask, W. D. S. Motherwell and W. Jones,. Pharmaceutical Cocrystallization: Engineering a Remedy for Caffeine Hydration, *Cryst. Growth Des*,. 2005, 5, 1013-1021
23. A. V. Trask, W. D. S. Motherwell and W. Jones, Physical Stability Enhancement of Theophylline via Cocrystallization, *Int. J. Pharm.*, 2006, 320, 114-123
24. T. Friščić. L. Fábián, J. C. Burley, D. G. Reid, M. J. Duer and W. Jones, Exploring the Relationship Between Co-Crystal Stability and Symmetry: is Wallach's Rule Applicable to Multi-Component Solids? *Chem. Commun.*, 2008, 1644-1646
25. R. D. B. Walsh, M. W. Bradner, S. Fleischman, L. A. Morales, B. Moulton, N. Rodríguez-Hornedo, M. J. Zaworotko, Crystal Engineering of the Composition of Pharmaceutical Phases, *Chem. Commun.*, 2003, 186-187

26. S. G. Fleischman, S. S. Kuduva, J. A. McMahon, B. Moulton, R. D. B. Walsh, N.Rodríguez-Hornedo, M. J. Zaworotko, Crystal Engineering of the Composition of Pharmaceutical Phases: Multiple-Component Crystalline Solids Involving Carbamazepine, *Cryst. Growth. Des,*. 2003, 3, 909–919

27. S. Karki, T. Friščić. L. Fábián, P. R. Laity, G. M. Day and W. Jones, Improving Mechanical Properties of Crystalline Solids by Cocrystal Formation: New Compressible Forms of Paracetamol, *Advanced Materials*, 2009, 21, 3905-3909

28. D. Braga, S. L. Giaffreda, F. Grepioni, A. Pettersen, L. Maini, M. Curzi, M. Polito, Mechanochemical Preparation of Molecular and Supramolecular Organometallic Materials and Ccoordination Networks, *Dalton Trans*., 2006, 1249-263

29. T. Friščić and W. Jones, Recent Advances in Understanding the Mechanism of Cocrystal Formation via Grinding, *Crystal Growth & Design*, 9, 2009, 1621-1637

30. D. Braga and F. Grepioni, Organometallic Polymorphism and Phase Transitions, *Chem. Soc. Rev.*, 2000, 29, 229-238

31. D. Braga and F. Grepioni, Reactions Between or Within Molecular Crystals, *Angew. Chem., Int. Ed.*, 2004, 43, 4002-4011

32. D. Braga, D. D'Addario, L. Giaffreda Stefano, L. Maini, M. Polito and F. Grepioni, Intra-Solid and Inter-Solid Reactions of Molecular Crystals: a Green Route to Crystal Engineering, Top. *Curr. Chem.*, 2005, 254, 71-94.

33. D. Braga, M. Curzi, E. Dichiarante, S. L. Giaffreda, F. Grepioni, L. Maini, G. Palladino, A. Pettersen, M. Polito, *Making Crystals from Crystals: a Solid-State Route to the Engineering of Crystalline Materials, Polymorphs, Solvates and Co-Crystals; Cosiderations on the Future of Crystal Engineering*, in Engineering of Crystalline Materials Properties, Springer, 2008, 131-156

34. G. Kaupp in *Compr. Supramol. Chem.*, 1996, 8, 381-423

35. V. V. Boldyrev and K. Tkacova, *J. Mater. Synth. Process.*, 2000, 8, 121–132

36. D. Braga, S. L. Giaffreda, F.Grepioni, M. Polito, Mechanochemical and Solution Preparation of the Coordination Polymers Ag[N(CH2CH2)3N]2[CH3COO].5H2O and Zn[N(CH2CH2)3N]Cl2, *CrystEngComm*, 2004, 6, 458-462

37. D. Braga, S. L. Giaffreda, M. Curzi, L. Maini, M. Polito, F. Grepioni, Mechanical Mixing of Molecular Crystals, *J. Therm. Anal. Cal.* 2007, 90, 115-123

38. V. V. Boldyrev, Mechanochemical Modification and Synthesis of Drugs, *J. Mat. Sci*., 2004, 39, 5117–5120

39. J. J Gilman, Mechanochemistry, *Science*, 1996, 274, 65

40. M. D. Hollingsworth, M. E. Brown, B. D. Santarserio, J. C. Huffmann, C. R. Goss, Template-Directed Synthesis of 1:1 Layered Complexes of .alpha.,.omega.-Dinitriles and Urea: Packing Efficiency versus Specific Functional Group Interactions, *Chem. Mater.* 1996, 6(8), 1227-1244

41. D. Cinčić, T. Friščić and W. Jones,. Isostructural Materials Achieved by Using Structurally Equivalent Donors and Acceptors in Halogen-Bonded Cocrystals, *Chem. Eur. J*., 2008, 14, 747-753

42. D. Braga and F. Grepioni in *Crystal Design*, ed. G. R. Desiraju, John Wiley & Sons, Weinheim, 2003

43. S. Karki, L. Fábián, T. Friščić and W. Jones, Powder X-ray diffraction as an emerging method to structurally characterise organic solids, *Org. Lett.* 2007, 9, 3133-3136

44. A. J. Cruz-Cabeza, G. Day, W. D. S. Motherwell and W.Jones, Prediction and Observation of Isostructurality Induced by Solvent Incorporation in Multicomponent Crystals, *J. Am. Chem. Soc.*, 2006, 128, 14466-14467

45. D. Braga, F. Grepioni, M. Polito, M. R.; Chierotti, S. Ellena, R. Gobetto, A Solid-Gas Route to Polymorph Conversion in Crystalline [FeII(5-C5H4COOH)2]. A Diffraction and Solid-State NMR Study, *Organometallics*, 2006, 25, 4627-4633

46. Z. J. Li, Y. Abramov, J. Bordner, J. Leonard, A. Medek, A. V. Trask, Solid-State Acid−Base Interactions in Complexes of Heterocyclic Bases with Dicarboxylic Acids: Crystallography, Hydrogen Bond Analysis, and ^{15}N NMR Spectroscopy, *J. Am. Chem. Soc.*, 2006, 128, 8199-8210

47. R. Gobetto, C. Nervi, E. Valfre, M. R. Chierotti, D. Braga, L. Maini, F. Grepioni, R. K.Harris, P. Y. Ghi, 1H MAS, 15N CPMAS, and DFT Investigation of Hydrogen-Bonded Supramolecular Adducts between the Diamine 1,4-Diazabicyclo-[2.2.2]octane and Dicarboxylic Acids of Variable Chain Length, *Chem. Mater.*, 2005, 17, 1457-1466

48. G. Day, J. A Zeitler,. W. Jones, T. Rades, P. F. Taday, Understanding the Influence of Polymorphism on Phonon Spectra: Lattice Dynamics Calculations and Terahertz Spectroscopy of Carbamazepine, *J. Phys. Chem. B.*, 2006, 110, 447-456

49. D. Braga, S. L. Giaffreda, F. Grepioni, L. Maini, M. Polito, Design, Synthesis, Characterization and Utilization of Hydrogen Bonded Networks Based on Functionalized Organometallic Sandwich Compounds and the Occurrence of Crystal Polymorphism, *Coord. Chem. Re*v., 2006, 250, 1267-1285

50. S.Watano, T. Okamoto, M. Tsuhari, I. Koizumi, Y. Osako, Development of a Novel Vertical High Shear Kneader and Its Performance in Wet Kneading of Pharmaceutical Powders, *Chem.Pharm. Bull.*, 2002, 50, 341-345

51. S. Watano, J. Furukawa, K. Miyanami, Y. Osako, Quantitative Evaluation of Kneading and Extrusion Processes by Pressure Transmission Characteristics of Wet Kneaded Masses, *Adv. Powder Technol.*, 2001, 12, 427-441

52. A. V. Trask and W. Jones, Crystal Engineering of Organic Cocrystals by the Solid-State Grinding Approach, *Top. Curr. Chem.*, 2005, 254, 41-70

53. A. R. Ling and J. L Baker, XCVI.—Halogen derivatives of quinone. Part III. Derivatives of quinhydrone, *J. Chem. Soc.*, 1893, 63, 1314-1327

54. A. O. Patil, D. Y Curtin, I. C. Paul, Solid-State Formation of Quinhydrones From their Components. Use of Solid-Solid Reactions to Prepare Compounds not Accessible from Solution, *J. Am. Chem. Soc.*, 1984, 106(2), 348-353

55. M. C. Etter, Z. Urbaňczyk-Lipkowska, M. Zia-Ebrahimi, T. W Panunto, Hydrogen Bond-Directed Cocrystallization and Molecular Recognition Properties of Diarylureas, *J. Am. Chem. Soc.*, 1990, 112(23), 8415-8426

56. R. P. Rastogi, P. S. Bassi, L. S. Chadha, Mechanism of the Reaction between Hydrocarbons and Picric Acid in the Solid State, *J. Phys. Chem.*, 1963, 67, 2569-2573

57. R. Kuroda, K.Higashiguchi, S. Hasebe, Y. Imai, Crystal to Crystal Transformation in the Solid State, *CrystEngComm*, 2004, 6, 463-468

58. K. Chadwick, R. J. Davey, W. Cross, How Does Grinding Produce Co-Crystals? Insights from the Case of Benzophenone and Diphenylamine, *CrystEngComm*, 2007, 9, 732-734

59. K. L. Nguyen, T. Friščić, G. M. Day, L. F. Gladden, W. Jones, Terahertz Time-Domain Spectroscopy and the Quantitative Monitoring of Mechanochemical Cocrystal Formation, *Nat. Mater.*, 2007, 6, 206-209

60. E. Lu, N. Rodrıíguez-Hornedo, R. Suryanarayanan, A Rapid Thermal Method for Cocrystal Screening, *CrystEngComm*, 2008, 10, 665-668

61. K. Seefeldt, J. Miller, F.Alvarez-Núñez, N. Rodríguez-Hornedo, Crystallization Pathways and Kinetics of Carbamazepine-Nicotinamide Cocrystals from the Amorphous State by *in situ* Thermomicroscopy, Spectroscopy, and Calorimetry studies, *J. Pharm. Sci.*, 2007, 96, 1147-1158

62. A. Jayasankar, A. Somwangthanaroj, Z. J. Shao, N. Rodríguez-Hornedo, Cocrystal Formation during Cogrinding and Storage is Mediated by Amorphous Phase, *Pharm. Res.*, 2006, 23, 2381-2392

63. N.Shan, F.Toda and W. Jones, Mechanochemistry and Co-Crystal Formation: Effect of Solvent on Reaction Kinetics, *Chem. Commun.*, 2002, 2372-2373

64. T. Friščić, A. V. Trask, W.Jones, W. D. S. Motherwell, Screening for Inclusion Compounds and Systematic Construction of Three-Component Solids by Liquid-Assisted Grinding, A*ngew. Chem., Int. Ed.*, 2006, 45, 7546-7550

65. A. V. Trask, J. van de Streek, W. D. S. Motherwell and W. Jones, Achieving Polymorphic and Stoichiometric Diversity in Cocrystal Formation: Importance of Solid-State Grinding, Powder X-ray Structure Determination, and Seeding, *Cryst. Growth Des.*, 2005, 5, 2233-2241

66. A. V. Trask, D. A. Haynes, W. D. S. Motherwell and W. Jones, Screening for Crystalline Salts via Mechanochemistry,.*Chem. Commun.*, 2006, 51–53

67. A. V Trask, N.Shan, W. D. S. Motherwell, W. Jones, S. Feng, R. B. H. Tan, K. J. Carpenter, Selective Polymorph Transformation via Solvent-Drop Grinding, *Chem. Commun*., 2005, 880–882

68. D. Braga, S. L. Giaffreda, K. Rubini, F. Grepioni, M. R. Chierotti, R. Gobetto, Making Crystals from Crystals: Three Solvent-Free Routes to the Hydrogen Bonded Co-Crystal Between 1,1'-di-pyridyl-ferrocene and anthranilic acid, *CrystEngComm*, 2007, 9, 39-45

69. S. Karki, T. Friščić, W. D. S. Motherwell and W. Jones, Screening for Pharmaceutical Cocrystal Hydrates via Neat and Liquid-Assisted Grinding, *Mol. Pharm*,. 2007, 4, 347-354

70. A. V. Trask, W. D. S. Motherwell and W. Jones, Solvent-Drop Grinding: Green Polymorph Control of Cocrystallisation, *Chem. Commun.*, 2004, 890-891

71. D. Braga, S. L Giaffreda, F. Grepioni, M. R. Chierotti, R. Gobetto, G. Palladino, M. Polito, Solvent effect in a "solvent free" reaction, *CrystEngComm*, 2007, 9, 879-881

72. R. A. Chiarella, R. J. Davey, M. L. Peterson, Making Co-Crystals — The Utility of Ternary Phase Diagrams, *Cryst. Growth Des.*, 2007, 7(7), 1223-1226

73. E. Pidcock, W. D. S. Motherwell, A Novel Description of the Crystal Packing of Molecules, *Crystal Growth & Design*, 2004, 4, 611-620

74. C. B. Aakeröy, J. Desper, B. A. Helfrich, P. Metrangolo, T. Pilati, G. Resnati, A. Stevenazzi, Combining Halogen Bonds and Hydrogen Bonds in the Modular Assembly of Heteromeric Infinite 1-D Chains, *Chem. Commun.*, 2007, 4236-4238

75. K. Bouchmella, B. Boury, S. G. Dutremez, A. van der Lee, Molecular Assemblies from Imidazolyl-Containing Haloalkenes and Haloalkynes: Competition between Halogen and Hydrogen Bonding, *Chem. Eur. J.*, 2007, 13, 6130-6138

76. S. L. Morissette, Ö. Almarsson, M. L. Peterson, J. F. Remenar, M. J.Read, A. V. Lemmo, S. Ellis, M. J. Cima, C. R.Gardner, High-throughput Crystallizations: Polimorphs, Salts, Co-crystals and Solvates of Pharmaceutical Solids, *Adv. Drug Delivery Rev.*, 2004, 56, 275-300

77. G. R. Desiraju, Supramolecular Synthons in Crystal Engineering-A New Organic Synthesis, *Angew. Chem., Int. Ed. Engl.*, 1995, 34, 2311-2327

78. C. B. Aakeröy, I. Hussain, S. Forbesa, J. Desper, Exploring the Hydrogen-Bond Preference of N–H Moieties in Co-Crystals Assembled *via* O–H(acid)···N(py) Intermolecular Interactions, *CrystEngComm*, 2007, 9, 46-54

79. C. B. Aakeröy, J. Desper, B. M. T. Scott, Balancing Supramolecular Reagents for Reliable Formation of Co-Crystals, *Chem. Commun.*, 2006, 1445-1447

80. D. Cinčić, T. Friščić and W. Jones, A Stepwise Mechanism for the Mechanochemical Synthesis of Halogen-Bonded Cocrystal Architectures, *J. Am. Chem. Soc.*, 2008, 130 (24), 7524-7525

81. C. B. Aakeröy, D. J. Salmon, M. M. Smith, J. Desper, Cyanophenyloximes: Reliable and Versatile Tools for Hydrogen-Bond Directed Supramolecular Synthesis of Co-Crystals, *Crystal Growth & Design*, 6(4), 2006, 1033-1042

82. M. A. Siegler, Y. Fu, G. H. Simpson, D. P. King, S. Parkin, C. P. Brock, An unexpected co-crystal with a variable degree of order: 1:1 *rac*-1,2-cyclohexanediol/triphenylphosphine oxide, *Acta Crystallogr.*, Sect. B, 2007, 3, 912-925

83. F. H. Allen, The Cambridge Structural Database: a Quarter of a Million Crystal Sstructures and Rising, *Acta Crystallogr*., Sect. B, 2002, *58*, 380-388

84. L. Fábián, Cambridge Structural Database Analysis of Molecular Complementarity in Cocrystals, *Cryst. Growth Des.* 2009, 9, 1436-1443

85. T. Friščić, S. L. Childs, S. A. A. Rizvi and W. Jones, The Role of Solvent in Mechanochemical and Sonochemical Cocrystal Formation: a Solubility-Based Approach for Predicting Cocrystallisation Outcome, *CrystEngComm,* 2009, 11, 418-426

86. M. Allesø, J. Rantanena, J. Aaltonen, C. Cornett, F. van den Berg, Solvent Subset Selection for Polymorph Screening, *J. Chemometrics*, 2008: 22: 621–631

87. M. Allesø, F. van den Berg, C. Cornett, F. S. Jørgensen, B. H. Sørensen, H. Lopez de Diego, L. Hovgaard, J. Aaltonen, J. Rantaneni, Solvent Diversity in Polymorphs Screening, *J. Pharmaceutical Sciences*, 2008, 97(6)

88.B. Sarma, N. K. Nath, B. R. Bhogala, A. Nangia, Synthon Competition and Cooperation in Molecular Salts of Hydroxybenzoic Acids and Aminopyridines, *Cryst. Growth Des.* 2009, 9(3), 1546-1557

89. S. Hilal, S. W. Karickhoff and L. A. Carreira, A Rigorous Test for SPARC's Chemical Reactivity Models: Estimation of More than 4300 Ionization pK(a)s, *Quant. Struc. Act. Rel.*, 1995, 14, 348-355

90. J.K.Maurin, M.Winnicka-Maurin, I.C.Paul, D.Y.Curtin, Hydrogen-Bonded Complex Formation of Oximes with Carboxylic Acids and with Amides. (*E*)-Acetophenone Oxime-Benzoic Acid (1/1) and (*E*)-Benzaldehyde Oxime-Benzamide (1/1), *Acta Crystallogr.,* Sect.B:Struct.Sci. 1993, 49, 90-96

91. A. Gavezzotti, *CrystEngComm,* Towards a Realistic mModel for the Quantitative Evaluation of Intermolecular Potentials and for the Rationalization of Organic Crystal Structures. Part I. Philosophy, 2003, 5, 429-438

92. A. Gavezzotti, Towards a Realistic Model for the Quantitative Evaluation of Intermolecular Potentials and for the Rationalization of Organic Crystal Structures. Part II. Crystal Energy Landscapes, *CrystEngComm,* 2003, 5, 439-446

93. C. A. Hunter, Quantifying Intermolecular Interactions: Guidelines for the Molecular Recognition Toolbox, *Angew. Chem. Int. Ed.*, 2004, 43, 5310-5324

94. A. Gavezzotti, Calculation of Lattice Energies of Organic Crystals: the PIXEL Integration Method in Comparison with More Traditional Methods, *Z. Kristallogr.*, 2005, 220, 499-510

95. A. Gavezzotti, *Molecular Aggregation – Structure Analysis and Molecular Simulation of Crystals and Liquids* (Oxford University Press, USA, 2007)

96. L. Stryer, *Biochemistry*; W.H. Freeman and Co., New York, 1988

97. J. Rebek, Simultaneous Encapsulation: Molecules Held at Close Range, *Angew. Chem., Int. Ed.*, 2005, 44, 2068-2078

98. T.-A. V. Khuong, J. E. Nunez, C. E. Godinez, M. A. Garcia-Garibay, Crystalline Molecular Machines: A Quest Toward Solid-State Dynamics and Function, *Acc. Chem. Res.*, 2006, 39, 413-422

99. M. W. Peczuh, A. D. Hamilton, Peptide and Protein Recognition by Designed Molecules, *Chem. Rev.* 2000, 100, 2479-2494

100. M. W. Hosseni, *Chem. Commun.*, Self-Assembly and Generation of Complexity, 2005, 5825-5829

101. L. R MacGillivray, G. S Papaefstathiou, T Friščić, T. D Hamilton, D.-K Bučar, Q. Chu, D. B. Varshney, I. G. Georgiev, Supramolecular Control of Reactivity in the Solid State: From Templates to Ladderanes to Metal−Organic Frameworks, *Acc. Chem. Res.* 2008, 41, 280–291

102. D. Braga and F. Grepioni, Reactions Between or Within Molecular Crystals, *Angew. Chem. Int. Ed.*, 2004, 43, 4002-4011

103. A. V. T. Trask, W. Jones, Crystal Engineering of Organic Cocrystals by the Solid-State Grinding Approach, *Top. Curr. Chem.*, 2005, 254, 41-70

104. M. Hasegawa, Topochemical Photopolymerization of Diolefin Crystals, *Pure Appl. Chem.*, 1986, 58, 1179-1188

105. G. M. J. Schmidt, Photodimerization in the Solid State, *Pure Appl. Chem.*, 1971, 27, 647-678

106. K. Osaki, G. M. J. Schmidt, Single-Crystal Diffraction Experiments in a Search for Direct Structural Evidence for Solid-State Reactions, *Isr. J. Chem.*, 1972, 10, 189-193

107. H. Nakanishi, W. Jones, J. M. Thomas, Topochemical single-crystal-to-single-crystal photodimerization, *Chem. Phys. Lett.*, 1980, 71, 44-48

108. Sortav, Blessing 1995

109. A. Altomare, M. C. Burla, M. Camalli, G. Cascarano, C. Giacovazzo, A. Guagliardi, A.G. Moliterni, G. Polidori, R. Spagna, *Sir97: A New Program For Solving and Refining Crystal Structures*, Istituto di Ricerca per lo Sviluppo di Metodologie Cristallografiche CNR, Bari, 1997

110. G. Sheldrick, *Shelxl97. Program for structure refinement*. University of Goettingen, Germany, 1997

111. L.J. Farrugia, *J. Appl. Cryst.* 1999, 32, 837-838

112. M. Nardelli, *J. Appl. Cryst.* 1995, 28, 659

113. F. H. Allen, O. Kennard, R. Taylor, *Acc. Chem. Res.* 1983, 16, 146-153

114. I. J. Bruno, J.C. Cole, P.R. Edgington, M. Kessler, C.F. Macrae, P. McCabe, J. Pearson, R. Taylor, *Acta Crystallogr.* 2002, B58, 389-397

Supplementary Material

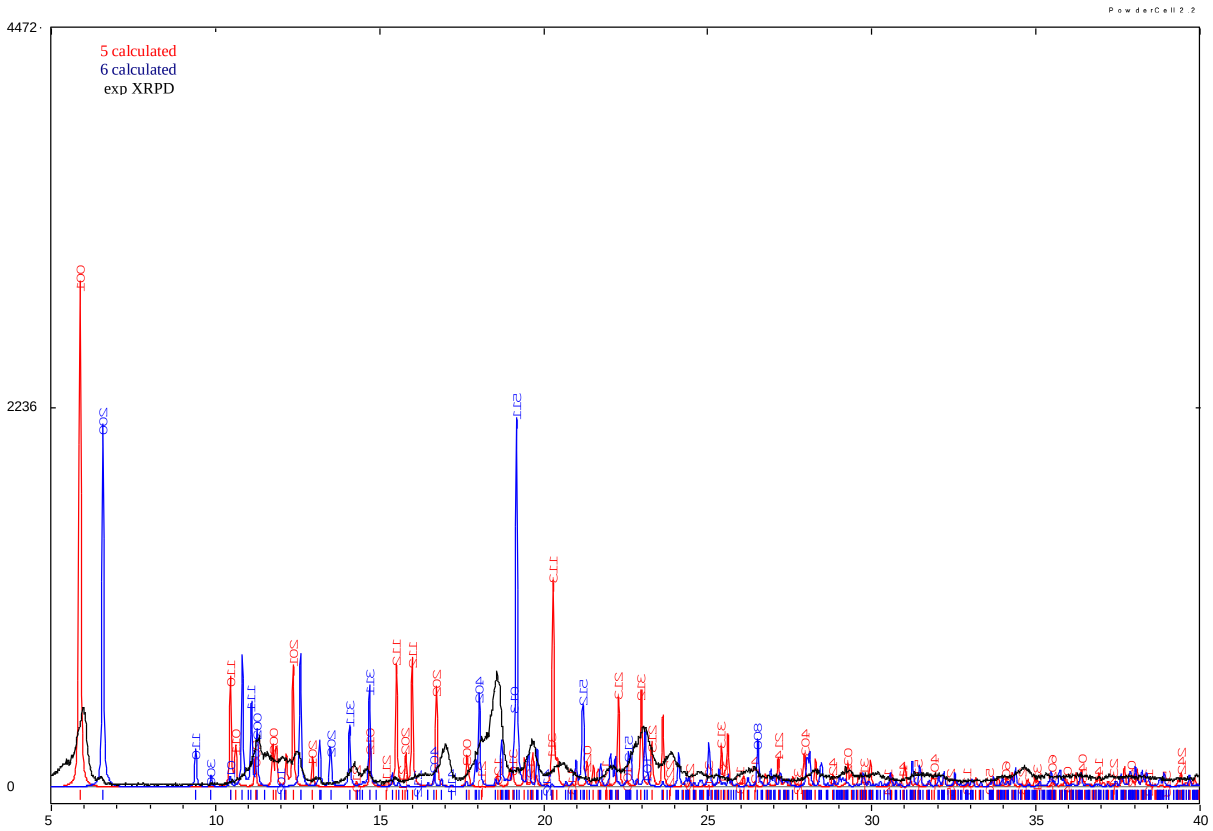

S1. Overlap between the experimental XRPD at ambient temperature of a mixture of **5**, **6** and **6’** (black) and of the simulated XRPD of **5** (red) and **6** (blue) (Part I)

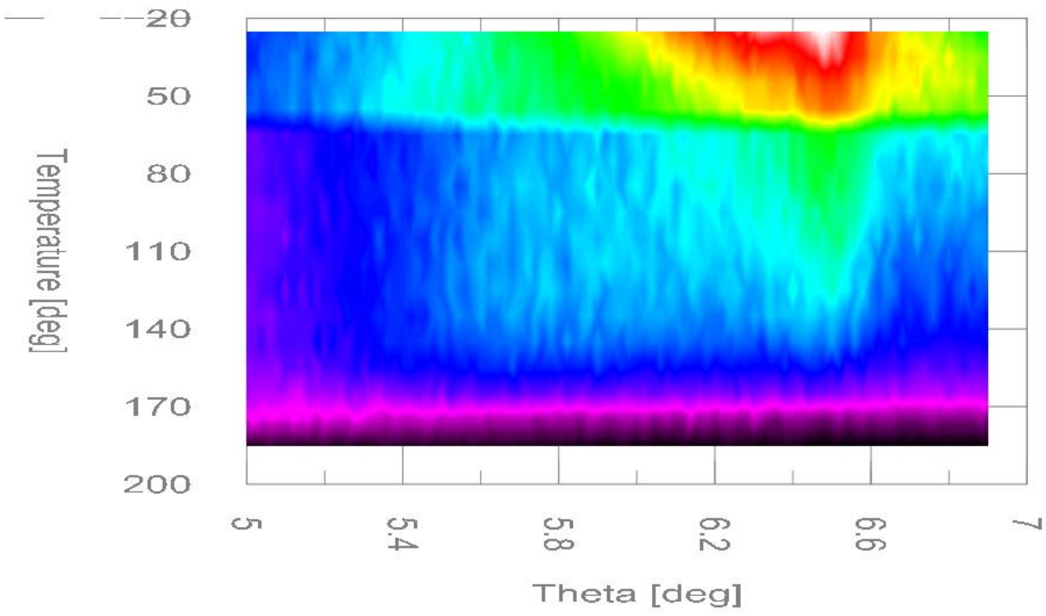

S2. Variable temperature XRPD of the solvate **8** in the 2θ range between 4.9-6.9°. The peak disappearance shows the formation of an amorphous phase, concomitantly with the desolvation process, above 55° (Part I)

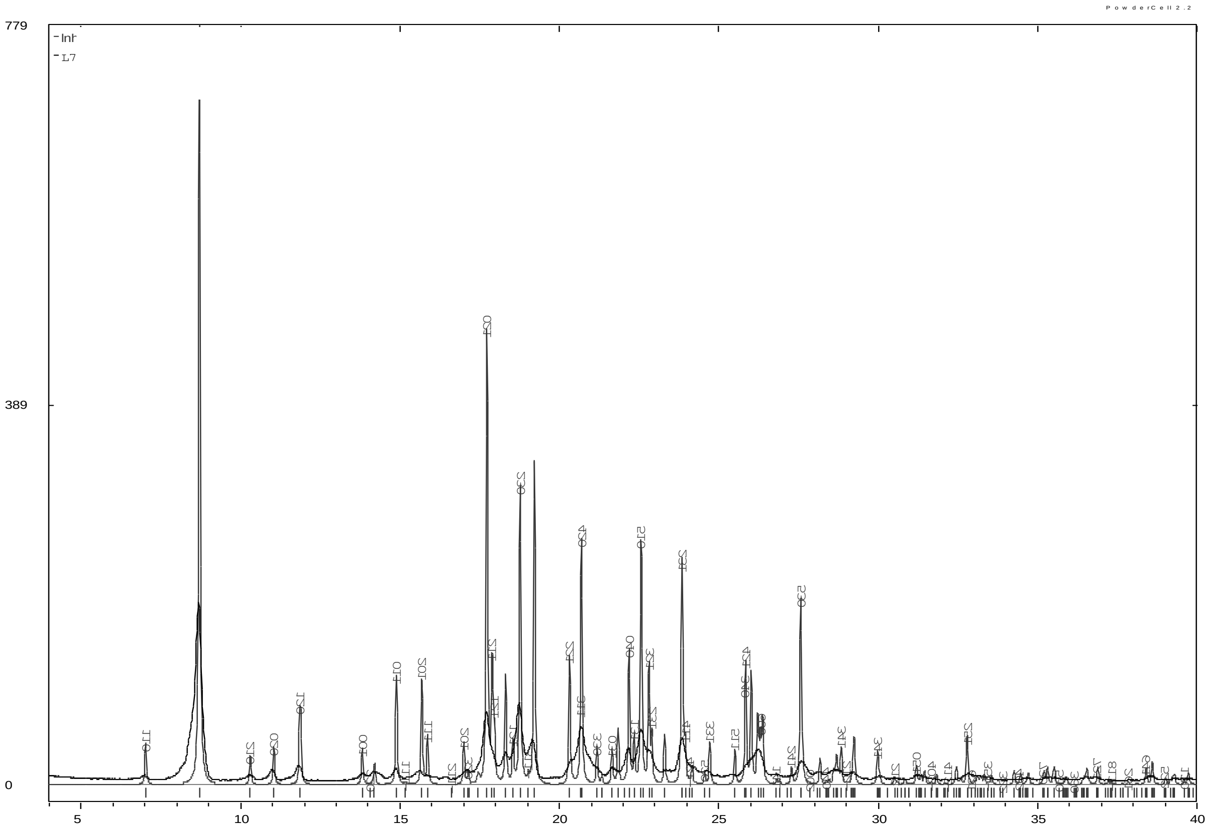

S3. Overlap between the experimental XRPD of the mixture of the toluene solvates **10a-c** after 1 week of exposure to acetone vapours (black) and of the simulated XRPD of the acetone solvate **11** (grey) (Part II). The picture shows the complete guest exchange

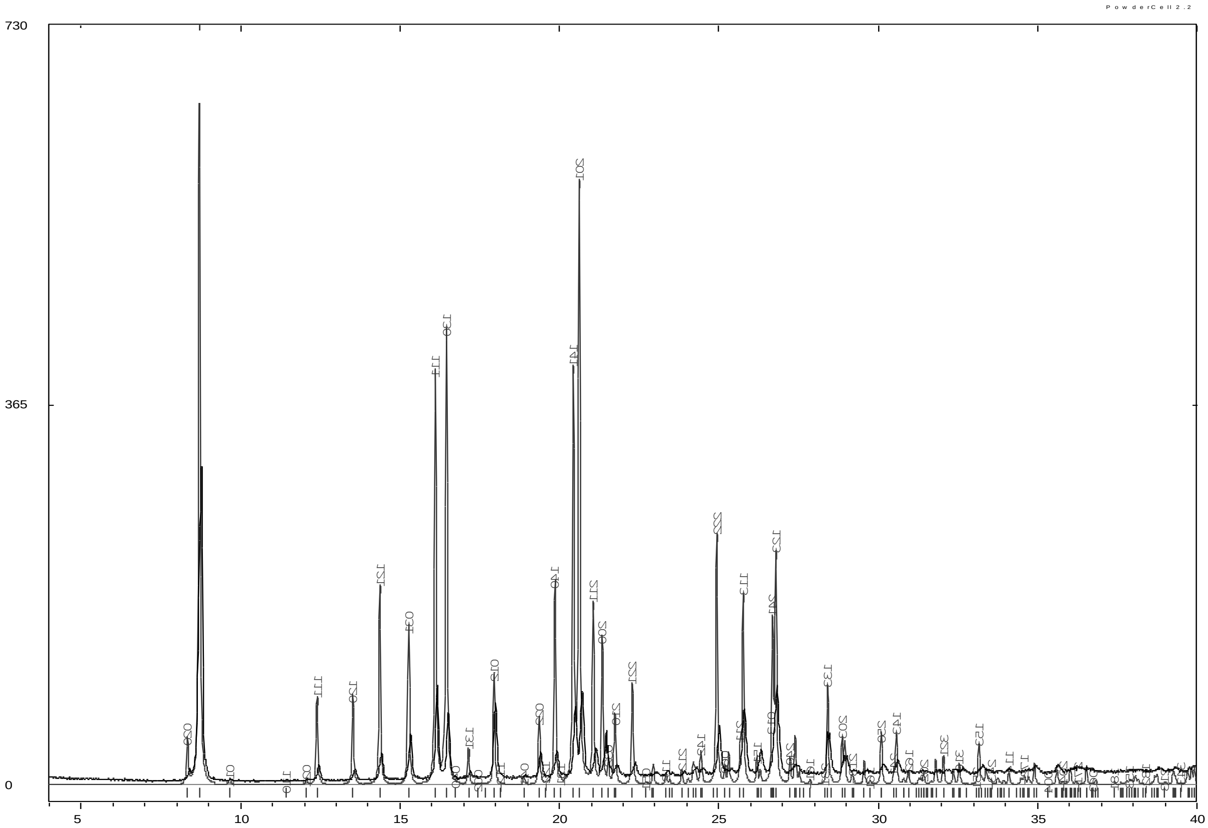

S4. Overlap between the experimental XRPD pattern of the mixture of the toluene solvates **10a-c** after 10 days of exposure to ether vapours (black) and of the simulated XPRD of the apohost **13** (grey) (Part II). The picture shows the quantitative obtaining of the non-solvate form.

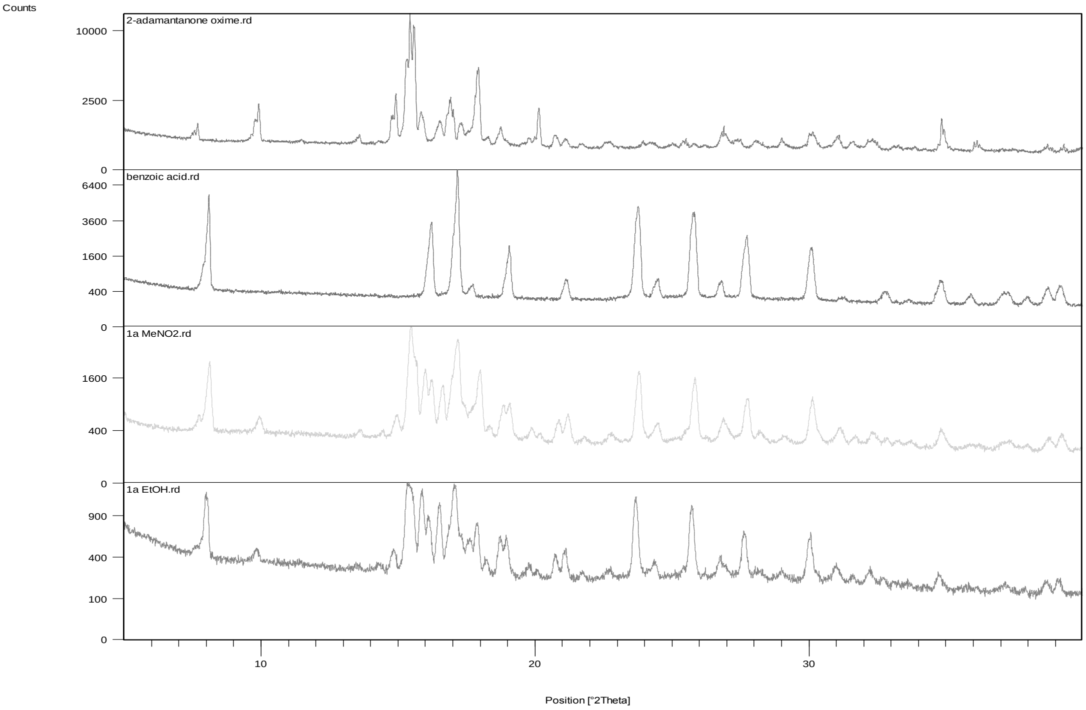

S5. From top to bottom: PXRD for 2-adamantanone oxime, benzoic acid and LAG product **1a** obtained using $MeNO_2$ and EtOH, respectively

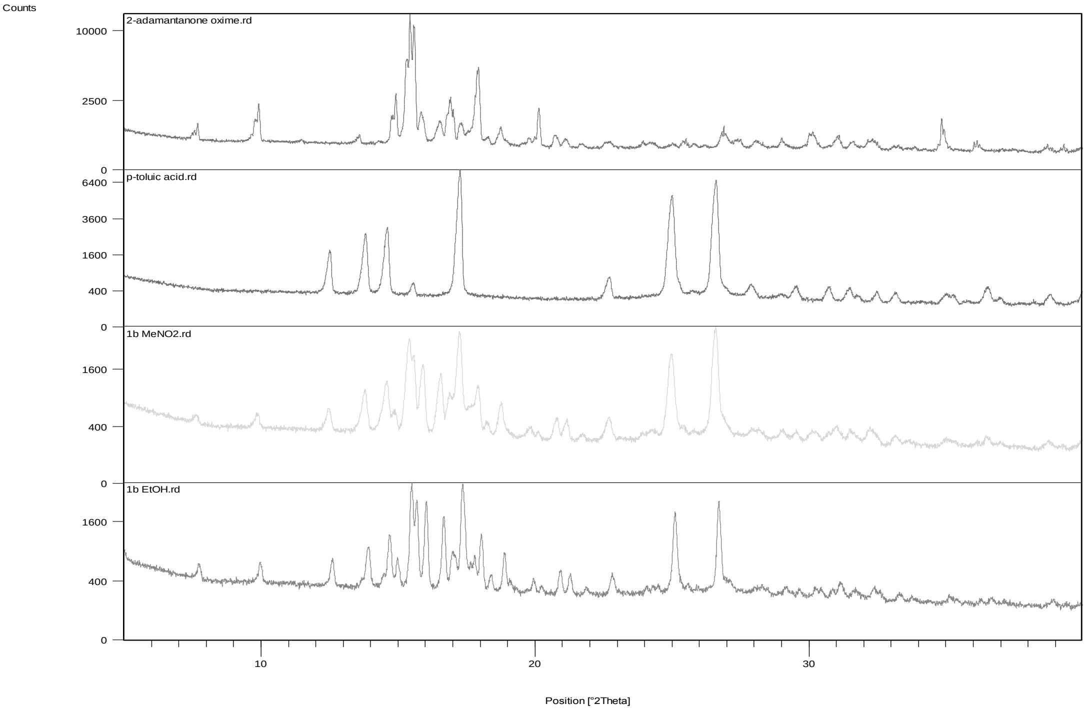

S6. From top to bottom: PXRD for 2-adamantanone oxime, o-toluic acid and LAG product **1b** obtained using $MeNO_2$ and EtOH, respectively

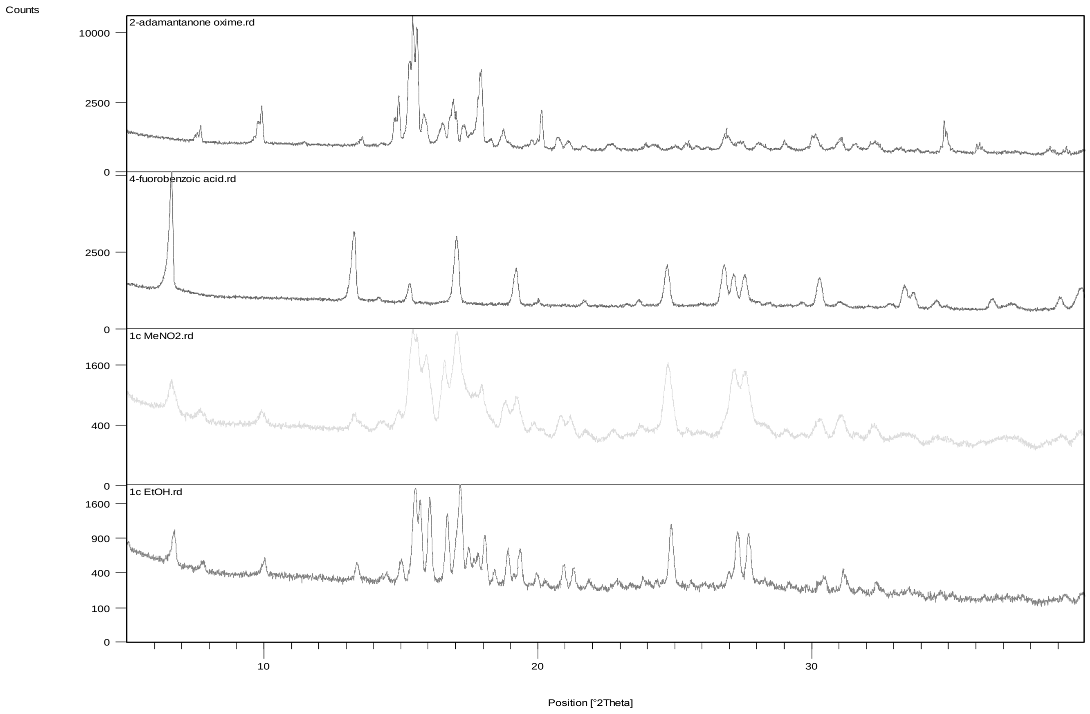

S7. From top to bottom: PXRD for 2-adamantanone oxime, p-fluorobenzoic acid and LAG product **1c** obtained using $MeNO_2$ and EtOH, respectively

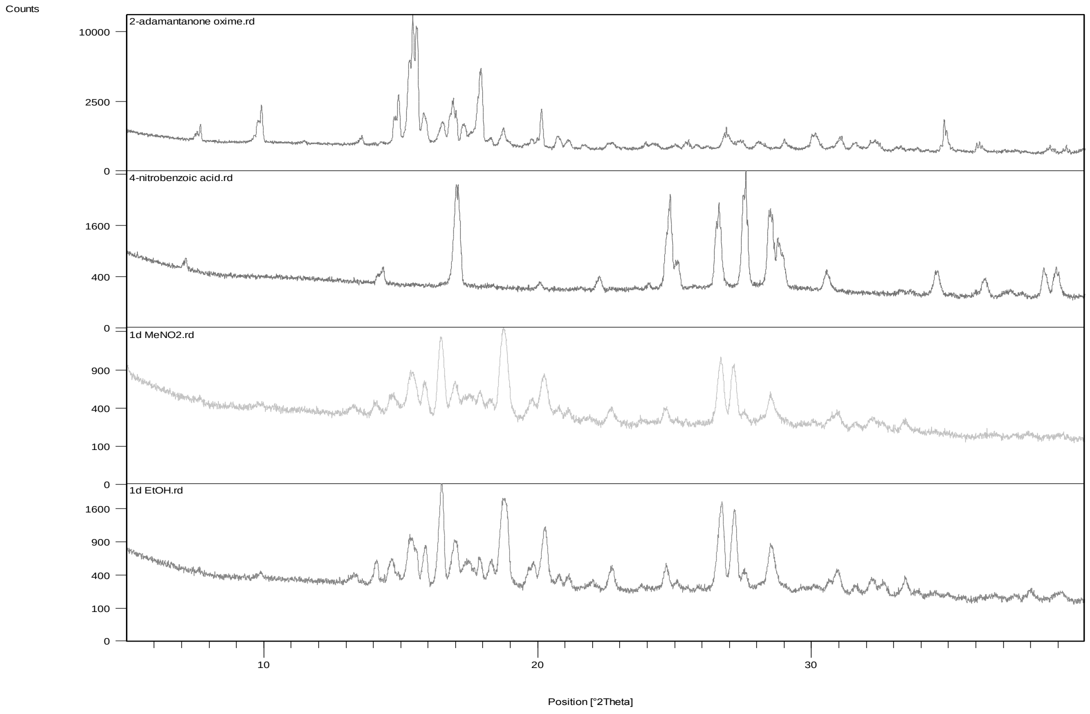

S8. From top to bottom: PXRD for 2-adamantanone oxime, 4-nitrobenzoic acid and LAG product **1d** obtained using $MeNO_2$ and EtOH, respectively

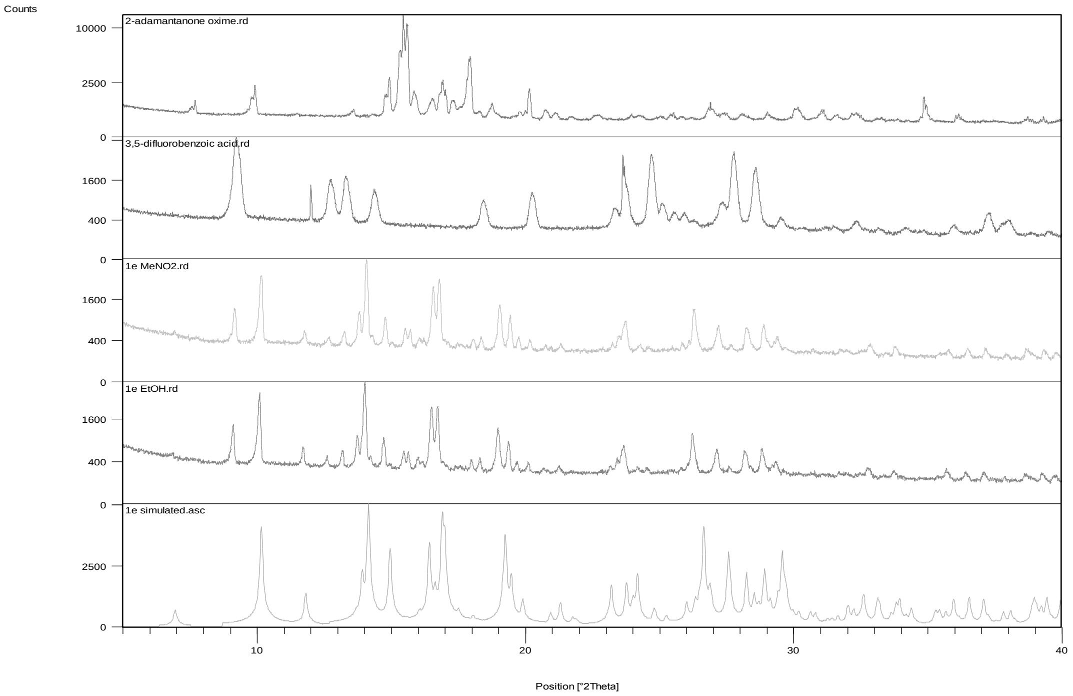

S9. From top to bottom: PXRD for 2-adamantanone oxime, 3,5-difluorobenzoic acid, LAG product **1e** obtained using $MeNO_2$ and EtOH and simulated PXRD of **1e**, respectively

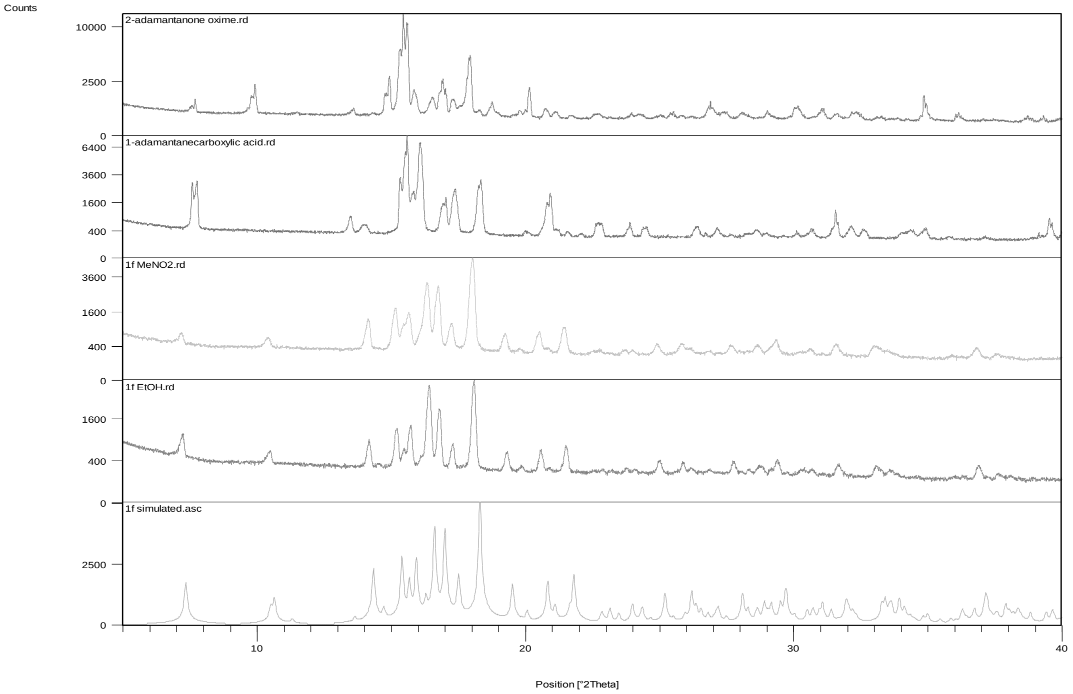

S10. From top to bottom: PXRD for 2-adamantanone oxime, 1-adamantanecarboxylic acid, LAG product **1f** obtained using $MeNO_2$ and EtOH and simulated PXRD of **1f**, respectively

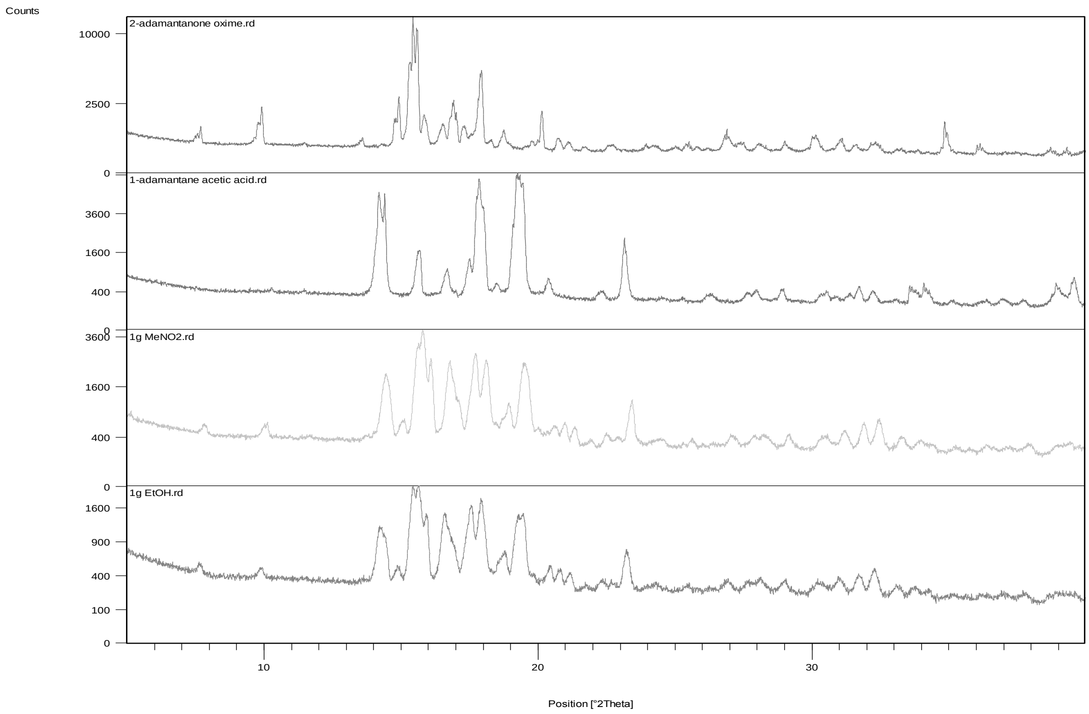

S11. From top to bottom: PXRD for 2-adamantanone oxime, 1-adamantane acetic acid and LAG product **1g** obtained using $MeNO_2$ and EtOH, respectively

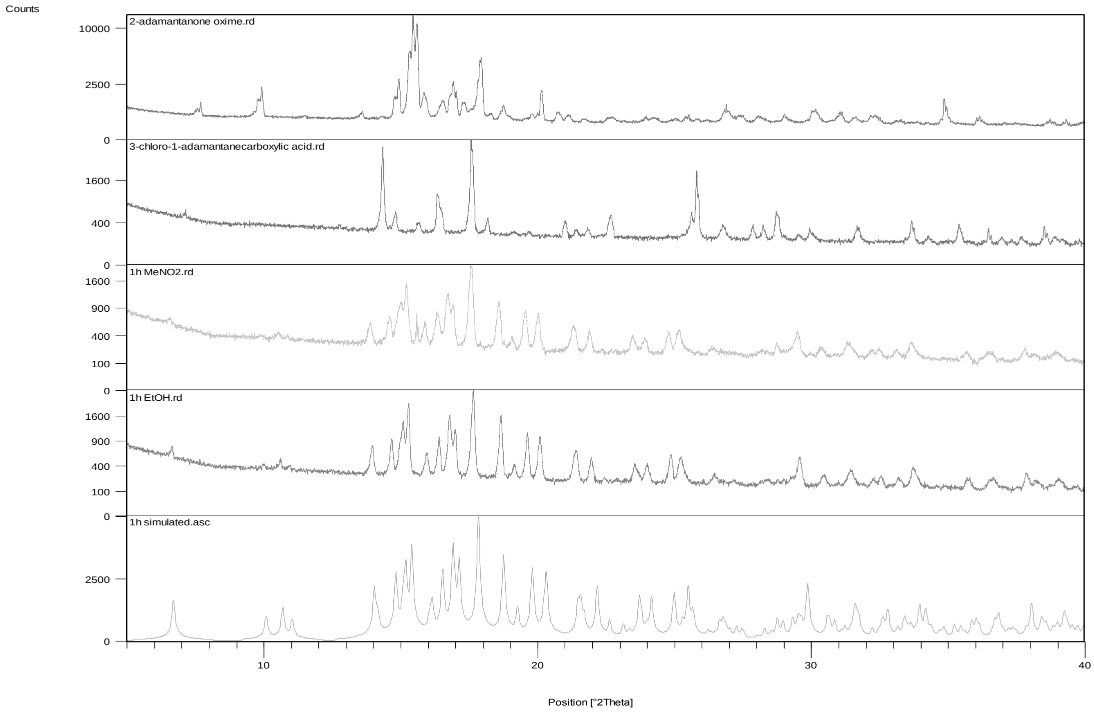

S12. From top to bottom: PXRD for 2-adamantanone oxime, 3-chloro-1-adamantanecarboxylic acid, LAG product **1h** obtained using $MeNO_2$ and EtOH and simulated PXRD of **1h**, respectively

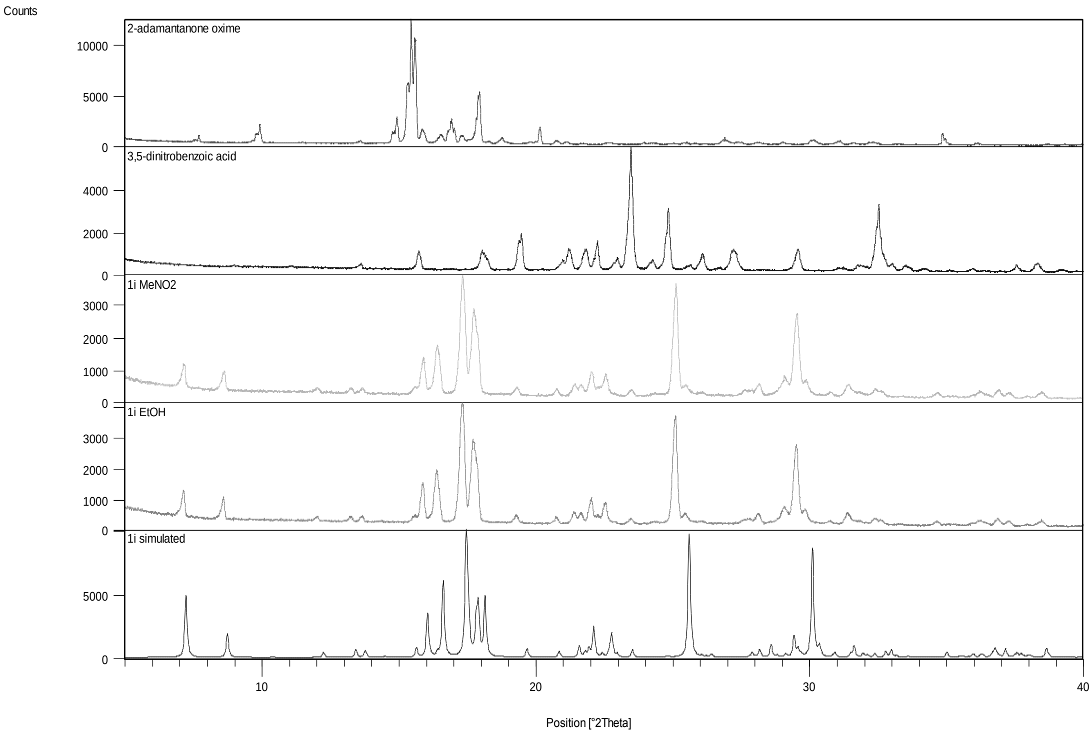

S13. From top to bottom: PXRD for 2-adamantanone oxime, 3,5-dinitrobenzoic acid, LAG product **1i** obtained using $MeNO_2$ and EtOH and simulated PXRD of **1i**, respectively

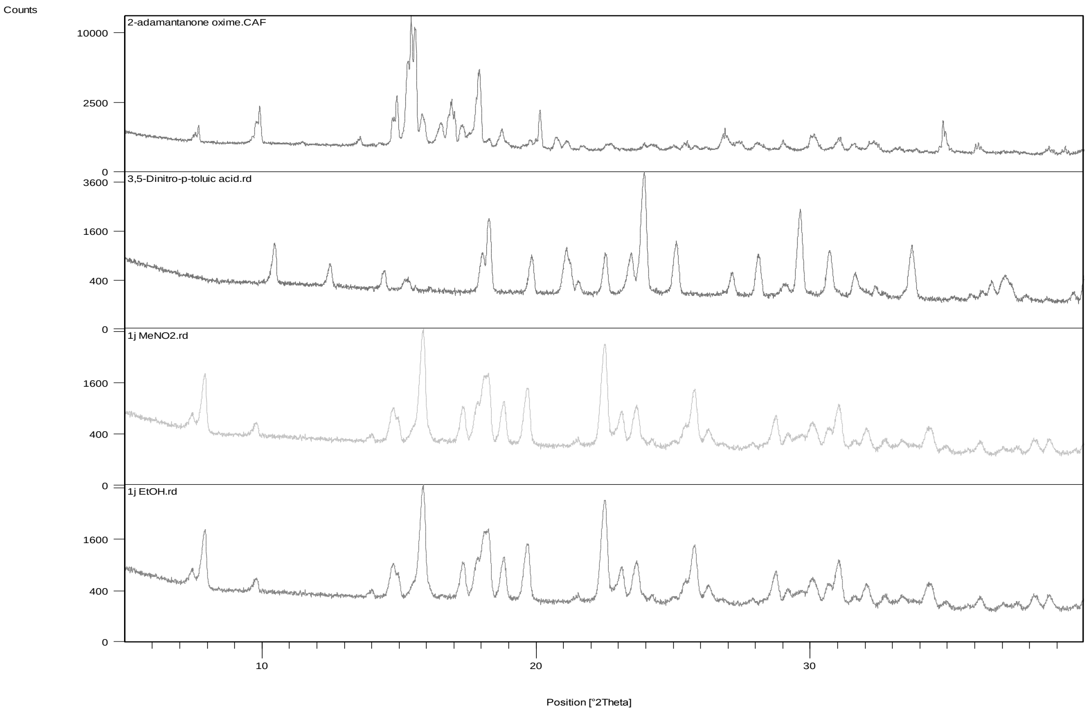

S14. From top to bottom: PXRD for 2-adamantanone oxime, 3,5-dinitro-p-toluic acid and LAG product **1j** obtained using $MeNO_2$ and EtOH, respectively

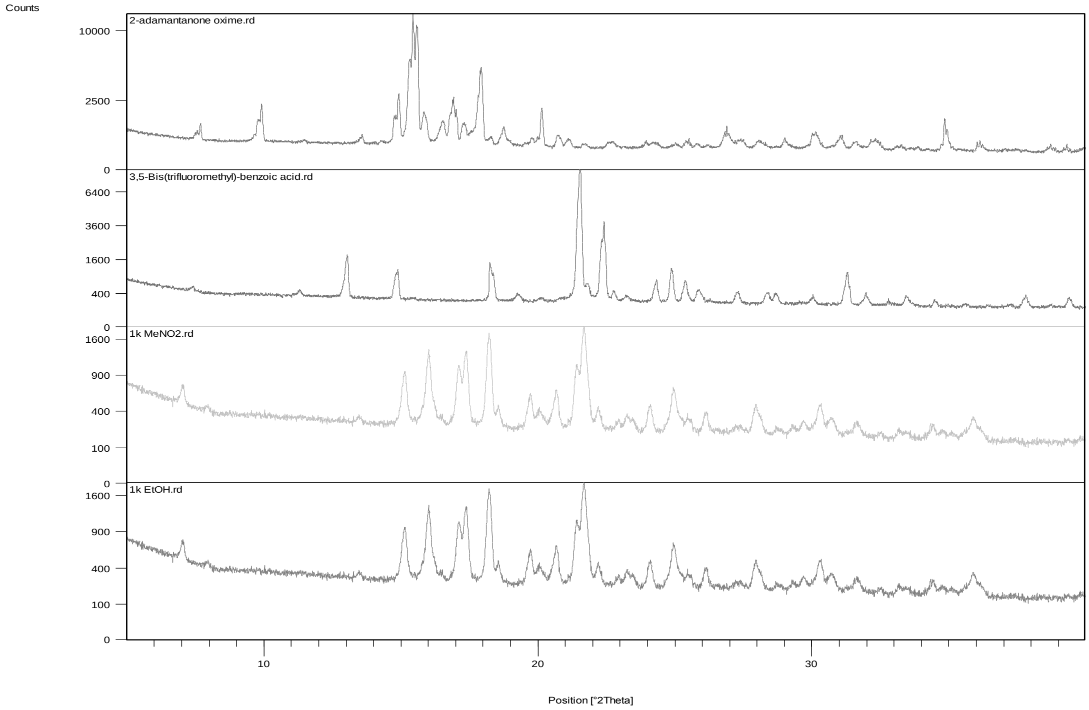

S15. From top to bottom: PXRD for 2-adamantanone oxime, 3,5-bis(trifluoromethyl)-benzoic acid and LAG product **1k** obtained using $MeNO_2$ and EtOH, respectively

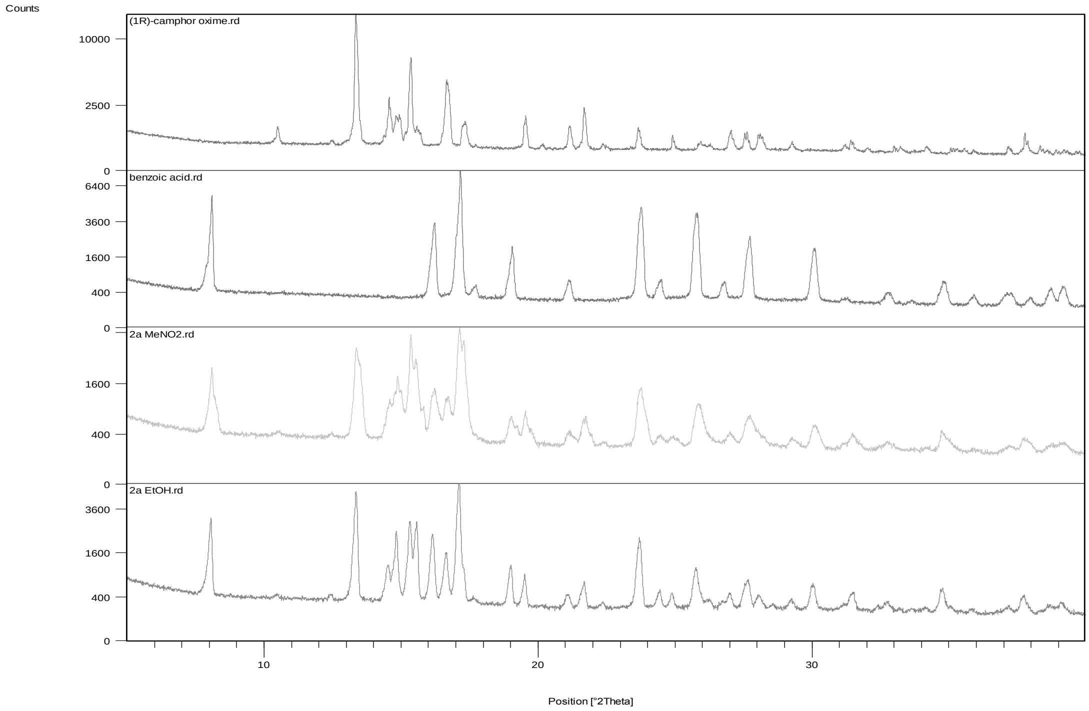

S16. From top to bottom: PXRD for (1R)-camphor oxime,benz oic acid and LAG product **2a** obtained using $MeNO_2$ and EtOH, respectively

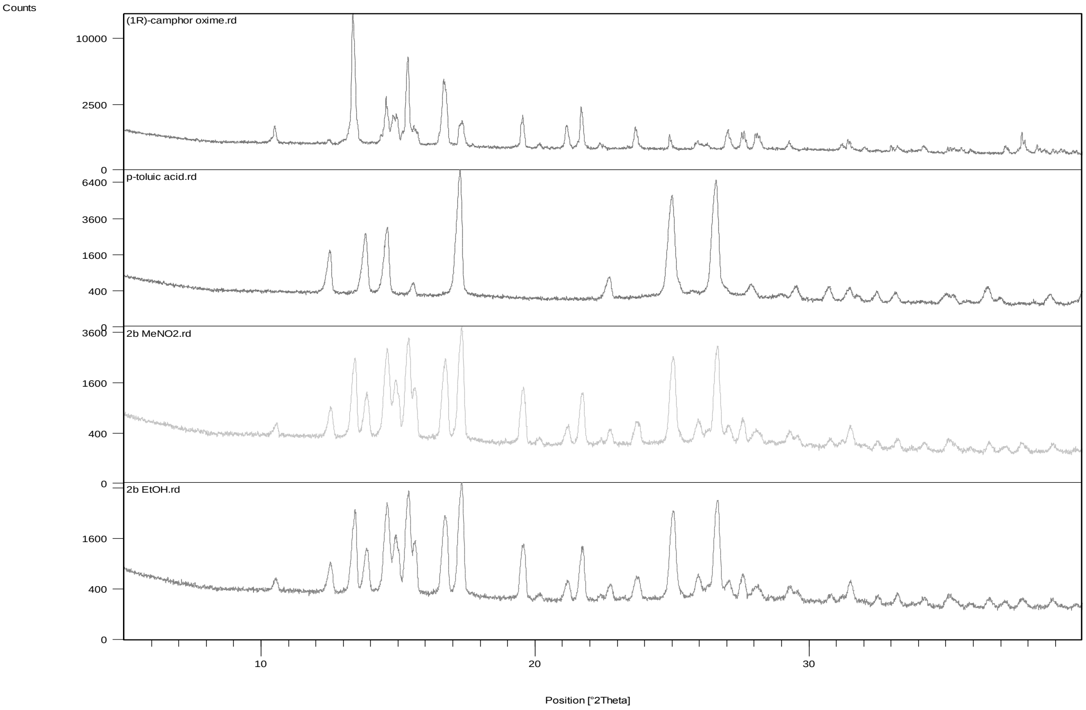

S17. From top to bottom: PXRD for (1R)-camphor oxime, o-toluic acid and LAG product **2b** obtained using $MeNO_2$ and EtOH, respectively

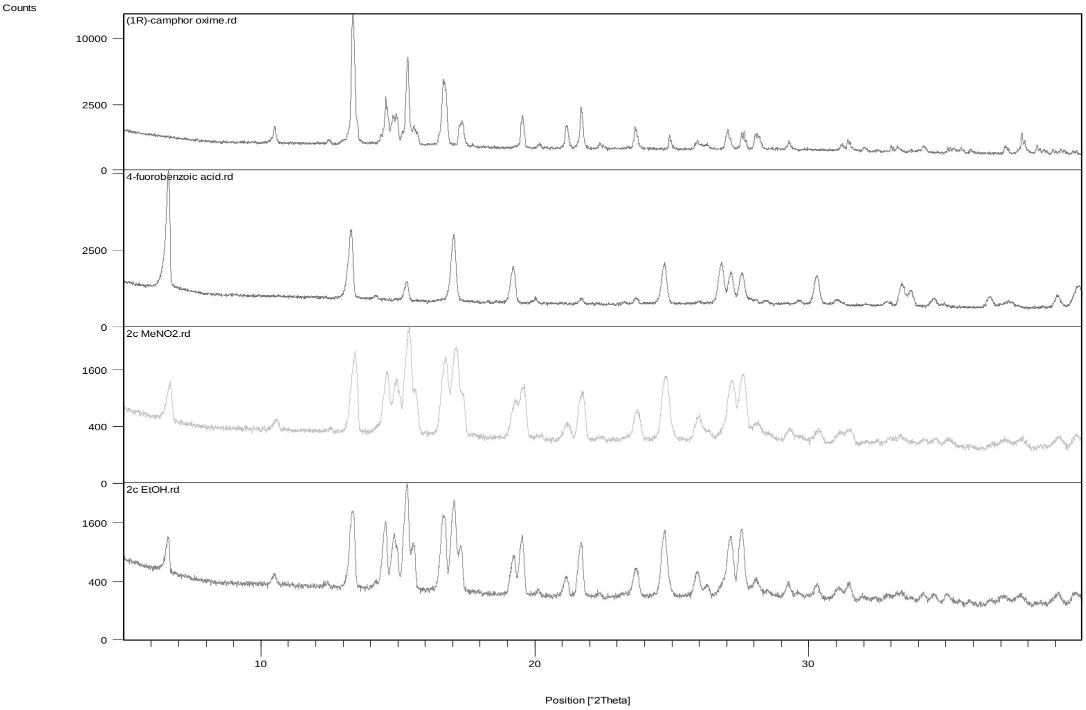

S18. From top to bottom: PXRD for (1R)-camphor oxime, p-fluorobenzoic acid and LAG product **2c** obtained using $MeNO_2$ and EtOH, respectively

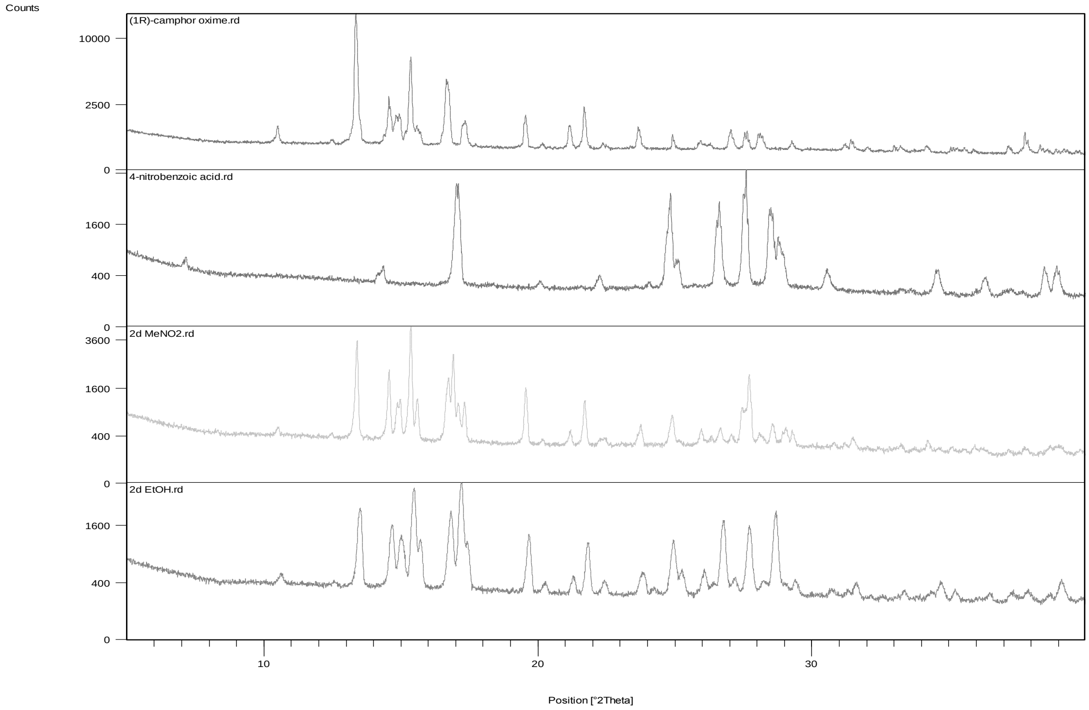

S19. From top to bottom: PXRD for (1R)-camphor oxime, 4-nitrobenzoic acid and LAG product **2d** obtained using $MeNO_2$ and EtOH, respectively

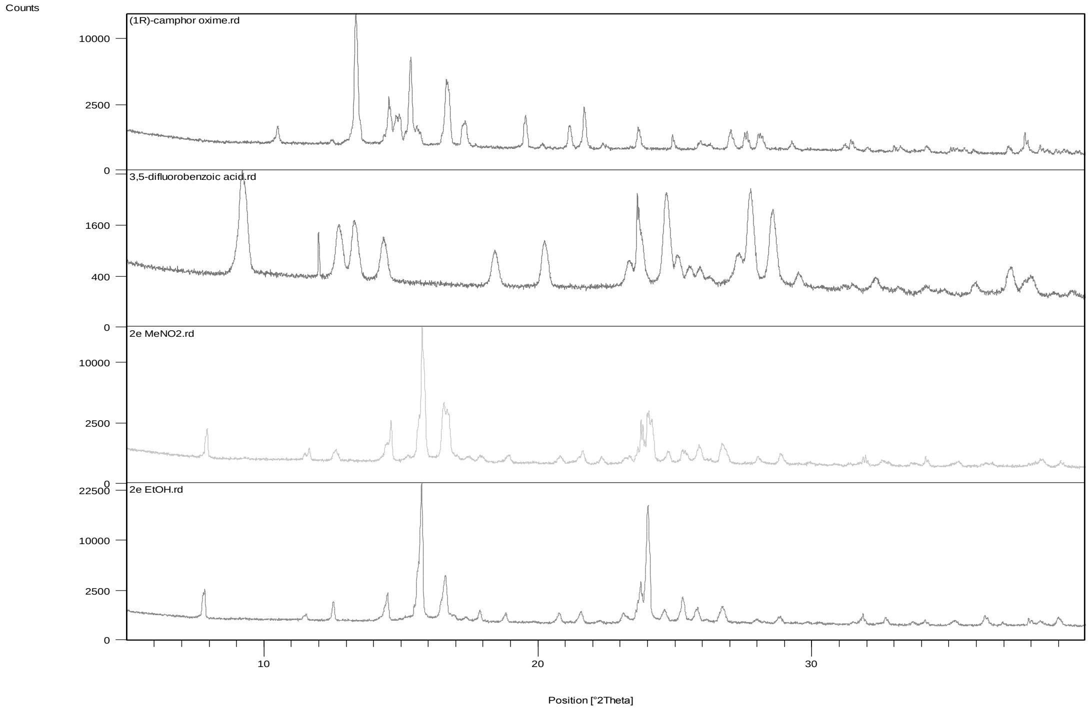

S20. From top to bottom: PXRD for (1R)-camphor oxime, 3,5-difluorobenzoic acid and LAG product **2e** obtained using $MeNO_2$ and EtOH, respectively

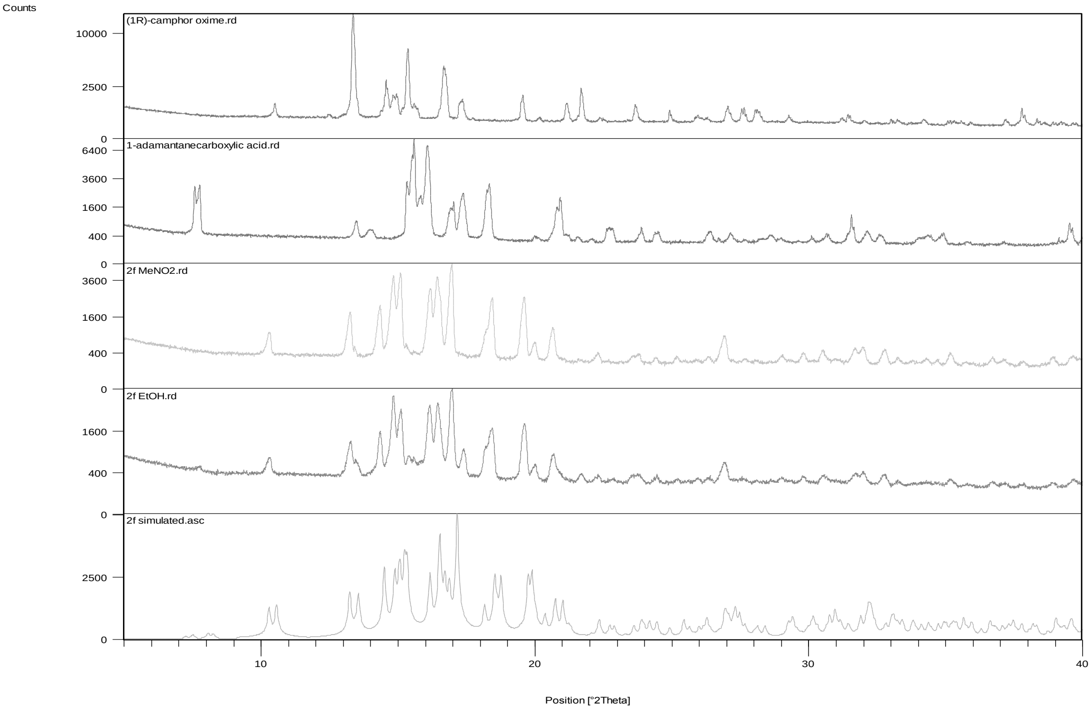

S21. From top to bottom: PXRD for (1R)-camphor oxime, 1-adamantanecarboxylic acid, LAG product **2f** obtained using $MeNO_2$ and EtOH and simulated PXRD of **2f**, respectively

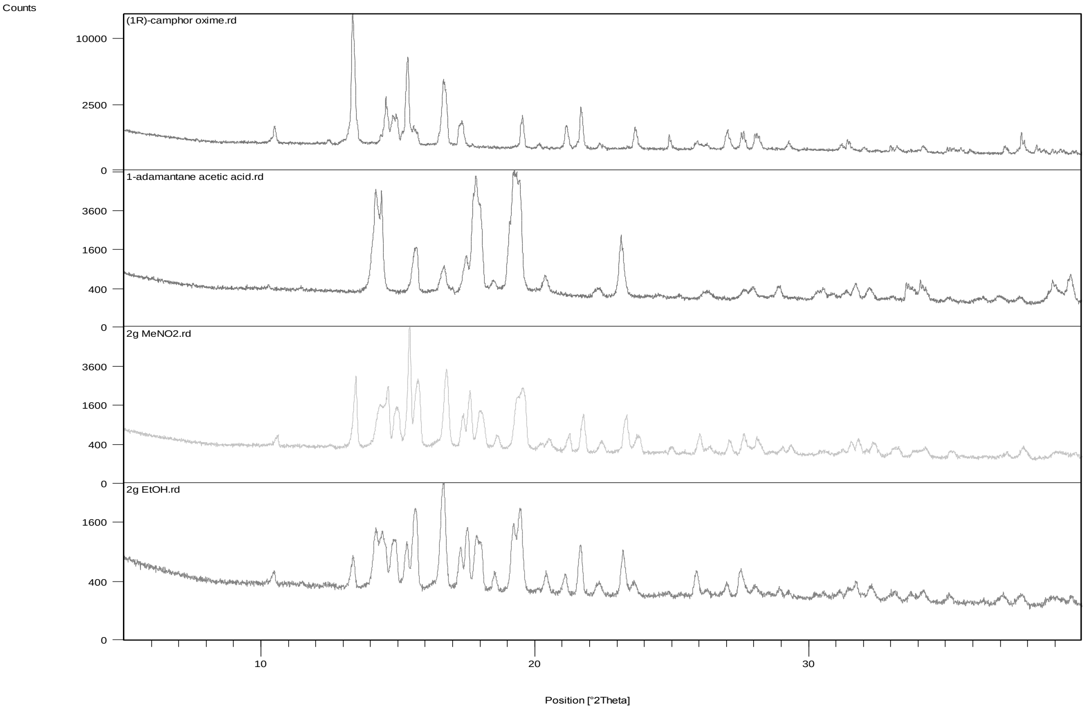

S22. From top to bottom: PXRD for (1R)-camphor oxime, 1-adamantane acetic acid and LAG product **2g** obtained using $MeNO_2$ and EtOH, respectively

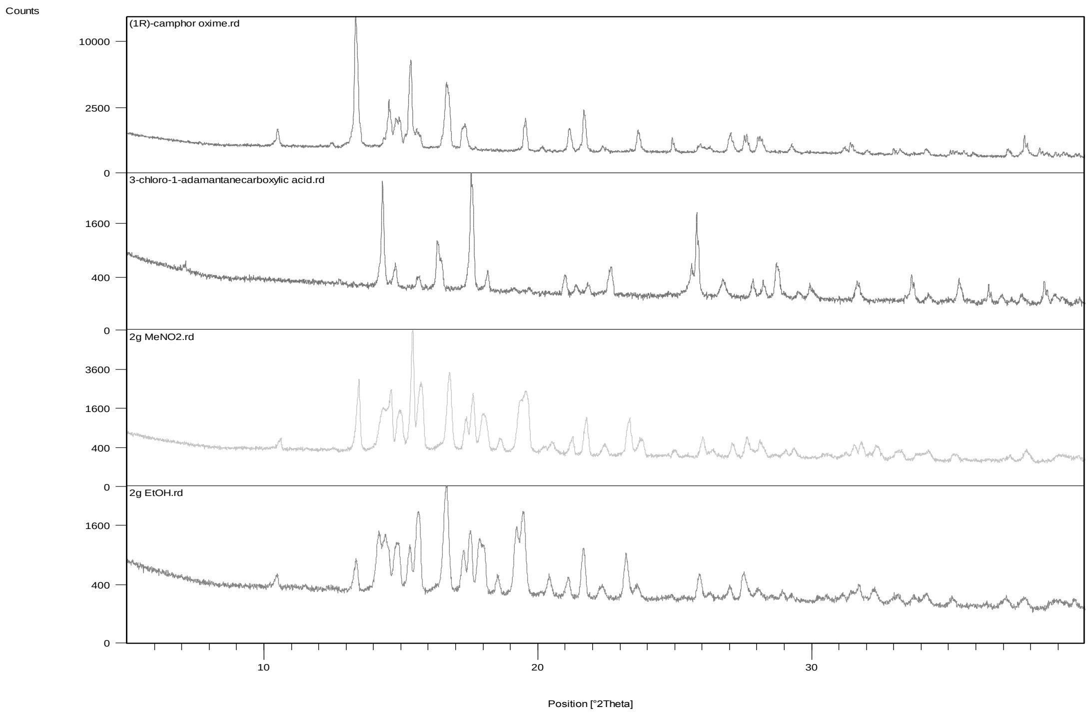

S23. From top to bottom: PXRD for (1R)-camphor oxime, 3-chloro-1-adamantanecarboxylic acid and LAG product **2h** obtained using $MeNO_2$ and EtOH, respectively

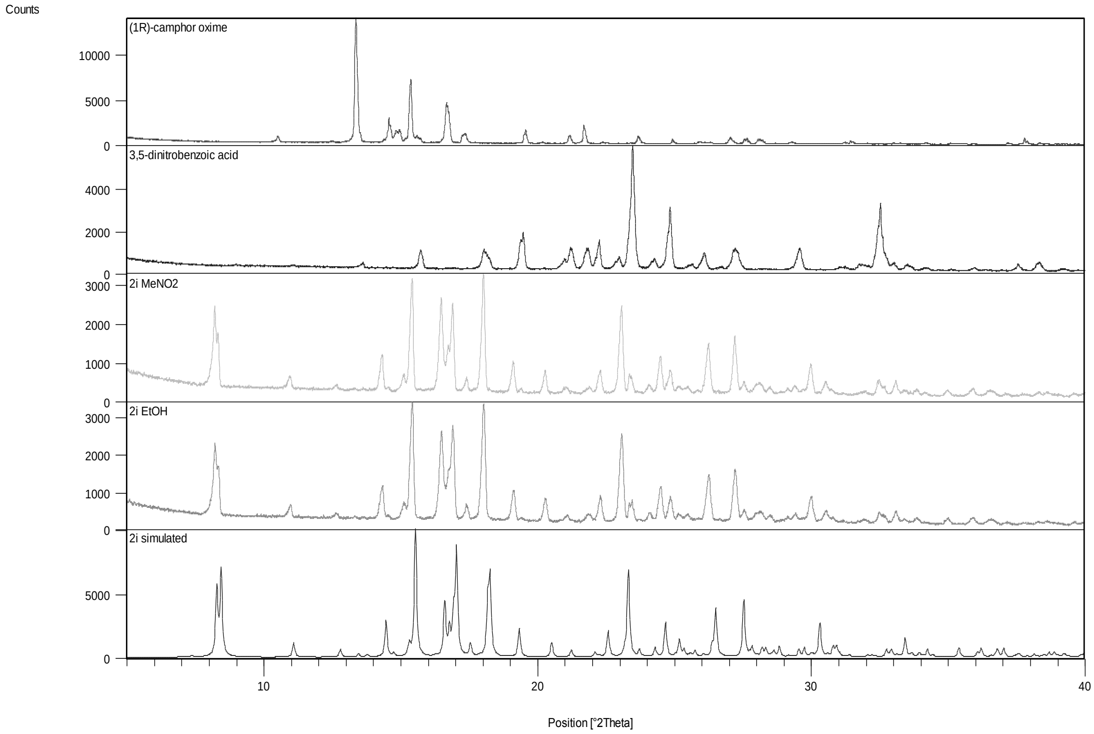

S24. From top to bottom: PXRD for (1R)-camphor oxime, 3,5-dinitrobenzoic acid, LAG product **2i** obtained using $MeNO_2$ and EtOH and simulated PXRD of **2i,** respectively

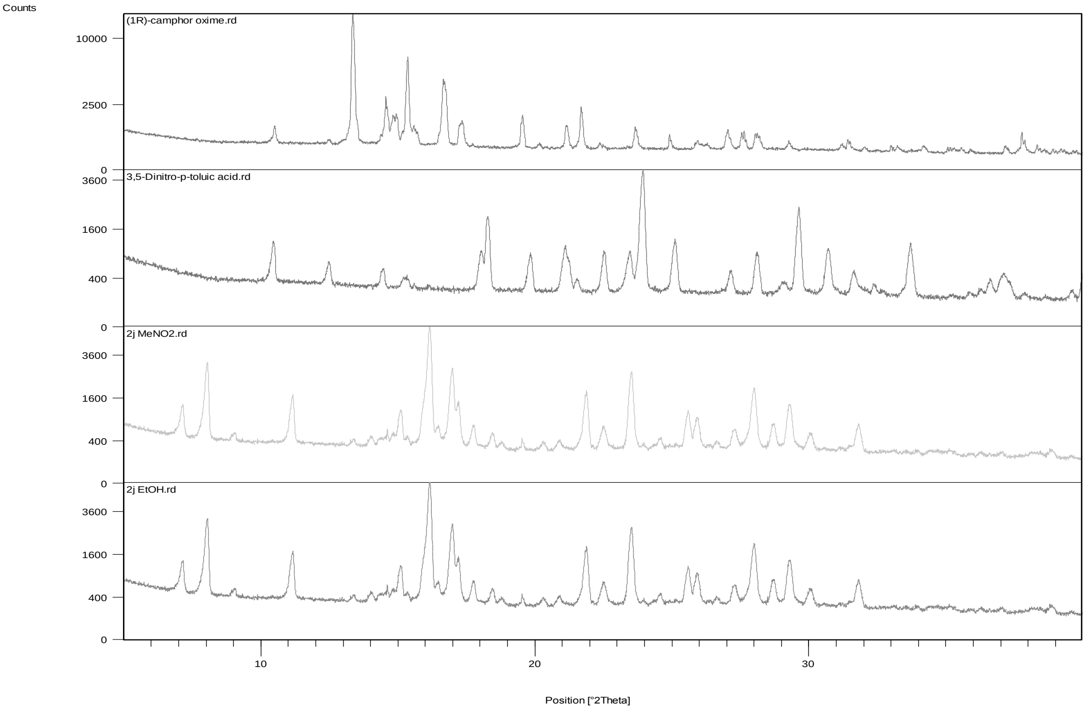

S25. From top to bottom: PXRD for (1R)-camphor oxime, 3,5-dinitro-p-toluic acid and LAG product **2j** obtained using $MeNO_2$ and EtOH, respectively

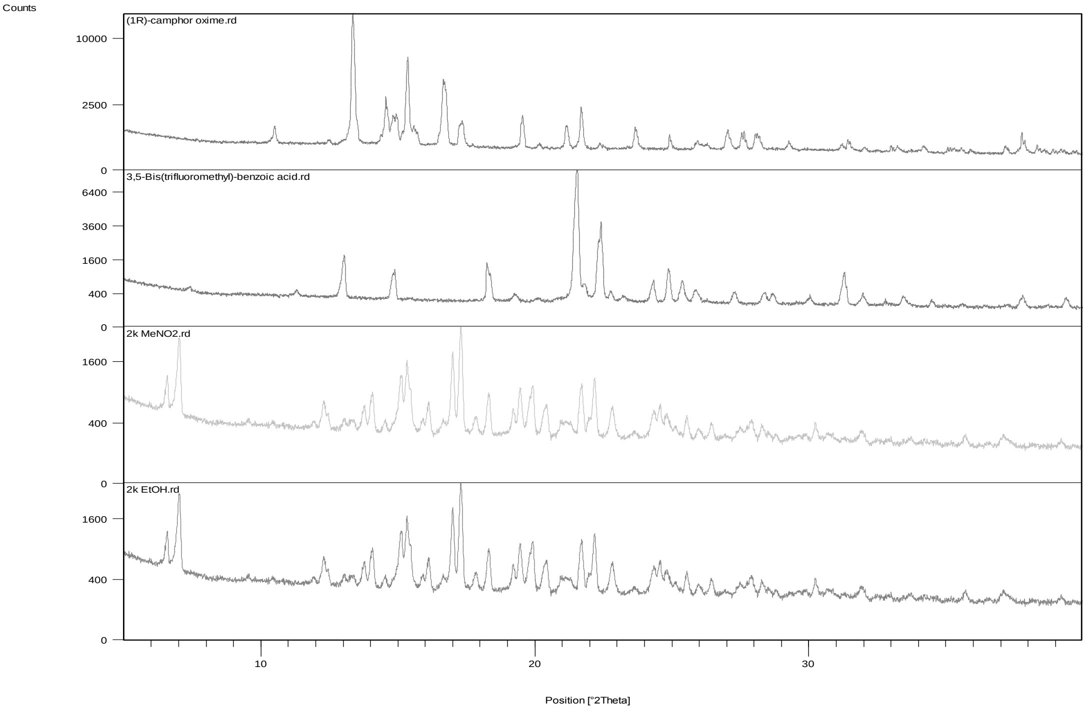

S26. From top to bottom: PXRD for (1R)-camphor oxime, 3,5-bis(trifluoromethyl)-benzoic acid and LAG product **2k** obtained using $MeNO_2$ and EtOH, respectively

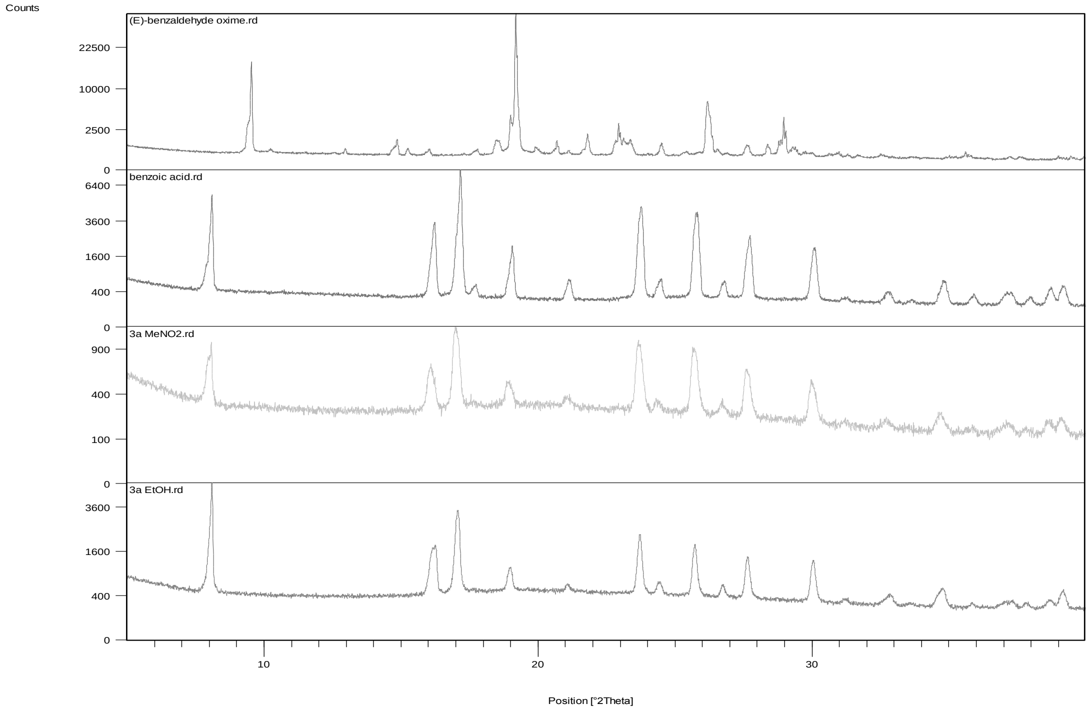

S27. From top to bottom: PXRD for (E)-benzaldehyde oxime, benzoic acid and LAG product **3a** obtained using $MeNO_2$ and EtOH, respectively

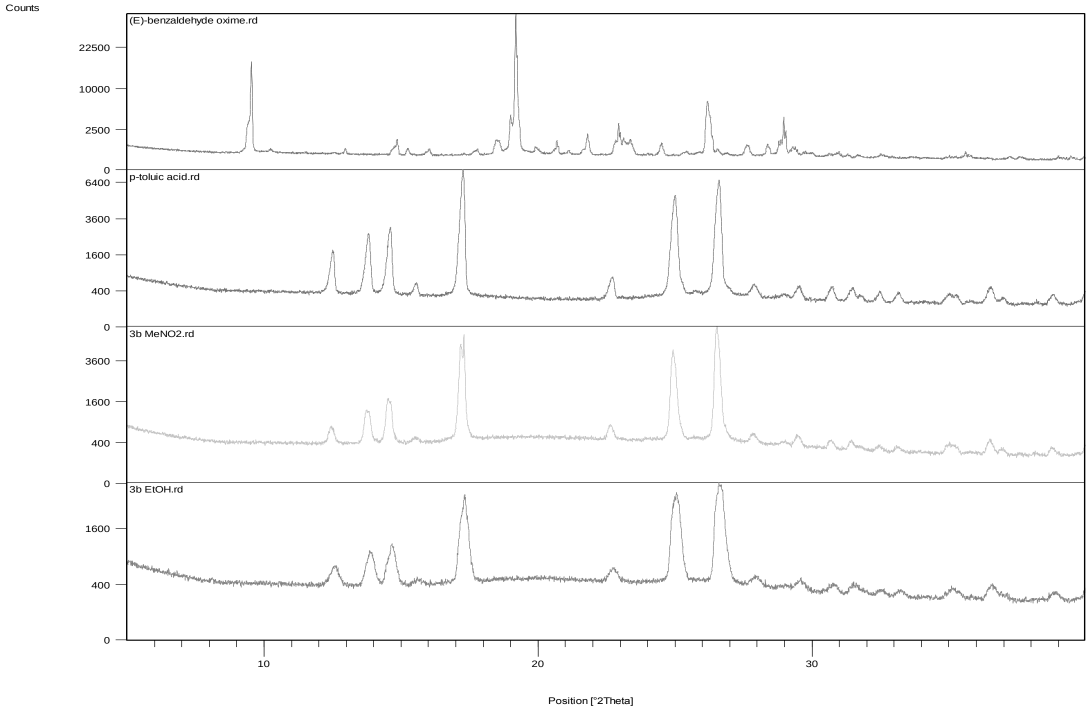

S28. From top to bottom: PXRD for (E)-benzaldehyde oxime, o-toluic acid and LAG product **3b** obtained using $MeNO_2$ and EtOH, respectively

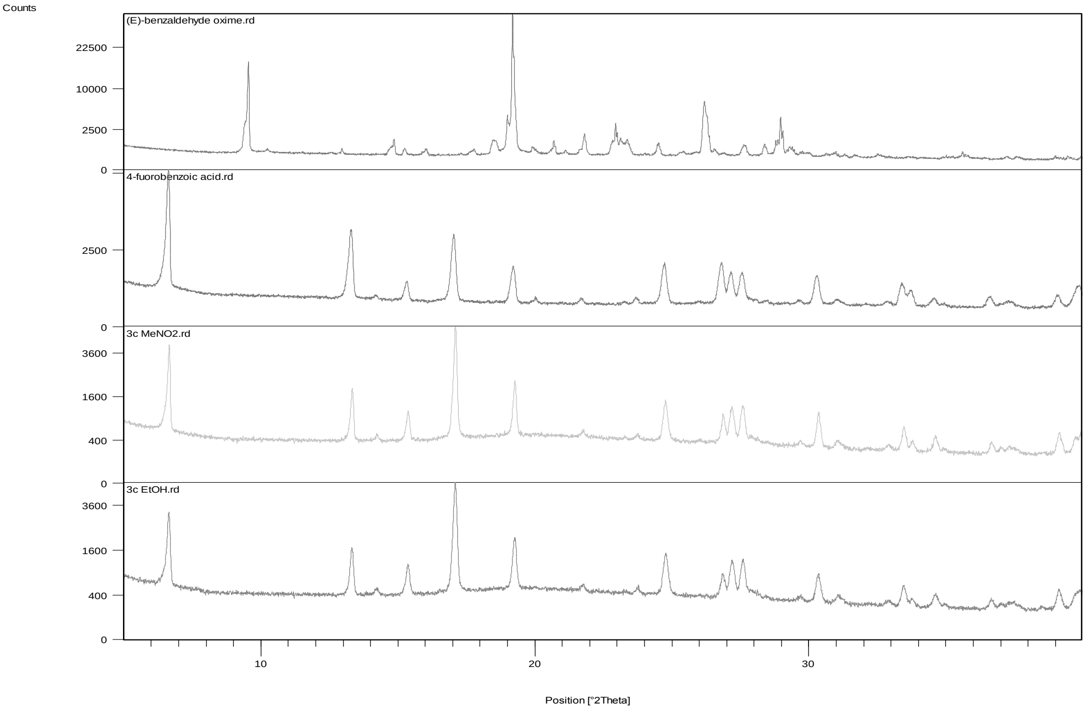

S29. From top to bottom: PXRD for (E)-benzaldehyde oxime, p-fluorobenzoic acid and LAG product **3c** obtained using $MeNO_2$ and EtOH, respectively

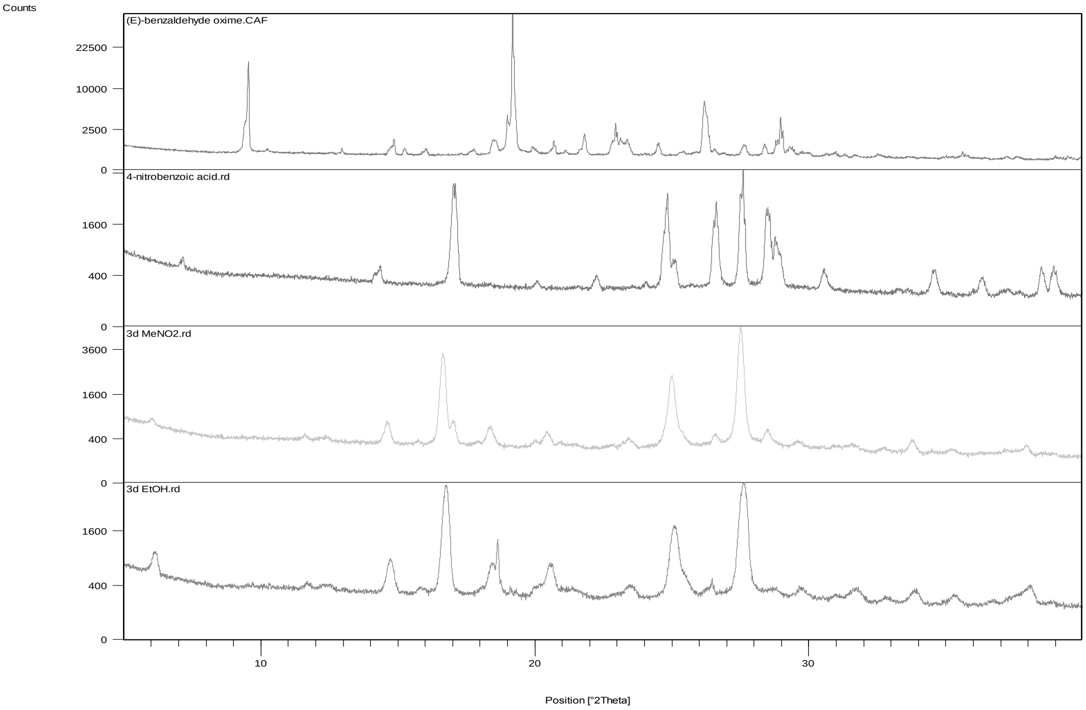

S30. From top to bottom: PXRD for (E)-benzaldehyde oxime, 4-nitrobenzoic acid and LAG product **3d** obtained using $MeNO_2$ and EtOH, respectively

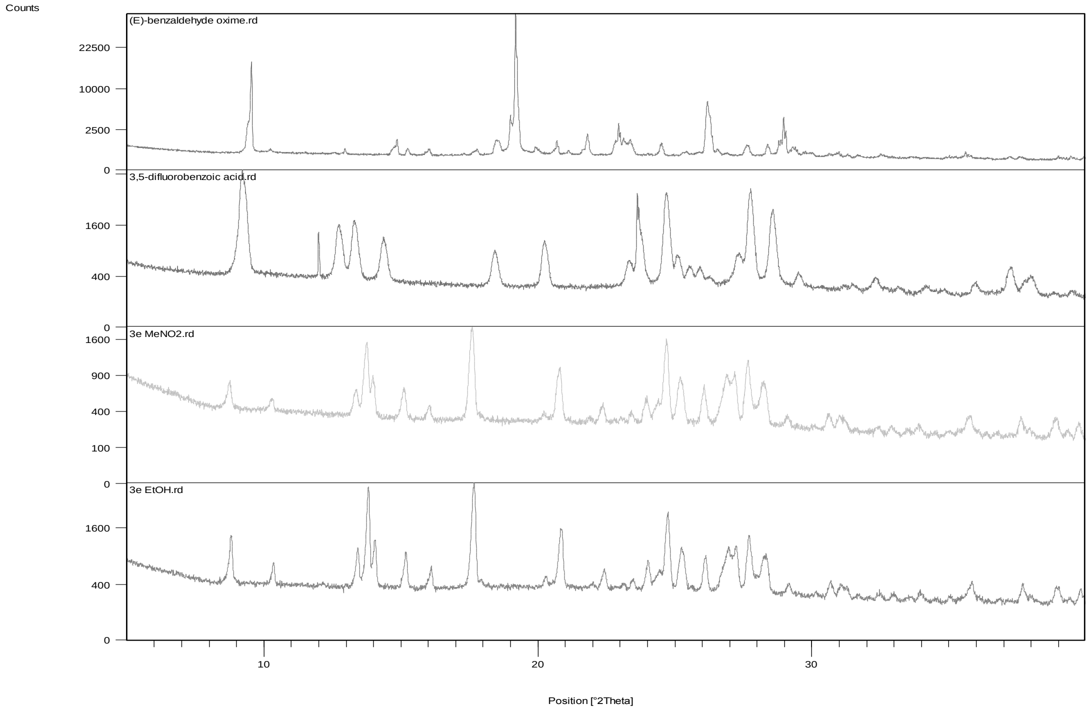

S31. From top to bottom: PXRD for for (E)-benzaldehyde oxime, 3,5-difluorobenzoic acid and LAG product **3e** obtained using $MeNO_2$ and EtOH, respectively

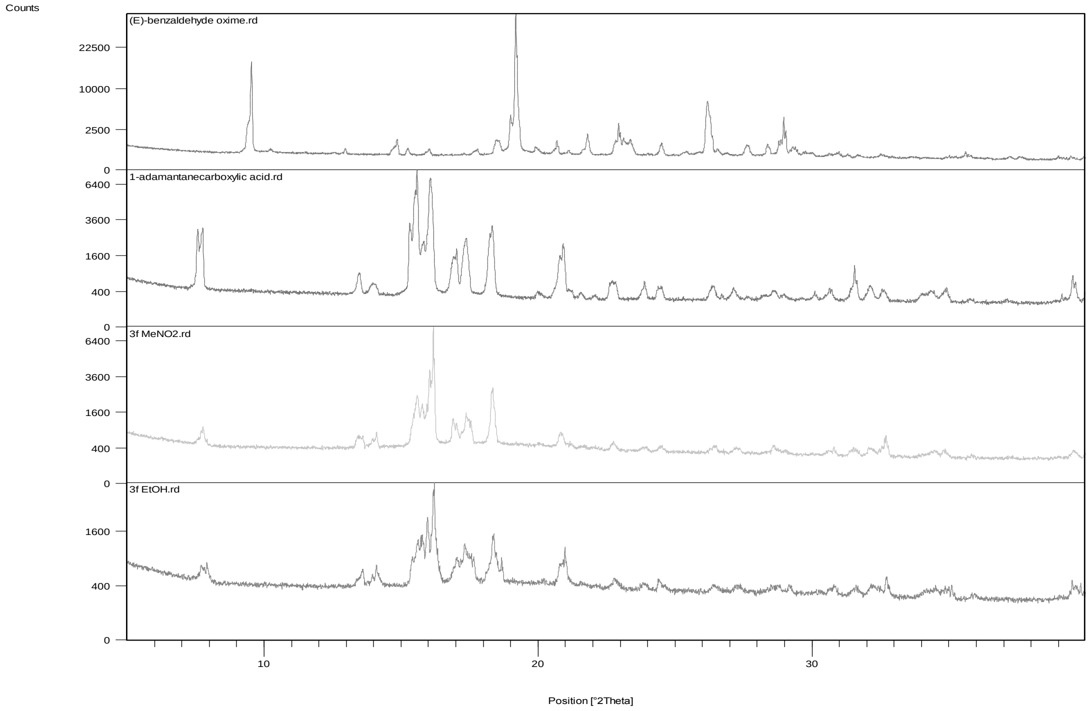

S32. From top to bottom: PXRD for (E)-benzaldehyde oxime, 1-adamantanecarboxylic acid and LAG product **3f** obtained using $MeNO_2$ and EtOH, respectively

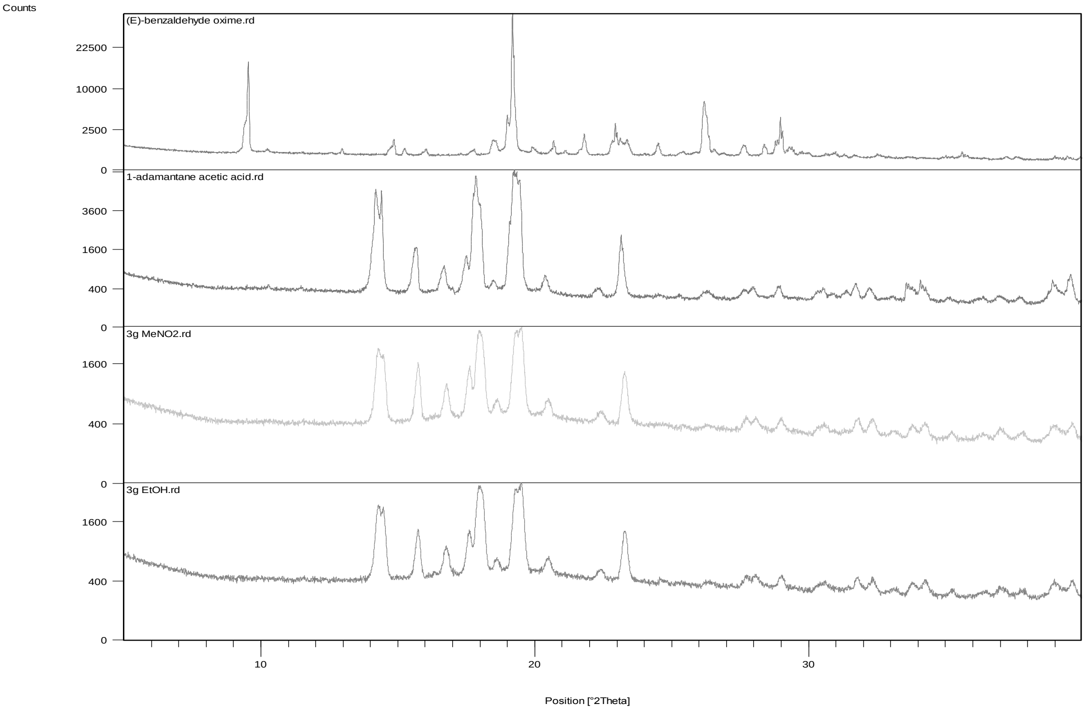

S33. From top to bottom: PXRD for (E)-benzaldehyde oxime, 1-adamantane acetic acid and LAG product **3g** obtained using $MeNO_2$ and EtOH, respectively

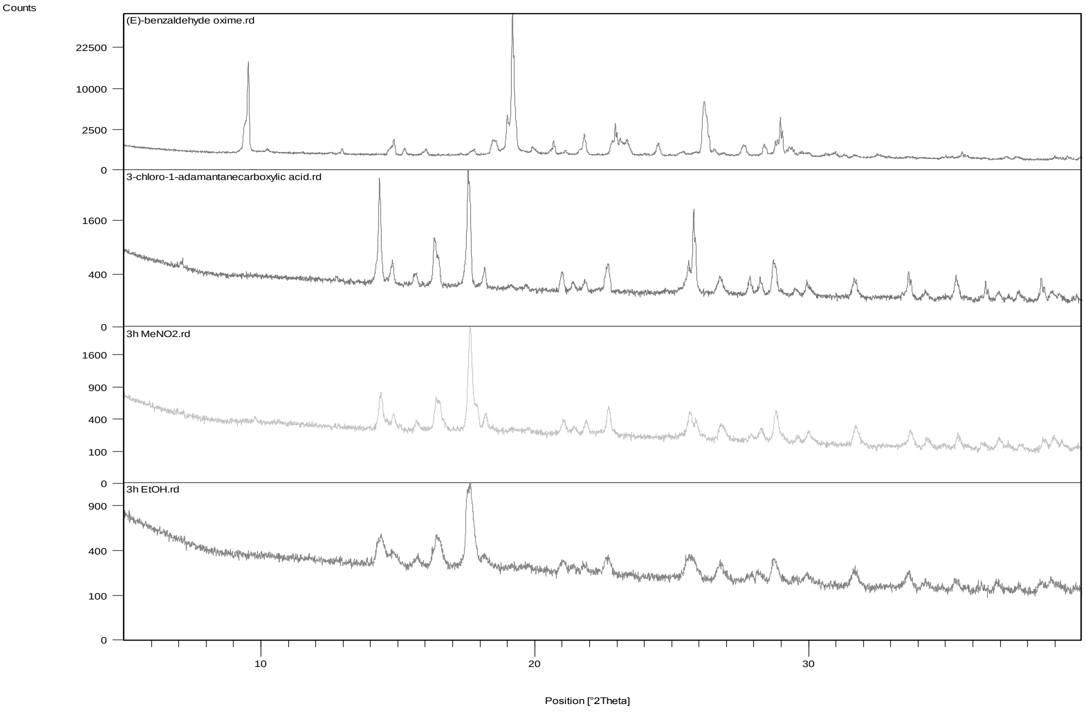

S34. From top to bottom: PXRD for (E)-benzaldehyde oxime, 3-chloro-1-adamantanecarboxylic acid and LAG product **3h** obtained using $MeNO_2$ and EtOH, respectively

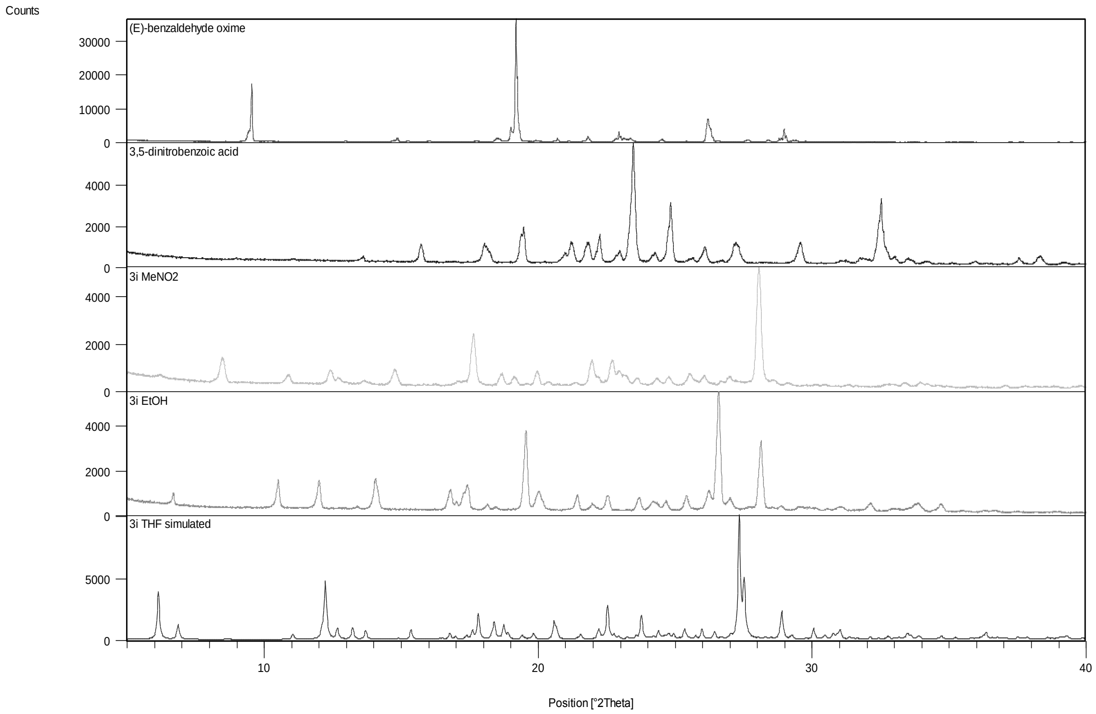

S35. From top to bottom: PXRD for (E)-benzaldehyde oxime, 3,5-dinitrobenzoic acid, LAG product **3i** obtained using $MeNO_2$ and EtOH and simulated PXRD of the THF solvate **3i,** respectively

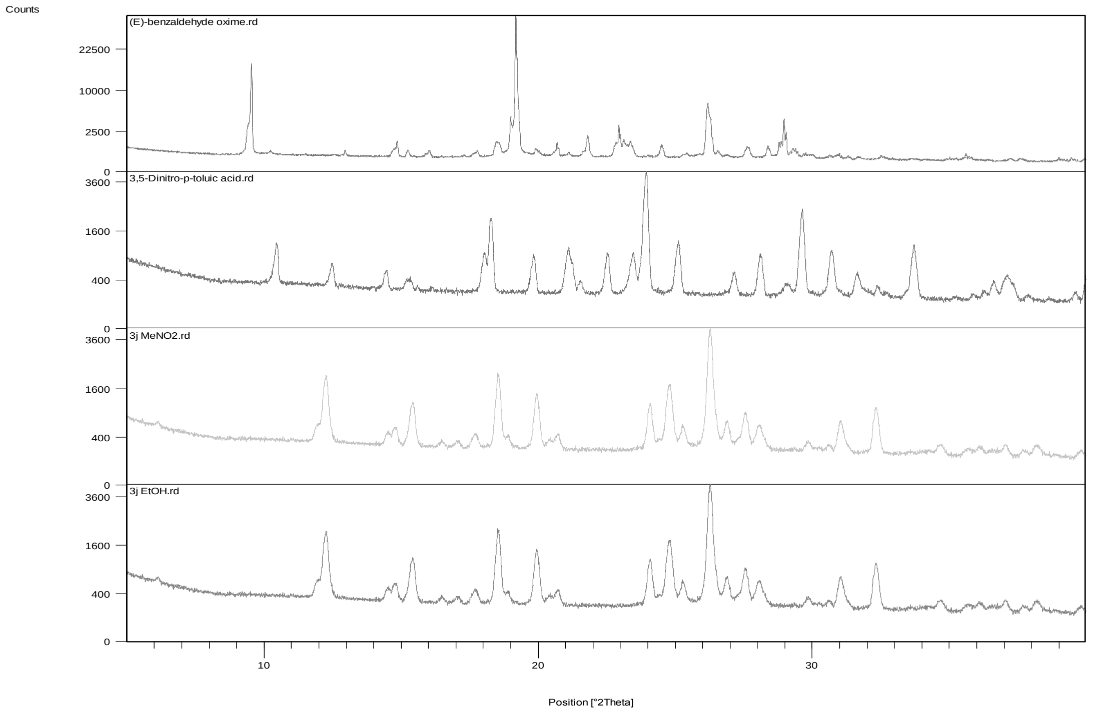

S36. From top to bottom: PXRD for (E)-benzaldehyde oxime, 3,5-dinitro-p-toluic acid and LAG product **3j** obtained using $MeNO_2$ and EtOH, respectively

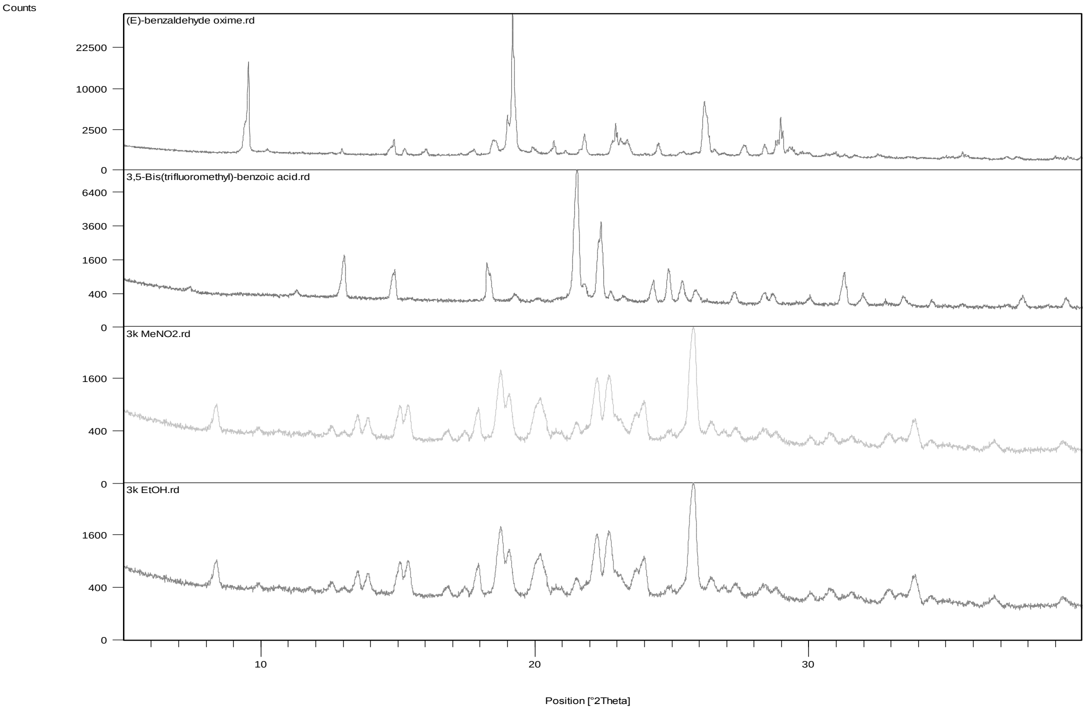

S37. From top to bottom: PXRD for (E)-benzaldehyde oxime, 3,5-bis(trifluoromethyl)-benzoic acid and LAG product **3k** obtained using $MeNO_2$ and EtOH, respectively

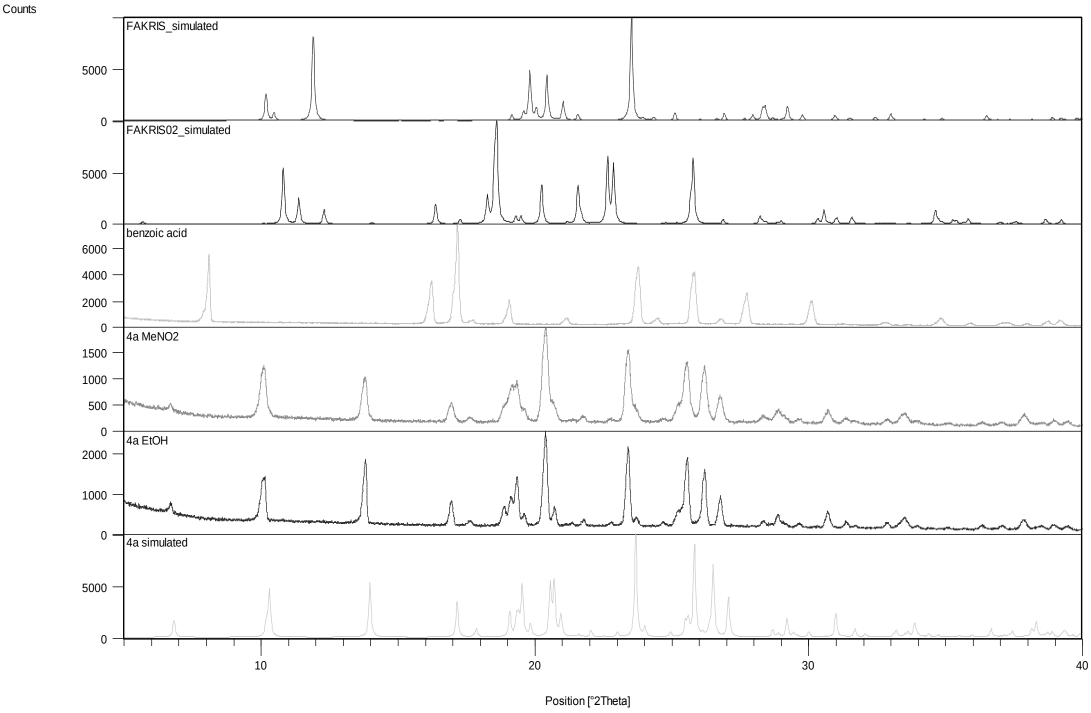

S38. From top to bottom: simulated PXRD for the two polimorphs of the acetophenone oxime, PXRD for benzoic acid, LAG product **4a** obtained using $MeNO_2$ and EtOH and simulated PXRD of **4a**, respectively

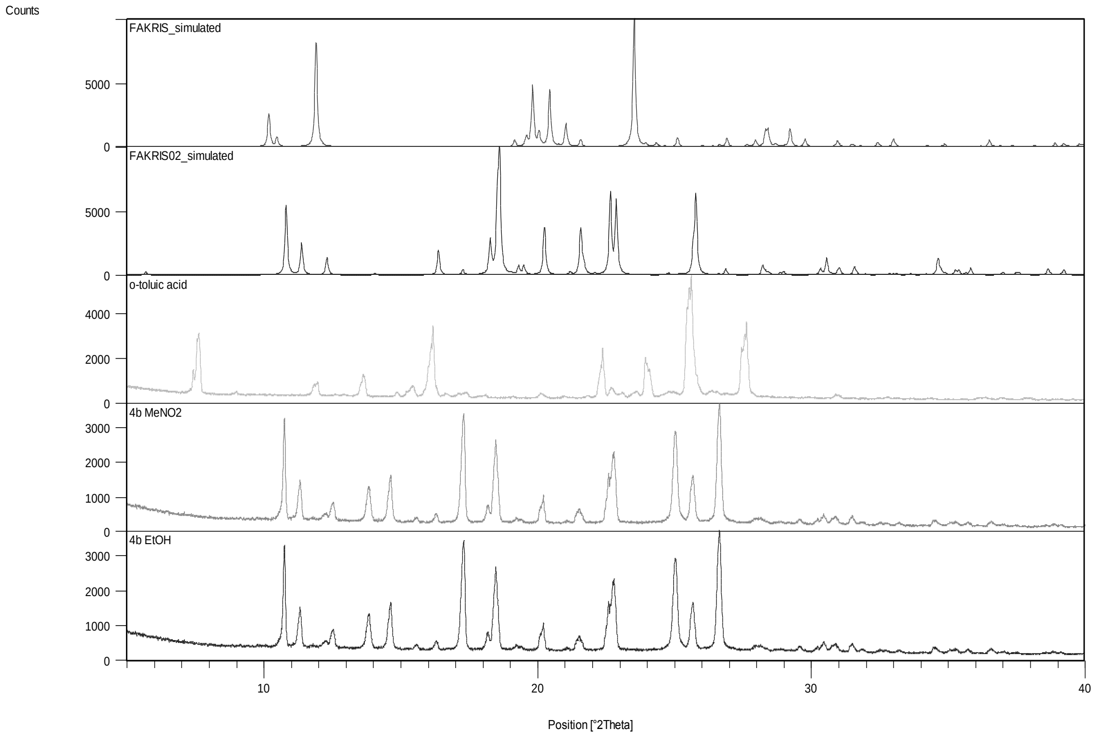

S39. From top to bottom: simulated PXRD for the two polimorphs of the acetophenone oxime, PXRD for o-toluic acid and LAG product **4b** obtained using $MeNO_2$ and EtOH, respectively

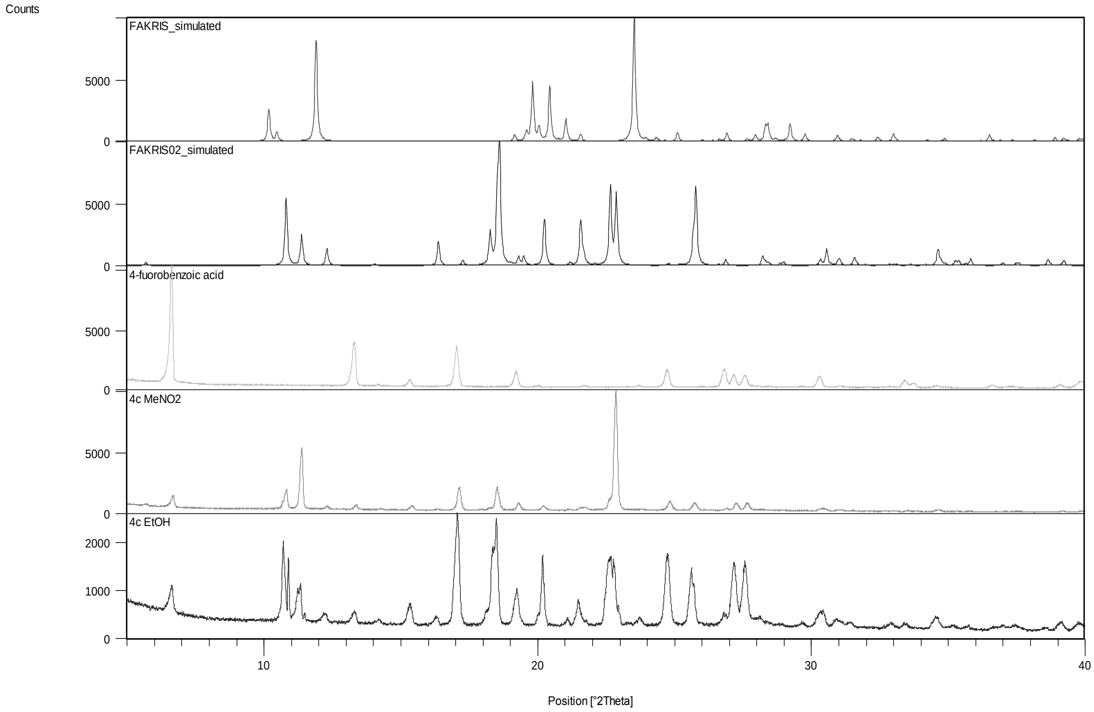

S40. From top to bottom: simulated PXRD for the two polimorphs of the acetophenone oxime, PXRD for p-fluorobenzoic acid and LAG product **4c** obtained using $MeNO_2$ and EtOH, respectively

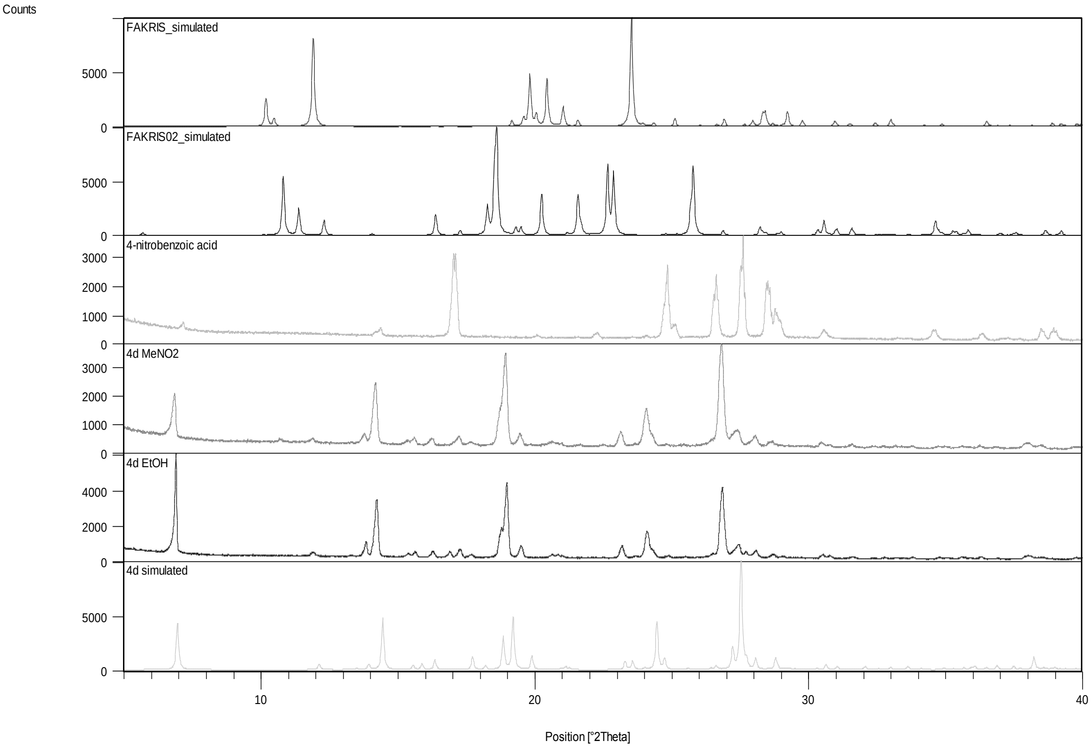

S41. From top to bottom: simulated PXRD for the two polimorphs of the acetophenone oxime, PXRD for benzoic acid, LAG product **4d** obtained using $MeNO_2$ and EtOH and simulated PXRD of **4d**, respectively

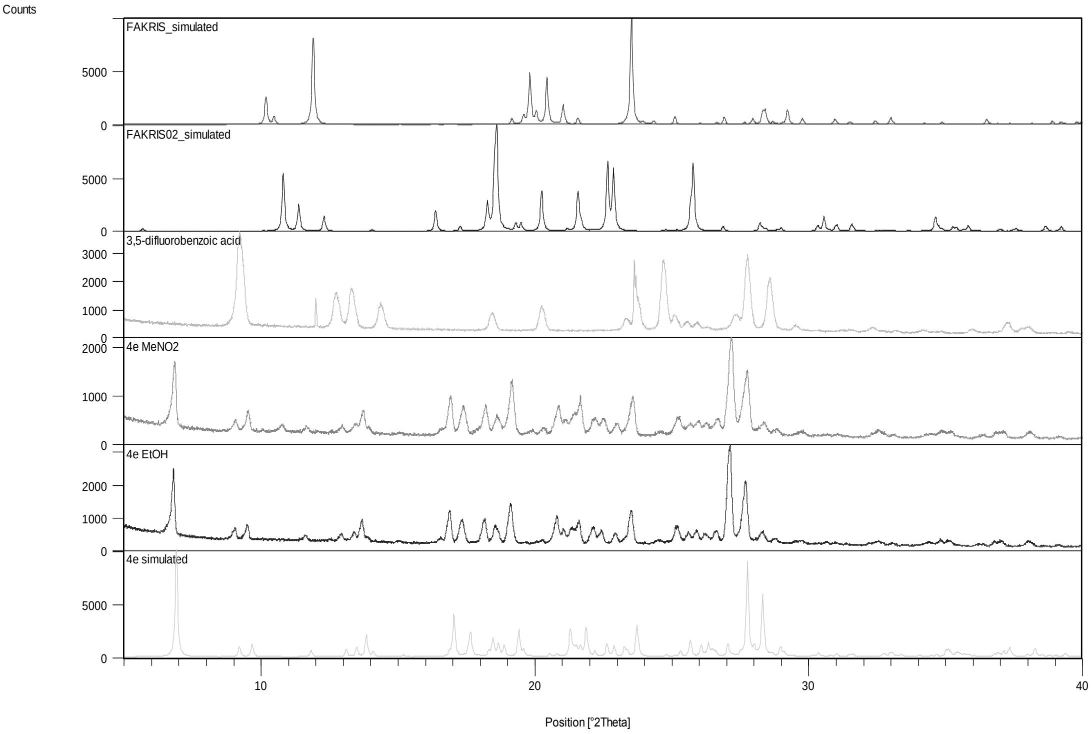

S42. From top to bottom: simulated PXRD for the two polimorphs of the acetophenone oxime, PXRD 3,5-difluorobenzoic acid, LAG product **4e** obtained using $MeNO_2$ and EtOH and simulated PXRD of **4e**, respectively.

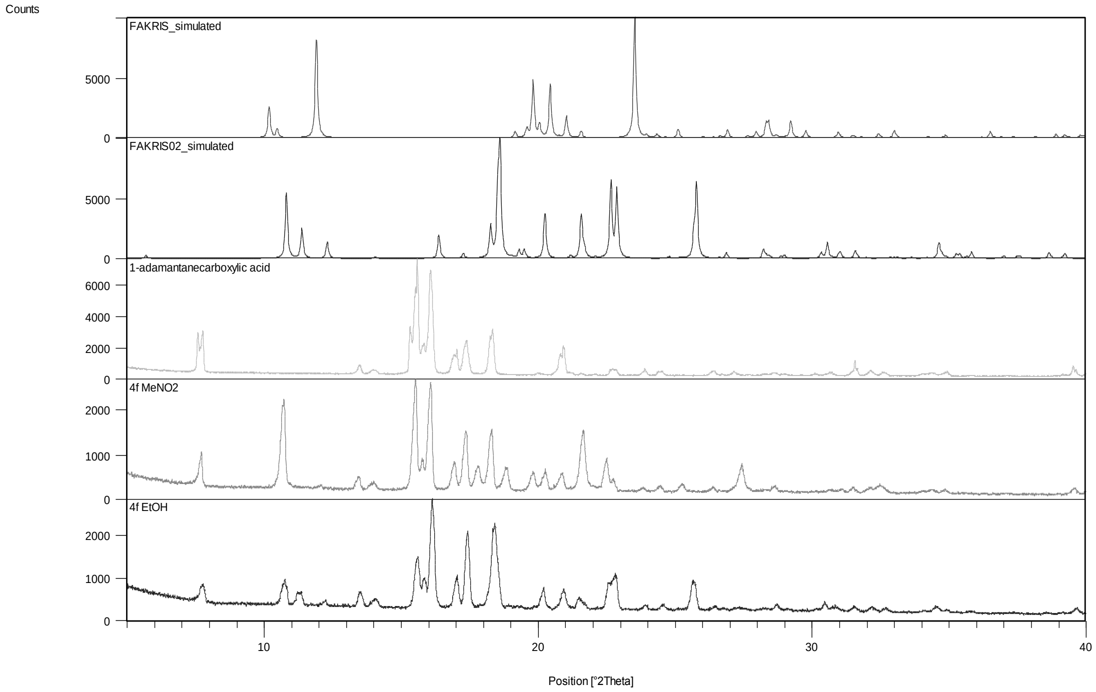

S43. From top to bottom: simulated PXRD for the two polimorphs of the acetophenone oxime, PXRD for 1-adamantanecarboxylic acid and LAG product **4f** obtained using $MeNO_2$ and EtOH, respectively

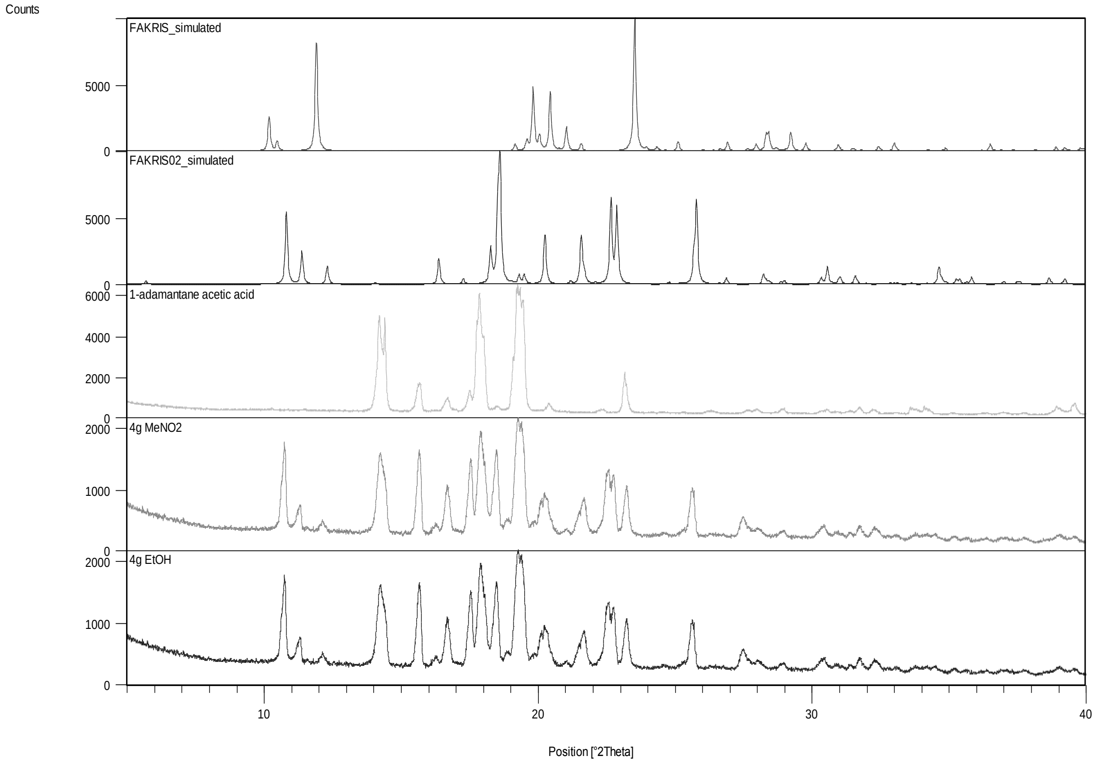

S44. From top to bottom: simulated PXRD for the two polimorphs of the acetophenone oxime, PXRD for 1-adamantane acetic acid and LAG product **4g** obtained using $MeNO_2$ and EtOH, respectively

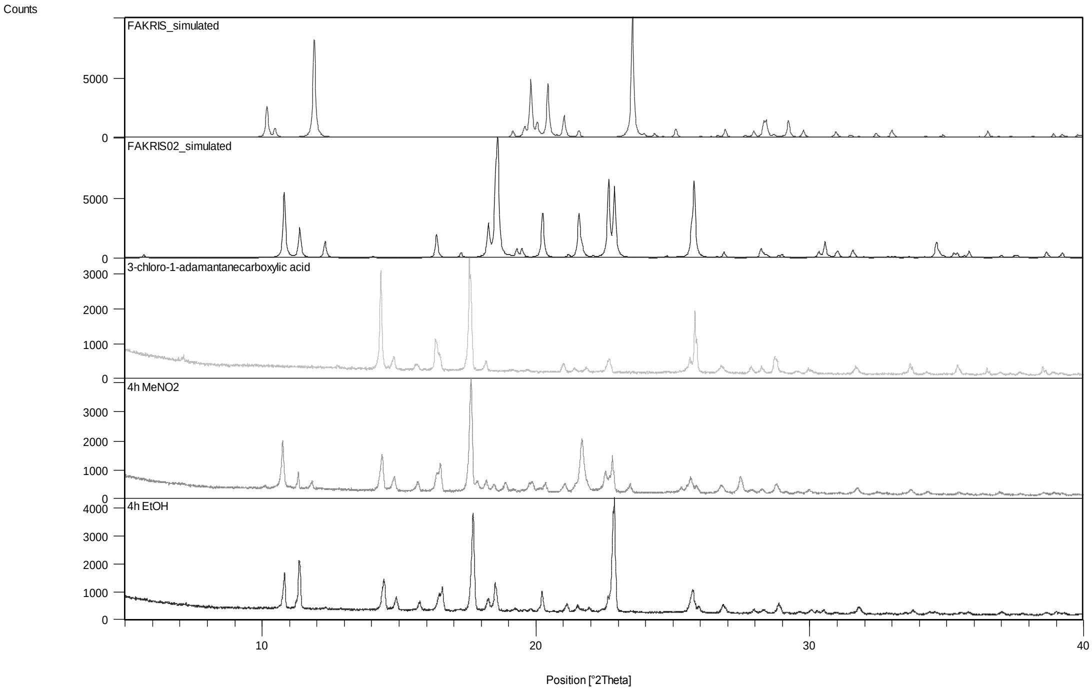

S45. From top to bottom: simulated PXRD for the two polimorphs of the acetophenone oxime, PXRD for 3-chloro-1-adamantanecarboxylic acid and LAG product **4h** obtained using $MeNO_2$ and EtOH, respectively

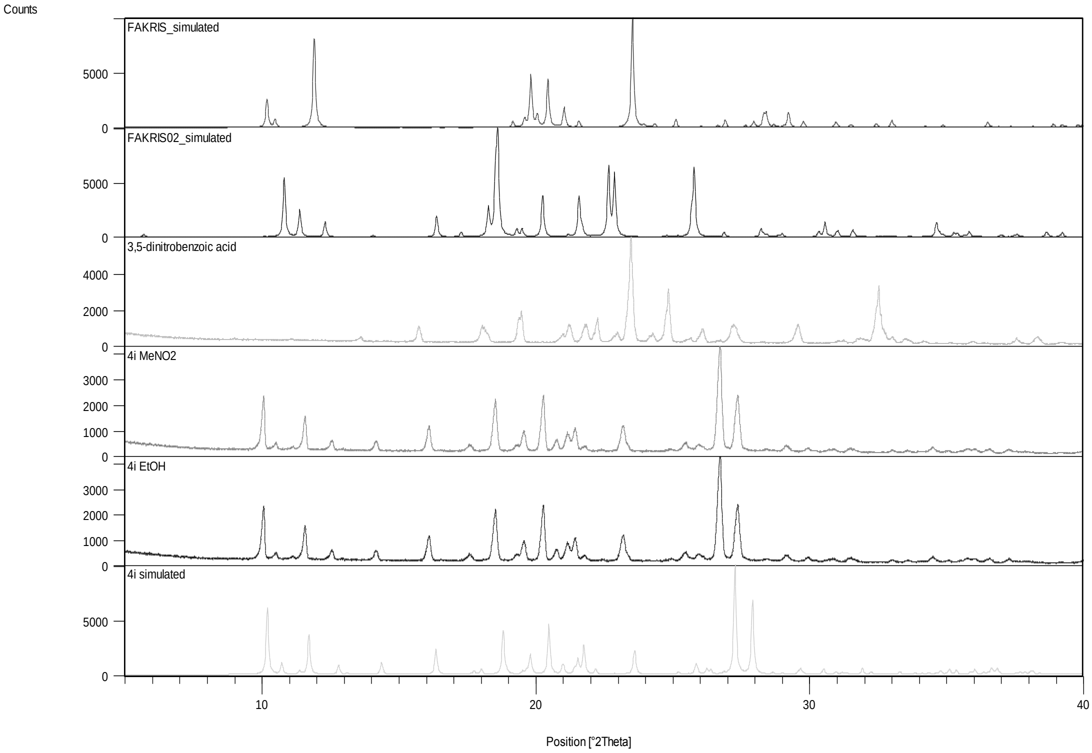

S46. From top to bottom: simulated PXRD for the two polimorphs of the acetophenone oxime, PXRD for 3,5-dinitrobenzoic acid, LAG product **4i** obtained using $MeNO_2$ and EtOH and simulated PXRD of **4i**, respectively

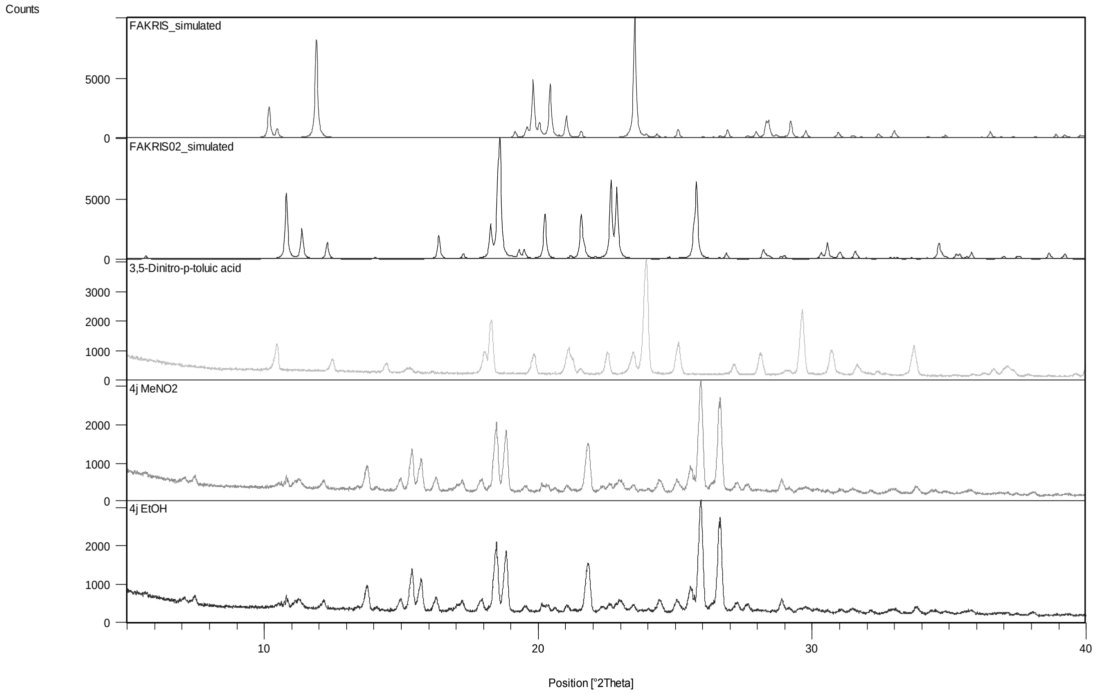

S47. From top to bottom: simulated PXRD for the two polimorphs of the acetophenone oxime, PXRD for 3,5-dinitro-p-toluic acid and LAG product **4j** obtained using $MeNO_2$ and EtOH, respectively

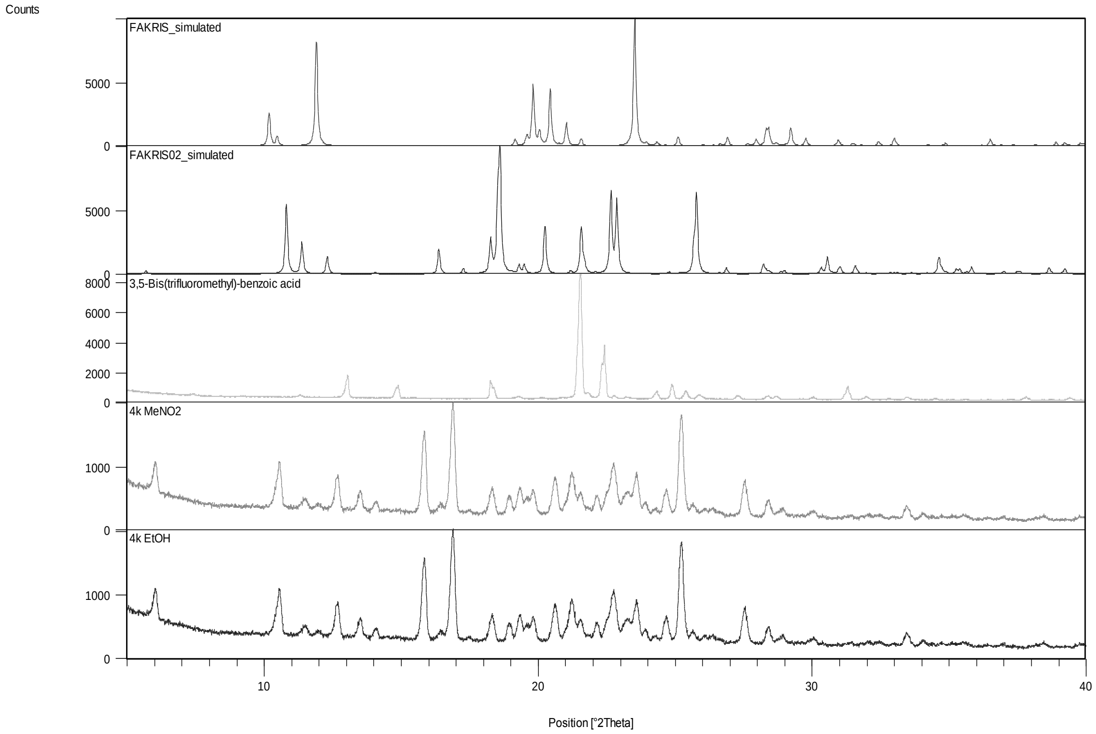

S48. From top to bottom: simulated PXRD for the two polimorphs of the acetophenone oxime, PXRD for 3,5-bis(trifluoromethyl)-benzoic acid and LAG product **4k** obtained using $MeNO_2$ and EtOH, respectively

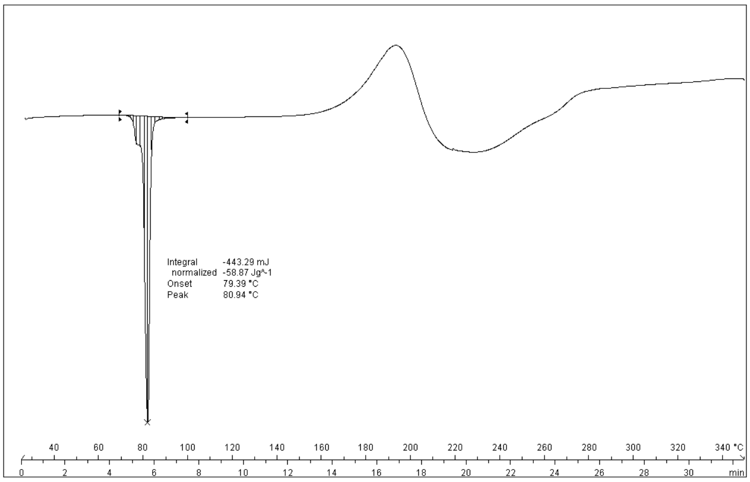

S49. DSC thermogram for the LAG product **1e**

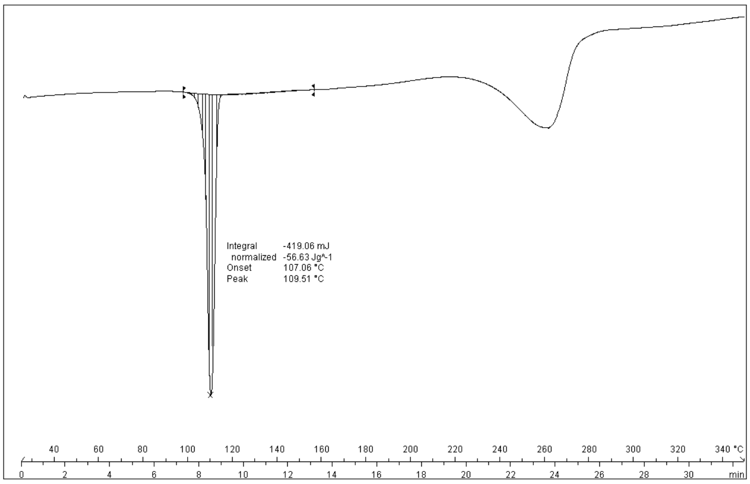

S50. DSC thermogram for the LAG product **1f**

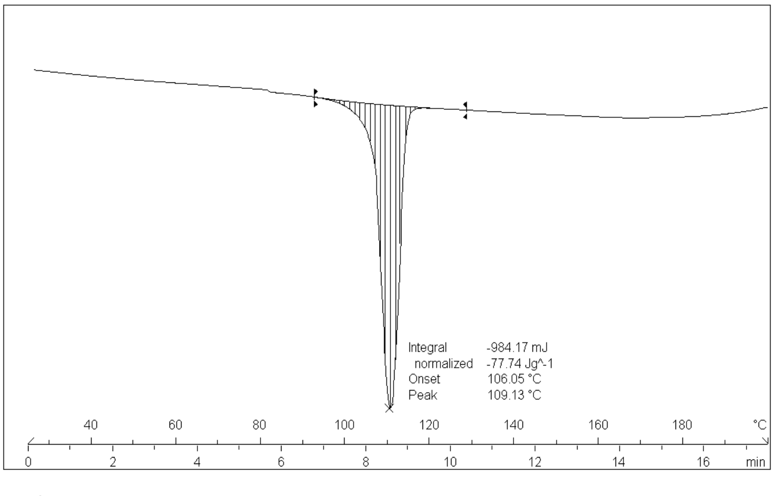

S51. DSC thermogram for the LAG product **1h**

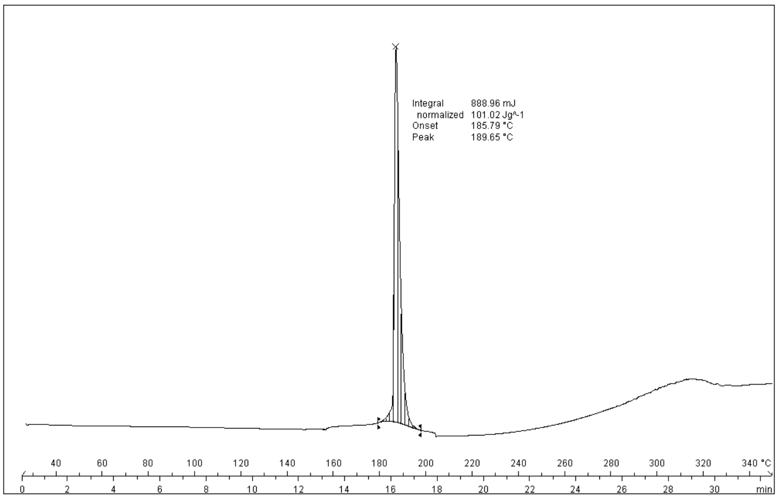

S52. DSC thermogram for the LAG product **1i**

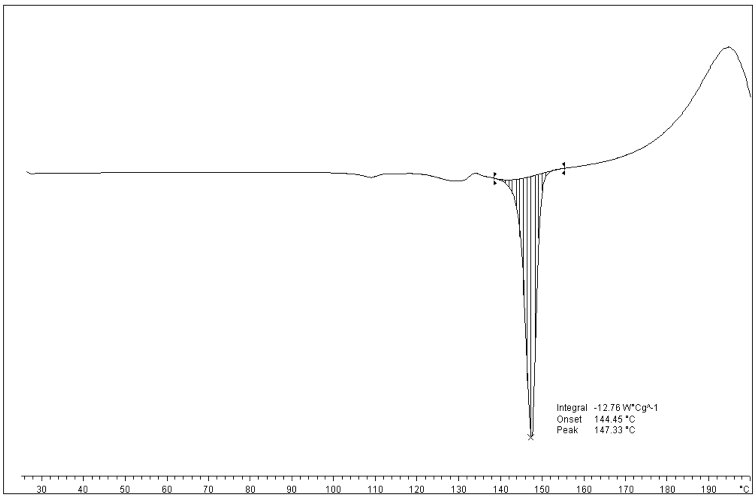

S53. DSC thermogram for the LAG product **1j**

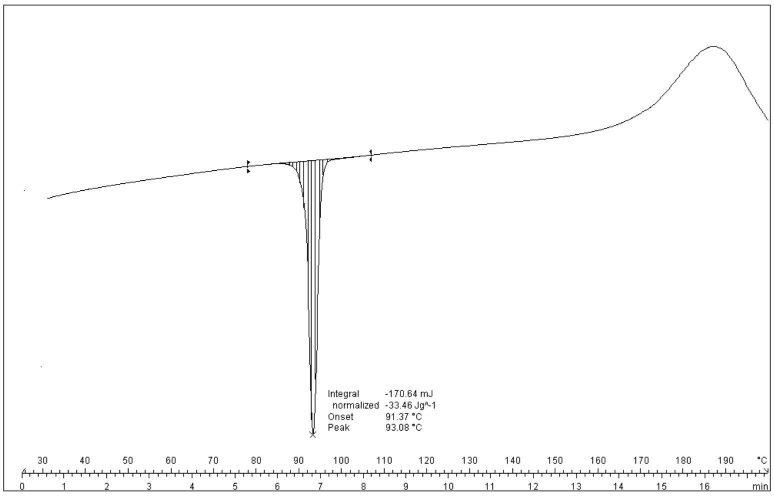

S54. DSC thermogram for the LAG product **1k**

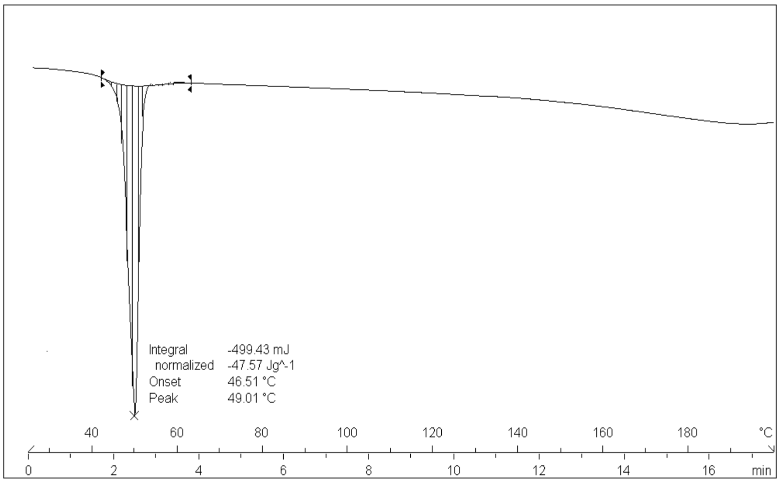

S55. DSC thermogram for the LAG product **2e**

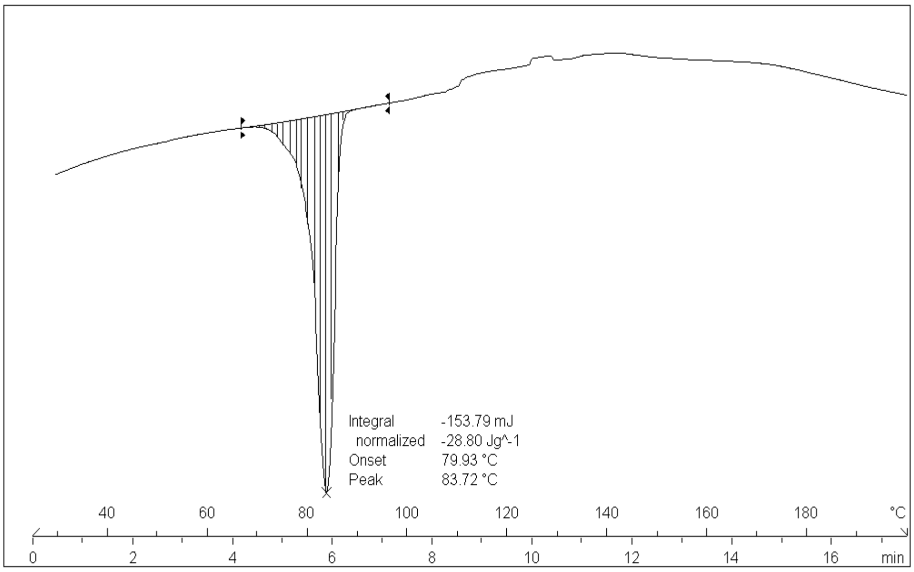

S56. DSC thermogram for the LAG product **2f**

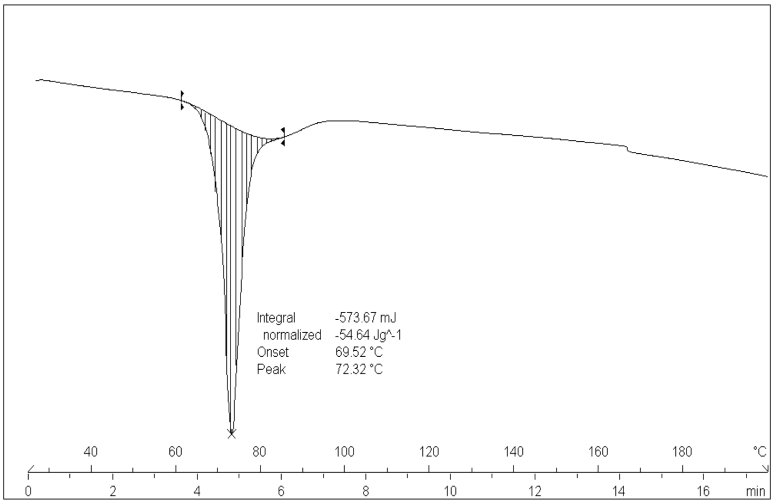

S57. DSC thermogram for the LAG product **2g**

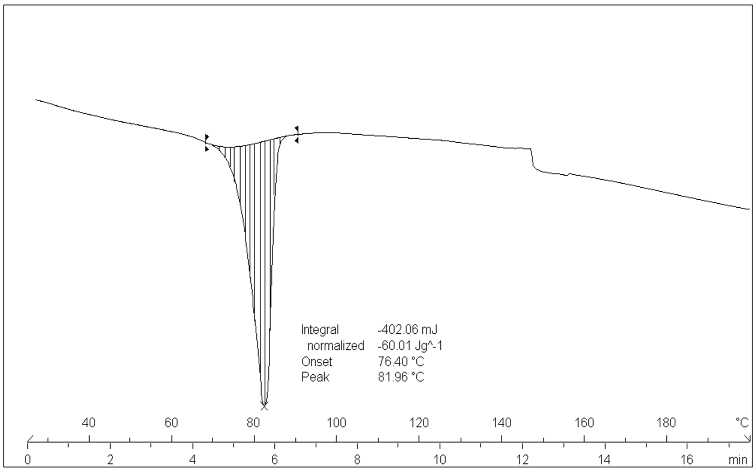

S58. DSC thermogram for the LAG product **2h**

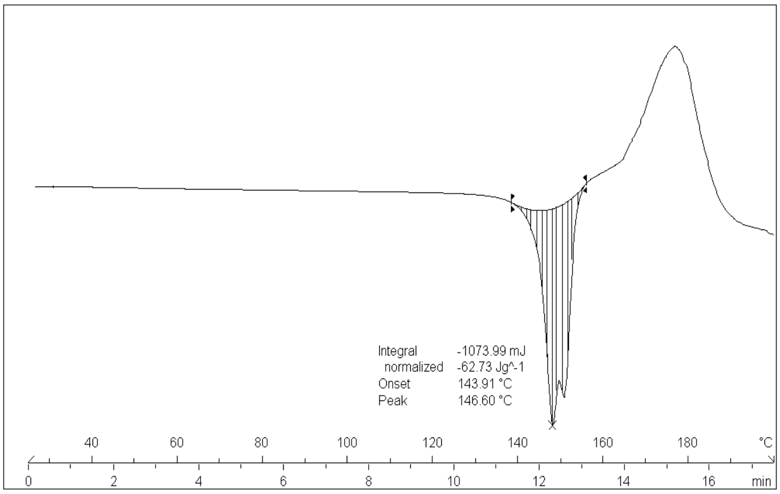

S59. DSC thermogram for the LAG product **2i**

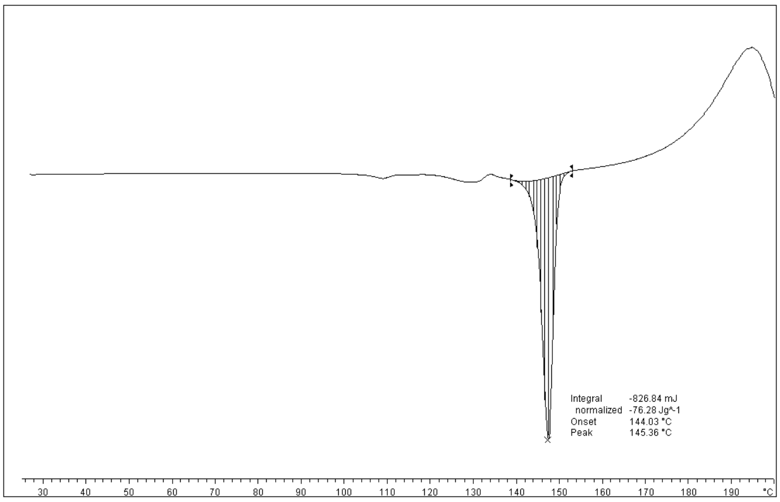

S60. DSC thermogram for the LAG product **2j**

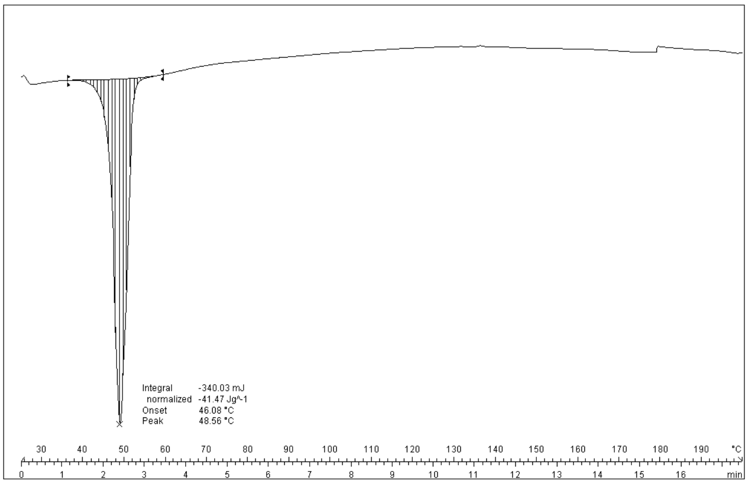

S61. DSC thermogram for the LAG product **2k**

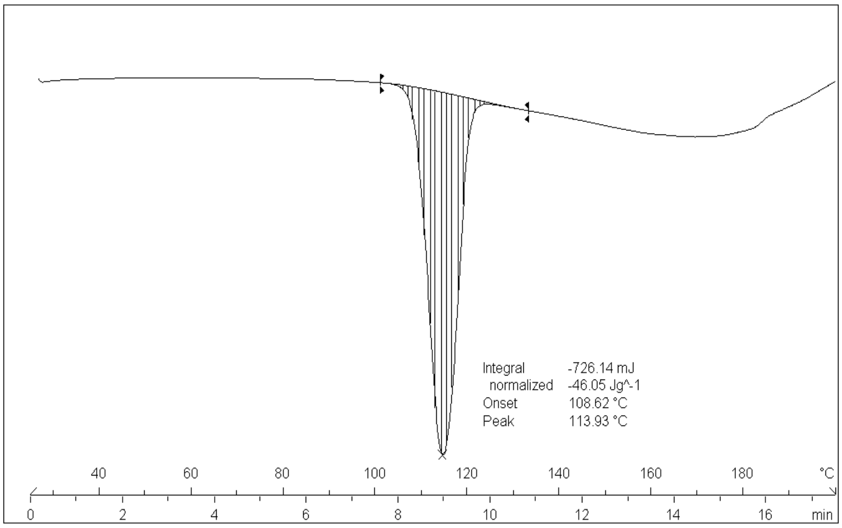

S62. DSC thermogram for the LAG product **3d**

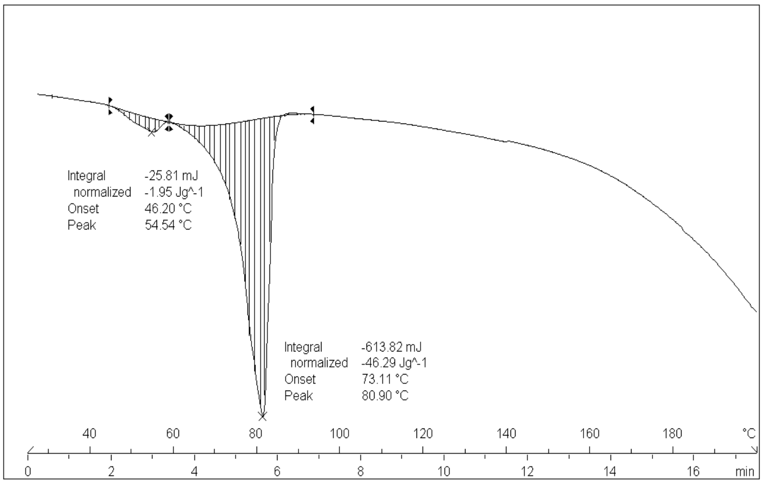

S63. DSC thermogram for the LAG product **3e**

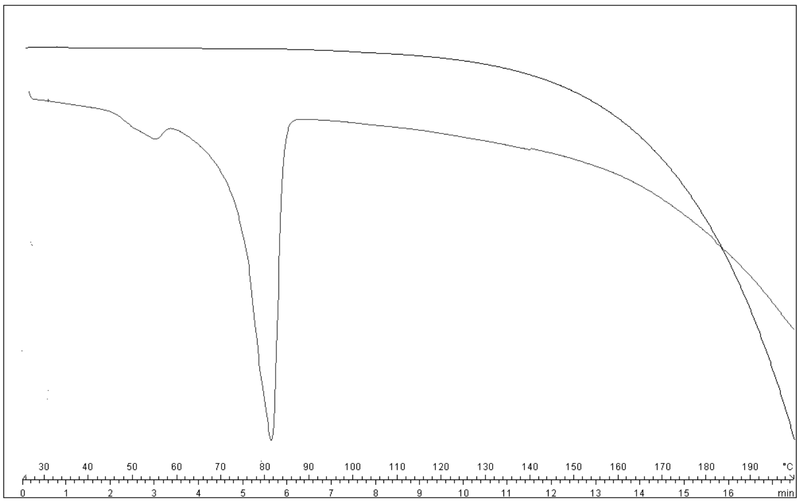

S64. DSC -TG thermograms for the LAG product **3e**

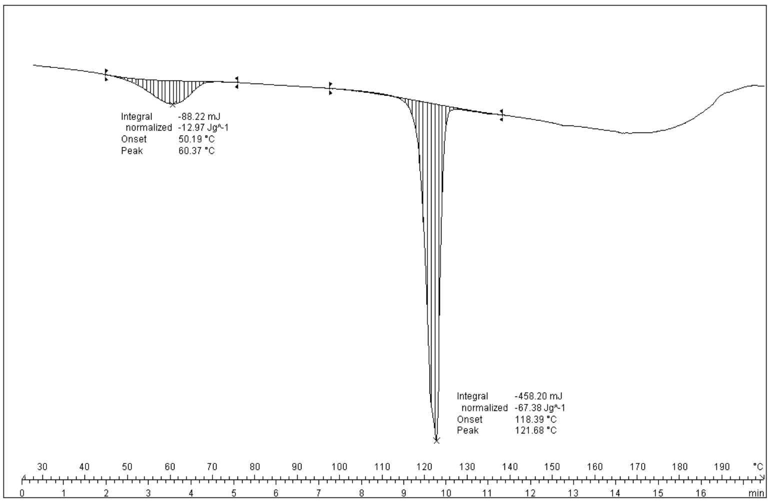

S65. DSC thermogram for the LAG product **3i** obtained using $MeNO_2$

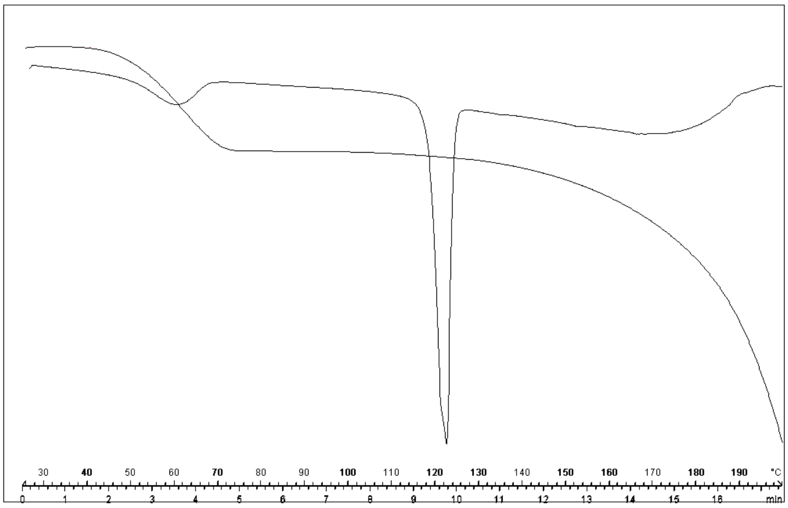

S66. DSC -TG thermograms for the LAG product **3i** obtained using $MeNO_2$

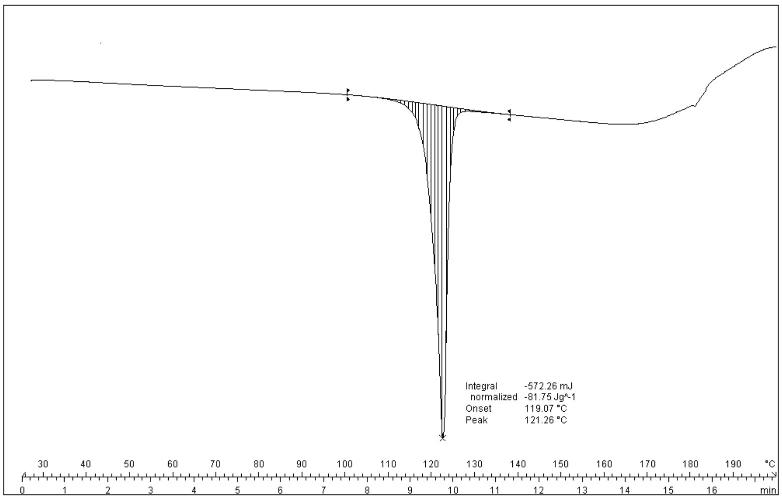

S67. DSC thermogram for the LAG product **3i** obtained using EtOH

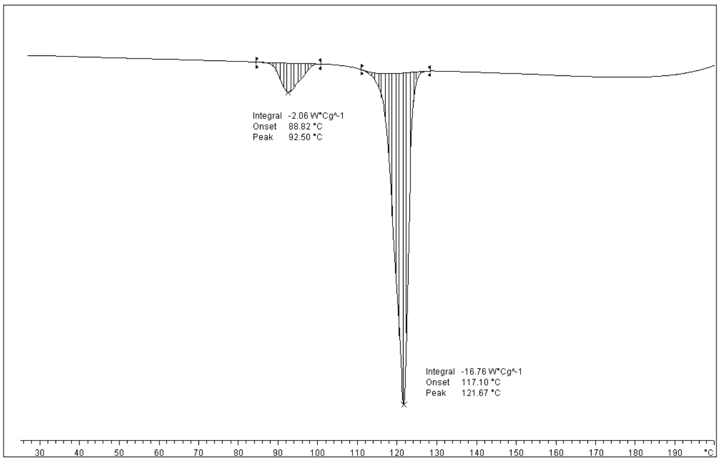

S68. DSC thermogram for the LAG product **3j**

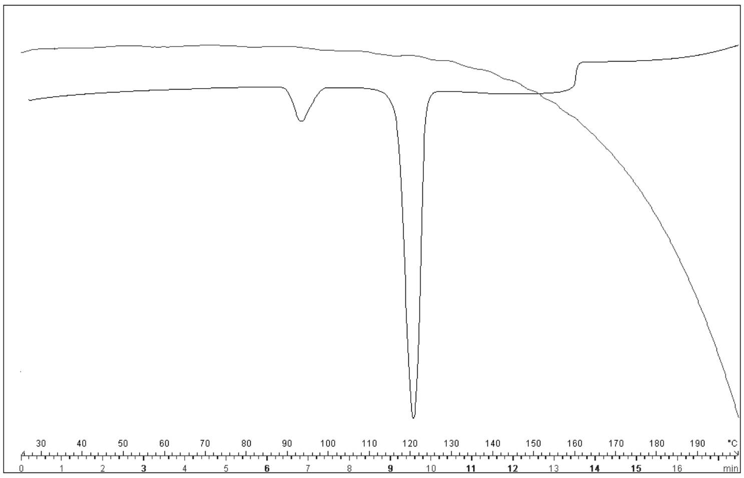

S69. DSC -TG thermograms for the LAG product **3j**

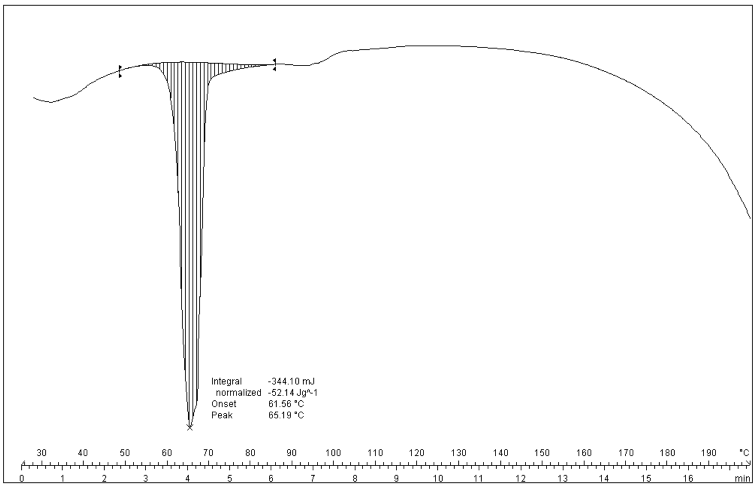

S70. DSC thermogram for the LAG product **3k**

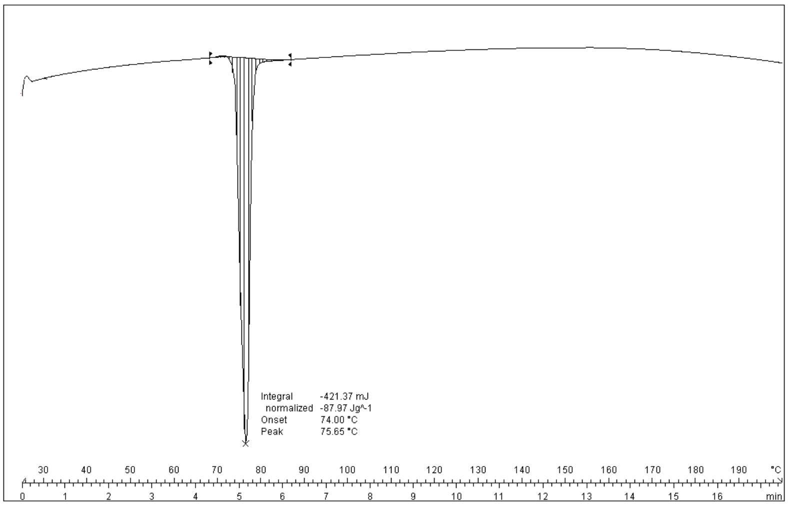

S71. DSC thermogram for the LAG product **4a**

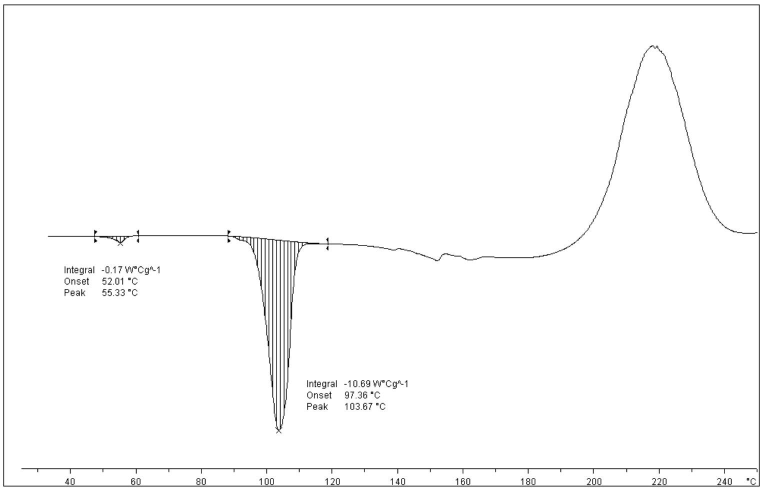

S72. DSC thermogram for the LAG product **4d**

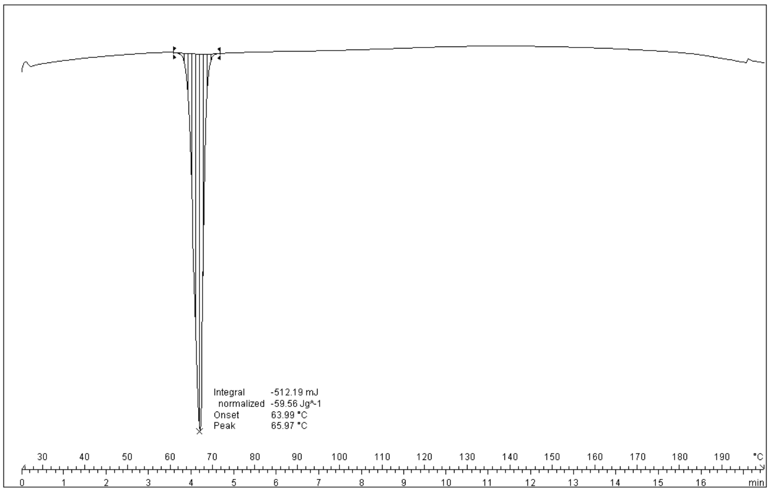

S73. DSC thermogram for the LAG product **4e**

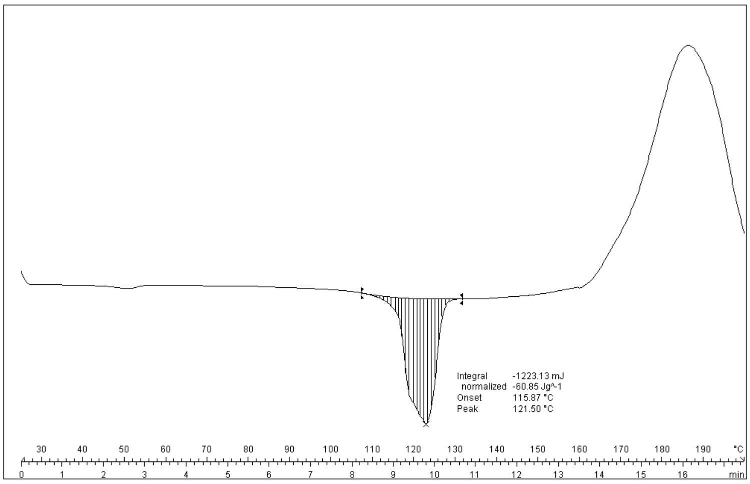

S74. DSC thermogram for the LAG product **4i**

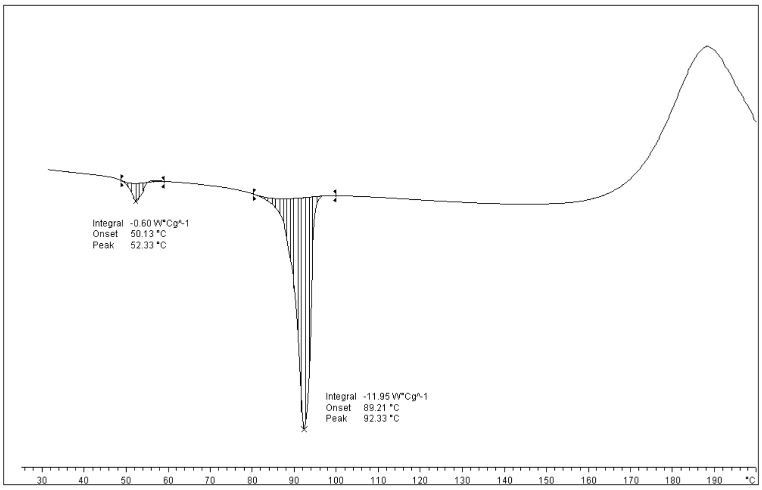

S75. DSC thermogram for the LAG product **4j**

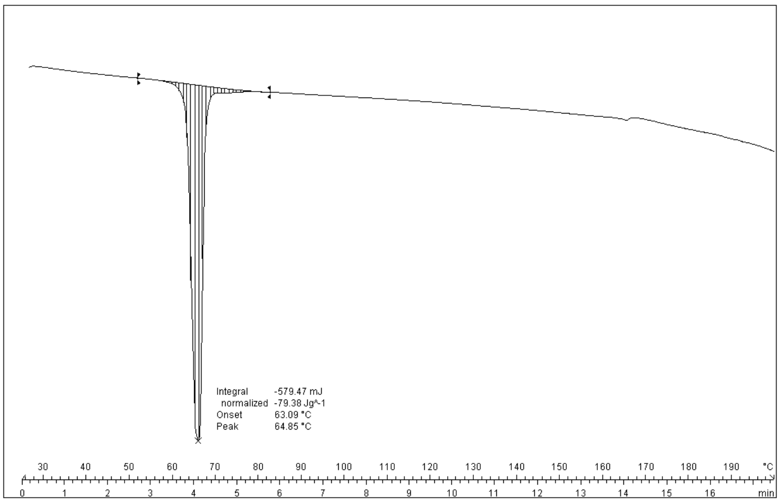

S76. DSC thermogram for the LAG product **4k**

Ringraziamenti - Acknowledgements

Vorrei ringraziare chi, direttamente o indirettamente, mi ha aiutato, ispirato o semplicemente incoraggiato.

Grazie a mamma e papà, ai quali dedico questa tesi.

Grazie alla Prof.ssa Alessia Bacchi e al Prof. Mauro Carcelli, ai quali sono grata per tutte le cose che mi hanno insegnato. Grazie a tutti i componenti del mio gruppo di ricerca: il Dott. Paolo Pelagatti, la Dott.ssa Dominga Rogolino, il Prof. Corrado Pelizzi. Grazie allo staff del laboratorio 077: Maria, Simone, Giulia, Cecilia, Silvio e Davide.

Grazie a Fabrizio, Francesco e Marco per la preziosa collaborazione.

Vorrei ringraziare tutti i componenti del Diparimento di Chimica Generale ed Inorganica dell' Università di Parma, con i quali ho condiviso lunghe giornate. In particolare la Dott.ssa Gnappi, Beppe & Marco, Marcello & Marcella, il team di beni culturali (Elisa, Michela, Francesca, Eleonora), tutti gli altri… Grazie mille ai tecnici del Laboratorio di Diffrattometria "Mario Nardelli": Daniele, Andrea e Ferdinando.

Grazie ai miei "colleghi" dottorandi: Valentina, Alessandro & Alessandro, Carla, Luca.

Per l'indimenticabile periodo trascorso a Cambridge… I would like to thank Prof. William Jones and Dr. Tomislav Friščić for allowing me to work in a fantastic team and in a so lovely town. I am grateful to Aurora and László for their helpful collaboration and incisive comments. Thank you to the team of the Material Chemistry Group: Catherine, Simon, Judas, Judit, Eloisa, Shyam, Daniele, Kashka, Andrew, Mark, Sharon, Daniel, Graeme, Peter, Filip, Lise and Chris with whom I have shared unforgettable days… and nights. Thank you to my italian-english friends Anna & Alessia and to my english housemates Marina & Gozde for the lovely time together in Cambridge and in London.

Thank you Giuseppe (che non segui le mode… le crei!!!)…un ringraziamento speciale per avermi guidato nei sotterranei dell'Università di Cambridge, per i mille sandwiches insieme e per aver condotto incolumi i miei averi a Milano attraverso la Manica!!!

Grazie a Giovanni & Sergio per le consulenze informatiche, all'indispensabile Sony Vaio e al mio efficientissimo Amilo…

Grazie alla nonna, a tutta la mia famiglia, ai libri, alla musica, al cinema, alle lezioni di pilates e a quelle di spinning…

… infine… grazie Rossella (sister a tutti gli effetti!!!)… senza di te sarei ancora in Stazione Centrale a Milano… con 40° e 40 Kg…

… semplicemente grazie …

“In the horizontal central strip there are birds and fish
equivalent to each other. We associate flying with sky,
and so for each of the black birds
the sky in which it is flying is formed by the four white fish
which encircle it. Similarly swimming makes us think of water,
and therefore the four black birds that surround
a fish become the water in which it swims."
M. C. Escher

Cover picture: **Sky and water I**
M. C. Escher, woodcut, 1938